UNIVERSIDAD DE GRANADA

ULTRASONICS LAB
TISSUE MECHANICS

FEASIBILITY OF USING TORSIONAL WAVES TO ASSESS VISCOELASTICITY OF CERVICAL TISSUE

BY:

Antonio Manuel Callejas Zafra

A THESIS SUBMITTED TO UNIVERSITY OF GRANADA
IN PARTIAL FULFILMENT OF THE REQUIREMENTS FOR THE DEGREE OF
DOCTOR OF PHILOSOPHY

ADVISOR:

Prof. Guillermo Rus Carlborg

PhD Program in Civil Engineering
Department of Structural Mechanics & Hydraulic Engineering
University of Granada
Granada (Spain)

September 2019

Editor: Universidad de Granada. Tesis Doctorales
Autor: Antonio Manuel Callejas Zafra
ISBN: 978-84-1306-361-4
URI: http://hdl.handle.net/10481/57975

Feasibility of using torsional waves to assess viscoelasticity of cervical tissue

Summary

The main objective of this thesis is to evaluate the viability of torsional waves to reconstruct mechanical parameters, elasticity, viscosity and open the way to nonlinearity, measuring in a human cervix *in-vivo* and enabling the technology as a diagnosis of preterm birth and other gestational disorders.

According to World Health Organization, 15 million babies are born preterm per year, this is, more than 1 in 10 newborns, and this number is rising in both developing countries and Europe. Worldwide, complications of preterm birth are the main cause of child mortality under five years of age. Prematurity often leads to long-term disabilities such as learning, visual, respiratory and hearing problems. On the opposite case, induction of labour is the main cause of fetal suffering. It happens in approximately 23.8% of cases worldwide, whilst the cesarean has to be carried out in 35.3% of the cases when the induction fails. Post-term pregnancy has associated maternal and perinatal complications. So far, no reliable clinical tool is available for quantitative and objective evaluation of cervical maturation. Current models based on cervical length, obstetric history, digital vaginal examination and echography of the cervix are not able to accurately predict a preterm birth with sufficient anticipation or the successful induction of labour. Even though there is an agreement that cervical ripening plays a fundamental role during pregnancy, histological changes and biomechanical properties of the cervix are not entirely characterized. The current lack of a clinical tool for the quantitative evaluation of the biomechanical parameters of the cervix is probably a barrier to advance in preventing spontaneous preterm birth and assessing the likelihood of successful induction of labour. Since 2012, the World Health Organization is encouraging to accelerate research into the causality of preterm birth, and to test effective approaches that would lead to save babies. Recently, elastography techniques are being put forward in the literature to assess quantitatively the stiffness of the cervix as a promising tool to estimate preterm birth risk, as well as to predict the success of induction of labour. However, important information about tissue state may be lost due to the neglect of viscosity because recent studies suggest that viscosity is another useful index of tissue health. Hence, deeper knowledge about the characterization of the viscoelastic behavior of cervical tissue could unleash its potential for additional clinical diagnostic information.

In this thesis, the emerging torsional wave elastography (TWE) technique, an alternative technique to dynamics methods, is proposed to provide a connection between torsional

waves and cervical viscoelasticity, facing towards the gestational assessment. In particular, we explore the robustness of the new proposed technique through a sensor sensitivity study involving two variables, the applied pressure and the angle of incidence sensor-phantom. This study falls into a preliminary analysis of the intra-operator dependency of the method. After the positive outcomes of the sensitivity analysis, a series of experiments were performed on *ex-vivo* human cervical tissue. The experiments aimed to combine information from rheometry and TWE providing two sources of data to find the most suitable rheological model that fits the cervical tissue behavior. Time-of-flight technique was employed to measure the shear wave group velocity, which is dependent on the envelope of the propagating wave. This study manifests that Kelvin-Voigt and its fractional derivative version models best describe torsional wave-interactions, demonstrating the dispersive nature of cervical tissue, in agreement with a common belief in literature.

On the one hand, a numerical approach was presented, whose purpose was to understand the torsional wave-tissue interactions, which may determine the optimal rheological model (elastic, Kelvin-Voigt or Maxwell models) that best describes the cervical tissue behaviour. The anatomy of the cervix has been taken into account in the models, considering epithelial and connective layers. The TWE probe transmits and receives a torsional wave that not only propagates along the surface of the cervix but also in-depth. Therefore, the wave not only interacts with the most superficial layer, the epithelium, but also with the immediately below layer made of connective tissue. Additionally, the boundary conditions of the numerical models implemented were determined via high-speed camera tests. A Probabilistic Inverse Problem (PIP) was described for ranking the most plausible model by comparing the *in-vivo* measurements in cervical tissues obtained from the TWE technique, with the synthetic signals from the 2D Finite Difference Time Domain (FDTD) wave propagation models. The results coincide with those obtained in the first contribution of this thesis, a Kelvin-Voigt model best describes torsional waves-tissue interactions. Once the viscoelastic model was selected, the parameters related to the model were reconstructed from 18 experimental measurements in pregnant women. The model parameters are epithelium shear modulus, epithelium viscosity, epithelium thickness, connective layer shear modulus and connective layer viscosity.

On the other hand, an experimental validation of the method proposed based on PIP approach to infer the KV viscoelastic properties from TWE technique was presented. In order to test the new reconstruction method, five *ad-hoc* oil-in-gelatine phantoms were fabricated with different gelatine batches, simulating the anatomy of the cervical tissue. The validation of the method was carried out by comparing the Kelvin-Voigt parameters reconstructed with the PIP in the five samples, with those inferred with the Shear Wave Elastography (SWE) technique (the gold standard in elastography) in each of the manufactured batched. In general, by the obtained results, it can be concluded that the viscoelastic parameters reconstructed by both procedures are similar, and therefore, this new method is validated for its use in the TWE technique. This work provides a valuable method that will allow a

better understanding of the changes in cervix viscoelasticity and lead to better methods of diagnosis of preterm birth and successful induction of labour.

The next contribution of this thesis is to propose a hyperelastic model based on Fourth Order Elastic Constants (FOEC) in the sense of Landau's theory to characterize the nonlinearity of cervical tissue and a validation of the mechanical parameters inferred in pregnant women. In particular, the nonlinear elastic properties of *ex-vivo* cervical tissue have been obtained for the first time by uniaxial tensile tests. The results of the proposed hyperelastic model were in good agreement with the results of the most used hyperelastic models in the literature, Mooney-Rivlin and Odgen models. Finally, the values of the shear modulus were extracted in the epithelial and connective layers directly by means of the FOEC proposed model, through the slope of the stress-strain curve in the linear region and through a combination of the two parameters of the Odgen model. The shear modulus was dependent on anatomical location of the cervical tissue. Variations of the same order of magnitude were obtained in the epithelial and connective layer after the reconstruction of the shear modulus with numerical models through the PIP procedure.

The last contribution of this thesis is to evaluate the feasibility and reliability of TWE technique to provide consistent data on the changes of the cervical tissue stiffness during pregnancy. The observed data support, firstly the hypothesis that torsional wave technique has the capacity to quantify cervical stiffness defined by its elastic modulus, and secondly, that shear stiffness decreases during pregnancy. The results showed, for the first time *in-vivo*, the viability of torsional waves to objectively measure cervical elasticity in pregnant women. Besides, the experimental results show that TWE technique is safe to be used in pregnant women. All the values obtained were far below the thresholds according to Food and Drug Administration guidelines reference parameters in Fetal Imaging and Other. The TWE technique might provide clinically relevant data on the cervical ripening in addition to that obtained from digital exploration and standard sonography.

Resumen

El principal objetivo de esta tesis es evaluar la viabilidad de las ondas de torsión para reconstruir parámetros mecánicos, elasticidad, viscosidad y abrir la puerta a la no linealidad, midiendo en cervix humano *in-vivo* y habilitando la tecnología como diagnóstico de parto prematuro y otros trastornos gestacionales.

Según la Organización Mundial de la Salud, 15 millones de bebés nacen prematuros al año, esto es, más de 1 de cada 10 recién nacidos, y este número está aumentando en Europa y en países en desarrollo. A nivel mundial, las complicaciones de parto prematuro son la principal causa de mortalidad infantil en menores de cinco años. La prematuridad a menudo conduce a discapacidades a largo plazo como el aprendizaje, problemas visuales, respiratorios y auditivos. En el caso opuesto, la inducción del parto es la principal causa de sufrimiento fetal. Ocurre en aproximadamente el 23.8% de los casos en todo el mundo, mientras que la cesárea debe realizarse en el 35.3% de los casos en los que falla la inducción. El embarazo postérmino tiene asociadas complicaciones maternas y perinatales. Hasta ahora, no hay una herramienta clínica disponible que sea fiable para la evaluación cuantitativa y objetiva de la maduración cervical. Los modelos actuales basados en la medida de la longitud cervical, historia obstétrica, el examen vaginal digital y la ecografía del cuello uterino no son capaces de predecir con precisión y suficiente anticipación el parto prematuro o el éxito de la inducción. Aunque existe un consenso acerca de que la maduración cervical desempeña un papel fundamental durante el embarazo, los cambios histológicos y las propiedades biomecánicas del cervix no se han caracterizado completamente. La falta actual de una herramienta clínica para la evaluación cuantitativa de los parámetros biomecánicos del cuello uterino es probablemente una barrera para avanzar en la prevención del parto prematuro y evaluar la probabilidad de éxito de la inducción del parto. Desde 2012, la Organización Mundial de la Salud está fomentando la aceleración de la investigación sobre la causalidad del parto prematuro y probando enfoques efectivos que conduzcan a salvar bebés. Recientemente, en la literatura se han presentado técnicas elastográficas para evaluar la rigidez del cervix cuantitativamente como una herramienta prometedora para estimar el riesgo de parto prematuro, así como para predecir el éxito de la inducción del parto. Sin embargo, se puede perder información importante sobre el estado del tejido debido a la no consideración de la viscosidad, ya que estudios recientes sugieren que la viscosidad es otro

biomarcador de la salud del tejido. Por lo tanto, un conocimiento más profundo sobre la caracterización del comportamiento viscoelástico del tejido cervical podría liberar su potencial para obtener información adicional de diagnóstico clínico.

En esta tesis doctoral, la técnica emergente de elastografía de ondas de torsión (TWE), una técnica alternativa a los métodos dinámicos, es propuesta para proporcionar una conexión entre las ondas de torsión y la viscoelasticidad cervical. En particular, exploramos la robustez de la nueva técnica propuesta a través de un estudio de sensibilidad del sensor de ondas de torsión que involucra dos variables, la presión aplicada y el ángulo de incidencia sensor-muestra. Este es un estudio preliminar para evaluar la dependencia intraoperadora del método. Después de los resultados positivos del análisis de sensibilidad, se realizaron una serie de experimentos en tejido cervical humano *ex-vivo*. Los experimentos tuvieron como objetivo combinar información de reometría y TWE, proporcionando dos fuentes de datos para encontrar el modelo reológico más adecuado que se ajuste al comportamiento del tejido cervical. Se empleó la técnica de tiempo de vuelo para medir la velocidad de grupo de las ondas de cizalla, la cual depende de la envolvente de la onda propagada. Este estudio manifiesta que los modelos viscoelásticos Kelvin-Voigt y su versión de derivada fraccional son los que mejor describen las interacciones de las ondas de torsión con el tejido, demostrando la naturaleza dispersiva del cervix, coincidiendo con las evidencias presentes en la literatura.

Por un lado, se presentó un enfoque numérico, cuyo propósito era comprender las interacciones de las ondas de torsión con el tejido, lo que determina el modelo reológico óptimo (modelos elástico, Kelvin-Voigt o Maxwell) que mejor describe el comportamiento del tejido cervical. La anatomía del cuello uterino se ha tenido en cuenta en los modelos, considerando las capas epitelial y conectiva. La sonda TWE transmite y recibe ondas de torsión que no solo se propagan a lo largo de la superficie del cuello uterino, sino también en profundidad. Por lo tanto, la onda no solo interactúa con la capa epitelial, sino también con la capa inmediatamente inferior, la capa conectiva. Además, las condiciones de contorno de los modelos numéricos implementados se determinaron mediante ensayos con cámara de alta velocidad. Se describió un problema inverso probabilista (PIP) para seleccionar el modelo más plausible al comparar las mediciones *in-vivo* en tejido cervical obtenidas con TWE, con las señales sintéticas de los modelos de propagación 2D implementados en diferencias finitas en el dominio del tiempo. Los resultados coinciden con los obtenidos en la primera contribución de esta tesis, el modelo Kelvin-Voigt es el que describe mejor las interacciones entre el tejido y las ondas de torsión. Una vez seleccionado el modelo viscoelástico, los parámetros relacionados con el modelo se reconstruyeron a partir de 18 mediciones experimentales en mujeres embarazadas. Los parámetros del modelo son el módulo de cizalla del epitelio, la viscosidad y el espesor de la capa epitelial y, el módulo de cizalla y la viscosidad de la capa conectiva.

Por otro lado, se presentó una validación experimental del método propuesto basado en el enfoque PIP para inferir las propiedades viscoelásticas Kelvin-Voigt usando la técnica

TWE. Para testear el nuevo método de reconstrucción, se fabricaron cinco muestras combinando diferentes lotes de gelatinas, para simular la anatomía del tejido cervical. La validación del método se realizó comparando los parámetros Kelvin-Voigt reconstruidos con el PIP en las cinco muestras, con los inferidos con la técnica de elastografía de ondas de cizalla (*gold standard* en elastografía) en cada uno de los lotes fabricados. En general, según los resultados obtenidos, se puede concluir que los parámetros viscoelásticos reconstruidos por ambos procedimientos son similares y, por lo tanto, este nuevo método está validado para su uso con la técnica TWE. Este trabajo proporciona un método valioso que permitirá una mejor comprensión de los cambios en la viscoelasticidad del cuello uterino durante el embarazo y conducirá a mejores métodos de diagnóstico para el parto prematuro y la inducción del parto.

La siguiente contribución de esta tesis consiste en proponer un modelo hiperelástico basado en las constantes elásticas de cuarto orden (FOEC) en el sentido de la teoría de Landau para caracterizar la no linealidad del tejido cervical y para validar los parámetros mecánicos inferidos en mujeres embarazadas. En particular, las propiedades elásticas no lineales del tejido cervical *ex-vivo* se obtuvieron por primera vez mediante pruebas de tracción uniaxiales. Los resultados del modelo hiperelástico propuesto eran similares a los resultados obtenidos con los modelos hiperelásticos más utilizados en la literatura, los modelos Mooney-Rivlin y Odgen. Finalmente, los valores del módulo de cizalla se obtuvieron en las capas epitelial y conectiva mediante el modelo FOEC propuesto, a través de la pendiente de la curva tensión-deformación en la región lineal y mediante una combinación de los parámetros del modelo Odgen. El módulo de cizalla dependía de la ubicación anatómica en el tejido cervical. Se obtuvieron variaciones del mismo orden de magnitud en las capas epitelial y conectiva después de la reconstrucción del módulo de corte con modelos numéricos a través del procedimiento de PIP.

La última contribución de esta tesis es la evaluación de la viabilidad y fiabilidad de la técnica TWE para proporcionar datos consistentes sobre los cambios en la rigidez del tejido cervical durante el embarazo. Los datos observados soportan, en primer lugar, la hipótesis de que la técnica TWE tiene la capacidad para cuantificar la rigidez cervical definida por su módulo elástico, y en segundo lugar, que la rigidez de cizalla disminuye durante el embarazo. Los resultados mostraron, por primera vez *in-vivo*, la viabilidad de las ondas de torsión para medir objetivamente la elasticidad cervical en mujeres embarazadas. Además, los resultados experimentales muestran que la técnica es segura para usarse en la práctica clínica. Todos los valores obtenidos estaban muy por debajo de los umbrales de los parámetros de referencia de la guía de la Administración de Alimentos y Medicamentos. La técnica TWE podría proporcionar datos clínicamente relevantes sobre la maduración cervical además de los obtenidos con la exploración digital y la ecografía estándar.

Acknowledgments

First of all I would like to express my gratitude to my academic advisor Dr. Guillermo Rus Carlborg, head of the Ultrasonics Laboratory of the Department of Structural Mechanics and Hydraulic Engineering. I will be eternally grateful to him, for believing in me and guiding me through this thesis. In particular, I thank his permanent patience, passion and dedication for research, for teaching me this perception and for constructive suggestions over the course of these years and, particularly during this last year. Everything mentioned above has played an imperative role in the successful of this dissertation and in my research career.

Second, I am very grateful to the universities and institutions that have received me as a guest researcher during the course of this project. I would like to express my gratitude to Carlos Martínez Bazán, professor of the Fluid Mechanics group in the University of Jaén, because he gave me the chance to use the high-speed camera belonging to his group, a key device for the development of this work. Also thanks to Juan de Vicente and José Morillas from the department of Applied Physics for contributing and collaborating with me in the experiments. Thank professor Nader Saffari, head of the Ultrasonics Group in the Department of Mechanical Engineering (UCL), not only because of the insightful meetings but also because I always felt welcome in my research stay in London. Finally, thanks to San Cecilio University Hospital in Granada, where we performed the women study.

Third, I thank all my colleagues of the Ultrasonics Laboratory Jorge Torres, Inas H. Faris, Antonio Gómez, Beatriz Blanco, Manuel Hurtado, Mariano Caruso, Rafa Marqués, Rafa Muñoz, Miguel Riveiro and José Cortés for making the everyday life at the laboratory enjoyable, and particularly for supporting me over the last few months, I am in debt to them. I would also like to specially thank Juan Melchor for his advice, insightful and thorough discussions, invaluable assistance and friendship.

Fourth, I would like to thank my family, for their patience, constant support and for helping me to overcome the most difficult times of this doctoral thesis. Specially to my parents Manuel and Aurora, my girlfriend Cristabel and my sister Ana, who have guided me on reaching this point in my life. I am in debt to them for their comprehension during these years.

Finally, this work has been supported by the Ministry of Educación, Cultura y Deporte of Spain through FPU grant FPU-15/01400.

Thesis

This thesis consist of a group of three contributions, shown below, which were published in a high-impact international journal.

1. A. Callejas, A. Gomez, J. Melchor, M. Riveiro, P. Massó, J. Torres, M. López-López and G. Rus. Performance study of a torsional wave sensor and cervical tissue characterization. *Sensors*, 17(9), 2017.
   The content of this contribution is shown in Chapters 6 and 11.

2. A. Callejas, A. Gomez, I. H. Faris, J. Melchor and G. Rus. Kelvin-Voigt parameters reconstruction of cervical tissue-mimicking phantoms using torsional wave elastography. *Sensors*, 19(15), 2019.
   The content of this contribution is shown in Chapters 8 and 13.

3. P. Massó, A. Callejas, J. Melchor, F. S. Molina and G. Rus. In-vivo measurement of cervical elasticity on pregnant women by torsional wave technique: a preliminary study. *Sensors*, 19(15), 2019.
   The content of this contribution is shown in Chapters 10 and 15.

The aforementioned papers were prepared in collaboration with co-authors. The author of this thesis is responsible for the major progress of work in these papers.

Abbreviations

ABC	Absorbing boundary conditions
ABS	Acrylonitrile Butadiene Styrene
ARF	Acoustic radiation force
ARFI	Acoustic radiation force impulse
CCI	Cervical consistency index
DE	Dynamic elastography
ECM	Extracellular matrix
FDA	Food and Drug Administration
FDTD	Finite difference time domain
FEAP	Finite element analysis program
FEM	Finite element model
FFT	Fast Fourier transform
FOEC	Fourth order elastic constants
GAGs	Glycosaminoglycans
GUI	Graphical user interface
HA	Hyaluronic acid
IFEA	Inverse finite element analysis
IQ	In-phase and quadrature
IQR	Interquartile range
ISPPA	Spatial peak pulse average intensity
ISPTA	Spatial peak temporal average intensity
KV	Kelvin-Voigt
KVFD	Kelvin-Voigt fractional derivative
M	Maxwell
MDG	Millennium development goals
MI	Mechanical index
MTL	Multiple track location
PBS	Phosphate buffered saline
PGs	Proteoglycans
PIP	Probabilistic inverse problem
PLA	Polylactic acid
pSWE	Point shear wave elastography

PTV	Particle tracking velocimetry
ROI	Region of interest
SCJ	Squamocolumnar junction
SDGs	Sustainable development goals
SE	Strain elastography
SMC	Smooth muscle cells
SPTB	Spontaneous preterm birth
sPTD	Spontaneous preterm delivery
SSI	Supersonic Imagine
SSR	Sum of squares of the regression
SST	Total sum of squares
SWE	Shear wave elastography
SWEI	Shear wave elasticity imaging
SWS	Shear wave speed
TE	Transient elastography
TH	Thickness
TOEC	Third order elastic constants
TOF	Time of flight
TU-SWE	Transurethral shear wave elastography
TWE	Torsional wave elastography
USTB	Ultrasound toolbox
WHO	World health organization
Z	Zener
3DMMRE	3D multifrequency magnetic resonance elastography

List of symbols

Symbol	Description
E	Young's modulus
μ	Shear modulus or Lame's second constant
ρ	Tissue density
K	Bulk modulus of elasticity or stiffness coefficient
c_s	Shear wave speed
ν	Poisson ratio
σ	Stress
ε	Strain
F_r	Acoustic radiation force
α_t	Tissue absorption
I	Spatial peak temporal average intensity or inertia moment
c	Speed of sound in tissue
$\mathbf{u}$	Vector of displacements
$\mathbf{f}$	Body force vector
λ	Lame's first constant, principal stretch or wavelength
σ_{ij}	Stress tensor
ε_{ij}	Strain tensor
δ	Kronecker delta or stress-strain phase lag
p	Hydrostatic pressure
v	Volumetric strain
τ_{ij}	Deviatoric stress tensor
d_{ij}	Deviatoric strain tensor
η	Shear viscosity
η^v	Volumetric viscosity
W	Strain energy
A	Third order elastic constant of Landau
D	Fourth order elastic constant of Landau
$tr\varepsilon$	Deformation trace
I_1	First invariant of strain
I_2	Second invariant of strain
I_3	Third invariant of strain
S_{ij}	Second Piola Kirchoff stress tensor
F	Deformation gradient tensor of volume force density
J	Determinant of the deformation gradient tensor or misfit function between model and observations
Ψ	Strain energy function
c_1, c_2	Mooney-Rivlin constants
μ_r	Infinitesimal shear modulus
α_r	Stiffening parameter

Symbol	Description
Θ	Torsion rotation
t	Time
ω	Natural frequency
n	Number of piezoelectric elements
a, b	Plane dimensions of the piezoelectric ceramic
d	Distance from the center of rotation
l^{eff}	Effective length between piezoelectric ceramics
h	Height of the cylinder or the ring
r	Radius of the cylinder or the ring or Pearson's correlation coefficient
m	Thickness of the ring in the radial direction
w/w	% Weight per weight
$^{\circ}C$	Degrees Celsius
G^*	Complex shear modulus
G'	Storage modulus
G''	Viscous or loss modulus
α	Fractional derivative power
μ_1, μ_2	Zener elasticities
σ_0	Stress amplitude
γ_0	Strain amplitude
∇u	Gradient of the displacement field
r, θ, z	Components in cylindrical coordinates
$\dot{v}_\theta$	Derivative of the velocity
$\ddot{u}_\theta$	Second derivative of the displacement
Δt	Time step
$\Delta r, \Delta z$	Space step of discretization
α_c	Correction factor
c_r	Factor of efficiency
Z	Shear impedance or acoustic impedance
t_T	Total time of simulation
n_{ABC}	Number of absorbing boundary conditions elements
N	Total population or random points
$\mathcal{O}$	Observations
$o_i(t)$	Observations signal vectors
$\mathfrak{D}$	Space of observations
$o^m(t)$	Model signals
$\mathcal{M}$	Model parameters
$\mathfrak{H}$	Manifold
$f(x)$	Information density function
$P(...), p(...)$	Probability
f^o	Experimental observations of the system
f^m	Numerical observations of the system
$\mathcal{H}$	Hypotheses of the models
$k, k', k_1, k_2, k_3, k_4$	Normalization constants
$\tilde{m}_i$	Change of variable
$\mathcal{N}$	Gaussian distribution

Symbol	Description
C	Covariance matrix
$\Delta\phi$	Phase change
ES	Effect size
F_c	Center frequency
P_0	Maximal acoustic pressure
T	Transmission coefficient
Z_{air}, Z_{water}	Acoustic impedance of the air and water
R^2	Coefficient of determination
p	P-value
$\mathbf{T}$	Piezoelectric material's stress
$\mathbf{C}_E$	Piezoelectric stiffness matrix
$\mathbf{S}$	Piezoelectric material's strain
$\mathbf{e}$	Piezoelectric coupling coefficient matrix
$\mathbf{E}$	Electric field
$\mathbf{D}$	Charge-density displacement
$\varepsilon_{\mathbf{S}}$	Permitivity coefficient matrix
L_{AB}	Length of the piezoelectric element in z direction
$\bar{\mathbf{E}}_3$	Average value of the electric field
$\mathbf{d}$	Piezoelectric coefficients matrix

Contents

List of Figures

List of Tables

Part I

INTRODUCTION

1

Context and motivation

The Sustainable Development Goals (SDGs), based on the achievements of the Millennium Development Goals (MDG), are an universal call for the adoption of measures by all countries to improve life for future generation [8, 9]. The reduction of preterm delivery was an urgent priority according to MDG 4, notwithstanding, only a few countries have achieved the goal, reducing child deaths by two thirds [10]. Despite the small progress, by 2030 the third SDG, "Good Health and Well-Being", is to reduce global maternal mortality rate to less than 70 per 100000, the neonatal mortality to at least 12 per 1000 births and the mortality of children under 5 years to 25 per 1000 live births [11].

Worldwide, according World Health Organization (WHO), 15 million babies are born preterm per year, this is, more than 1 in 10 newborns, and this number is rising in both developing countries and Europe [12]. Preterm birth, also known as premature birth, is the birth of a baby that occurs at a gestational age of less than 37 weeks, unlike the normal about 37-40 weeks. Complications of preterm birth are the main cause of child mortality under five years of age, dying a million children every year [13]. Prematurity often leads to long-term disabilities as learning, respiratory distress syndrome, visual and hearing problems. Clinical and social risk factors of preterm birth have been identified to develop feasible and cost-effective care measures to save children [12]. Nonetheless, a high proportion of spontaneous preterm birth remains unpredictable. Despite there is an agreement that cervical ripening plays a fundamental role during pregnancy, histological changes and biomechanical properties of the cervix are not entirely characterized. A better understanding of these causes would offer effective interventions to prevent premature birth, and consequently, the reduction of infant mortality and morbidity [14].

On the opposite case, post-term pregnancy is a singleton pregnancy that occurs at a gestational age of more than 42 weeks. Associated complications are divided into perinatal and maternal. Relative to the first, intrauterine infection, macrosomia, meconium staining of the amniotic fluid and high perinatal mortality rated compared with term pregnancies [15]. Maternal complications include perineal injury, labor dystocia and cesarean delivery. There are two actions to manage post-term pregnancy: expectant management with serial fetal monitoring and elective induction of labour [16]. Compared with expectant management, induction of labour is associated with reduced perinatal deaths and no increase in the rate of cesarean section [16, 17]. Induction of labour is the treatment or process to start labour. According to the recommendations of the WHO, pregnancy is induced by manually rupturing the amniotic membranes or by administering drugs that contain oxytocin or prostaglandins to the woman [18]. Nowadays, this happens in approximately 23.8% of cases worldwide, whilst the cesarean has to be carried out in 35.3% of the cases when the induction fails, increasing the risk in future pregnancies [19, 20]. Induction of labour is the main cause of fetal suffering, and is hypothesized to be conditioned to the elastic feasibility of the cervical tissue. A functional anticipation (even of a few days) diagnostic tool would open the door to a new generation of preventive screenings and personalized interventions.

The understanding of changes in the biomechanical state of the cervix during the gestation process is a challenging problem apart from being a pressing need for obstetricians as a potential preterm birth and induction of labour prevention tool [21]. Bishop's score is the current standard method to assess the odds of spontaneous preterm delivery and the success of the induction. This procedure consists in subjective palpation of the cervix by the practitioner, and is therefore a highly subjective and unreliable method [22, 23]. Measurement of cervical length by transvaginal ultrasonography at approximately 18 weeks of gestation is currently used to predict the risk of preterm labor. A short cervix identified at this time point is associated with a significantly elevated risk of preterm delivery. Numerous studies have shown an inverse relation between cervical length measured by transvaginal ultrasonography and frequency of preterm birth [24, 25]. Notwithstanding, this method yields an unsatisfactory percentage of accurate predictions around 60%, and some patients whose cervical length is short do not have a preterm delivery. Nonetheless, Bishop's score has proven to be more reliable than echographic assessment of cervical length at term in predicting the success of labour induction [26]. Current models based on cervical length, obstetric history, digital vaginal examination and echography of the cervix are not able to accurately predict a preterm birth with sufficient anticipation, and there is a lack of evidence on how to prevent preterm delivery [27, 28]. Despite there is an agreement that cervical ripening plays a fundamental role during pregnancy, histological changes and biomechanical properties of the cervix are not entirely characterized. The current lack of a clinical tool for the quantitative evaluation of the biomechanical parameters of the cervix is probably a barrier to advance in

preventing spontaneous preterm birth [29]. Since 2012, the WHO is encouraging to accelerate research into the causality of preterm birth, and to test effective approaches that would lead to save babies.

Recently, elastography techniques are being put forward in literature to assess quantitatively the stiffness of the cervix as a promising tool to estimate preterm birth risk, as well as to predict the success of labor induction [30, 31, 32, 33, 34]. Strain elastography or quasi-static elastography is a technique for imaging of strain and elastic modulus changes in soft tissues. The tissue is manually compressed with the probe and the strain is quantified as the ratio of the anterior-posterior distance, before (reference configuration) and after compression application. Finally, by measuring the stress applied on the tissue and performing corrections due to the nonuniform stress field, an elastic modulus profile is reconstructed through a cross-correlation algorithm [35, 36]. Despite the simplicity and compatibility of the technique with standard equipment, it presents unclear results regarding reproducibility and associations between stiffness and gestational age [37, 38, 39]. The main drawbacks are the high dependence of the applied pressure by the practitioner and the difficulty to deform deep organs due to the compression is manually generated [40, 41].

In contrast, dynamic elastography techniques have the strength to provide the absolute quantitative values of stiffness as an objective criterion to evaluate the process of cervical ripening [42, 43]. This technology relies on shear ultrasonic waves that travel through the soft tissue. Under the assumptions of homogeneity, non viscosity, isotropy, and semi-infinite medium, the measurement of shear wave propagation speed allows characterizing shear stiffness [44]. Although these techniques have been successfully applied in other soft tissues such as liver or breast as diagnostic tool [45, 46], its potential application to cervical tissue still remains unclear. In fact, cervical tissue is heterogeneous, anisotropic and viscous, composed of active cells embedded in an extracellular matrix in which approximately 80% is water and 20 % dry tissue [47, 48]. In contrast to compressional waves, which are mostly sensitive to the fluid phase, shear waves are mostly sensitive to the solid phase, especially the extracellular matrix and collagen architecture. Fibrillar collagen is the main constituent in dry tissue, responsible for the elasticity, which determines a cross-linked network enclosed by a ground substance of viscous proteoglycans and glycosaminoglycans [49, 50]. However, viscoelastic parameters of cervical tissue have scarcely been studied so far in medical diagnosis [51, 52], but the few references present in the literature, none in tests in pregnant women *in-vivo*, suggest that viscoelastic properties are particularly sensitive to the gestation process [53, 54, 55, 56, 57, 58]. Therefore, a deeper knowledge about the characterization of the viscoelastic behavior of cervical tissue could soon unleash its potential for additional clinical diagnostic information.

An alternative technique to dynamics methods is the emerging torsional wave elastography technique that uses a torsional wave sensor for the viscoelastic characterization of cervical tissue [59, 60]. Torsional waves are shear elastic waves that propagate soft tissue radially and in-depth generating a pseudo-spherical propagation pattern. A mathematical

result by Reissner and Sagoci in 1944 [61] renders the torsional wave formulation seed that will be elaborated. One of the advantages of this technique, in contrast to commercial shear transducers, is that significant limitations caused by the difficulty of the separation between longitudinal and shear waves are overcome. The sensor can isolate a pure shear wave, avoiding the possibility of multiple reflections in small organs, as is the case of cervical tissue. The other advantages are the low energy deposited in the medium compared to ARF-based techniques, the wide range of frequencies analyzed, including frequencies higher than the range used by ARFI techniques (i.e. 200-1500 Hz vs 300-600 Hz), and the frequency of data acquisition (above 1.5 kHz). Application of torsional waves to sense soft tissue architecture could enable a new class of biomarkers that quantify the mechanical functionality of cervical tissue. We aim at linking variations at the macroscopic scale that characterize cervical ripening with mechanical properties assessed by torsional waves, to finally evaluate the feasibility of torsional wave elastography to be a complementary diagnostic tool for preterm birth and labour induction success.

2 Objectives

The need to characterize changes in cervical tissue during pregnancy impels us to unify viscoelasticity and different methods that could be useful as medical diagnostic tools. So far, no reliable clinical tool is available for quantitative and objective evaluation of cervical maturation [62]. Current models based on cervical length, obstetric history, digital vaginal examination and echography of the cervix are not able to accurately predict a preterm birth with sufficient anticipation or the successful induction of labour [24, 25, 26, 27, 28]. Even though there is an agreement that cervical ripening plays a fundamental role during pregnancy, histological changes and biomechanical properties of the cervix are not entirely characterized. Recently, elastography techniques are being put forward in the literature, however, important information about the cervical tissue state may be lost due to the neglect of viscosity and nonlinearity [30, 31, 32, 33, 34].

To this end, this thesis aims at evaluating the viability of torsional waves to reconstruct mechanical parameters, elasticity, viscosity and open the way to nonlinearity, measuring in a human cervix *in-vivo* and enabling the technology as a diagnosis of preterm birth and the success of induction of labour. To reach this target, the following research steps are considered, in basis of hypothesis:

1. The novel technique based on the propagation of torsional waves through the tissue carries the necessary information to interrogate the mechanical properties of soft tissues. By contrast, quantitative elastography presents relevant limitations related to the pressure applied during the measurement, the separation of shear waves and longitudinal waves and multiple reflections and diffraction of shear waves in complex structures [63, 34].

Hypothesis 1: Changes in the consistency of the soft tissues can be evaluated by torsional waves through the quantification of mechanical properties.

Research objective 1: To propose and evaluate the feasibility of a novel Torsional Wave Elastography technique to objectively quantify the viscoelastic properties of soft tissues, and specifically the cervix [1].

2. The quantification of changes in the biomechanical state of the cervix during the gestation process is a challenging problem. The preterm birth is the main cause of infant mortality and morbidity and evaluating the viscoelastic mechanical parameter changes during pregnancy is a pressing need for obstetricians as a potential preterm birth prevention tool [64, 12].

   Hypothesis 2: Understanding the interaction of torsional waves with the histology of cervical tissue is a key to the reconstruction of viscoelastic properties through a inverse problem methodology. An appropriate rheological model helps to reconstruct the mechanical properties in the epithelial and connective layers of cervical tissue from torsional wave propagation.

   Research objective 2: To rank the most plausible rheological model to infer the viscoelastic behavior of cervical tissue in different layers using a probabilistic inverse procedure and explore the possibility of quantifying both elasticity and viscosity from the selected rheological model.

3. Validation is a crucial step when using numerical models for simulating physical phenomena, such is the propagation of torsional waves in this case [65]. Validation can be achieved by different means, for instance by comparing the observations from experimental work against a computational model. The model is validated when a certain level of agreement is reached.

   Hypothesis 3: An appropriate method based on a PIP procedure to infer the Kelvin-Voigt (KV) properties in cervical tissue from TWE may provide information on how the viscoelastic parameters change during the gestational period.

   Research objective 3: Propose and experimentally validate a method based on PIP approach to infer the KV viscoelastic properties in cervical tissue from TWE technique [2].

4. The theory of linear elasticity is often employed to interpret results of the mechanical tests on soft tissues with the objective of characterizing the mechanical behavior of analyzed samples and to simulate these tissue behavior [66, 67]. Notwithstanding, in linear elasticity small deformations are considered, while as most of the soft biological

[1] Research objective corresponding to the contribution: A. Callejas, A. Gomez, J. Melchor, M. Riveiro, P. Massó, J. Torres, M. López-López and G. Rus. Performance study of a torsional wave sensor and cervical tissue characterization. *Sensors*, 17(9), 2017.

[2] Research objective corresponding to the contribution: A. Callejas, A. Gomez, I. H. Faris, J. Melchor and G. Rus. Kelvin-Voigt parameters reconstruction of cervical tissue-mimicking phantoms using torsional wave elastography. *Sensors*, 19(15), 2019.

tissues, the mechanical behavior of the cervix is nonlinear under large deformations [68]. The accurate description of soft tissues involves more sophisticated, accurate and reliable theories.

Hypothesis 4: A new hyperelastic model, based on the Landau's theory, used to fit the experimental data from an uniaxial tensile test in cervix, could explain the nonlinear behavior of cervical tissue under large deformations.

Research objective 4: To propose a hyperelastic model based on Fourth Order Elastic Constants in the sense of Landau's theory to characterize the nonlinearity of cervical tissue and validate the mechanical parameters inferred in *Research objective 2*.

5. Elastography, which maps tissue mechanical properties, provides an additional and clinically relevant information related to changes in tissue consistency. Quasi-static elastography methods have shown unclear results regarding reproducibility and associations between stiffness and gestational age, due to the dependence on user interaction [37, 38, 39, 69]. In contrast, dynamic elastography techniques, which relies on shear ultrasonic waves that travel through the soft tissue, have the strength to provide the absolute quantitative values of stiffness as an objective criterion to evaluate the process of cervical ripening [42, 70, 43]. An alternative dynamic technique allows the precise interrogation of soft tissue mechanical functionality in cylindrical geometries, as is the case of cervix, that are challenged by current elastography approaches in small organs.

   Hypothesis 5: Torsional Wave Elastography may objectively quantify the decrease of cervical stiffness related to gestational age.

   Research objective 5: Evaluate the feasibility and reliability of Torsional Wave Elastography technique to provide consistent data on the changes of the cervical tissue stiffness during pregnancy [3].

[3]Research objective corresponding to the contribution: P. Massó, A. Callejas, J. Melchor, F. S. Molina and G. Rus. In-vivo measurement of cervical elasticity on pregnant women by torsional wave technique: a preliminary study. *Sensors*, 19(15), 2019.

3

The cervical tissue

The purpose of this chapter is to provide, from a global point of view, knowledge of the structure, behavior and functions of cervical tissue. A literature review is shown in this chapter, highlighting the anatomy, histology, components of the extracellular matrix (ECM) and changes in those components during cervical ripening. This microstructural knowledge of the tissue will be fundamental to understand the changes from the macrostructural point of view studied in this thesis.

3.1 Anatomy and histology

The cervix or the uterine cervix is a cylindrical and fibrous connective tissue located at the lower part of the uterus, connecting the uterus with the vagina (see Figure 3.1) [71]. The uterine cervix is about 3 cm long and 2 cm in diameter (see Figure 3.2) [72]. Uterosacral and cardinal ligaments keep it in place and during pregnancy fetal membranes are attached to it [73]. The uterine cavity connects to the cervix through the *internal os*, whilst the cervix connects to the vagina through the *external os*. The endocervix is the portion of cervix that is located immediately after the *external cervical os*. The cervical tissue plays a crucial role during the gestation, acting as a gatekeeper supporting the fetus inside the uterus and keeping it safe from external hazard [74, 50, 75]. It suffers a drastic maturation that is carried out over the course of pregnancy [75, 76, 77].

3.1.1 The extracellular matrix

Histologically the cervical tissue is composed of active cells, basically smooth muscle cells (SMC) and fibroblast, embedded in an ECM [47, 48]. The ECM ensures the strength and

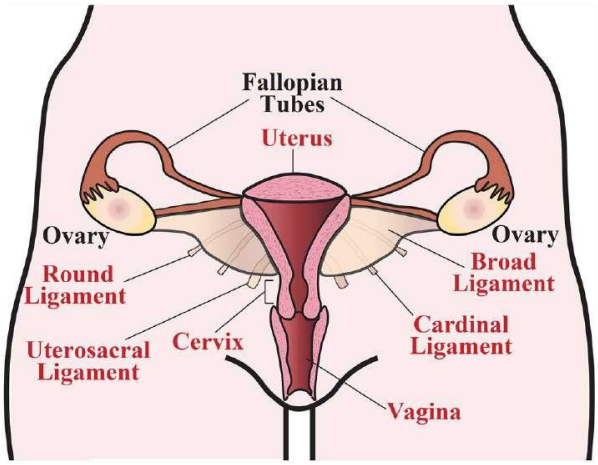

Figure 3.1: Female reproductive organs and supportive connective tissues. Source: [1].

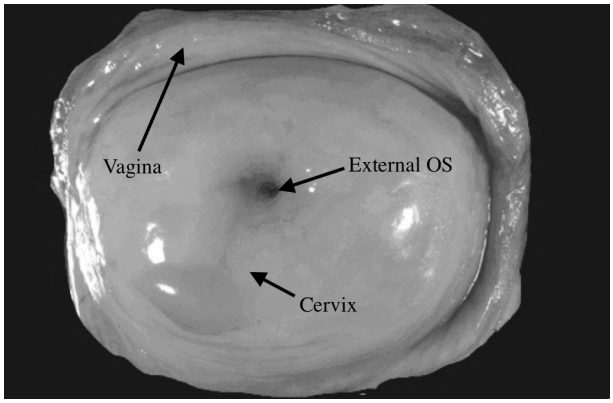

Figure 3.2: Normal cervix nulliparous. Source: adapted from [2].

integrity of the cervix, resisting shear deformation, through a fibrous scaffold [78]. This matrix presents a composition with two main parts: extracellular fluid with a content around 75-80 %, and dry tissue 20-25 % (see Figure 3.3). Fibrillar collagen is the main constituent in dry tissue, which determines a cross-linked network interlaced with the elastin protein, enclosed by a ground substance of viscous proteoglycans and glycosaminoglycans [49, 50]. This behavior of the ECM constituents suggests the study of the cervical tissue from the viscoelastic point of view, poorly studied to date [53].

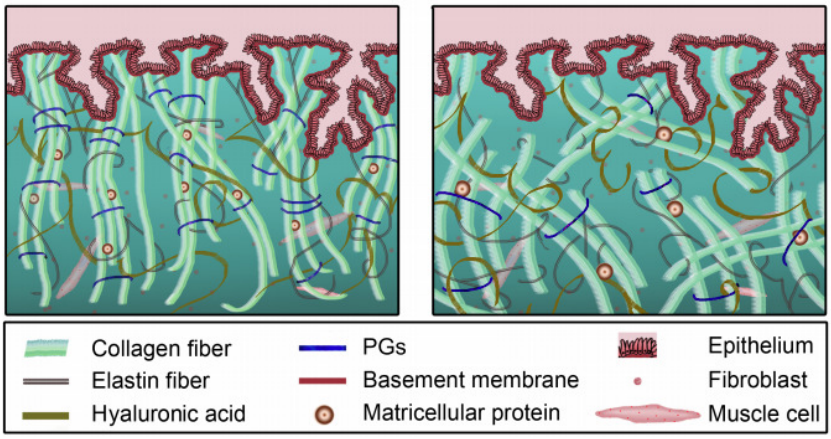

Figure 3.3: Histological components of the extracellular matrix of cervical tissue. Comparison between constituents in non-pregnant woman (left image) and close to childbirth (right image). The constituents are described in the lower legend. PGs: proteoglycans.

The collagen present in the cervix, which represents the 85 % of dry tissue, is divided into two types, I (67 %) and III (33%), a content that does not change throughout pregnancy [79, 80, 81]. The cervical tissue also has a type IV collagen content that can be considered negligible. The structure of collagen fibers is hierarchical, composed by molecules with a triplet amino acid sequence, forming a helical structure (tropocollagen) [82]. Hydroxyproline provided the stability of tropocollagen. Afterwards, the cross-link formation is determined by the hydroxylation, providing the union of fibrils [83, 84]. Fibrils joined in parallel form the collagen fibers, which measure between 1 and 20 μm [85, 86]. Crimping, the diameter and interfibrillar space define the morphology of the collagen [87, 88, 89, 90, 91]. Collagen is the main responsible for the resistance of the ECM under the stresses that it undergoes during pregnancy [49, 92, 93]. Aspden studied the different prevalent directions that the collagen fibers follow within the tissue by X-ray [94]. Three preferred directions were found, the outermost and innermost zones of the cervix with the fibers preferentially aligned in the longitudinal direction (to resist tensile loads), and the middle zone with the fibers following a circumferential direction (to resist loads due to dilatation). More recent studies corroborate the preferred distribution of collagen fibers in the three indicated areas [95, 96].

Another of the components that grants elasticity to the ECM is elastin. This component presents a small composition (0.9 % - 2.9 %) [97, 98], therefore, compared to collagen, it does not contribute significantly to the mechanical strength of the cervix. The elastic modulus

for elastin reported by the literature is 1 MPa [99, 100] versus that of collagen 400 MPa [101, 102, 103]. Its distribution is centered near the *external os*, reducing when approaching the *internal os*, where the amount of smooth muscle increases. Several studies concluded that apart from supporting the collagen network, they influence the mechanical response of the cervix [104, 105]. In conclusion, elastin complements collagen in the structural behavior of tissue, returning cervical tissue to its shape after delivery [98].

Glycosaminoglycans (GAGs) and proteoglycans (PGs) represent 0.2 % - 1.5 % of dry tissue. Proteoglycans and water with proteins form the ground material of the gelatinous matrix. A core protein that covalently bonds with GAGs composes PGs [106, 107]. It is worth pointing out that, one of the properties that hyaluronic acid has, a fundamental component of the GAGs, is the behavior as a lubricants or mechanical damping force to support the loads to which the tissue is subjected, providing it a viscous character [108, 109, 88, 54].

3.1.2 The epithelial layer

The study of the superficial layer of the cervix, the epithelial layer, has special interest in this thesis due to the elastography technique proposed for the mechanical characterization of the tissue. The innovative technique, Torsional Wave Elastography, is based on the propagation of torsional waves through the surface of the cervical tissue, as well as in-depth, interacting with the different layers of which the tissue is composed.

The epithelium has a merely protective function against infections and mechanical aggressions [72] (Figure 3.6). It is a tissue formed by intimately linked, flat or prismatic cells, whose collagen content is minimal, according to the literature <1% of type-IV was reported by [110].

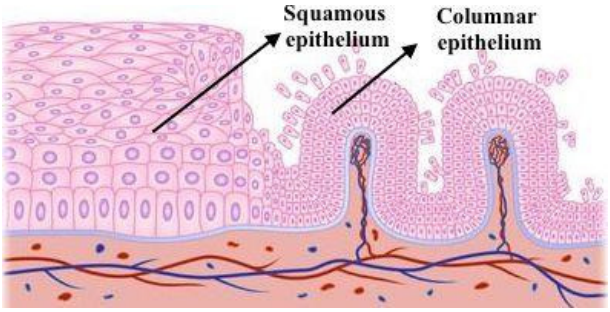

Figure 3.4: Squamous and columnar epithelium. Source: adapted from [3].

The leap of layers between the endocervix and ectocervix is an area called squamocolumnar junction (SCJ), which separates the squamous epithelium from the columnar epithelium (see Figure 3.4) [78]. The SCJ is usually located at the beginning of the cervical canal, although it varies with age, pregnancy and the menstrual cycle. It is worth pointing out that the epithelium undergoes many structural transformations during its life. The essential change is due to the development of a new squamous epithelium within the columnar epithelium that lines the cervical canal and the ectocervix, a process known as metaplasia (see Figure 3.5) [78, 4].

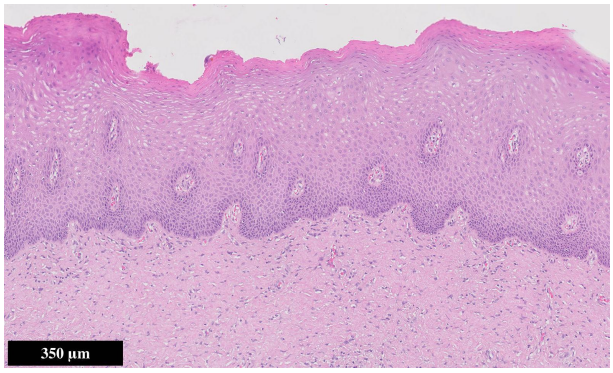

Figure 3.6: Cervical tissue micrograph. Upper layer: epithelium. Bottom layer: connective layer.

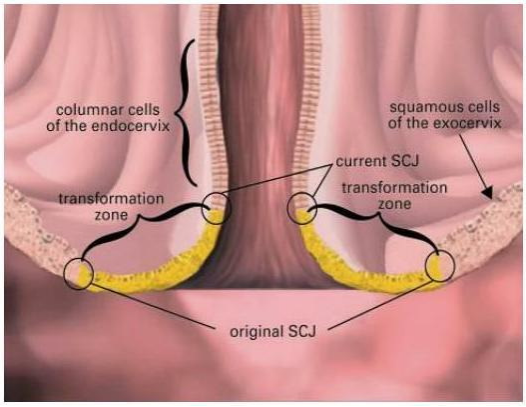

Figure 3.5: Metaplasia, development of a new squamous epithelium within the columnar epithelium that lines the cervical canal and the ectocervix. [4].

A basement membrane separates the squamous epithelium from the fibrous stroma. The hormonal state of the subject is one of the factors that determines the thickness of the epithelium. The epithelium is not stimulated in young girls and elderly women. However, this tissue layer responds to hormonal stimulation by producing proliferation during the sexually mature period. During this phase, progesterone acts on the intermediate layer causing thickening [111]. One of the few studies about the epithelial tissue morphology in pregnant women was carried out by Danforth in 1950 [112]. The results showed a thickness of the squamous epithelium around 0.45-0.5 mm, while the thickness of the squamocolumnar junction was 0.35-0.4 mm. A later study evaluated the effect of pregnancy on the cervical squamocolumnar junction [113]. In this work it was concluded that the more weeks of gestation, the greater the probability that part of the columnar epithelium was found in the ectocervix.

3.2 Changes in cervical tissue during pregnancy

The remodeling process during pregnancy that cervix undergoes depends on each patient [114, 115, 116] and is due to numerous interactions at the biochemical level between the

constituents of the extracellular matrix. Four are the phases that govern this remodeling process: softening, ripening, dilation and postpartum [76].

The softening occurs in the first month and is the longest and first phase of remodeling. The result is the reduction in resistance motivated by a disorganization of collagen structure, increase in water content and proteoglycans [117]. In spite of that, tissue integrity is maintained. Additionally, the epithelium secretes mucus to protect the cervix against possible infections.

Few weeks before parturition the cervical ripening phase begins. Rapid changes characterize this process, in which the tensile strength or integrity decreases until delivery. Hyaluronic acid (HA) unbalances the collagen network, decreasing its mechanical resistance due to the increase in tissue hydration and, consequently, collagen solubility [109, 118].

In the final phase of pregnancy, dilatation occurs in order to allow passage of fetus. Before that, a new regulation of hormones and myometrium contractions produces biochemical changes [75, 119]. The mechanical resistance is lost by breaking the hyaluronic acid bonds to trigger a short duration of labor [120].

In the postpartum phase, the tensile strength is recovered to avoid infections and to prepare for possible future pregnancies. The water content decreases and there is an upregulation of synthesis of ECM constituents to return the cervix to the original state [121].

The main components of cervical tissue that govern remodeling are water content, collagen, and proteoglycans and glycosaminoglycans. It is well know by the scientific community that the water content increases by approximately 5 % [88, 122, 123]. A study carried out by Myers et al. confirmed that the increase of water content in the tissue decreases the mechanical capacity of the cervix [124]. The main responsible for the change in the resistance of the cervix is the collagen. During the maturation, there is a disorganization in the collagen network that entails cervical insufficiency. An increase in solubility occurs during pregnancy, going from 37 % to 80 % in the third trimester [88]. It has been shown that this increase produces a reduction in cervical stiffness in both humans and animals [125, 124]. However, there is no consensus on the variation of collagen content during pregnancy. Some authors maintain that there is an increase of 40 % [123, 126], while others are not in favor of decreasing during the remodeling [88, 98]. Regarding the morphology of collagen, the diameter and pores between fibers increase form early to late pregnancy, due to the weakening of collagen cross-linking [54]. At the end of gestation, a noticeable decrease (between 40-50 %) occurs in the content of PGs, that produces dispersion in the collagen network. Finally, changes in the content of GAGs has been reported by several authors during pregnancy [88, 123, 109]. Before delivery, dermatan sulfate reduces its content by 15 % [109, 127]. On the other hand, the increase of HA, favors collagen disorganization, hydration and cervical distensibility [128].

3.3 Methods to obtain cervical elasticity

The need to relate the cervical remodeling with changes that occur in the consistency of the cervix has led to the emergence of methods that quantify it. The two most prominent methods for evaluating cervical tissue elasticity are presented briefly in this section.

3.3.1 Elastography methods

The purpose of elastography methods is to map the elasticity of the tissue through the induction of displacements in the same. Strain, displacements or shear wave speed are the parameters inferred from the tissue motion. One of the oldest techniques is static elastography, that consists of applying an external compression to the tissue and comparing the images obtained before and after that deformation [35, 36]. The aforementioned technique presents a series of limitations that have been reported by several studies [38, 69]. In contrast, dynamic elastography techniques appear with the objective of solving the limitations presented by static elastography, specially to obtain quantitative elasticity maps. The physical principle on which they are based is the propagation of shear waves through the tissue. Chapter 4 briefly describes the elastography techniques that have been used for the mechanical characterization of cervical tissue.

3.3.2 Aspiration technique

The aspiration technique is one of the few quantitative *in situ* and *in vivo* methods to obtain the biomechanical properties of cervical tissue. The method consists of measuring the pressure necessary to displace the cervical tissue 4 millimeters. After that, the strain-stress curve of the tissue is estimated using a camera and a mirror housed in the sensor. The pressure needed to deform the tissue is a measure of its stiffness. Mazza et al. [129] carried out an *ex vivo* and *in vivo* study in non pregnant cervices. The results obtained were not as promising as it was expected due to the variability between patients. Nevertheless, posterior studies showed consistent results with the cervical remodeling process [130, 74]. The stiffness of the cervical tissue in pregnant women decreases with respect to non pregnant women. In the same way, the stiffness during the gestational age decreases, recovering the initial value (non pregnant woman) at 6 weeks after delivery. The main disadvantage of this technique is that it only obtains information from a specific area of the cervical tissue, not inferring information about its heterogeneity.

4

Elastography methods: principles and techniques

In this chapter, the different elastography techniques are described in detail. We focus on two main methods that have been employed in clinical practice, quasi-static and dynamic elastography [70]. It is worth pointing out the dynamics methods, and specifically Torsional Wave Elastography, which is the core of this thesis. Finally, the state of the art of elastography applications for cervical tissue is presented at the end of this chapter.

4.1 Background

The ancient technique of palpation is the origin of elastography, used for the detection of cancerous tumors [131]. The technique consists of evaluating hardness of patient's tissue by a manual inspection. Nowadays, it is still used in clinical practice, i.e., Bishop's test that assesses the cervix hardness in labor and helps to predict whether induction of labor will be required. The main disadvantage is that it is a subjective technique, besides being a method that can only be employed in organs accessible by the practitioner's hand.

Elastography has become a technique applied in clinical practice since 80's [132]. All the elastography techniques are based on the same principle: generation of motion on the tissue and the mechanical characterization of the same is performed through the post-processing of the displacements. The mechanical excitations employed by different techniques are static compression, monochromatic or transient vibration. Strain, displacements or shear wave speed are the parameters inferred from the tissue motion.

Attending to the elasticity of soft tissues, two parameters are used frequently, Young's modulus (E) and shear modulus (μ). In the current elastographic techniques, these parameters are obtained by carrying out the following two procedures: (i) using the Hooke's law to reconstruct E; (ii) tracking the shear wave speed to calulate E or μ. In ultrasonic imaging [133, 134, 135, 136] longitudinal waves travel through the tissue generating an image that is representative of the echoes, produced by variations in ρ (tissue density) or K (the bulk modulus of elasticity). Its speed is very quickly in soft biological tissues (around $1540m/s$). However, shear waves travel (around $1-10m/s$) much slower than longitudinal waves. The relationship between shear modulus and shear wave speed is as follows,

$$c_s = \sqrt{\frac{\mu}{\rho}} \tag{4.1}$$

The shear modulus is related to the Young's modulus through the equation $\mu = \frac{3KE}{9K-E}$. Compared to longitudinal waves, shear waves are rapidly attenuated in soft tissues. The shear modulus μ varies by a factor of more than 10^5, while the bulk modulus K varies no more than 12% over the whole range of soft tissues, which means that shear waves are more sensitive to changes in the consistency of tissues than longitudinal waves. Assuming the hypothesis of quasi-incompressibility of soft tissues ($\nu \simeq 0.5$) due to the high water content they have, homogeneity, isotropy and non-viscosity, the Young's modulus is approximated as: $E = 3\mu$. Although these hypotheses are usually considered by some of the commercial dynamic techniques, soft tissues have a non-homogeneous, anisotropic and viscoelastic behavior. Specifically, due to viscoelasticity, the speed of the shear waves depend on the frequency. The evaluation of viscoelasticity, although according to the literature is poorly studied in cervical tissue to date, is one of the cores of this dissertation.

4.2 Quasi-static techniques

Strain Elastography (SE) or quasi-static elastography is a technique for imaging of strain and elastic modulus changes in soft tissues. This was introduced by Ophir et al. [137] in 1991 for the first time. The Hooke's law is the basis of this method, $\sigma = E\epsilon$, which relates the stress, σ, to strain, ε, through an elastic constant that is the Young's modulus. The tissue is manually compressed with the probe as it can be seen in Figure 4.1. Then, the tissue strain is quantified as the ratio of the anterior-posterior distance, before (reference configuration) and after compression application [35]. The strain profile along the transducer axis is reconstructed through a cross-correlation algorithm [36]. Then, by measuring the stress applied on the tissue and performing corrections due to the nonuniform stress field, an elastic modulus profile is obtained.

Despite the simplicity and compatibility of the technique with standard equipment, it presents the following drawbacks [42, 138, 139]. The difficulty to deform deep organs due to the compression is manually generated; the reconstructed deformation gradient map does not consider the boundary conditions [40, 140, 141]; for the correct interpretation of images,

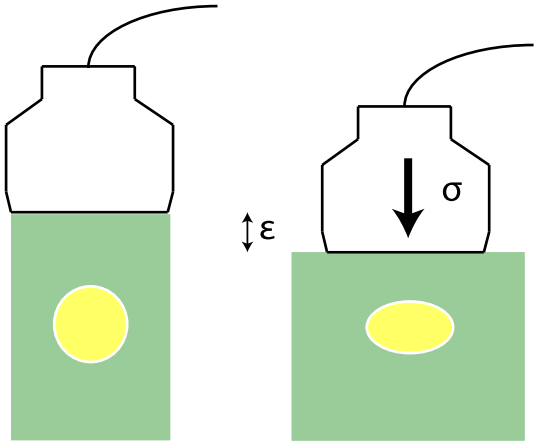

Figure 4.1: Schematic representation of the principle of strain elastography. Tissue deformation is induced by the probe.

uniform compression should be applied by the practitioner; measurements are highly dependent on the pressure applied [30, 41, 142, 143, 144, 145] and, therefore, the local Young's modulus can not be quantitatively estimated; the fluid can be displaced, producing a time-dependent reduction in the strain in nearby tissue [141].

The disadvantage of not being able to transmit the deformation to deep tissues can be solved by cardiovascular pulsation or respiration [146]. Although this alternative can be used for evaluating disease progression in chronic liver disease [147], the other drawbacks have to be taken into consideration. Despite its limitations, SE has been efficiently applied to breast lesion characterization and widely validated by many authors [148, 149].

4.3 Dynamic techniques

Dynamic elastography (DE) techniques appear with the objective of solving the limitations presented by SE, specially to obtain quantitative elasticity maps. The physical principle on which they are based is the propagation of shear waves through the tissue, which can be generated by a vibrating force in sonoelastography [150], a given frequency shift in vibroacoustography [151], in transient elastography [152] is a short impulse or acoustic radiation force in ARFI, SWE and Supersonic Imagine (SSI) [153, 154].

4.3.1 Transient elastography

The term "transient elastography" refers to transient elasticity methods in which the transient shear waves are generated mechanically and then measured. This technique appeared in the late 1990s [155, 156, 157] to overcome the drawbacks of sonoelastography [158, 159] and magnetic resonance elastography [160]. In dynamic elastography methods, when stimulated with a continuous vibration, interference nodes caused by reflections at boundaries are presented. The transient excitation allows separation between shear waves and longitudinal waves without taking into account the boundary conditions, avoiding the interference nodes within the sample. To clarify the terminology used in this thesis, the term

transient elastography (TE) refers to methods that use a vibrating external push to induce shear waves.

The TE technique consist of a mechanical actuator and a single ultrasound transducer, both are placed on the same axis. A transient impulse is generated on the sample and the shear wave induced that travels through the tissue is recorded [152, 156]. A cross-correlation algorithms are used to track the displacements generated by the shear wave propagation. These algorithms are applied to the raw ultrasound A-lines which are divided into segments as a function of depth [157]. In order to follow the displacements generated by the shear wave propagation, frame rates of several thousand per second are obtained. Using the equation $\mu = \rho c_s^2$, the shear modulus value is obtained from the shear wave speed [152].

The device manufactured by Echosens (commercially known as *FibroScan* ®) allows the characterization of the mechanical properties of the liver fibrotic state. It permits a reduction of 50% of liver biopsies in the evaluation of chronic liver illnesses [161, 162]. The system is not an ultrasound scanner and no elastograms or ultrasound images are provided.

The two-dimensional transient elastography appeared with the development of ultrafast imaging based on ultrasound plane wave emission [163]. The new technique provides a 2D elasticity modulus map of the tissue [164]. The ultrasound imaging array was fixed to a vibrator which induces a quasi-plane shear wave. The drawbacks of this device were that it was heavy, difficult to use in practice and bulky [165].

4.3.2 Acoustic radiation force impulse

Acoustic Radiation Force Impulse (ARFI) imaging emerged in 2001 by Nightingale et al. [166]. The basis of the ARFI imaging technique is ARF excitation force, generated by a focused ultrasound pulse with longer length and/or higher power than conventional B-mode imaging pulses [167, 168]. The acoustic radiation force is proportional to tissue absorption (α_t), main cause of attenuation [169], and the spatial peak temporal average intensity (I), and inversely proportional to the speed of the sound in the tissue (c), as shown in [167],

$$F_r = \frac{2\alpha_t I}{c} \tag{4.2}$$

The technique generates localized displacements in the range 1 to $10\mu m$ employing a focused ultrasound beam [170, 171]. The values usually adopted of the duration acoustic pulses in diagnostic ultrasound are below $0.02\ ms$, however, the use of longer pulses ($0.05 - 1\ ms$) generate deformations of the order of microns. ARFI generates displacements in the location of force application, region of interest (ROI), and then are tracked with correlation-based time delay estimators [170]. The resulting tissue displacement, monitored by the same transducer that induces movement, is obtained using RF-echo tracking, and shown as a qualitative elastogram within a small ROI [172]. Obtaining a qualitative map of tissue stiffness is not possible since ARF amplitude is tissue dependent and usually unknown, therefore, similar results are obtained compared to the images generated in SE.

In contrast, quantitative elasticity maps can be reconstructed by analyzing ARFI-induced shear wave propagation [153, 173, 174], as with shear wave elasticity imaging [174].

Several studies have confirmed the feasibility of this technique, specifically in breast [175] and prostate [176]. The commercial elastography system is developed by Siemens and known as *VirtualTouch Imaging* ^{TM}. Compared to SE, this technique is less user-dependent, shows better SNR at depth, and can be used almost everywhere, in all the places where the energy coming from the transducer can be focused [43, 171].

The shear wave can be generated with ARFI, and its arrival time at nearby A-lines is tracked to get the average shear wave speed in a region of interest (ROI) [177]. This procedure is known as point shear wave elastography (pSWE) [43]. A great advantage is the penetration that this technique has, being able to reach depths larger than 8 cm [178]. One of the most important applications is the quantification of diffuse liver disease.

4.3.3 Shear Wave elastography

Shear wave elastography (SWE) is a technique that consists of inducing displacements that generate shear waves using ARF. The difference with pSWE is that SWE generates a tissue elastogram in real time. *SuperSonic Imagine* is one of these techniques [153, 179]. The procedure carried out by this technique to calculate speed maps is divided in three steps: acoustic radiation force excitation, ultrafast imaging acquisition and generation of speed maps [180].

- *Excitation by ARF.* The idea of SSI is to focus the ultrasound beams successively at different depths to create quasi plane shear wave [181]. A *Mach-cone* is created since the speed of the shear wave source moved in depth is higher than the shear wave speed of the tissue [182]. This is the effect that gives the method its name, supersonic shear imaging.
- *Acquisition by ultrafast imaging.* The shear waves induced are imaged at a rate of 5000 frames per second. This allows averaging the acquired images to obtain a better image quality [165].
- *Calculation of speed maps.* The shear wave speed map is reconstructed using a time-of-flight algorithm. Usually, three *Mach cones* are used in order to solve the drawback that in the push zone no elasticity values can be obtained. Finally, the three maps are combined with a quality criterion such as a local weighting in order to reconstruct the entire image of the medium [183].

Tissues subjected to radiation pressure may suffer heating and cavitation [184]. Therefore, it is important to follow the specifications described in the Food and Drug Administration (FDA) to insure that these two effects remain below damaging thresholds [185]. There are three parameters that should be evaluated according to the acoustic output: the mechanical index (MI), the spatial peak pulse average intensity ($ISPPA$), and the spatial peak temporal average intensity ($ISPTA$).

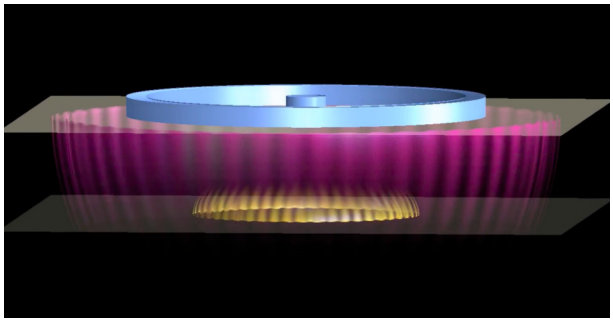

Figure 4.2: Representation of the principle of torsional wave elastography for the characterization of cervical tissue. Tissue deformation is induced by the electromechanical actuator located in the center. The signal is received by a receiver ring circumferentially aligned with the electromechanical actuator.

4.3.4 Torsional Wave elastography

The origin of torsional waves lies in the mathematical formulation proposed by Reissner and Sagoci in 1944 [61]. Then, a new family of sensors based on torsional waves was patented, such as the US 5321333 A [63], which belonged to the field of low frequency sensors for the generation or reception of torsional shear waves in a substantially solid medium. This technique solved the problem of the strong attenuation of induced shear waves, providing a new way for the development of new noninvasive tissue characterization techniques [186, 187]. However, these new techniques presented disadvantages such as the frequency of propagation generated, the range of frequencies studied or the volume and weight of the devices used.

Torsional waves are shear elastic waves that propagate through soft tissue radially and in-depth generating a pseudo-spherical propagation pattern (Figure 4.2). Application of torsional waves to sense soft tissue architecture has been proved to enable a new class of biomarkers that quantify the mechanical functionality of soft tissue [186]. The proposed torsional wave elastography (TWE) technique is an emerging technique that uses a torsional wave sensor for the viscoelastic characterization of cervical tissue [60, 59]. The basic principle is the generation of torsional waves and the reception of them after traveling through the tissue. The sensor comprises a rotational electromechanical actuator and a receiver ring circumferentially aligned (a detailed description of the probe can be found in Chapter 6). One of the advantages of this technique, in contrast to commercial shear transducers, is that significant limitations caused by the difficulty of the separation between longitudinal and shear waves are overcome. The sensor can isolate a pure shear wave, avoiding the possibility of multiple reflections in small organs, as is the case of cervical tissue. The other advantages are the low energy deposited in the medium compared to ARF-based techniques, the wide range of frequencies analyzed, including frequencies higher than the range used by ARFI techniques (i.e. 200-1500 Hz vs 300-600 Hz), and the frequency of data acquisition (above 1.5 kHz).

Some other elastography techniques based on specific applications have also been developed. A new transurethral elastography technique, named Transurethral Shear Wave Elastography (TU-SWE), has been in silico tested for the diagnosis of prostate cancer and the focal thermal ablation monitoring of such tumours [65]. The principles are the same as those on which the previous probe is based, transmission of torsional waves into the prostate by applying oscillatory rotational forces on the urethral wall. Imaging is based on the reception of shear wave echoes generated by changes in the shear modulus distribution of the prostatic tissue, which can be associated with the presence of a lesion, as either a prostate tumor or a thermal lesion.

According to the authors, some claimed advantages of this technique over other elastography techniques for prostate are [65, 188]: compatibility with monitoring transrectal therapies since the access channel is the urethra; shorter distance, and therefore better accessibility, between the source and the anterior zone of the prostate compared with transrectal elastography techniques; the possibility of using frequencies higher than the usual range of ARF-based techniques, i.e. above 400-500 Hz, due to the use of mechanical actuators as an excitation source; capacity of scanned the whole gland volume simultaneously; low deformation of the gland since the probe can be fabricated flexible; and finally lower expected levels of energy and therefore, a lower thermal index compared with ARF-based techniques. Nonetheless, some possible drawbacks can be also encountered: increase in the risk of urinary infection if the probe is not properly sterilised; patients resistance to the transurethral insertion as it can be seen as a more invasive way of access compared with the rectal passage; slipping or incomplete mechanical contact between emitters and receivers and the prostate which would impede the correct transmission and detection of shear waves.

Torsional wave elastography has shown in vitro the potential of quantifying viscosity, from the wave attenuation and frequency dispersion curve [60], as well as the elastic nonlinearity, by adapting the ultrasonic harmonic generation technique [189]. In this dissertation, we propose the novel TWE technique to evaluate the feasibility in the quantification of viscoelastic properties of soft tissues, and specifically the cervical tissue.

4.4 Elastography applications for cervical tissue

Characterizing the viscoelastic properties of cervical tissue could be a key in the prediction of preterm birth or successful induction of labor. The cervical insufficiency is intimately related to the mechanical properties of the cervix, which are sensitive to the changes in collagen organization. Notwithstanding, to date, most studies rely on changes in stiffness during cervical remodeling, rather than considering the interactions between the fluid and solid phase of the tissue, responsible for viscoelasticity.

The SE method has been the most applied technique in the characterization of the mechanical state of the cervix. The first study that identified typical changes in cervical tissue elasticity correlated with the week of gestation or the age of the pregnant woman was carried out by Thomas [190]. The results found showed age-related differences in cervical elasticity.

Different authors later studied the reliability of employing quasi-static methods to quantify the cervical elastography during pregnancy [38, 69]. Molina et al. [38] studied the inter-intra operator repeatability in measurements in four areas in a total of 112 singleton pregnancies. No statistically significant differences were found in measurements, except in the zone in which the force of the probe is received directly. These measurement obtained could be a mere reflection of the displacement applied by the probe. Hernandez-Andrade et al. [69] analysed the associations between cervical strain and cervical length and gestational age in two different areas and in 262 pregnant women. Spatial variability was found in the stiffness and a strong correlation between cervical length and cervical strain, however, there was no significant correlation between gestational age and cervical strain. One of the challenges of SE is a standardization of the pressure applied during measuring. Several studies were carried out in order to discuss about this problem [191, 138, 139]. Alternative procedures to evaluate the tissue strain have been motivated by challenge of standardization. The aforementioned methods are often named quantitative elastography despite using quasi-static techniques to obtain the elasticity of the tissue [35, 39, 192]. The aim of these methods is to obtain the maximum deformability of the cervical tissue and measure the ratio of the anteroposterior cervical diameter compressed and uncompressed through the cervical consistency index (CCI). The results of these works showed repeatability in measurements and correlations between cervical length and gestational age with tissue strain. Despite this, there is no consensus that solves the main limitation of SE technique, the unknown applied pressure induced by tissue deformation, both in the prediction of premature birth [138, 193, 194] and in the success of the induction of labor [31, 195, 35, 196, 32].

Dynamic elastography techniques, providing a quantitative description of tissue stiffness through shear wave propagation analysis, are the alternative to quasi-static methods. Shear Wave Elasticity Imaging (SWEI) is one of the most used methods. This technique has been widely employed for the quantification of changes in cervical tissue [44, 197, 198, 199, 200]. Carlson et al. measured shear wave speed in human hysterectomy samples. The aim of this study was to distinguish between ripened and unripened cervices and detect the variability in different zones of the cervix. The promising results found with SWE showed sensitivity to differentiate between ripened and unripened state and confirmed spatial variability in the cervical tissue. In the previous study, only an average value of the shear wave speed was provided in a particular ROI. Feltovich et al. [42] proposed the elastic modulus as a potential biomarker for the detection of preterm birth. The range of SWE values varies from 1.2 to 5.5 m/s whilst the elastic modulus varies more than 80kPa.

Peralta et al. [34] explored, for the first time, the feasibility of SWE to evaluate cervical ripening during pregnancy. The cervical stiffness was measured in four different anatomical regions in 42 women between 17 and 43 years of age and at 6-41 weeks of gestation. Results showed significant associations between shear stiffness with the gestational age and the remaining time for delivery. Moreover, the variability of shear stiffness within the cervix was confirmed.

Significant differences were found between the external and internal os and superior and inferior portions of the cervix. Internal os and inferior cervix showed high values of elasticity compared to external os and superior portions of the cervix [38, 41, 201]. Focusing on the internal os, under small strain values it is unlikely to experience spontaneous preterm birth [41]. Similar results were obtained in the study carried out by Muller et al. [33] in which values of the shear wave speed in pregnant women were compared to a control group. In the work performed by Carlson et al. [198], cervical ripening was induced through the application of prostaglandin and shear wave speed was quantified before and after maturation. Results showed a decrease in the shear wave speed 4 hours after prostaglandin application (2.53 ± 0.75 m/s before and 1.54 ± 0.31 m/s after application). A comparison of shear wave speed (SWS) measurements between pregnant women in first trimester and third trimester was performed, providing results of 4.42 ± 0.32 m/s and 2.13 ± 0.66 m/s respectively.

More recently, several studies have been carried out about the use of shear wave elastography to assess the cervical ripening [55, 202, 200, 56]. Hernandez et al. studied the risk of spontaneous preterm delivery (sPTD) with SWE in pregnant women between 18 and 24 weeks of gestation [55]. They concluded that a soft cervix, defined as an SWS $< 25^{th}$ percentile for gestational age at 18-24 weeks of gestation, increases the risk of sPTD, independently of cervical length and a history of previous preterm deliveries. Subsequently, a study with the same range of gestational ages (18 to 24 weeks) was carried out by Suthasmalee et al. [202]. Unlike the previous study, there was no significant association between cervical stiffness and gestational age. In addition, cervical shear wave elasticity in preterm and term groups was not significantly different. Carlson et at. used an ultrasound system equipped with a prototype catheter transducer to detect changes in cervical softness employing SWEI in early versus late pregnancy [200]. Their results suggested that SWEI techniques could be promising for detecting changes in cervical ripening. The calculated SWS were 4.42 ± 0.32 m/s for the first trimester and 2.13 ± 0.66 m/s for the third trimester. A study performed by Rosado-Mendez et al. investigated the ability of SWEI to characterize cervical ripening in the pregnant and nonpregnant Rhesus macaque [56]. The cervix was explored transabdominally with a typical array abdominal transducer and transrectally with a prototype intracavitary linear array transducer. Significant reductions of shear wave speed versus gestational age were showed with both techniques. A more recent study evaluated cervical softening during pregnancy with the SWEI technique [203]. This was the first time a longitudinal study of cervix stiffness was conducted in pregnant women. A constant fractional reduction (about 4% per week) in shear wave speed with increasing gestational age was found. The study also demonstrated changes in shear wave speed along the length of the cervix (softest at the distal end). It is necessary to standardize the SWEI technique for its use in clinical practice by using SWS as a biomarker in detecting changes in cervical tissue consistency.

SWEI technique in cervical tissue presents some limitations: first, the shear wave is highly attenuating due to the microstructure of the cervix and secondly, the difficulty of

producing adequate shear waves in cervical tissue boundaries. An alternative dynamic technique, called Torsional Wave Elastography technique, has recently been proposed [60, 59]. This is based on the propagation of shear waves through the cervical tissue not only in-depth but also radially, which makes the technique suitable for applications such as the cervix, due to its curved geometry. Axis-symmetric waves allows the precise interrogation of soft tissue mechanical functionality in cylindrical geometries, that are challenged by current elastography approaches in small organs. Another advantage of this technique is the energy deposited on the tissue during the measurement compared to SWEI, in addition to avoid the multiple reflections and dispersion of shear waves in small organs. Torsional wave elastography has shown *in vitro* the potential of quantifying viscosity, from the wave attenuation and frequency dispersion curve [60]. All the details of this contribution are shown in Chapters 6 and 11.

It is well known that viscosity, present in most soft biological tissues, has important effects on wave propagation, increasing attenuation and generating frequency dispersion. MacFarlin et al. investigated the changes in ultrasonic attenuation in the evaluation of spontaneous preterm birth (SPTB). Two groups were evaluated, one between 17-21 weeks of gestation and another at full term birth. They concluded that attenuation decreases during pregnancy, and this could be a potential biomarker to identify women at risk for SPTB [57]. Shear wave dispersion characterization has been gaining interest in the medical community for the evaluation of the changes in the consistency in cervical tissue. As an example of this, the study carried out by Rosado-Mendez et al. quantified the viscosity of 14 unripened and 13 ripened cervix specimens from Rhesus macaques by the slope of the phase velocity vs. frequency, using SWEI [53]. The results of the study suggest that cervix requires consideration of structural heterogeneity and viscosity.

A study carried out by Jiang et al. applied 3D multifrequency MR elastography (3DMMRE) for viscoelastic characterization of the uterine tissue in healthy volunteers [52]. Two independent parameters were reconstructed, the magnitude (responsible for the elasticity) and the phase angle of the complex shear modulus (responsible for the viscosity). As a result, the uterine corpus showed higher elasticity, but similar viscosity compared with the cervix.

Yao et al. measured the compressive viscoelastic mechanical parameters of human cervical tissue from hysterectomies using a indentation technique [58, 201]. The viscoelastic parameters were reconstructed by fitting the stress-relaxation response of the samples using an inverse finite element analysis (IFEA). The time-dependent behavior of the cervix (considering small deformations, 25%) can be modeled by the parameters reconstructed in this study.

5 Theoretical background

This chapter is aimed to briefly outline the mechanical equations of wave propagation, together with the equations of hyperelasticity that govern the behavior of cervical tissue.

5.1 Mechanical wave equations in soft tissue

It is well known the equations that govern the propagation of mechanical waves through a medium. Considering an isotropic elastic medium, the classical Navier equation is [204],

$$\rho \frac{\partial^2 \mathbf{u}}{\partial t^2} = (\lambda + \mu)\nabla(\nabla \cdot \mathbf{u}) + \mu \nabla^2 \mathbf{u} + \mathbf{f} \tag{5.1}$$

where $\mathbf{u}$ is the vector of displacements, $\mathbf{f}$ the body force vector, ρ the density of the medium and λ and μ Lame's parameters.

Equation 5.1 is the result of the combination of the following three equations:

- Dynamic equilibrium equation,

$$\rho \frac{\partial^2 u_i}{\partial t^2} = \frac{\partial \sigma_{ij}}{\partial x_j} + f_i \tag{5.2}$$

- Kinematic equation,

$$\varepsilon_{ij} = \frac{1}{2}\left(\frac{\partial u_j}{\partial x_i} + \frac{\partial u_i}{\partial x_j}\right) \tag{5.3}$$

- Constitutive equation for an elastic medium,

$$\sigma_{ij} = \lambda \delta_{ij} \varepsilon_{kk} + 2\mu \varepsilon_{ij} \tag{5.4}$$

where σ and ε are the stress and strain tensor respectively, and δ the Kronecker delta.

To simulate the behavior of soft tissues, it is common and useful in practice the division of tensors into volumetric and deviatoric components. In this thesis, this is the formulation adopted for the deduction of the equations that govern the propagation of torsional waves through cervical tissue.

$$\sigma_{ij} = \underbrace{-p\delta_{ij}}_{\text{volumetric}} + \underbrace{\tau_{ij}}_{\text{deviatoric}}, p = -\frac{1}{3}\sigma_{kk} \tag{5.5}$$

$$\epsilon_{ij} = \underbrace{-v\delta_{ij}}_{\text{volumetric}} + \underbrace{d_{ij}}_{\text{deviatoric}}, v = -\frac{1}{3}\epsilon_{kk} \tag{5.6}$$

where p is the hydrostatic pressure, v the volumetric strain, τ_{ij} the deviatoric stress tensor and d_{ij} the deviatoric strain tensor.

The equations presented above are based on the assumption that the medium is isotropic and elastic, notwithstanding, soft tissues are viscoelastic media, therefore, a different law is required. Following the references found in the literature [65, 205, 206, 207], the linear and viscous terms are adopted for the 3D Kelvin-Voigt model,

$$p = \underbrace{3Kv}_{\text{linear elastic}} + \underbrace{3\eta^v\dot{v}}_{viscous} \tag{5.7}$$

$$\tau_{ij} = \underbrace{2\mu d_{ij}}_{\text{linear elastic}} + \underbrace{2\eta\dot{d}_{ij}}_{\text{viscous}} \tag{5.8}$$

where K is the compressional modulus, and η and η^v are the shear and volumetric viscosity respectively.

Special attention deserve two of the most viscoelastic models contrasted in the literature, these are the Kelvin-Voigt and Maxwell models. For the case of Kelvin-Voigt, the total stress is the sum of the elastic and viscous terms (see Figure 5.1 b). Besides, the shear wave propagation produces stress components of the same nature, therefore only deviatoric components are adopted ($p = v = 0$).

$$\sigma_{ij} = \tau_{ij} = 2\mu d_{ij} + 2\eta\dot{d}_{ij} = 2\mu\epsilon_{ij} + 2\eta\dot{\epsilon}_{ij} \tag{5.9}$$

On the other hand, considering Equation 5.9 and assuming absence of compressional waves in the propagation, only elastic and viscous components of the deviatoric term of the strain tensor are adopted,

$$d_{ij} = \underbrace{\frac{\tau_{ij}}{2\mu}}_{\text{elastic}}, \dot{d}_{ij} = \underbrace{\frac{\tau_{ij}}{2\eta}}_{\text{viscous}} \tag{5.10}$$

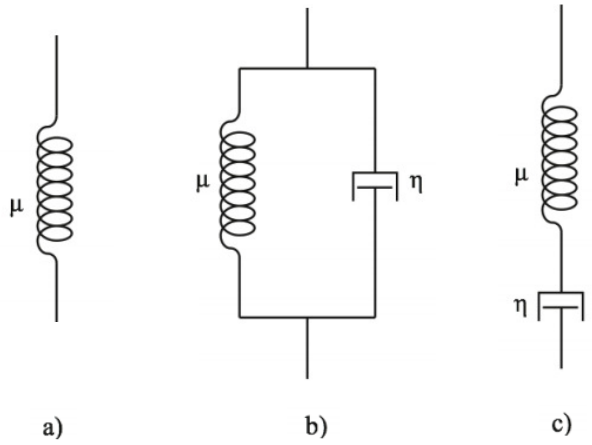

Figure 5.1: Viscoelastic models. (**a**) the elastic model; (**b**) the Kelvin-Voigt model; (**c**) the Maxwell model.

The constitutive equation for the 3D Maxwell model is obtained by adding the elastic and viscous terms presented in Equation 5.10 (see Figure 5.1 c). The same simplification as in the Kelvin-Voigt case is adopted in this case ($p = v = 0$).

$$\dot{d}_{ij} = \frac{\dot{\tau}_{ij}}{2\mu} + \frac{\tau_{ij}}{2\eta} \tag{5.11}$$

5.2 Theory of hyperelastic models

This section shows the theoretical relationship between stress and strain for a proposed hyperelastic model based on the Fourth Order Elastic Constants in the sense of Landau's theory, Mooney-Rivlin and Odgen models.

5.2.1 Proposed Fourth Order Elastic Constants nonlinear model

Nonlinear Fourth Order Elastic Constants (FOEC) are defined in the sense of Landau's theory [208] to establish a strain energy function, considering the medium incompressible valid for hyperelastic regime as defined Hamilton [209] as,

$$W = \mu I_2 + \frac{1}{3} A I_3 + D I_2^2 \tag{5.12}$$

where $I_1 = \mathrm{tr}\varepsilon$, $I_2 = \mathrm{tr}\varepsilon^2$ and $I_3 = \mathrm{tr}\varepsilon^3$ are the classical invariant of deformation defined by Cemal et al. [210], ε is the Green strain tensor, μ is the shear modulus and A and D are the Third and Fourth Order Elastic Constants of Landau respectively. The Second Piola Kirchoff stress tensor is determined by a constitutive law as follows,

$$S_{ij} = \frac{\partial W}{\partial \varepsilon_{ij}} \tag{5.13}$$

where ε is the Green-Cauchy strain tensor defined in terms of displacement field $u = x - X$ as the difference between actual and initial position respectively. This strain tensor is defined, according to the large deformation theory, as,

$$\varepsilon_{ij} = \frac{1}{2}(u_{i,j} + u_{j,i} + u_{k,i}u_{k,j}) \tag{5.14}$$

Under the hypothesis of a tensile test setup, the initial conditions are described in Figure 5.2.

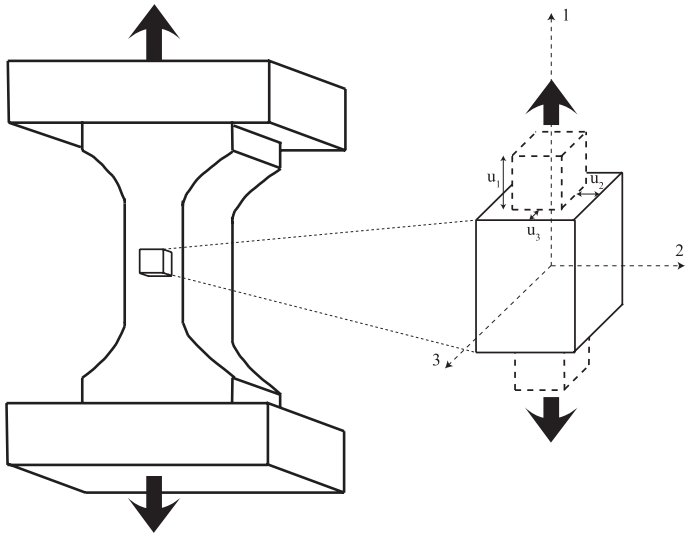

Figure 5.2: Left: scheme of the uniaxial tensile test. Right: zoom of a differential element of the sample.

where the displacements are defined in three directions as,

$$\begin{aligned} u_1 &= ax_1 \\ u_2 &= -bx_2 \\ u_3 &= -bx_3 \end{aligned} \tag{5.15}$$

In this case the Green-Cauchy strain tensor defined in equation 5.14 may be described in matrix form as,

$$\varepsilon_{ij} = \begin{pmatrix} a + \frac{1}{2}a^2 & 0 & 0 \\ 0 & -b + \frac{1}{2}b^2 & 0 \\ 0 & 0 & -b + \frac{1}{2}b^2 \end{pmatrix} \tag{5.16}$$

To describe the Second Piola-Kirchoff stress tensor in nonlinear regime, it is necessary to determine the invariant I_3 in terms of strains.

$$\begin{aligned} I_3 &= \varepsilon_{11}^3 + \varepsilon_{22}^3 + \varepsilon_{33}^3 \\ \frac{\partial I_3}{\partial \varepsilon_{ij}} &= \begin{pmatrix} 3\varepsilon_{11}^2 & 0 & 0 \\ 0 & 3\varepsilon_{22}^2 & 0 \\ 0 & 0 & 3\varepsilon_{33}^2 \end{pmatrix} \end{aligned} \tag{5.17}$$

The constitutive law for tensile test case in direction 1 is deduced by the expression,

$$S_{11} = 2\mu a + (\mu + A)a^2 + (A + 4D)a^3 \tag{5.18}$$

The relationship between the Cauchy stress tensor and the Second Piola-Kirchoff stress tensor is defined as,

$$\sigma_{ij} = J^{-1} F_{ij} S_{ij} F_{ij}^T \tag{5.19}$$

where F is the deformation gradient tensor and $J = det(F)$.

The derivation of Cauchy stress tensor in the context of weakly nonlinear elasticity [211] yields the constitutive law defined in high order as follows,

$$\sigma_{11} = 2\mu a + (5\mu + A)a^2 + (7\mu + 3A + 4D)a^3 + \left(\frac{5}{2}\mu + 3A + 8D\right) a^4 + \frac{5}{2}(A + 4D)a^5 \tag{5.20}$$

5.2.2 Mooney-Rivlin model

The Mooney-Rivlin model, originally derived by Mooney in 1940 [212] was formulated in terms of the Cauchy-Green deformation tensor invariants by Rivlin [213].

$$\Psi = \sum_{i=1}^{2} c_i \left(I_i - 3\right) \tag{5.21}$$

where c_1 and c_2 are the material parameters, I_1 and I_2 the first and second strain invariants respectively and Ψ the strain energy function.

In the case of an uniaxial tension ($\sigma = \sigma_1$, $\sigma_2 = \sigma_3 = 0$) the Cauchy stress as a function of the strain invariants is

$$\sigma = 2\left(\lambda^2 - \frac{1}{\lambda}\right)\left(\frac{\partial \Psi}{\partial I_1} + \frac{1}{\lambda}\frac{\partial \Psi}{\partial I_2}\right) \tag{5.22}$$

where $\lambda = \lambda_1$ (λ_1 is the principal stretch in 1 direction) and the invariants from the Cauchy-Green tensor for an incompressible hyperelastic material subjected to an uniaxial tension are defined as [214],

$$\begin{aligned} I_1 &= \lambda^2 + \frac{2}{\lambda} \\ I_2 &= 2\lambda + \frac{1}{\lambda^2} \\ I_3 &= 1 \end{aligned} \tag{5.23}$$

For the Mooney-Rivlin model, the Cauchy stress obtained employing 5.22 and using two parameters (c_1 and c_2) is,

$$\sigma_{\text{Mooney}} = 2\left(\lambda^2 - \frac{1}{\lambda}\right)\left(c_1 + c_2\frac{1}{\lambda}\right) \tag{5.24}$$

5.2.3 Odgen model

The strain energy function in the Odgen model, developed in 1972 [215], is described by,

$$\Psi = \sum_{r=1}^{N} \frac{\mu_r}{\alpha_r} \left(\lambda_1^{\alpha_r} + \lambda_2^{\alpha_r} + \lambda_3^{\alpha_r} - 3 \right) \tag{5.25}$$

where μ_r (infinitesimal shear modulus) and α_r (stiffening parameter) are material constants, and λ_1, λ_2 and λ_3 are the principal stretches. Taking into account that for an incompressible material, $\lambda_1 = \lambda$ and $\lambda_2 = \lambda_3 = 1/\sqrt{\lambda}$, equation 5.25 is simplified into [214],

$$\Psi = \sum_{i=1}^{N} \frac{\mu_r}{\alpha_r} \left[\lambda^{\alpha_r} + 2 \left(\frac{1}{\sqrt{\lambda}} \right)^{\alpha_r} - 3 \right] \tag{5.26}$$

The Cauchy stress tensor as a function of the principal stretches for an incompressible material is,

$$\sigma_1 = \lambda_1 \frac{\partial \Psi}{\partial \lambda_1} - \lambda_3 \frac{\partial \Psi}{\partial \lambda_3} \tag{5.27}$$

Finally, using the equation 5.27, the Cauchy stress using two parameters (μ_r and α_r) is obtained as follows,

$$\sigma_{Odgen} = \mu_r \left(\lambda^{\alpha_r} - \lambda^{-\alpha_r/2} \right) \tag{5.28}$$

The shear modulus μ in the Odgen model results from the expression,

$$\mu = \frac{\mu_r \alpha_r}{2} \tag{5.29}$$

Part II

METHODOLOGY

6

Feasibility of a novel Torsional Wave Elastography technique

This chapter aims to present the novel technique, Torsional Wave Elastography (TWE) technique, and evaluate the feasibility, sensitivity and capability to objectively quantify the viscoelastic properties of cervical tissue [1]. One contribution was a sensitivity study in tissue mimicking phantoms to evaluate the robustness of the new proposed TWE technique for its use in clinical practice. The variables object of the study were both, the applied pressure and the angle of incidence sensor-sample. The second contribution was a cervical tissue characterization by fitting the experimental data with four rheological models.

Section 6.1 outlines the structure of the torsional wave sensor with an optimal design necessary to avoid the resonant frequency in the emitter and the receiver (Section 6.2). Then, the experimental setup and protocol are presented in Sections 6.3 and 6.4. The signal processing procedure to reconstruct viscoelastic properties is widely explained in Sections 6.5 and 6.6. In Section 6.7, four rheological models are presented to understand the dispersive behavior of cervical tissues under shear wave propagation. Finally, the rheometry experiments and the viscoelastic parameters reconstruction procedure are shown in Sections 6.8 and 6.9 respectively.

[1] Contribution: A. Callejas, A. Gomez, J. Melchor, M. Riveiro, P. Massó, J. Torres, M. López-López and G. Rus. Performance study of a torsional wave sensor and cervical tissue characterization. *Sensors*, 17(9), 2017.

6.1 Structure of the sensor

The torsional device is composed of an emitter, a receiver and a casing that holds both. The emitter, responsible for the transmission of the wave which travels through the phantom, consists of a PLA (polylactic acid) disk, printed in 3D, whose rotational movement is due to an electromechanical actuator (see Figure 6.1b). This actuator is covered by a Faraday's cage of aluminum paper to nullify any effect of external electromagnetic fields. To improve the attachment between the aluminum and the actuator, a silver conductive epoxy, used as adhesive that increases the conductivity, is used. The actuator is excited electrically by a wave generator, where some parameters like frequency, voltage or working cycle are controlled.

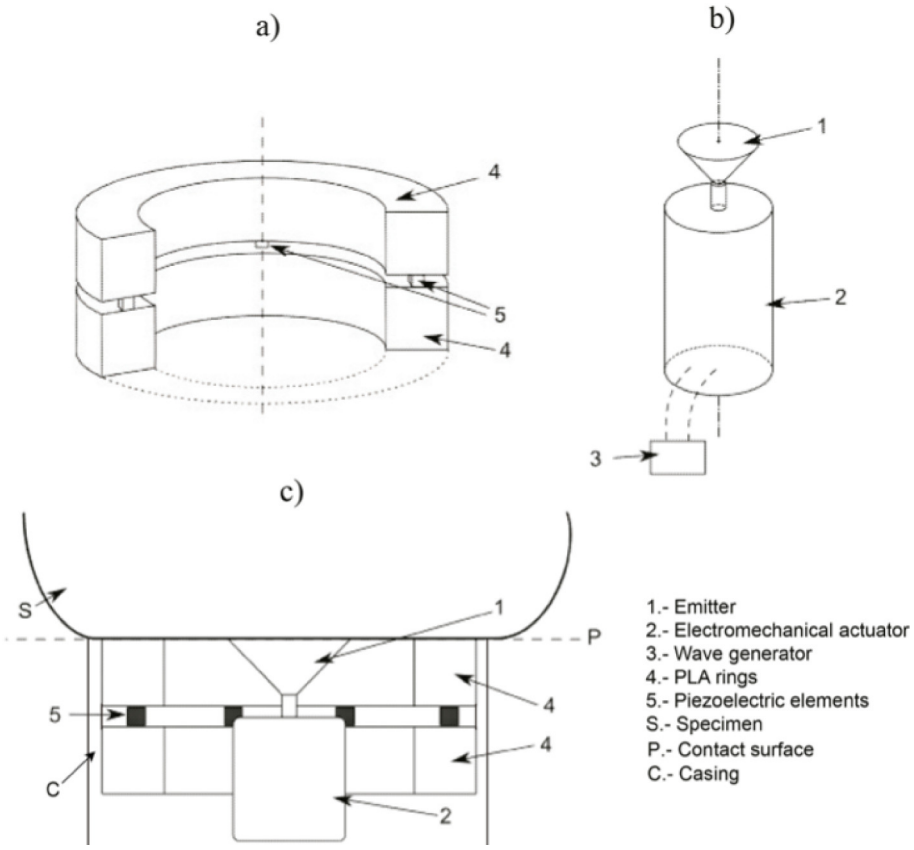

Figure 6.1: Schematic view of the sensor elements. (**a**) the receiver; (**b**) the emitter; (**c**) contact sensor–phantom.

The receiver, showed in Figure 6.1a, is formed by two PLA rings with four slots in the inner face of the ring, where the four ceramic piezoelectric elements, whose material is NCE51, are fitted. The rings mentioned above provide the inertia to reduce the resonant frequency and the stiffness to reduce dilatational waves. The array of transversely-polarized piezoceramic elements is connected to the ring by silver conductive epoxy. The piezoceramic elements are responsible for transforming the mechanical movement into an electric signal. Thus, each piezoelectric element is in contact with two electrodes of different charges.

The third part is a casing with geometrical and material selection to control the mechanical cross-talk and hold the emitter and the receiver (see Figure 6.1c). This configuration eliminates the masking p-waves that systematically arises at the boundaries of the regular contact or comb transducers [216].

6.2 Simplified analytical model

To respond to the principles of an optimal design of a torsional wave sensor considering the extraction of biomechanical properties, it is necessary to compute Finite Element Models (FEM) as a first step [217, 216, 218]. Thus, the resonant frequency can be determined for torsional waves for the emitter and the receiver using Finite Element Analysis Program (FEAP) software [219]. Therefore, a simplified model with a disk as a transmitter and a ring as a receiver (to facilitate the accessibility of experimental measurements) was developed to validate the output of resonant frequency of FEM.

The fundamentals of a simplified analytical model for an oscillatory movement of a torsional sensor are shown as follows. Consequently, the piezoelectricity coupling is introduced as a strain law uniformly distributed and directly proportional to the electrical field [220].

A single degree of freedom system is established, where the eigenproblem is reduced to a single frequency and a single mode. The movement is assumed to be subjected to the torsion rotation Θ in radians. In addition, the dynamic equilibrium of torsional moment is defined as:

$$K\Theta + I\frac{d^2\Theta}{dt^2} = 0, \tag{6.1}$$

where K is the stiffness coefficient measured in [Nm/rad] and I is the inertia moment. The steady-state solution has the following expression:

$$\Theta = \Theta^0 \sin(\omega t), \tag{6.2}$$

where ω is the natural frequency valid for the equilibrium Equation (6.1).

Considering the subsystem eigenfrequency in the case of cylinder mass and analyzing the relationship between the equations of equilibrium and the moment of inertia for a cylinder, the frequency obtained is derived as

$$f = \frac{1}{2\pi}\sqrt{\frac{nabd^2\mu}{\frac{\pi}{2}l^{\text{eff}}hr^4\rho}}. \tag{6.3}$$

Subsequently, in the case of ring mass, analyzing the subsystem eigenfrequency with the same equilibrium equation and the moment of inertia of a ring shape, we extract the next frequency

$$f = \frac{1}{2\pi}\sqrt{\frac{nabd^2\mu}{2\pi l^{\text{eff}}hmr^3\rho}}, \tag{6.4}$$

where n is the number of piezoelectric elements, a and b are the plane dimensions of the piezoelectric ceramic, d the distance from the center of rotation, μ the shear modulus, l^{eff} the effective length between piezoelectric ceramics, h the height of the cylinder or the ring, r the radius of the cylinder or the ring, m the thickness of the ring in the radial direction and ρ the density of the mass blocks.

The sensor is designed with a cylinder mass and a ring mass for each inertia subsystems of emission and reception. Then, their eigenfrequencies are fitted to optimize the resonant amplification.

Finally, the frequency of resonance obtained from FEM simulation is analyzed measuring the time between peaks of cycles. The result coincides with the resonance frequencies of the transducer described in the Table 6.1 with a percentage of error below 1% in each case.

Disc Frequency [Hz]	2.80×10^4
Ring Frequency [Hz]	2.82×10^4
FEM Frequency [Hz]	2.82×10^4
Error 1 (%)	0.68
Error 2 (%)	0.04

Table 6.1: Results of the validation analytic design versus Finite Element Analysis Program. Percentage of error for the frequencies of the disc and ring.

6.3 Experimental setup

The gelatine gels and cervical tissues were excited by a low-frequency sine-burst at different frequencies (from 300 Hz to 1000 Hz). Excitation signals were generated by an arbitrary wave generator (Agilent 33220A, Santa Clara, CA, United States) and amplified (Radio Frequency Power Amplifier 150 A, 150 W, 100 MHz) before reaching the disk emitter. Measurements were acquired for 16 V mechanical actuator voltage amplitude that provides particle displacements at the emitter surface. The transmitted shear wave motion was propagated across the homogeneous phantoms and recorded by the receiver. Pre-amplification of received signal (Olympus, 576, 172 $\times$ 42.5 dB, Waltham, MA, United States) and low-pass filtering is necessary for recording a signal of greater amplitude than the signal noise level. The wave generator is synchronized with the oscilloscope (HDO 4034, 350 MHz, 2.5 GS/s, Santa Clara, CA, United States) to record the start of the signal. As a final step, a Matlab (Release 2014b, MathWorks, Natick, United States) optimization algorithm yields the shear wave speed. The experimental setup of the specimens is shown in Figure 6.2.

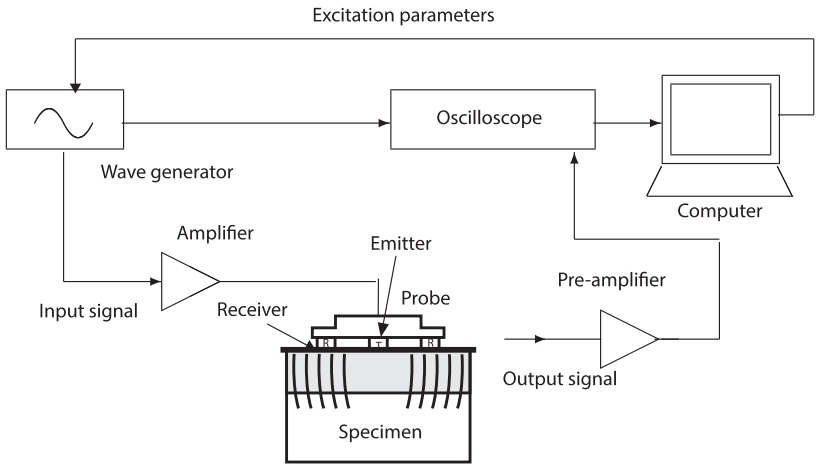

Figure 6.2: Experimental configuration of the excitation–propagation measurement system.

6.4 Specimens and experimental protocols

6.4.1 Sensitivity study

Gelatine samples from porcine skin (Type A, 300 Bloom, G2500, Sigma-Aldrich, St. Louis, MO, USA) were constructed to test the sensor sensitivity under different applied pressures, sensor–specimens and different angles of incidence. Six homogeneous phantoms with 8% and 10% (w/w) gelatine concentrations were tested. Gelatine powder and purified water at 90 °C were stirred for 10 min to ensure gelatine dissolution. Molten gelatine was cast in cylindrical molds (6.8 cm diameter, 1.35 cm height) and kept at room temperature for 2 h before being stored in the refrigerator at 5 °C. The phantoms were taken out one day after being stored in the fridge and were tested when they reached the laboratory temperature (22 ± 1 °C).

All measurements were carried out with the same experimental protocol. A counterweight device was specifically designed to control the applied pressure and the angle of incidence phantom surface–sensor (see Figure 6.3). The phantoms were excited with a range of frequencies from 300 to 1000 Hz to avoid resonance phenomena in the rings. The phantoms were positioned at the balance to quantify the applied force during the measurement. Measurements from four applied pressures (from 4.81 to 24.06 kPa) and two angles of incidence phantom surface-sensor (0 and 7.5°) were performed. The material density used was 1000 kg/m^3.

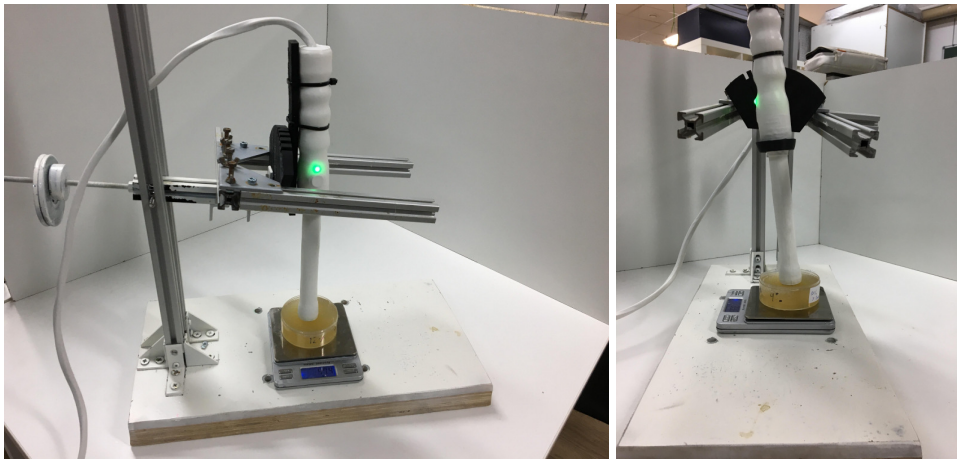

(a) (b)

Figure 6.3: A counterweight device to control the applied pressure (phantom positioned on a balance) and the angle of incidence phantom-sensor. (**a**) angle of incidence 0°; (**b**) angle of incidence 7.5°.

6.4.2 Cervical tissue characterization

To obtain the viscoelastic properties, an *ex-vivo* test on human cervical tissue samples from 3 healthy women aged from 55 to 74 years old were carried out using TWE and rheometry techniques (see Figure 6.4). Patient consent (the study was conducted according to the Declaration of Helsinki Principles and the agreement of the ethical committees of the University of Granada and the Universitary Hospital Complex of Granada) was obtained before carrying out the measurements. All patients were diagnosed with uterine prolapse (II and III grade) that required a partial or complete hysterectomy. The surgical procedures were performed at the San Cecilio University Hospital, Granada (Spain). The organs were placed in Phosphate Buffered Saline (PBS) and transferred to the Pathological Anatomy Laboratory in a refrigerator. The specimens were tested with the torsional wave sensor before being excised for rheometry experiments. Two pins were placed along the contours to prevent distortion of the tissue, and the cervix was placed on top of a rectangular piece of sound-absorbing rubber. Both measurements were performed at room temperature and typically within 2.5 h after being transferred to the laboratory, measuring three times each sample to obtain the mean and standard deviation. Given the independence of the applied pressure and the angle of incidence sensor-specimen in the sensitivity study, the cervical tissue samples were tested with the torsional wave sensor using the same range of frequencies (from 300 to 1000 Hz). After that experiment, circumferential samples were cut by a pathologist for rheometry experiments, 20 mm in diameter and 3–5 mm thick.

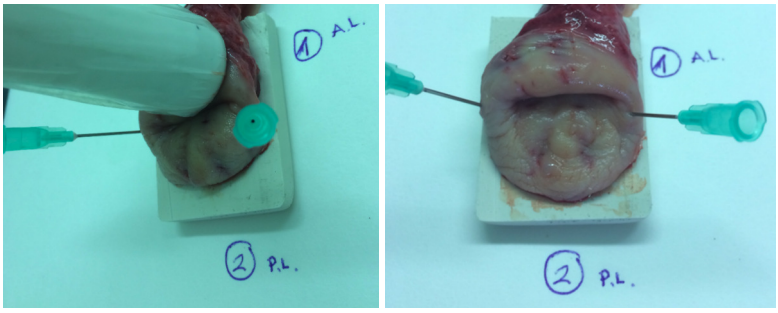

(a) (b)

Figure 6.4: (**a**) Measurement with the torsional wave sensor of a cervical tissue sample; (**b**) cervical tissue sample.

6.5 Time of flight-signal processing

Time of flight calculation is conceptually simple, although it is necessary to introduce simplifying hypotheses. Physically, S-type waves are originated by the actuator and are transmitted through the specimen to the piezoelectric sensor, where they produce the deformation thereof and, consequently, an electric potential capturable by an oscilloscope.

In a purely theoretical approach, the signal in the sensor channel has null amplitude until the shear wave reaches the sensor producing a non-zero amplitude response. In practice, the presence of undesired interference signals from multiple sources requires a measurement and processing protocol to improve the quality of the resultant signal.

The signal processing includes the average of multiple measurements to decrease noise. Thereby, multiple identical measurements spaced by a relaxation time to completely dissipate previous waves were used. In addition, a low-pass filter in frequency domain with a cutoff frequency of 8000 Hz was applied to eliminate distortions generated from the electronics that controls the equipment.

Averaging and filters did not completely eliminate the electromagnetic coupling between emission and reception channels. This situation means that the received signal had an instant response time. Several tests suggest that the electromagnetic coupling component depends, on first approximation, only on the emitted signal power and in certain cases on external environmental components, like a remarkable increase of the humidity. In this work, the "calibration" measurement (without contact with the specimen) and the measurement of the specimen had the same coupling component. Thus, subtracting the calibration measurement from the measured signal, this effect can be eliminated.

The analysis of the resultant signal allows obtaining a first time of flight time measurement as the difference between the starting time of the received signal and the starting time of the excitation signal. Certain simplifications must be assumed for this analysis since there are phenomena such as imperfect centering of the transmitter with respect to the four piezoelectric receivers and transient effects associated with the engine start, high frequencies transmission and other effects whose quantification are beyond the scope of this work.

6.6 Shear speed from time of flight

Ideally, the shear velocity can be calculated directly from the time of flight

$$Velocity = \frac{Distance}{Time\ of\ flight}. \tag{6.5}$$

However, the time of flight measured directly from the sensor signal is not the correct wave time of flight time because there is a delay associated with multiple effects (transmission in the PLA, delays related to electronics and piezoelectric devices...). These types of effects can be combined into a single delay time factor, so the Equation (6.5) results in

$$Velocity = \frac{Distance}{Time\ of\ flight - delay}. \tag{6.6}$$

This internal delay is characteristic of the measurement configuration and must be estimated previously. Assuming that the internal delay depends only on the material and the frequency excitation, time of flight of measurements at different distance emitter-receiver can be extended to zero distance obtaining a non-zero value of time that is the delay searched.

6.7 Rheological models

Similarly to many soft tissues, the behavior of cervical tissue can be modeled as linear viscoelastic media and several models have been already studied [7, 221, 222]. Here, we propose the Kelvin–Voigt, Kelvin–Voigt Fractional Derivative, Maxwell and Zener models, which are the most widely used (see Figure 6.5).

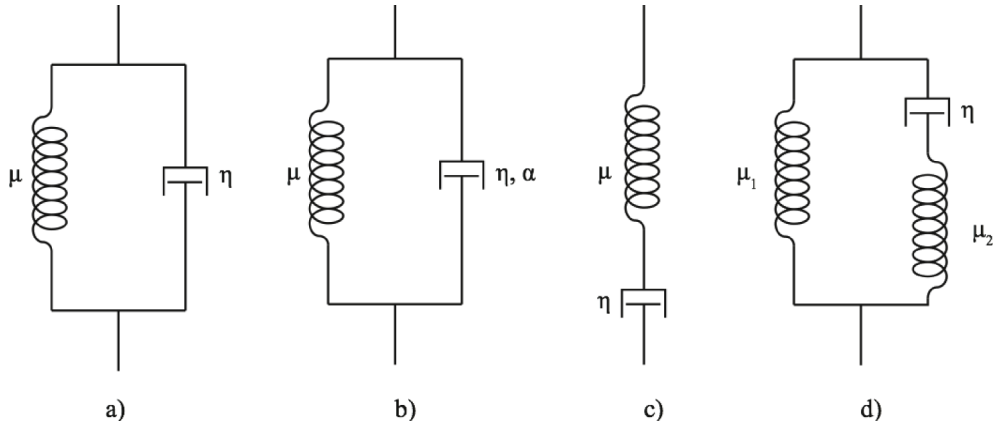

Figure 6.5: Rheological models. (**a**) the Kelvin–Voigt model; (**b**) the Kelvin–Voigt Fractional Derivative model; (**c**) the Maxwell model; (**d**) the Zener model.

The viscoelastic modulus (G^*) (Equation (6.7)), which is composed of a real part ($G^{'}$), elastic or storage modulus and an imaginary part ($G^{''}$), viscous or loss modulus, characterizes the viscoelasticity of the material [223]:

$$G^* = G^{'}(\omega) + iG^{''}(\omega). \tag{6.7}$$

The following rheological models relate the elasticity and viscosity by the complex shear modulus.

The Maxwell model (M) can be represented by a spring and a dashpot in series, as shown in the Figure 6.5. The complex shear modulus for this model is,

$$G^{*M}(\omega) = \frac{\mu\eta\omega^2}{\mu^2 + \omega^2\eta^2} + i\frac{\mu^2\eta\omega}{\mu^2 + \omega^2\eta^2}. \tag{6.8}$$

The Kelvin–Voigt (KV) rheological model is characterized by elastic μ and viscous η coefficients. This rheological model consists of a spring and a dashpot placed in parallel, which describes tissues as solids that can creep but show little stress relaxation. The corresponding complex shear modulus for the KV model is,

$$G^{*KV}(\omega) = \mu_1 + i\omega\eta, \tag{6.9}$$

where μ_1 is the shear elasticity (in *Pa*) and η is the shear viscosity (in Pa $\cdot$ s).

The Kelvin–Voigt Fractional Derivative model (KVFD), obtained by a generalization of the Kelvin–Voigt model, is a three-parameter fractional-order model. The first derivative in time in the KV model is replaced by a fractional-order derivative of order α [224]. The complex shear modulus for the KVFD model is [225, 226]

$$G^{*KVFD}(\omega) = \mu_1 + \eta\omega^\alpha cos(\frac{\alpha\pi}{2}) + i\eta\omega^\alpha sin(\frac{\alpha\pi}{2}), \tag{6.10}$$

where α is the fractional derivative power ($0 \leq \alpha \leq 1$).

The Zener model (Z) expresses both the stress relaxation and the creep in linear viscoelastic polymeric solids [227]. The complex shear modulus for the Zener model in the frequency response is given by [228]

$$G^{*Z}(\omega) = \frac{\mu_1\mu_2^2 + \omega^2\eta^2(\mu_1 + \mu_2)}{\mu_2^2 + \omega^2\eta^2} + i\frac{\mu_2^2\eta\omega}{\mu_2^2 + \omega^2\eta^2}, \tag{6.11}$$

where μ_1 and μ_2 are the elasticities (in Pa) and η is the shear viscosity (in Pa $\cdot$ s).

Dispersion curves are plots of shear wave speed (c_s) as a function of angular frequency ω. For mass density ρ, the relationship between c_s and the complex shear modulus is well known to be [229]

$$c_s(\omega) = \sqrt{\frac{2(G'^2 + G''^2)}{\rho(G' + \sqrt{G'^2 + G''^2})}}. \tag{6.12}$$

6.8 Rheometry experiments

Rheometry is a technique that studies the relationship between stress–strain in materials that are capable of flowing, thus allowing to get mechanical properties related to elasticity and viscosity, which usually leads to the development of a constitutive relation. In this work, these properties were evaluated under shear stress with a controlled-rate magnetorheometer

(MCR 300 Physica-Anton Paar, Graz, Austria) (see Figures 6.6 and 6.7). As inertia of the sample was negligible in oscillatory shear deformation, it required that a small phantom thickness compared with the wavelength of shear waves propagated through the medium at the frequency of oscillation [230]. The measuring system geometry was a 20 mm diameter parallel plate set for a gap width dependent on the sample thickness, as a rule 3–5 mm.

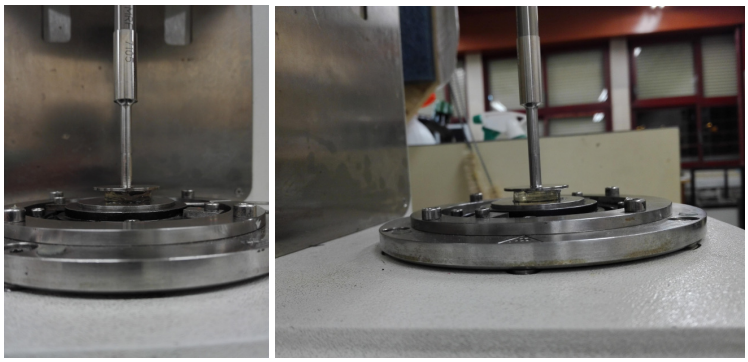

(a) (b)

Figure 6.6: Viscoelastic characterization of gelatine samples. (**a**) Front view of rheometer (**b**) Lateral view of rheometer.

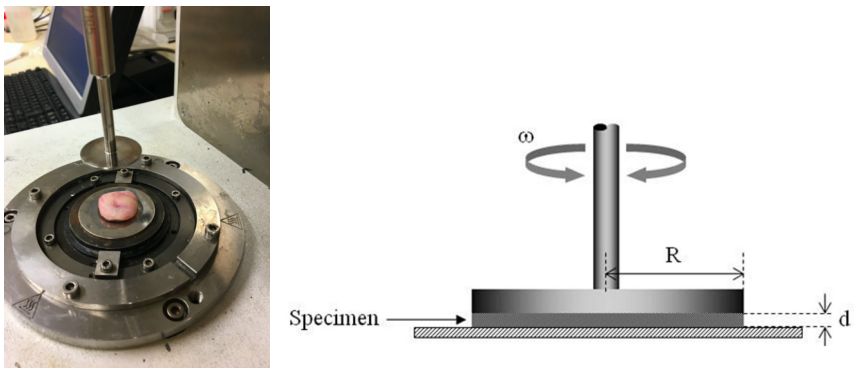

(a) (b)

Figure 6.7: (**a**) A controlled-rate magnetorheometer MCR 300 Physica-Anton Paar, Graz, Austria. Pink matter corresponds to the cervical tissue sample. (**b**) Schematic view of the rheometer.

All measurements were conducted at room temperature to avoid loss of consistency. The experiment started with a squeezing compression of the rotor plate, no less than 0.2 N, for preventing slippery conditions. To ensure the reproducibility of the measurements, a pre-shear (10 cycles at 1 Hz) was applied with a waiting time of 10 s before measuring. The samples were subjected to a sinusoidal shear stress and the corresponding shear strain was measured, according to the constitutive equation for linear viscoelastic materials where

$$\sigma = \sigma_0 e^{i(\omega t)} \tag{6.13}$$

$$\gamma = \gamma_0 e^{i(\omega t - \delta)} \tag{6.14}$$

are, respectively, the shear stress and strain, σ_0 is the stress amplitude, γ_0 the strain amplitude, ω the angular frequency, and δ the stress–strain phase lag. Two oscillatory tests were planned to obtain the viscoelastic modulus (G^*).

The experiments were [231, 232]: (i) amplitude sweep: frequency was kept constant at 1, 2, 5, 10 and 20 Hz, and shear amplitude was varied up to values in which nonlinear behavior was reached. Nonlinearity was developed and was clearly distinguishable when $G^{'}$ and $G^{''}$ were not only functions of ω but also strongly depended on γ_0. The frequency range was not higher owing to the linearity of oscillations that can not be ensured when the rotor (upper plate) and the sample inertia effects become significant at high frequencies [230]; and (ii) frequency sweep: shear amplitude was kept constant into the viscoelastic limit region, determined by the previous test and the frequency was swept from 0.5 Hz to 100 Hz logarithmically to obtain the oscillograms ($G^{'}$ and $G^{''}$ as a function of ω).

6.9 Viscoelastic parameters reconstruction

The characteristic parameters of a viscoelastic material were obtained fitting the experimental results with the rheological models indicated in the previous section. Two different techniques (rheometry and TWE) were used in each sample of cervical tissue. For each sample and methodology, velocities at several frequencies were calculated and the mean of the velocities over all the measurements were used for further analysis.

In the rheometry study, the real and the imaginary parts of the viscoelastic modulus were obtained from the rheometer and the shear wave speed was calculated directly using Equations (6.7) and (6.12). For the torsional wave sensor, the shear wave speeds were obtained following the approach depicted in Section 6.5. The high differences on the frequency ranges of the two techniques should be noted.

Every set of measurements was fitted to the models to obtain the parameter values. This adjustment was made by means of an inverse problem using a combination of genetic algorithms and quasi-Newton type optimization algorithms.

Three approaches were used and represented varying the fitted data using (a) shear wave speeds exclusively from rheometry, (b) speeds exclusively from the torsional sensor, and (c) all of the available data. The fitting procedure was applied to each tissue sample to obtain the average adjustment curves (including standard deviations). Two options were available: using the average values of the parameters to generate average curves or directly averaging the values of the curves. It should be highlighted that these adjustments are not equal since the models were nonlinear. The first approach was used in this work.

7

Viscoelastic model class selection for cervical tissue

This chapter aims at providing a method for ranking the most plausible rheological model with the purpose of understanding the interaction of torsional waves with the anatomy of cervical tissue. The final aim of this study is to reconstruct the viscoelastic parameters with the selected rheological model. A Probabilistic Inverse Problem (PIP) was employed for ranking the most plausible model by comparing the *in-vivo* measurements in cervical tissue obtained from the TWE technique with the synthetic signals from the 2D Finite Differente Time Domain (FDTD) wave propagation models.

Section 7.1 shows the three bilayer viscoelastic models considered with the purpose of understanding the interaction of torsional waves with the histology of tissue. In Section 7.2, the three proposed models of torsional wave propagation are implemented in cylindrical coordinates using 2D FDTD method. Section 7.3 outlines a cross-sectional study in pregnant women to obtain *in-vivo* experimental signals from cervical tissue using TWE technique. Finally, a PIP, based on information theory, for ranking the viscoelastic model that best explain the cervical tissue behavior under torsional wave propagation is presented in Section 7.4.

7.1 Rheological models

The increasing interest in elastography techniques for measuring viscoelastic parameters in cervical tissue is demanding appropriate viscoelastic models (micro-structural, rheological and continuum). The rheological models explain the gross tissue mechanical parameters in the simplest possible terms [233]. A study that explores the importance of the heterogeneous multi-scale nature of cervical tissue for quantifying both the elasticity and viscosity from

Viscoelastic Models	Epithelial layer	Connective Layer
Elastic model	μ th	μ
Kelvin-Voigt model	μ th η	μ η
Maxwell model	μ th η	μ η

Table 7.1: This table summarizes the parameters used for the epithelial and connective layer and for the three models. Shear stiffness μ, shear viscosity η and epithelium thickness th.

shear waves was carried out by Peralta et al. [234]. The work demonstrated that, among the models studied, the best rheological model to describe cervical tissue is Maxwell's law. In contrast, Callejas et al. [60] characterized the viscoelastic properties of cervix hysterectomies by fitting the experimental data obtained with torsional wave elastography with four different viscoelastic models (Kelvin-Voigt, Kelvin-Voigt Fractional Derivative, Maxwell and Zener model). Notwithstanding, the work concluded that the Kelvin-Voigt model and its fractional derivative version fit the cervix experimental data successfully. The Kelvin-Voigt model was the simplest model that best fit the stress-strain relationship of the *ex-vivo* human cervical tissue.

According to the previous experiences, the experimental system was idealized by a set of three simplified viscoelastic models in which the transmitted torsional waves propagate and interact with cervical tissue until they were received by the probe. The three viscoelastic models tested were: 1. Elastic bilayer, 2. Kelvin-Voigt bilayer, and 3. Maxwell bilayer.

There is a need for understanding cervical tissue behavior considering multilayer models, since torsional waves propagate through the surface and in-depth tissue. The elastic model is defined in terms of the stiffness (μ) for the epithelium and connective layer. The Kelvin-Voigt and Maxwell models are not only defined in terms of the shear stiffness for each layer and epithelium thickness (th) but also in terms of shear viscosity (η) of the epithelium and connective layer.

The three models are summarized in Table 7.1.

7.2 Finite difference time-domain method

Wave propagation equations are usually solved by numerical methods when they are either impossible to obtain or impractical. Nowadays, the most employed methods to simulate physical phenomena are the Finite Element method (FEM) and the Finite Difference method. The advantages of FDTD versus FEM are the reduction in computing time and the less storage space needed [235]. The drawback is that it is necessary to perform the discretization of the equations. FDTD method is a finite difference method in the time domain. This method was selected due to its flexibility, speed and simplicity for implementing rheological models like the ones that will be presented below. The first to introduce this method was Yee in 1996

[236] to replace Maxwell's equations by a set of finite difference equations. Madariaga [237] was the first that applied the algorithm to elastic equations.

In this section, an FDTD method is developed, adapted from a previous work by Virieux [238], to model the propagation of torsional waves in three two-dimensional models of cervical tissue. Since torsional waves propagate with axial symmetry from the center of the probe, where the mechanical actuator is placed, the formulation is developed in cylindrical coordinates [60]. According to the histology of the cervix, two layers have been taken into account (Figure 7.1). Three different viscoelastic models have been compared. In the following subsections, we will deduce the equations that govern the torsional wave propagation for each viscoelastic model.

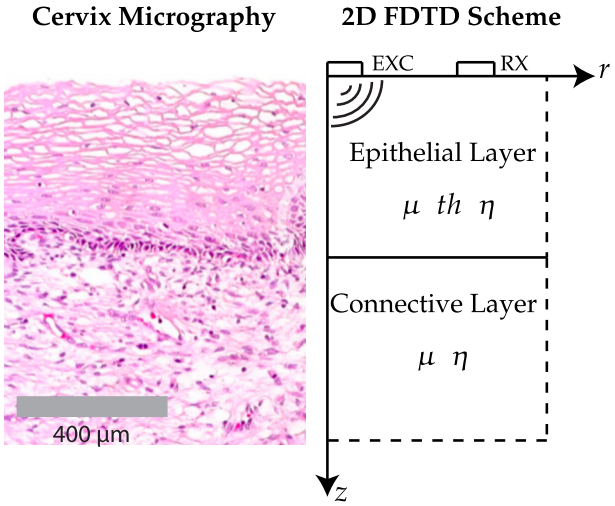

Figure 7.1: Cervix micrography versus two dimensional finite difference time domain scheme. Source: adapted from [2].

7.2.1 Elastic model

The dynamic equilibrium equation independent of the coordinate system is as follows:

$$\nabla\sigma + F = \rho\ddot{u} \tag{7.1}$$

where ρ denotes the tissue density, σ the stress tensor, u particle displacement and F is the volume force density.

Taking into account cylindrical coordinates, the equations for each component are [239]:

$$\begin{aligned}
\rho\ddot{u}_r &= \frac{\partial\sigma_{rr}}{\partial r} + \frac{1}{r}\frac{\partial\sigma_{r\theta}}{\partial\theta} + \frac{\partial\sigma_{rz}}{\partial z} + \frac{1}{r}(\sigma_{rr} - \sigma_{\theta\theta}) + F_r \\
\rho\ddot{u}_\theta &= \frac{\partial\sigma_{r\theta}}{\partial r} + \frac{1}{r}\frac{\partial\sigma_{\theta\theta}}{\partial\theta} + \frac{2}{r}\sigma_{r\theta} + \frac{\partial\sigma_{\theta z}}{\partial z} + F_\theta \\
\rho\ddot{u}_z &= \frac{\partial\sigma_{rz}}{\partial z} + \frac{1}{r}\frac{\partial\sigma_{\theta z}}{\partial\theta} + \frac{1}{r}\sigma_{rz} + \frac{\partial\sigma_{zz}}{\partial z} + F_z
\end{aligned} \tag{7.2}$$

The relation between the stress and the strain tensors is established with the following constitutive equation:

$$\sigma_{ij} = \lambda \epsilon_{kk} \delta_{ij} + 2\mu \epsilon_{ij} \tag{7.3}$$

where λ and μ are the Lamé constants and ϵ is the strain tensor.

Finally, the displacement field u is related to the strain tensor ϵ according to the kinematic relation as follows:

$$\epsilon = \frac{1}{2}\left[\nabla u + (\nabla u)^T\right] \tag{7.4}$$

The components of the gradient of a displacement field in cylindrical coordinates are:

$$\nabla u = \begin{bmatrix} \frac{\partial u_r}{\partial r} & \frac{1}{r}\frac{\partial u_r}{\partial \theta} - \frac{u_\theta}{r} & \frac{\partial u_r}{\partial z} \\ \frac{\partial u_\theta}{\partial r} & \frac{1}{r}\frac{\partial u_\theta}{\partial \theta} + \frac{u_r}{r} & \frac{\partial u_\theta}{\partial z} \\ \frac{\partial u_z}{\partial r} & \frac{1}{r}\frac{\partial u_z}{\partial \theta} & \frac{\partial u_z}{\partial z} \end{bmatrix} \tag{7.5}$$

As discussed above, when considering axial symmetry in the problem, the derivatives with respect the angle θ ($\frac{\partial}{\partial \theta} = 0$) are neglected. Besides, only displacements in the θ component are considered ($u_r = u_z = 0$) due to the nature of torsional waves.

The remaining equations in cylindrical coordinates for the elastic model after simplifying the problem, as well as transformations to remove one-time derivative ($\ddot{u}_\theta = \dot{v}_\theta$, $\dot{v}_\theta$ is the derivative of the velocity with respect the θ component), are:

$$\begin{cases} \rho \dot{v}_\theta = \dfrac{\partial \sigma_{r\theta}}{\partial r} + \dfrac{2}{r}\sigma_{r\theta} + \dfrac{\partial \sigma_{\theta z}}{\partial z} \\ \dot{\sigma}_{r\theta} = \mu\left[\dfrac{\partial v_\theta}{\partial r} - \dfrac{v_\theta}{r}\right] \\ \dot{\sigma}_{\theta z} = \mu \dfrac{\partial v_\theta}{\partial z} \end{cases} \tag{7.6}$$

7.2.2 Kelvin-Voigt model

Taking into account the dynamic equilibrium equation (Equation 7.2), the kinematic relation (Equation 7.4) and the constitutive equation (Equation 5.9), the remaining equations in cylindrical coordinates for the Kelvin-Voigt model after simplifying the problem (considering axial symmetry), as well as transformations to remove one time derivative ($\ddot{u}_\theta = \dot{v}_\theta$) are:

$$\begin{cases} \rho\dot{v}_\theta = \dfrac{\partial\sigma_{r\theta}}{\partial r} + \dfrac{2}{r}\sigma_{r\theta} + \dfrac{\partial\sigma_{\theta z}}{\partial z} \\ \dot{\sigma}_{r\theta} = \mu\left[\dfrac{\partial v_\theta}{\partial r} - \dfrac{v_\theta}{r}\right] + \eta\left[\dfrac{\partial\dot{v}_\theta}{\partial r} - \dfrac{\dot{v}_\theta}{r}\right] \\ \dot{\sigma}_{\theta z} = \mu\dfrac{\partial v_\theta}{\partial z} + \eta\dfrac{\partial\dot{v}_\theta}{\partial z} \end{cases} \tag{7.7}$$

7.2.3 *Maxwell model*

Considering the dynamic equilibrium equation (Equation 7.2), the kinematic relation (Equation 7.4) and the constitutive equation (Equation 5.11), the remaining equations in cylindrical coordinates for the Maxwell model after simplifying the problem, as well as transformations to remove one time derivative ($\dot{u}_\theta = \dot{v}_\theta$) are:

$$\begin{cases} \rho\dot{v}_\theta = \dfrac{\partial\sigma_{r\theta}}{\partial r} + \dfrac{2}{r}\sigma_{r\theta} + \dfrac{\partial\sigma_{\theta z}}{\partial z} \\ \sigma_{r\theta} + \dfrac{\eta}{\mu}\dot{\sigma}_{r\theta} = \eta\left[\dfrac{\partial v_\theta}{\partial r} - \dfrac{v_\theta}{r}\right] \\ \sigma_{\theta z} + \dfrac{\eta}{\mu}\dot{\sigma}_{\theta z} = \eta\dfrac{\partial v_\theta}{\partial z} \end{cases} \tag{7.8}$$

7.2.4 *Space-time grid discretization*

The classical time-staggering approach used in FDTD literature consist of calculating stress and strain components in a half-step time instant from the corresponding time instant of the displacements [238]. However, in this work, all stress, strain and displacement components are computed at the same time interval, according to Orescanin et al. [206]. Uniform time intervals have been sampled via $t = n\Delta t$ for an integer n and a time step Δt.

Spatial discretization was employed using the staggered grid showed in Figure 7.2. The stress components are placed at grid positions that are offset by a half-step from the corresponding velocity component. Space was uniformly sampled, with $a = i\Delta r/2$ and $b = j\Delta z/2$ for integers a, b and space step of discretization Δr and Δz.

Model parameters, such as shear stiffness and viscosity, have been introduced into the model by setting their values at the grid points of the discretized space domain for each viscoelastic model.

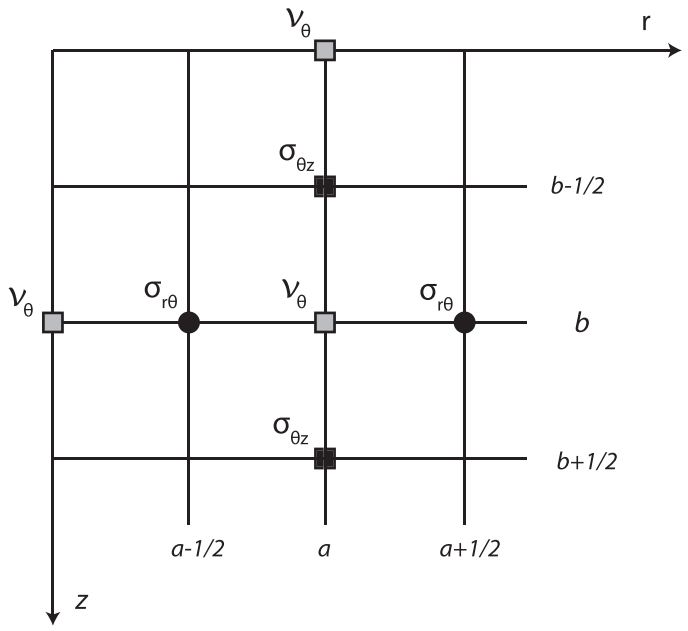

Figure 7.2: Staggered grid discretization illustrating the locations of variables. Velocity (v_θ), and stresses ($\sigma_{r\theta}$,$\sigma_{\theta z}$).

7.2.5 *Approximation of derivatives*

The equations of the wave propagation (systems of equations 7.6, 7.7 and 7.8) for each of the viscoelastic models presented in previous sections have been discretized according to Taylor series expansions [240].

A first-order accurate centered scheme finite difference discretization has been employed for derivatives with respect to one of the spatial variables (r or z):

$$\left.\frac{\partial f(x,t)}{\partial x}\right|_{x_i,t_n} = \frac{f\left(x_{i+\frac{1}{2}},t_n\right) - f\left(x_{i-\frac{1}{2}},t_n\right)}{\Delta x} + O(\Delta x^2) \tag{7.9}$$

where f is an arbitrary function within the domain of interest, x one of the spatial variables r and z, t represents time, and Δx is the spatial step for each variable.

For first order time derivative, the backward finite difference scheme was chosen:

$$\frac{\partial f(x,t)}{\partial t}\Big|_{x_i,t_{n+1}} = \frac{f\left(x_i,t_{n+1}\right) - f\left(x_i,t_n\right)}{\Delta t} + O(\Delta t) \tag{7.10}$$

The derivation of the discrete systems of equations (7.6, 7.7 and 7.8) for each viscoelastic model is described in the following equations (Equations 7.11 to 7.19).

1. Elastic model discretization:

$$\begin{aligned} v_\theta\Big|_{a,b}^{n+1} = v_\theta\Big|_{a,b}^{n} + \left(\frac{\Delta t}{\rho\Delta r} + \frac{\Delta t}{r\rho}\right)\sigma_{r\theta}\Big|_{a+\frac{1}{2},b}^{n} + \left(-\frac{\Delta t}{\rho\Delta r} + \frac{\Delta t}{r\rho}\right)\sigma_{r\theta}\Big|_{a-\frac{1}{2},b}^{n} + \\ + \frac{\Delta t}{\rho\Delta z}\sigma_{\theta z}\Big|_{a,b+\frac{1}{2}}^{n} - \frac{\Delta t}{\rho\Delta z}\sigma_{\theta z}\Big|_{a,b-\frac{1}{2}}^{n} \end{aligned} \tag{7.11}$$

$$\sigma_{r\theta}\Big|_{a-\frac{1}{2},b}^{n+1} = \sigma_{r\theta}\Big|_{a-\frac{1}{2},b}^{n} + \left(\frac{\mu\Delta t}{\Delta r} - \frac{\mu\Delta t}{2r}\right) v_\theta\Big|_{a,b}^{n+1} + \left(-\frac{\mu\Delta t}{\Delta r} - \frac{\mu\Delta t}{2r}\right) v_\theta\Big|_{a-1,b}^{n+1} \tag{7.12}$$

$$\sigma_{\theta z}\Big|_{a,b+\frac{1}{2}}^{n+1} = \sigma_{\theta z}\Big|_{a,b+\frac{1}{2}}^{n} + \frac{\mu\Delta t}{\Delta z} v_\theta\Big|_{a,b+1}^{n+1} - \frac{\mu\Delta t}{\Delta z} v_\theta\Big|_{a,b}^{n+1} \tag{7.13}$$

2. Kelvin-Voigt model discretization:

$$\begin{aligned} v_\theta\Big|_{a,b}^{n+1} = v_\theta\Big|_{a,b}^{n} &+ \left(\frac{\Delta t}{\rho\Delta r} + \frac{\Delta t}{r\rho}\right) \sigma_{r\theta}\Big|_{a+\frac{1}{2},b}^{n} + \left(-\frac{\Delta t}{\rho\Delta r} + \frac{\Delta t}{r\rho}\right) \sigma_{r\theta}\Big|_{a-\frac{1}{2},b}^{n} + \\ &+ \frac{\Delta t}{\rho\Delta z} \sigma_{\theta z}\Big|_{a,b+\frac{1}{2}}^{n} - \frac{\Delta t}{\rho\Delta z} \sigma_{\theta z}\Big|_{a,b-\frac{1}{2}}^{n} \end{aligned} \tag{7.14}$$

$$\begin{aligned} \sigma_{r\theta}\Big|_{a-\frac{1}{2},b}^{n+1} = \sigma_{r\theta}\Big|_{a-\frac{1}{2},b}^{n} &+ \left(\frac{\mu\Delta t}{\Delta r} - \frac{\mu\Delta t}{2r} + \frac{\eta}{\Delta r} - \frac{\eta}{r}\right) v_\theta\Big|_{a,b}^{n+1} + \\ &+ \left(-\frac{\mu\Delta t}{\Delta r} - \frac{\mu\Delta t}{2r} - \frac{\eta}{\Delta r}\right) v_\theta\Big|_{a-1,b}^{n+1} \\ &+ \left(-\frac{\eta}{\Delta r} + \frac{\eta}{r}\right) v_\theta\Big|_{a,b}^{n} + \frac{\eta}{\Delta r} v_\theta\Big|_{a-1,b}^{n} \end{aligned} \tag{7.15}$$

$$\begin{aligned} \sigma_{\theta z}\Big|_{a,b+\frac{1}{2}}^{n+1} = \sigma_{\theta z}\Big|_{a,b+\frac{1}{2}}^{n} &+ \left(\frac{\mu\Delta t}{\Delta z} + \frac{\eta}{\Delta z}\right) v_\theta\Big|_{a,b+1}^{n+1} + \left(-\frac{\eta}{\Delta z} - \frac{\mu\Delta t}{\Delta z}\right) v_\theta\Big|_{a,b}^{n+1} - \\ &- \frac{\eta}{\Delta z} v_\theta\Big|_{a,b+1}^{n} - \frac{\eta}{\Delta z} v_\theta\Big|_{a,b}^{n} \end{aligned} \tag{7.16}$$

3. Maxwell model discretization:

$$\begin{aligned} v_\theta\Big|_{a,b}^{n+1} = v_\theta\Big|_{a,b}^{n} &+ \left(\frac{\Delta t}{\rho\Delta r} + \frac{\Delta t}{r\rho}\right) \sigma_{r\theta}\Big|_{a+\frac{1}{2},b}^{n} + \left(-\frac{\Delta t}{\rho\Delta r} + \frac{\Delta t}{r\rho}\right) \sigma_{r\theta}\Big|_{a-\frac{1}{2},b}^{n} + \\ &+ \frac{\Delta t}{\rho\Delta z} \sigma_{\theta z}\Big|_{a,b+\frac{1}{2}}^{n} - \frac{\Delta t}{\rho\Delta z} \sigma_{\theta z}\Big|_{a,b-\frac{1}{2}}^{n} \end{aligned} \tag{7.17}$$

$$\begin{aligned} \sigma_{r\theta}\Big|_{a-\frac{1}{2},b}^{n+1} = \left(1 - \frac{\mu\Delta t}{2\eta}\right) \sigma_{r\theta}\Big|_{a-\frac{1}{2},b}^{n} &- \frac{\mu\Delta t}{2\eta} \sigma_{r\theta}\Big|_{a+\frac{1}{2},b}^{n} + \left(\frac{\mu\Delta t}{\Delta r} - \frac{\mu\Delta t}{2r}\right) v_\theta\Big|_{a,b}^{n+1} \\ &- \left(\frac{\mu\Delta t}{\Delta r} + \frac{\mu\Delta t}{2r}\right) v_\theta\Big|_{a-1,b}^{n+1} \end{aligned} \tag{7.18}$$

$$\begin{aligned} \sigma_{\theta z}\Big|_{a,b+\frac{1}{2}}^{n+1} = \left(1 - \frac{\mu\Delta t}{2\eta}\right) \sigma_{\theta z}\Big|_{a,b+\frac{1}{2}}^{n} &- \frac{\mu\Delta t}{2\eta} \sigma_{\theta z}\Big|_{a,b-\frac{1}{2}}^{n} + \frac{\mu\Delta t}{\Delta z} v_\theta\Big|_{a,b+1}^{n+1} - \\ &- \frac{\mu\Delta t}{\Delta z} v_\theta\Big|_{a,b}^{n+1} \end{aligned} \tag{7.19}$$

7.2.6 Boundary conditions

The boundary conditions of the problem are the excitation source at the surface of the cervical tissue (Equation 7.20), the absence of the shear stress (Equation 7.21) and the absence of the velocity (Equation 7.22) on the same interface and the absorbing boundary conditions (ABC) (see Figure 7.3).

- For the excitation signal, the values have been set for each time step n at the grid points that represent the contact between the emitter and the cervical tissue (more details in *High-Speed Camera Measurements* subsection).
- The grid points on the reception place have been simulated by the absence of velocity due to the pressure that the receiver exerts on the cervical tissue. The average stress $\sigma_{\theta z}$ was obtained on the reception place. The stress on the piezoelectric element is approximately the stress on the tissue by a correction factor α_c. The calculation of that factor is detailed in the following subsection *Transmission coefficient*. Finally, the stresses received by the piezoelectric element were transformed into voltage terms using the constitutive equations of piezoelectricity (see Appendix E).
- The grid points on the surface cervix-vagina that were not used for the above boundary condition, are set with the absence of stress ($\sigma_{\theta z} = 0$).
- Finally, in order to model the infinite half-space, all waves that are reaching the two remaining outer grid edges must be transmitted and absorbed. The ABC consist in a set of absorbing elements whose attenuation factor is leaded by an exponential law [234, 241]. The attenuation law ensures the reduction of reflections, thus simulating an infinite boundary condition.

$$v_\theta(r_{excitation}, 0, t_n) = v_{\theta,excitation}(t_n) \tag{7.20}$$

$$\sigma_{\theta z}(r, 0, t_n) = 0 \tag{7.21}$$

$$v_\theta(r_{reception}, 0, t_n) = 0 \tag{7.22}$$

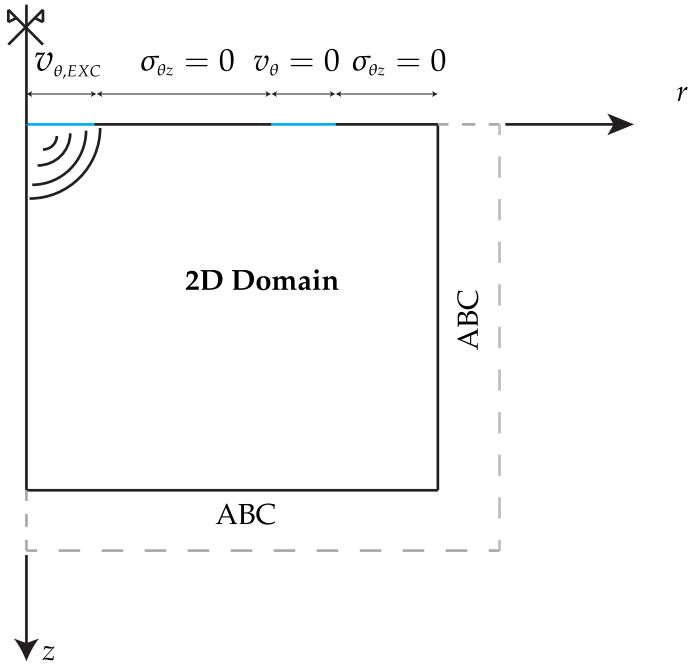

Figure 7.3: Spatial distribution of the boundary conditions of the model. 2D domain surrounded by absorbing boundary conditions, excitation, reception ($v_\theta = 0$) and free surface conditions ($\sigma_{\theta z} = 0$).

Transmission coefficient

Knowing the different layers of the receiver, cervical tissue - PLA ring - piezoelectric element (Figure 7.5), the stress on the piezoelectric element (NCE51) is approximately the stress on the tissue by a correction factor α_c,

$$\frac{\sigma_{\theta z}^{NCE51}}{\sigma_{\theta z}^{tissue}} = \alpha_c = c_r \cdot \text{transmission Tissue-PLA} \cdot \text{transmission PLA-NCE51} \tag{7.23}$$

where $c_r \simeq 10\%$ is a factor of efficiency in the transmission of the wave by PLA [189].

The transmission coefficient between cervical tissue and PLA is calculated through the shear impedance of both media (see Table 7.2),

$$T_{Tissue-PLA} = \frac{2 \cdot Z_{PLA}}{Z_{Tissue} + Z_{PLA}} = 1.98 \tag{7.24}$$

where $Z = c \cdot \rho$ is the shear impedance, c the torsional wave speed and ρ the density of the medium.

The transmission coefficient in terms of stresses between PLA and NCE51 is taken from literature [189] (see Appendix E).

High-speed camera measurements - experimental setup

High-speed camera measurements were carried out in order to establish the boundary conditions of the numerical model through the measurement of the displacement of particles

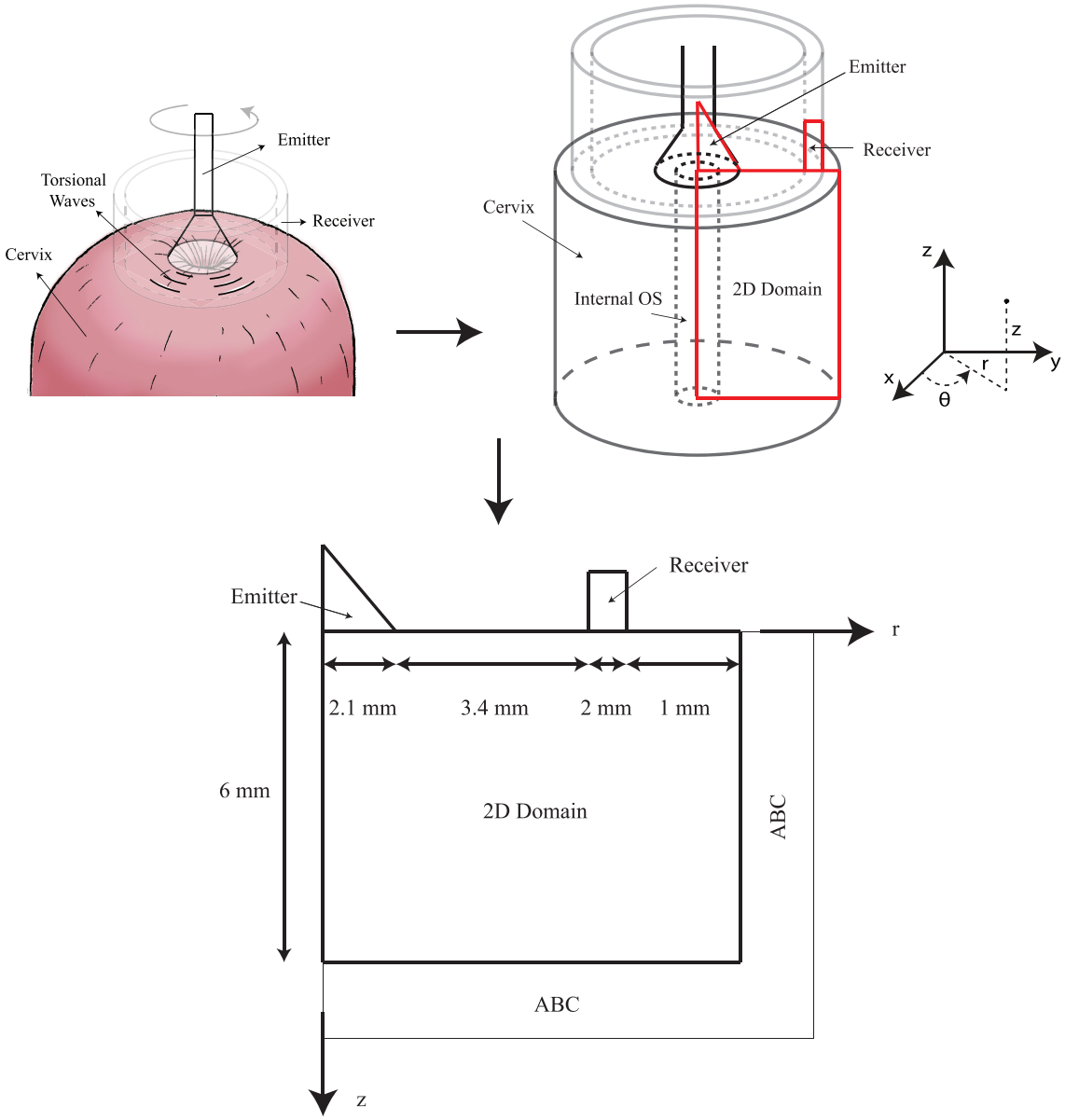

Figure 7.4: From the 3D model to a 2D model in cylindrical coordinates. 2D section contour in red line.

Medium	$\rho(kg/m^3)$	$c(m/s)$	$Z(kg/(m^2s))$
Cervical tissue	1000	2	2000
PLA	1180	200	236000

Table 7.2: Acoustic impedance for cervical tissue and PLA. Density ρ, torsional speed c and acoustic impedance Z of each medium.

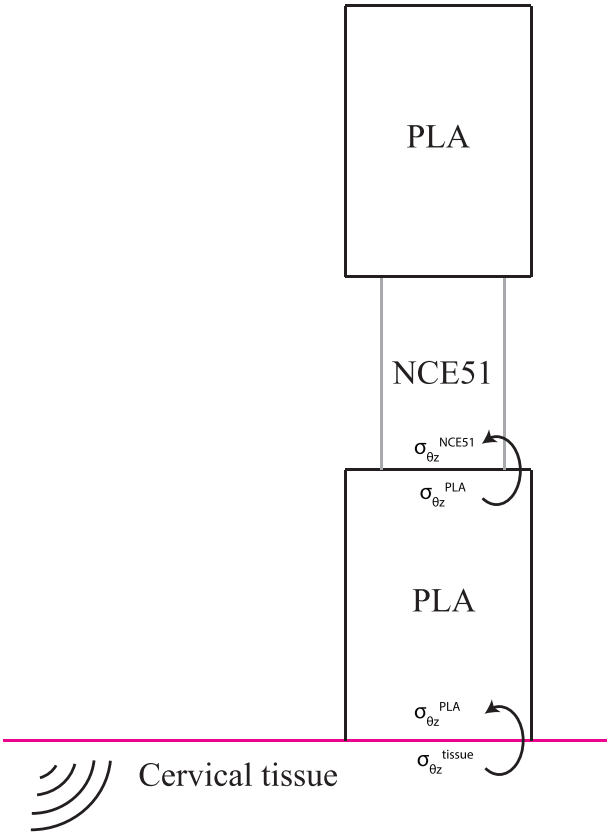

Figure 7.5: Different layers of the receiver (PLA-NCE51-PLA). Transmission coefficient Cervical Tissue - PLA, PLA - NCE51.

within a tissue-mimicking phantom resulting from the excitation of the electromechanical sensor actuator. A plane of basalt microparticles, embedded in the surface of the phantom (see Figure 7.7b), has been used to reconstruct the excitation in displacement after using a custom particle tracking algorithm, see subsection *Particle tracking procedure* and Appendix A. The reconstructed excitation signal was introduced in each of the FDTD viscoelastic models as a boundary condition.

Experimental tests were performed at the University of Jaén (Spain). The experimental setup is shown in Figure 7.7a. The electromechanical actuator was in contact with the tissue mimicking phantom, placed on an elevated platform. The procedure to make the phantoms takes into account the steps detailed by Dunmire et al.[242] (more details can be found in section 8.1). Two different phantoms were fabricated, the first one contains 7.5% gelatine and 5% oil, and the second one 10% gelatine and 5% oil. A high-speed camera (Fast-cam SA1, Photron Inc., San Diego, California, USA) with a zoom objective (VZM 450i, Zoom Imaging Lens, Edmund Optics Inc., Barrington, USA) was pointing towards a 45° mirror placed below the platform (Figures 7.7 and 7.8).

The pressure applied between the phantom and the probe was studied in order to control the slippery conditions. A wide range of pressures ranging from 30 to 150 grams was established according to the results of the study carried out by Callejas et al. [60]. To do

this, first, a balance was placed in the place where the phantom was going to be placed, the desired pressure was applied, then, the balance was removed and the phantom was placed in the same position so that the pressure measured was correct. Finally, the raw recording was made and the process was repeated for each pressure increase. To control the slippery conditions, a pattern was drawn on the disk emitter. Visually, it was analyzed if there was sliding between the disk and the phantom by comparing the reference pattern of the disk with the plane of basalt microparticles.

The excitation signal was a low-frequency sine-burst with a range of frequencies from 300 to 1200 Hz. Excitation signals were generated by an arbitrary wave generator (Agilent 33220A, Santa Clara, CA, United States) and amplified (Radio Frequency Power Amplifier 150 A, 150 W, 100 MHz) before reaching the disk emitter. Measurements were acquired for 16 V mechanical actuator voltage amplitude that provides particle displacements at the emitter surface. All the recordings were carried out checking the laboratory temperature, it was 20 $\pm$ 1°C. Changes in the behavior of the gelatine phantoms could be produced with variation in the temperature of few degrees. To prevent that change in the mechanical properties, the ingredients of the gelatine include formalin. This component increases the melting point of the phantom (approximately 32°C) and maintains the mechanical properties with temperature variations. This increase in temperature is due to the light source necessary to make the recording, therefore the exposure time of the phantom was the lowest possible, i.e. 0.9 s. The distance between the light source KL-2500-LCD (Schott North America Inc., NY, USA, a 250 W cold halogen lamp) and the gelatine was about 10 cm. According to the manufacturer, the luminous flux at the tip of the fibre optic bundle was around 1300 lm. During the recording, the temperature of the gelatine was not measured due to limitations in the laboratory equipment. However, the experimental setup was chosen to reduce the temperature increases and consider that this increase was negligible, i.e. the use of formalin in the mixture, no variations of laboratory temperature, the large distance between the phantom and the light source, the short exposure time to the light.

Particle tracking procedure

A particle tracking code was developed and implemented in MATLAB ® (Release 2018b, MathWorks, Natick, United States) for obtaining the displacements in the phantom from the optical experiments described in subsection *High Speed Camera Measurements*. More details about the algorithm are shown in Appendix A. In order to improving the frames quality, image processing treatments were carried out.

The procedure to track the displacements of the basalt microparticles is explained as follows (see Figure 7.6).

The raw recordings were obtained at 10,000 fps in order to get a time step between frames (768x768 resolution) of 0.1 milliseconds. Then, they were decomposed into a sequence of frames that depend on time. After that, the appearance of the frames was improved in order to obtain a better contrast between the basalt microparticles and the background. In the Figure 7.7b is can be appreciated the resulting image after improving the contrast.

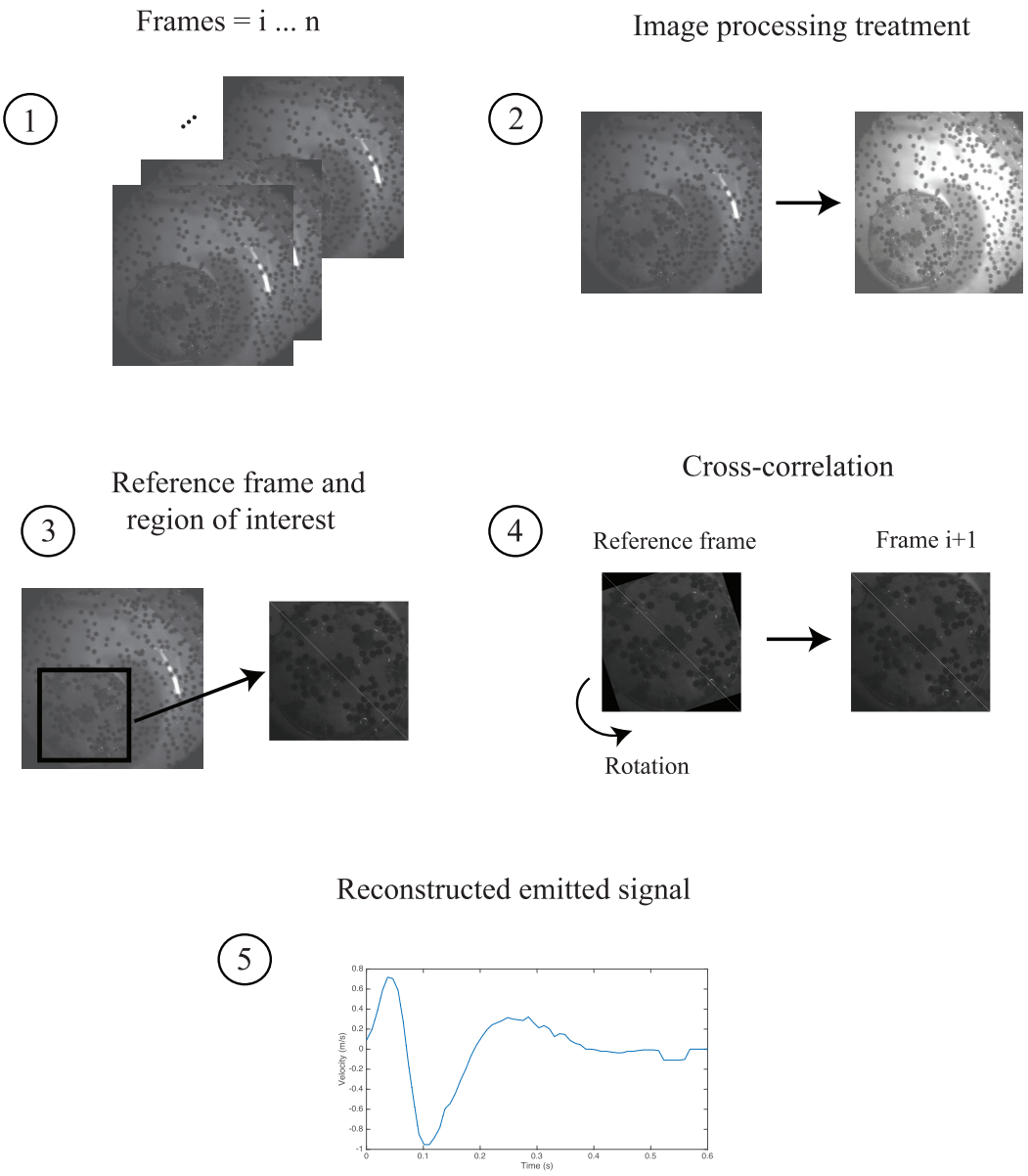

Figure 7.6: Flowchart summarizing the algorithm of cross-correlation to reconstruct the emitter signal.

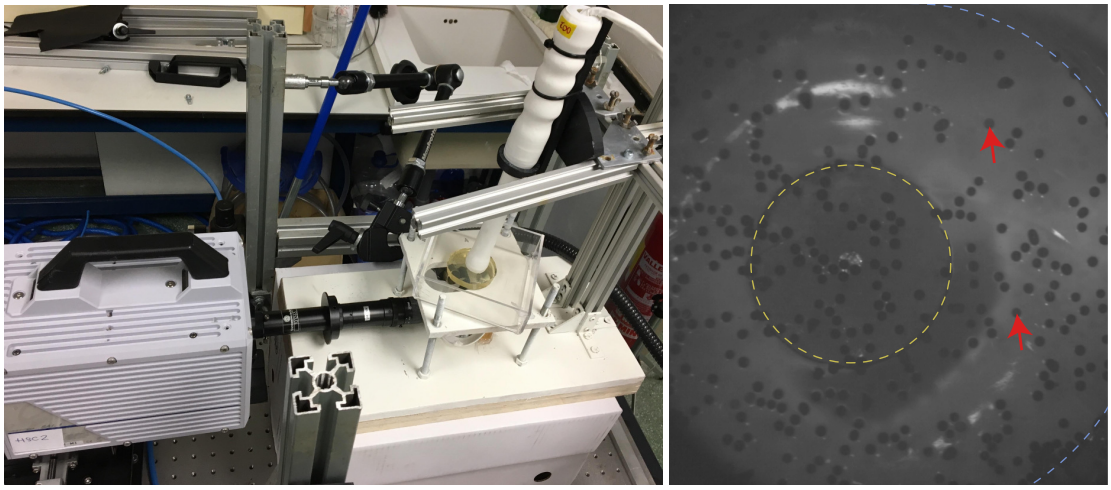

(a) (b)

Figure 7.7: Optical test using a high-speed camera. (**a**) Experimental setup; (**b**) Frame from a high-speed camera recording on a plane of basalt microparticles. The contour of the disk emitter is marked in yellow dashed line and the contour of the receiver in blue. Red arrows are pointing to the basalt microparticles.

Cross-correlation procedure was implemented for the particle tracking method. The first step is to select a reference frame from the decomposed images before the emitter started the rotation. Second, the center of the disk emitter was calculated. Third, the analysis area was selected by means of a square containing the emitting disk, being tangent to it. Then a circumference of the diameter of the disk emitter was generated and centered on the previously calculated point. Using this circumference, the image was cropped, leaving only only the area of the disk emitter. After the preprocessing of the frames, one by one were cross-correlated with their rotated versions from the reference image, until the whole area was swept. The reference image was rotated with an angle increment of 0.1 sexagesimal degrees in order to obtain a reconstructed emitted signal of considerable precision. The calculated center of the disk emitter was employed for the rotation. The angular displacement of each frame was found by calculating the angle that yielded the maximum coefficient of correlation.

Finally, the linear displacement was obtained by transforming the angular displacement, thus getting a time-space plot of the reconstructed emitted signal.

7.2.7 Stability conditions

A balance between accuracy and computational cost may be considered when modeling with FDTD methods. In this sense, two types of numerical errors can appear in the simulations [243].

One group of errors is the phase errors. Because the models used are viscoelastic in nature, dispersion effects have to be studied. Although lower rates can be found in the literature

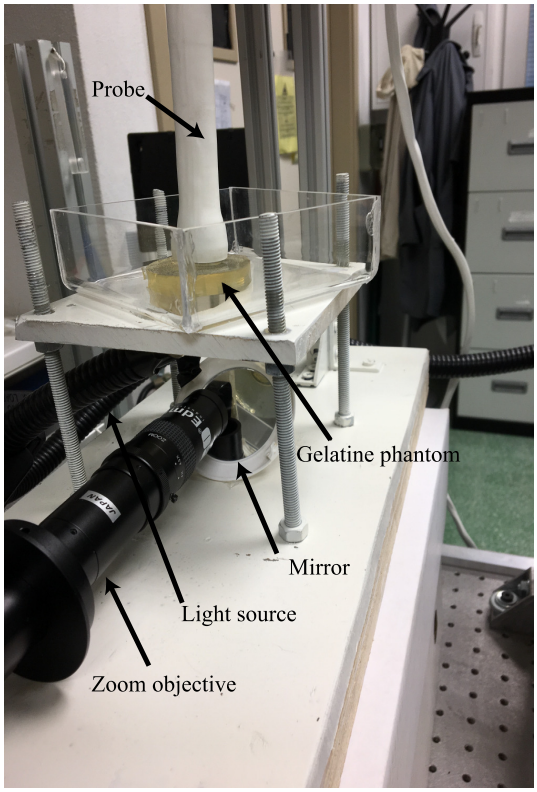

Figure 7.8: Experimental configuration of the optical test using a high-speed camera. Gelatine phantom on top of the transparent platform. Light source and high-speed camera (zoom objective) pointing towards the phantom and the mirror respectively. The probe was in contact with the gelatine phantom.

[206, 244], numerical simulations were carried out with a minimum rate of 28 spatial intervals per wavelength λ in order to reduce numerical dispersion. Spatial steps (Δr or Δz) must be less than the wavelength divided by 28 (Equation 7.25). A verification test for numerical dispersion errors was performed (see *Convergence study of viscoelastic models*, 12.2 subsection).

$$28 \cdot \max(\Delta r, \Delta z) < \lambda_{\min} \tag{7.25}$$

The second group of errors is the amplitude errors. In order not to obtain a scheme unstable and not to obtain an exponential growth of amplitudes, the time step must be chosen small enough. The stability criterion to obtain the maximum Δt is a function of the geometrical, material and space discretization parameters [244, 245, 246].

$$\max(c_s)\Delta t \leq \left(\frac{1}{\Delta r^2} + \frac{1}{\Delta z^2} \right)^{-\frac{1}{2}} \tag{7.26}$$

where $\max(c_s)$ is the maximum torsional wave velocity of the expected wave propagation.

Parameter	Description	Value
Δr	r spatial step	75 μm
Δz	z spatial step	75 μm
Δt	time interval	1 μs
t_T	total time of simulation	12 ms
n_{ABC}	number of ABC elements	100

Table 7.3: Values of the employed parameters for all the simulations by using the FDTD model.

The selected values of the parameters used for all the numerical FDTD simulations are summarized in Table 7.3.

7.3 Experimental measurements

A cross-sectional study in pregnant women was carried out to obtain experimental signals from cervical tissue using the torsional wave probe presented in [60, 247].
The test was performed at Complejo Hospitalario Universitario de Granada. Declaration of Helsinki was taking into account in the study. Approvals of the Ethical Committee in Human Research of University of Granada and Ethical Commission and Health Research of San Cecilio University Hospital in Granada were achieved.

A total of 18 healthy women were recruited in the study. All had uncomplicated singleton pregnancies at a median of 26.4 (from 16wk to 35wk+5d) weeks of gestation, see Table 7.4. The subjects enrolled in the test provided an agreement by previously signing the written consent and reading the patient's information sheet.
For the exploration with TWE, the pregnant were asked to pour their bladder and were placed in the dorsal lithotomy position. The gynecologist employed a speculum for the repositioning of the cervix and placed the probe in the desired position. The intravaginal probe was allocated in contact with the center of the cervical external OS. Proper placement of the probe for measurement is essential to consider the hypothesis of axial symmetry.

7.4 Probabilistic inverse problem

We propose the technique based on Probabilistic Inverse Problem with logical inference framework to evaluate the most plausibility of the physical modelization for the particular case of characterizing a viscoelastic material [248]. The proposed framework is based on a new metric of information density that does not take into account Cox's normalization to get a more simplified formulation. The idea is to combine two information density functions

Characteristics	Value
Total population (N)	18
Gestational age at elastography test (weeks)	26.4 (16w - 35w+5d)
Nulliparous (N)	2 (11 %)
Cervical length (mm)	33 (10 - 49)

Table 7.4: Quantified parameters of the study. Dataset is shown as median (range) or n (%).

from different sources: (i) experimental observations and (ii) mathematical models. The Figure 7.11 shows the details of the procedure to solve the problem.

7.4.1 Definition of basic variables

According to the two sources mentioned above, the observations $\mathcal{O}$ are signals vectors $o_i(t)$, although may also be single signal. The space of observations $\mathfrak{D}$ from the experimental signals is defined as $\mathcal{O}^o = \{o_i^o(t)\}$, and from the model signals as $\mathcal{O}^m = \{o_i^m(t)\}$. In this thesis, the experimental signals were obtained using the torsional sensor and the model signals were synthetic signals that come from the numerical models.

The model parameters $\mathcal{M}$ are set of physical parameters that define a manifold $\mathfrak{H}$. The physical parameters employed were shear stiffness μ, shear viscosity η and the thickness of the epithelial layer. These parameters are the input of the numerical models that simulate the cervical tissue behavior under torsional wave propagation. The output is the signal received by the model.

7.4.2 Definition of information density

Information densities are defined to describe the observations $\mathcal{O}$ and model parameters $\mathcal{M}$ instead of univocal values due to the uncertainty of the data. The conception of Cox [249] to define the information density was adopted. Therefore, the probabilities that are established as a consequence of this logical framework are objective and the logical relations in that axiomatization [250, 251, 252].

Particularly, the information density $f(x)$ is defined by an event or value x as a nonnegative real $f(x) \in \mathcal{R}^+$ whose value is zero when the event is impossible and the larger the more plausible.

According to the normalization requirement of Kolmogorov axioms or Cox's postulates, the probability P of any events A, B satisfy [253],

1. Non-negativity: $P(A) \geq 0$.

2. Finite additivity: $P(A \cup B) = P(A) + P(B) \; \forall \; A, B | A \cap B = \emptyset$.

3. Normalization: $P(\Omega) = 1$.

Specifically, not considering the normalization axiom in the definition of the information density f, the formulation is simplified by comparing it with the Bayesian inverse problem or the theory of Tarantola.

The conditional probability of Bayesian statistics requires an implication due to a cause-effect between the model parameters and the outputs provided by the model. One uses probability as logic, and the alternative one interprets it as information content. In the inverse problem framework proposed by Rus et al. [248], this implication is not necessary.

7.4.3 Information theory inverse problem

As shown in the flow chart Figure 7.11, we introduce two sources of information, i) a source from the experimental observations of the system f^o, and ii) a source from the numerical model of the system f^m. The probabilistic logic conjunction operator consists of considering both propositions simultaneously, $\{f^o \; and \; f^m\}$, as,

$$\begin{aligned} f(\mathcal{O}, \mathcal{M}, \mathcal{H}) &= \{f^o(\mathcal{O}, \mathcal{M}, \mathcal{H}) \; and \; f^m(\mathcal{O}, \mathcal{M}, \mathcal{H})\} \\ &= f^o(\mathcal{O}, \mathcal{M}, \mathcal{H}) f^m(\mathcal{O}, \mathcal{M}, \mathcal{H}) \end{aligned} \tag{7.27}$$

where $\mathcal{H}$ are the hypotheses on the models considered, in this case, elastic, KV and Maxwell models.

Generalizing, the information state for multiple models providing information can be expressed as,

$$\begin{aligned} f(\mathcal{O}, \mathcal{M}, \mathcal{H}) &= \{f^o \; and \; f^{m_1} \; and \; f^{m_2} \; and \; \ldots\} \\ &= f^o(\mathcal{O}, \mathcal{M}, \mathcal{H}) f^{m_1}(\mathcal{O}, \mathcal{M}, \mathcal{H}) f^{m_2}(\mathcal{O}, \mathcal{M}, \mathcal{H}) \ldots \end{aligned} \tag{7.28}$$

The independence of of the experimental measurements coming from the sensor with the techniques to reconstruct experimental information on model parameters yields that the joint density can be split as the product $f^o(\mathcal{O}, \mathcal{M}, \mathcal{H}) = f^o(\mathcal{O}) f^o(\mathcal{M}) f^o(\mathcal{H})$. The term $f^o(\mathcal{M}) = 1$ is the noninformative density function or constant. For the model information, f^m, this is not true due to the relationship between observations and model.

The joint probability is employed in order to reconstruct the probability for the model parameters $\mathcal{M}$ after fixing the model hypothesis $\mathcal{H}_j$, by obtaining the marginal probability (see Figure 7.11) for the observations $\mathcal{O} \in \mathfrak{O}$ and provided the model hypothesis $\mathcal{H}_k \in \mathfrak{H}$ is assumed to be true ($f^o(\mathcal{H} = \mathcal{H}_k) = 1$),

$$f(\mathcal{M})\big|_{\mathcal{H}=\mathcal{H}_k} = k_1 \int_{\mathfrak{O}} f^o(\mathcal{O}) f^o(\mathcal{M}) f^m(\mathcal{O}, \mathcal{M}, \mathcal{H}) d\mathcal{O} \tag{7.29}$$

where the removed model hypothesis probability is replaced by the normalization constant k_1 that can be dropped due to f is unscaled. The noninformative distribution $f^o(\mathcal{M}) = 1$ represents the absence of prior information about the model parameters, yielding,

$$f(\mathcal{M})\big|_{\mathcal{H}=\mathcal{H}_k} = \int_{\mathfrak{O}} f^o(\mathcal{O}) f^m(\mathcal{O}, \mathcal{M}, \mathcal{H}) d\mathcal{O} \tag{7.30}$$

Model parametrization

Considering the presented inverse problem, the model parameters used must be Jeffrey's type, with the particularity of being positive and as popular as their inverses [254]. The formulation presented is similar to the Bayesian framework if parameters are of Jeffrey's type except for a constant. Therefore, the advantages are that all noninformative densities are constant and dropped from the formulation.

For the use of Jeffrey's parameters, it is necessary to map the parameter space with a logarithmic change of variable [217, 218]. The change of variable is performed through a mapping from $\tilde{m}_i \in [0, 1]$ to a predefined range of parameter values that have physical sense $m_i \in [m_i^{\text{inf}}, m_i^{\text{sup}}]$, in order to improve numerical stability,

$$\tilde{m}_i = \frac{ln\left(\frac{m_i}{m_i^{\text{inf}}}\right)}{ln\left(\frac{m_i^{\text{sup}}}{m_i^{\text{inf}}}\right)} \qquad m_i = m_i^{\text{inf}} e^{\tilde{m}_i ln\left(\frac{m_i^{\text{sup}}}{m_i^{\text{inf}}}\right)} \tag{7.31}$$

Discrete observations with Gaussian uncertainties

It is considered that the observations follow a Gaussian distribution $\mathcal{O} \sim \mathcal{N}(E[\mathcal{O}^o], C^o)$, with mean $\mathcal{O}^o$ and C^o the covariance matrix that represent the error noise [255, 256, 257]. It is also assumed that the data of the models follow a Gaussian distribution $\mathcal{O} \sim \mathcal{N}(\mathcal{O}^m, C^m)$. On the one hand, according to laboratory experience, covariance for observations was considered constant, 2×10^{-4}. On the other hand, for the calculation of the covariance from the models, the following procedure was carried out (see Scheme 7.10). First, 2000 random signals were generated considering the range of parameters of each model. Second, for each of these signals, 48 signals with 10% noise were generated in terms of the value of the parameters. Then, the mean and standard deviation were calculated at each of the points of the 48 signals. Finally, the mean and standard deviation of each of the 2000 subgroups were combined and the covariance of the final group, which represents all the subgroups, was calculated. In Figure 7.9, the sum of the covariance of the observations and the Kelvin-Voigt model can be observed. It can be observed that, for this model, Kelvin-Voigt, as well as for the other models (elastic and Maxwell), the numerical errors are negligible compared to the experimental ones.

Recall that the observations that come from the torsional sensor measurements and from the numerical models $\mathcal{O}$, are signals vectors $\mathcal{O} = \{o_i\}$, $i \in [1...N_i]$, and supposing that exist independence of information and the product is equal to a sum within the exponential and the Gaussian distribution that allows an explicit expression of probability densities,

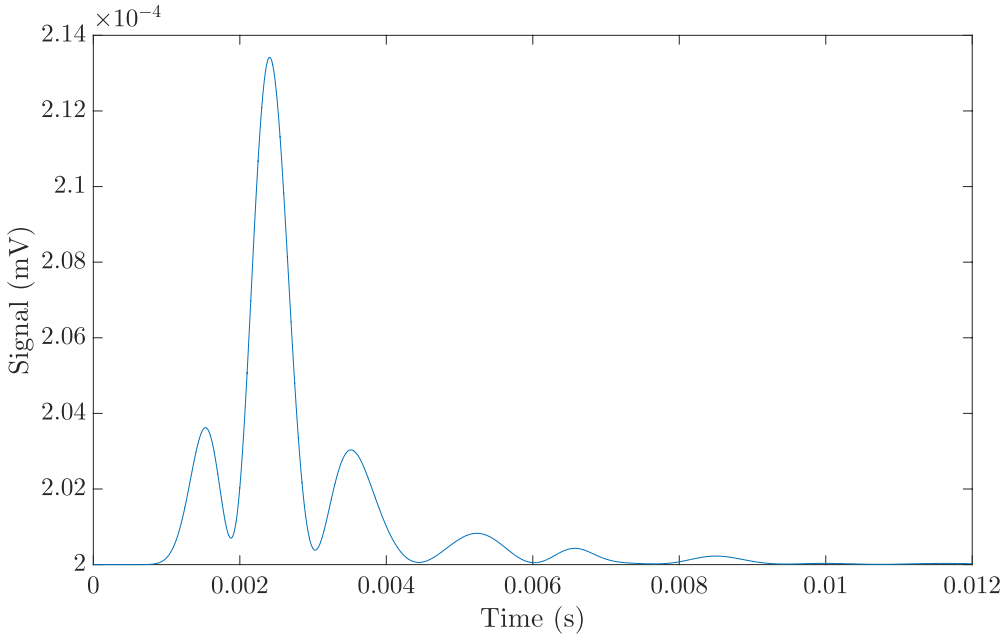

Figure 7.9: Covariance signal for the Kelvin-Voigt model, also considering the covariance for observations, 2×10^{-4}. Each point of the signal is the combined covariance of the 2000 subgroups randomly simulated.

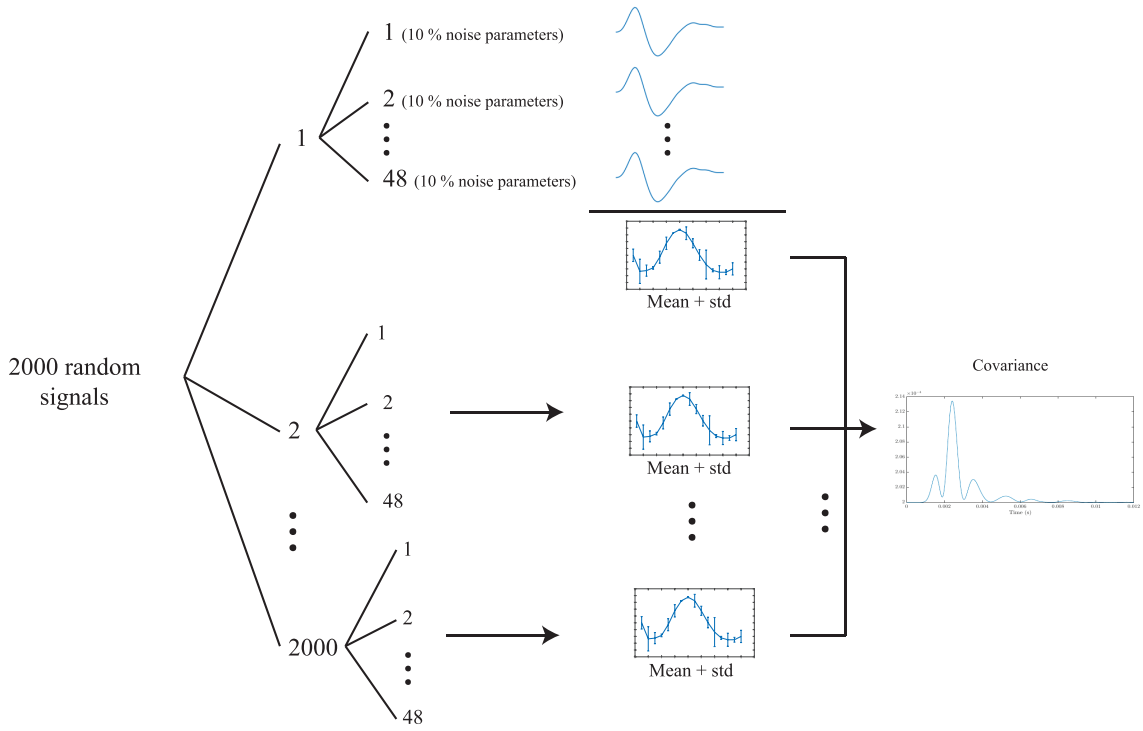

Figure 7.10: Scheme to calculate the covariance of viscoelastic models.

$$f^o(o_i(t)) = k_2 \exp\left\{ -\frac{1}{2} \int \sum_{i,j=1}^{N_i} (o_i(t) - o_i^o(t)) \left(C_{ij}^o\right)^{-1} \left(o_j(t) - o_j^o(t)\right) dt \right\} \tag{7.32}$$

$$f^m(o_i(t), \mathcal{M}, \mathcal{H}_k) = k_3 \exp\left\{ -\frac{1}{2} \int \sum_{i,j=1}^{N_i} (o_i(t) - o_i(t, \mathcal{M}, \mathcal{H}_k)) \left(C_{ij}^m\right)^{-1} \left(o_j(t) - o_j(t, \mathcal{M}, \mathcal{H}_k)\right) dt \right\} \tag{7.33}$$

$$\Rightarrow f(\mathcal{M})\big|_{\mathcal{H}=\mathcal{H}_k} = k_4 \exp^{\overbrace{\left\{ -\frac{1}{2} \int \sum_{i,j=1}^{N_i} (o_i(t, \mathcal{M}, \mathcal{H}_k) - o_i^o(t)) \left(C_{ij}^o + C_{ij}^m\right)^{-1} \left(o_j(t, \mathcal{M}, \mathcal{H}_k) - o_j^o(t)\right) dt \right\}}^{-J(\mathcal{M}, \mathcal{H}_k)}} \tag{7.34}$$

$J(\mathcal{M}, \mathcal{H}_k)$ represents a function that relates observations of the system and observations of the models.

$$f(\mathcal{M})\big|_{\mathcal{H}=\mathcal{H}_k} = k_4 e^{-J(\mathcal{M}, \mathcal{H}_k)} \tag{7.35}$$

The information-theoretic inverse problem framework is applied, describing the process of parametrization, the operation with discrete observation data of signals, and two key extensions: to hypothesis testing $\mathcal{H}_k$ and to parameter optimization $\mathcal{M}$.

To derive the effectiveness of the PIP method, the following inverse problem is solved. The outcomes are the constitutive viscoelastic mechanical parameters of the cervical tissue evaluated. However, the extended formulation allows the ranking of the plausibility of three several models detailed below,

The three hypothesis considered are:

$\mathcal{H}_1$: Linear elasticity that additively combines the shear modulus of epithelial and connective tissue, $\mu^E_{epithelial}$ and $\mu^E_{connective}$, respectively, and thickness of the propagation governed by the law described in Equation 7.6.

$\mathcal{H}_2$: Kelvin-Voigt linear viscoelastic model, with shear stiffness and shear viscosity parameters for epithelial and connective layers respectively, $\mu^{KV}_{epithelial}$, $\eta^{KV}_{epithelial}$, $\mu^{KV}_{connective}$, $\eta^{KV}_{connective}$ introduced in Equation 7.7, taking into account the thickness of the epithelial tissue th.

$\mathcal{H}_3$: Maxwell linear viscoelastic model, with parameters, $\mu^M_{epithelial}$, $\eta^M_{epithelial}$, $\mu^M_{connective}$, $\eta^M_{connective}$ and the thickness of the epithelial layer th as in Kelvin-Voigt hypothesis but derived in terms of Equation 7.8.

The values of the search range of the parameters have been taken according to scientific evidence, see Table 7.5.

To solve how much reliability is there in the assumed mechanical among a set of candidates, or which model complexity is best by assuming known or unknown viscoelastic

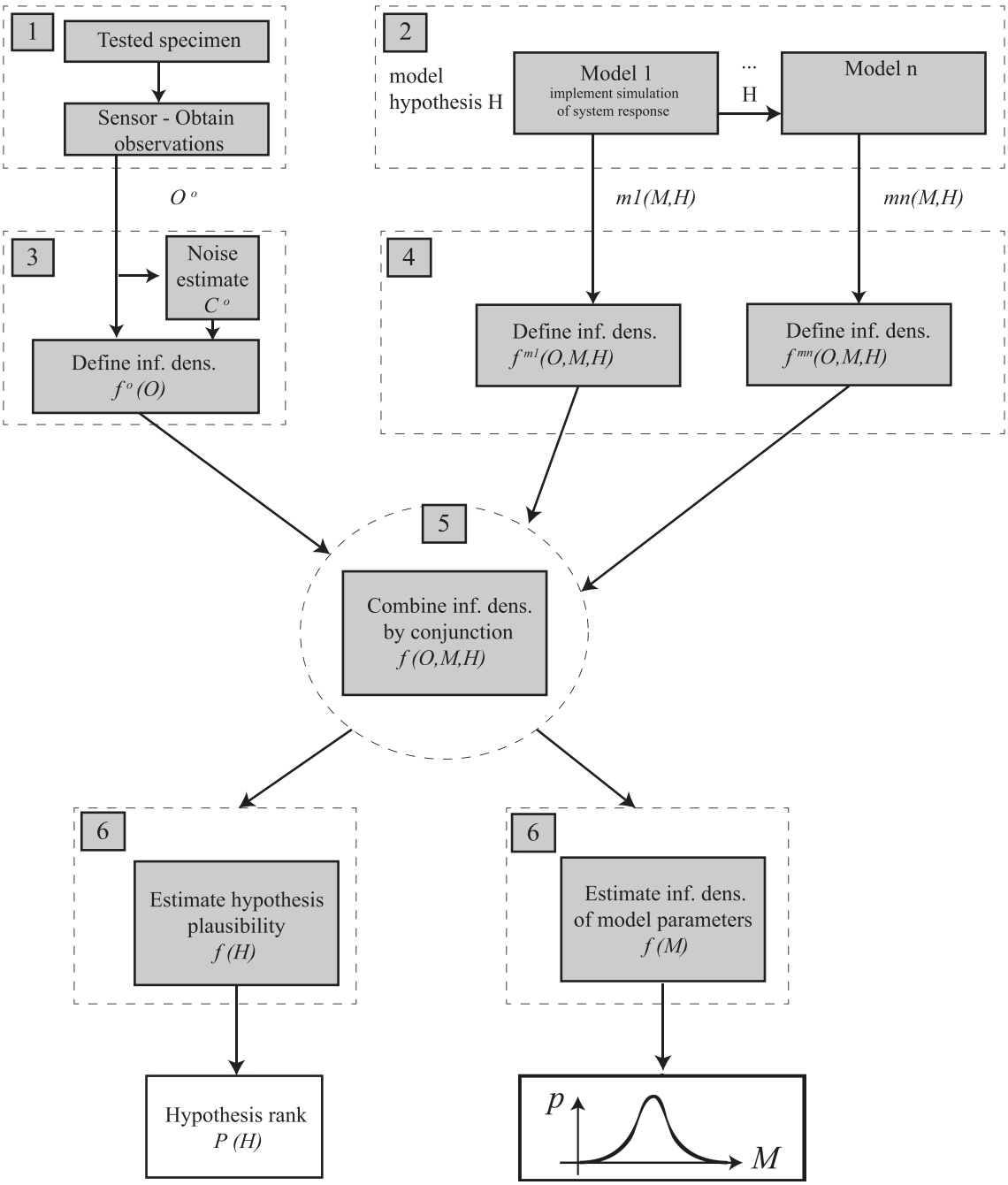

Figure 7.11: Flowchart of the complete information theoretic probabilistic inverse problem. The abbreviation ″inf. dens.″ is referred to information density.

Viscoelastic Model	Parameter	Search Range
Elastic [7, 6]	$\mu^{E}_{epithelial}$	0-20 kPa
	th	0-2000 μm
	$\mu^{E}_{connective}$	0-50 kPa
Kelvin-Voigt [7, 6]	$\mu^{KV}_{epithelial}$	0-20 kPa
	th	0-2000 μm
	$\eta^{KV}_{epithelial}$	0-5 Pa $\cdot$ s
	$\mu^{KV}_{connective}$	0-50 kPa
	$\eta^{KV}_{connective}$	0-5 Pa $\cdot$ s
Maxwell [7, 6]	$\mu^{M}_{epithelial}$	0-20 kPa
	th	0-2000 μm
	$\eta^{M}_{epithelial}$	0-30 Pa $\cdot$ s
	$\mu^{M}_{connective}$	0-50 kPa
	$\eta^{M}_{connective}$	0-30 Pa $\cdot$ s

Table 7.5: Search range of the parameters for the three FDTD models.

constants, the model hypothesis raking of the three hypothesis described previously is computed using,

$$f(\mathcal{H}) = k' f^{0}(\mathcal{H}) \int_{\mathfrak{M}} f(\mathcal{M})\big|_{\mathcal{H}=\mathcal{H}_k} d\mathcal{M} = k' I \tag{7.36}$$

where $\mathcal{M}$ are the model parameters, f^{0} is a source from experimental observations of the system and the normalization constant k' can be solved from the theorem of total probability over all hypothesis $\mathfrak{H} = \{\mathcal{H}_k\}$ in order to obtain probabilities, $\sum_{\mathfrak{H}} p(\mathcal{H}_k) = 1$ [258].

To clarify the degrees of hypothesis reliability are presented in % by rescaling the information density from,

$$p(\mathcal{H} = \mathcal{H}_k) = k'' \int_{\mathfrak{M}} e^{-J(\mathcal{M},\mathcal{H}_k)} d\mathcal{M}, \qquad k'' = \frac{1}{\sum_k \int_{\mathfrak{M}} e^{-J(\mathcal{M},\mathcal{H}_k)} d\mathcal{M}} \tag{7.37}$$

where J corresponds to a misfit function between model and observations. The integral in the next equation,

$$\int_{\mathfrak{M}} \hat{f}(\mathcal{M})\big|_{\mathcal{H}=\mathcal{H}_k} d\mathcal{M} = 1 = kI, \qquad I = \int_{\mathfrak{M}} e^{-J(\mathcal{M},\mathcal{H}_k)} d\mathcal{M} \quad \Rightarrow \quad k = \frac{1}{I} \tag{7.38}$$

is approximated computationally by a standard Quasi-Monte Carlo sampling being $\hat{f}(\mathcal{M})\big|_{\mathcal{H}=\mathcal{H}_k}$ the classical probability densities, which approximates the integral of any integrand $f(x)$ that depends on the parameters x over a parameter subspace Ω using,

$$\int_{\Omega} f(x) = \frac{1}{N} \sum_{n=1}^{N} f(x_i) \tag{7.39}$$

where the integrand $f(x)$ is assessed at N random points $x_i \in \Omega$ called samples. The accurate of the algorithm is defined by the number of samples, they have been chosen as $N = 2^{16}$ points. This integral is uniquely calculated at the computation of the model class selection. The fitting is quantified by its plausibility shown in the ranking in Figure 12.5.

8

Validation of the KV reconstruction parameters method in cervical tissue-mimicking phantoms

This chapter describes a new method to reconstruct the Kelvin-Voigt viscoelastic parameters of cervical tissue-mimicking phantoms by TWE technique [1]. The reconstruction method, based on the PIP approach shown in Chapter 7, is presented and experimentally validated against SWE, the gold standard technique in elastography [259]. Particular emphasis is given to the ability of modeling bilayer phantoms that mimic the histological structure of the cervical tissue. The main goal of this study was to validate the new proposed method to reconstruct the viscoelastic parameters with the aim of using it in the characterization of cervical tissue in clinical practice.

Section 8.1 details the fabrication procedure of tissue-mimicking phantoms according to previous references found in literature. In sections 8.2 and 8.3, it is shown the experimental setup and protocol to characterize the phantoms with Shear Wave Elastography and Torsional Wave Elastography respectively. The 2D FDTD Kelvin-Voigt propagation model is presented in Section 8.4. Section 8.5 outlines the procedure to fit the dispersion shear wave speed curve obtained after analyzing SWE measurements. Finally, a PIP similar to the one explained in Chapter 7 is presented in Section 8.6. The cited procedure is performed to reconstruct the phantom viscoelastic parameters by comparing the experimental signals using the TWE technique and the synthetic signals from the FDTD KV model.

[1] Contribution: A. Callejas, A. Gomez, I. H. Faris, J. Melchor and G. Rus. Kelvin-Voigt parameters reconstruction of cervical tissue-mimicking phantoms using torsional wave elastography. *Sensors*, 19(15), 2019.

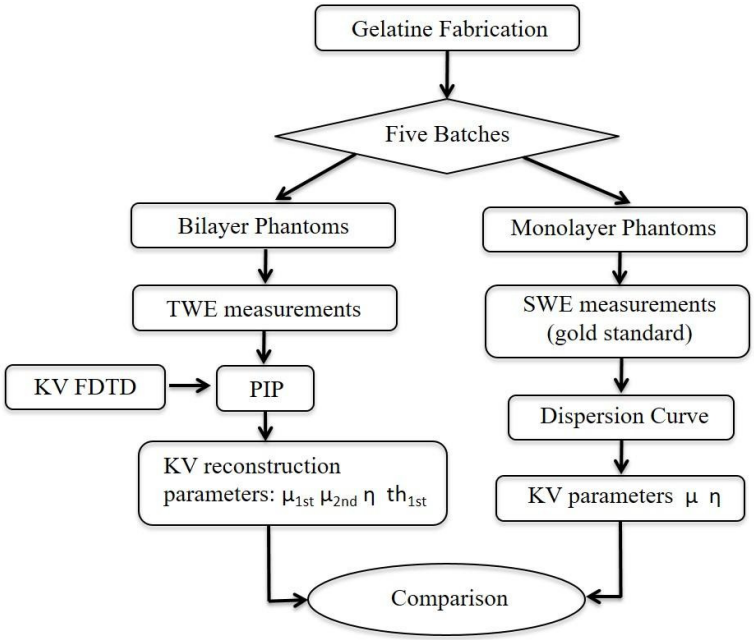

Figure 8.1: Schematic flowchart used for validating the KV viscoelastic model.

8.1 Tissue-mimicking phantom fabrication

The viscoelastic characterization of the cervical tissue requires the use of a model that simulates the torsional wave propagation. According to the results of the work carried out by Callejas et al. [60], the KV model is the simplest model that best fit the *ex-vivo* cervical tissue experimental results. The next step after selecting the model is its validation, which consists of measuring tissue-mimicking phantoms with TWE technique and comparing against SWE, a well-known technique by the scientific community.

Fabrication of tissue-mimicking phantoms is straightforward in general and has been described by taking into account characteristics from the recipe by [242]. After studying different ingredients and fabrication methods, the ingredients found in Table 8.1 were proposed. Potassium sorbate was included to keep the phantom from early decay due to bacterial and fungal activity. The formalin ingredient was used to raise the melting point of the gelatine, stabilizing the response of the phantom properties to room temperature variations and as a cross-linking agent. Finally, sodium dodecyl sulfate (surfactant) was added for a better mixture of oil with water. Phantoms contain different concentrations of gelatine and oil to mimic the elastic and viscous parameters of cervical tissue. In addition, the constituent oil generates scattering for the visualization of the shear wave propagation through the phantom with SWE technique. Three different gelatine percentages were considered (7.5, 10 and 15 %) as well as two percentages of oil (5 and 10 %).

Taking into account the nature of the cervical tissue, composed of epithelial and connective layers, the phantoms were fabricated considering two layers. The specific percentages of gelatine, oil and the thickness of the first layer (simulating the epithelial layer of the cervix) have been chosen to simulate the viscoelastic properties of the cervical tissue according to

Tissue-mimicking phantom constituents	
Ingredient	**Supplier, type**
Gelatine	Fisher Chemical, Gelatine General purpose grade
Formalin (0.24 cc)	Sigma Aldrich, Formaldehyde sol. 37% wt in H_2O
K-Sorbate (1.62 g)	Alfa Aesar, Potassium sorbate, 99%
Lubricating Oil	50501 TDI 5W40
Surfactant (0.5 g)	Sodium dodecyl sulfate, ACS reagent, $\geq$ 99%
H_2O (100 mL)	Laboratory distilled water

Table 8.1: Ingredients of the gelatine solution for the tissue-mimicking phantoms. The amount of gelatine and oil was varied for each batch (percentage specified in Table 8.2).

the evidence found in the literature [234, 6, 7]. For this purpose, five different phantoms have been fabricated. The ingredients that interfere with the parameters of the KV model are those that have been varied (gelatine, oil and layer thickness), the rest were kept constant (formalin, K-sorbate, surfactant and H_2O). The aim is to vary each of the parameters of each phantom that are reconstructed and verify that the PIP is capable of reconstructing them. Details about the percentages of gelatine and oil, as well as the thickness of the two layers are given in Table 8.2.

Phantoms	**Layer**	**Gelatine** (%)	**Oil** (%)	**Th** (mm)
1	First layer	7.5	5	1
	Second layer	15	5	15
2	First layer	10	5	1
	Second layer	15	5	15
3	First layer	7.5	5	1
	Second layer	10	5	15
4	First layer	7.5	10	1
	Second layer	15	10	15
5	First layer	7.5	5	0.5
	Second layer	15	5	15

Table 8.2: Percentages of gelatine and oil wt/wt, as well as the thickness (Th) of the two layers for each of the five phantoms.

The procedure carried out for the fabrication of the phantoms required for measurements with TWE technique is listed below. The phantoms for the measurements with SWE technique have been manufactured with the same batches for the TWE phantoms but in round molds of larger diameter (7 cm) and greater depth (6 cm) for correct measurement with the above technique. The steps followed to fabricate the phantoms are based on the procedure followed by Dunmire et al. [242].

1. Weigh and prepare each of the components listed in Table 8.1.
2. Add the K-sorbate to the distilled water and begin mixing for five minutes.
3. Add the surfactant and keep mixing for another 5 minutes.

4. Add the oil with the previous solution and mix manually at a rate that minimized the formation of air bubbles and the formation of large clumps.
5. Heat the combined solution at a rate of approximately 1°C per minute.
6. Gradually add the gelatine powder to the combined solution.
7. Allow 5-10 minutes to verify that the gelatine is well mixed.
8. Cover and heat the solution to 85°C at a rate of approximately 1°C per minute.
9. Hold the solution between 85°C and 90°C for 90 minutes.
10. Cool the mixture from 85°C to 40°C at a rate of 1°C per minute.
11. Add the formalin and mix the solution for 5 minutes.
12. Pour the mixture into the round molds (5 cm in diameter) until the thickness of the connective layer is reached. A thickness of 15 mm has been considered to avoid interference in the measurements due to reflections with the bottom of the gelatine.
13. Wait until the mixture reaches 37°C-38°C.
14. While the first batch is getting cold, repeat steps 1 to 11 with the ingredients needed to fabricate the first layer.
15. When both batches reach the temperature of 37°C-38°C, carefully pour the second batch (first layer) on the first batch using a syringe. According to the dimensions of the mold, the volume of gelatine necessary to reach the required thickness is calculated.
16. Leave the phantom to solidify at room temperature for 2 hours before being stored in the refrigerator.
17. Remove the phantom from the refrigerator and left at room temperature for 6 h.

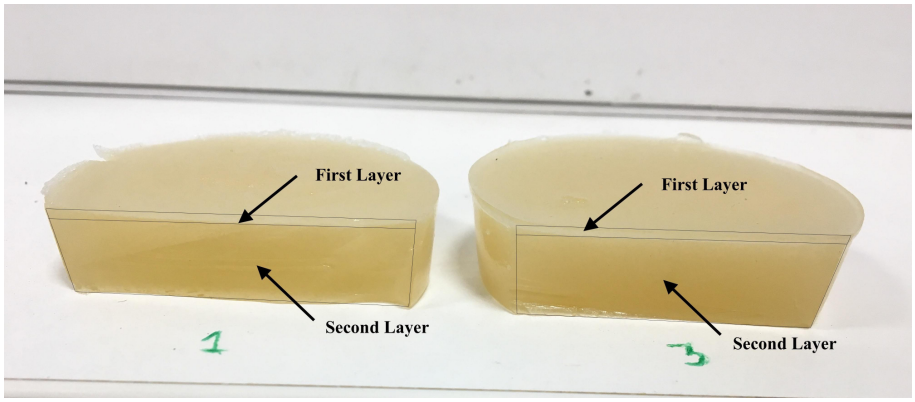

Figure 8.2: Phantoms number 1 and 3. The phantoms were unmolded and cut to appreciate the two layers of which they are composed.

8.2 SWE characterization of the phantoms

Mechanical properties of soft tissue are directly related to the speed of the waves propagating through it [5, 260, 261, 262]. A perturbation in the media is needed in order to capture shear waves. In this work, Acoustic Radiation Force (ARF) is used to excite the tissue producing its deformation; tissue displacements are generated due to this focused ARF and induce shear waves that propagate away from this push.

A programmable research ultrasound system (Vantage, 128 Verasonics Inc., Kirkland WA, USA) was configured to provide both the B-mode image and the shear wave motion speed. A linear-array transducer with a center frequency of 7.8 MHz and properties shown in Table 8.3 was used for imaging ($L11-5v$, Verasonics Inc.). Each of the five phantoms was imaged three times and shear wave speeds were estimated. All the measurements were performed at laboratory temperature ($22 \pm 1\ ^{\circ}C$). Verasonics offers big flexibility in sequence design and permits access to raw data from each element of the array [263]. Verasonics uses the MATLAB programming environment (Release 2018b, MathWorks, Natick, United States), the user needs to write a program script to generate the imaging sequence. Several types of pushing sequences can be used to generate shear waves, in this work Multiple Track Location (MTL) SWE Imaging is used for a single focused push for the center of the frequency of 7.8 MHz. Scanning process of a gelatine phantom with the Verasonics system is shown in Figure 8.3.

Number of elements	128
Pitch (mm)	0.3
Elevation focus (mm)	18
Sensitivity (dB)	-52$\pm$3

Table 8.3: Properties of the $L11-5v$ Verasonics transducer

In Table 8.4, the SWE acquisition parameters used in this paper are shown. Push transmit frequency and track frequency are set to the center of the transducer. However, in this work, lower track transmit frequency was used to successfully receive the harmonic frequency in the case of harmonic tracking. Furthermore, for push transmit frequency, a lower frequency was also used to minimize underestimation of tracked tissue displacement due to speckle shearing within the track point spread function. In this paper, we used a push frequency that is in the lower -25 dB bandwidth of the transducer to expand the push beam keeping a high transmit efficiency [264, 265].

Parameter	$L11-5v$
Push frequency (MHz)	4.8
Track frequency (MHz)	5.6
Push duration $(cycles)$	1000
Pulse repetition interval (μs)	100
Excitation Voltage (V)	28
Focal distance (mm)	20

Table 8.4: SWEI acquisition parameters for $L11-5v$ Verasonics transducer

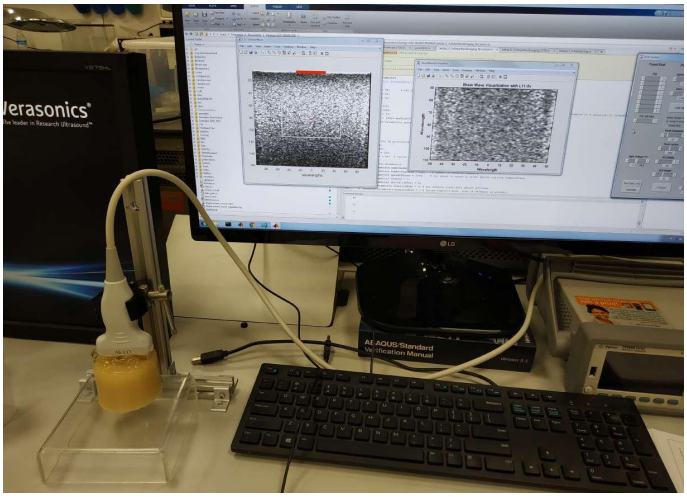

Figure 8.3: Experimental setup of Verasonics measurements.

8.2.1 Tissue motion estimation

The Loupas algorithm was used to estimate the axial displacements [266]. This is done by postprocessing the In-phase and Quadrature (IQ) data obtained from the shear wave propagation as follows (see Figure 8.4):

- Generate the push sequence (Create displacements).
- Transmit shear waves according to the push sequence.
- Record shear wave propagation during a period of time.
- Transfer the recorded RF to the host computer, then transform RF data to IQ data.
- Call the Ultrasound Toolbox (USTB) with the IQ data and post-process using Loupas 2D autocorrelator.

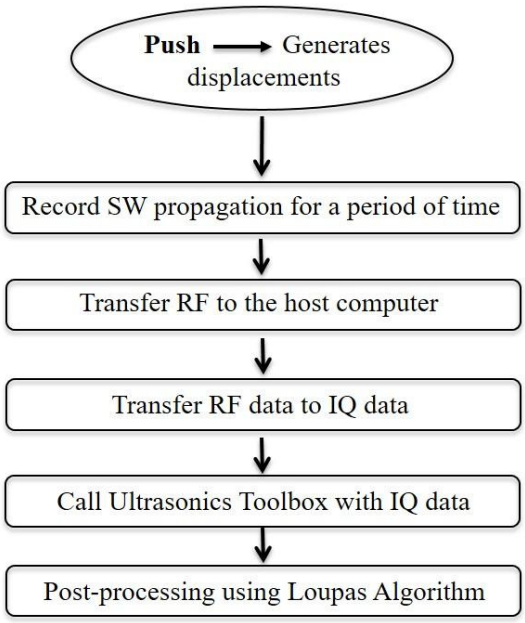

Figure 8.4: Schematic flowchart used for postprocessing IQ data.

Although Verasonics offers postprocessing of IQ data using the Kasai algorithm, it is recommended to use Loupas 2D autocorrelator. This is because Kasai's algorithm uses a constant frequency to compute the phase shift: the center frequency of the transducer. However, the center frequency of RF-echoes decreases along with the axial depth, and Loupas approach corrects the mean RF frequency along with each axial extent and this leads to getting more accurate results. In this paper post-processing of the IQ data measured was done using the USTB [267].

8.2.2 Dispersion shear wave speed curve

From the displacement field resulted from SWE excitation, the dispersion shear wave speed curve was obtained for each batch of single-layer phantom. Using the curve as a reference, the viscoelastic tissue properties can be extracted by fitting the data with a mechanical model of the tissue. For a linear, elastic, isotropic, homogeneous and unbounded material, the shear wave speed (c_s) is expressed in terms of the shear elasticity μ and density ρ by the relation:

$$c_s = \sqrt{\frac{\mu}{\rho}} \tag{8.1}$$

In contrast, for a viscoelastic material described by the KV model, the shear wave speed is not a constant value, it depends on the angular frequency (ω) [268, 269].

$$c_s(\omega) = \sqrt{\frac{2(\mu^2 + \omega^2\eta^2)}{\rho(\mu + \sqrt{\mu^2 + \omega^2\eta^2})}} \tag{8.2}$$

where η is the KV shear viscosity of the sample. The density of soft tissue is usually assumed to be 1000 kg/m^3.

This dispersion, shown in the frequency-dependent phase velocity and shear attenuation is the consequence of the propagation of the shear waves through the tissue [153]. The phase shear wave speed was obtained using the equation:

$$c_s(\omega) = \frac{\omega \Delta r}{\Delta \phi(\omega)} \tag{8.3}$$

A Fast Fourier Transform (FFT) of the tissue speed field has been used to obtain the phase change $\Delta\phi(r, t)$ of the wave over the traveled distance Δr at each frequency [270, 271]. Finally, the dispersion curve obtained was fitted by Equation 8.2 to get the shear elasticity (μ) and the shear viscosity (η). Appendix B contains the MATLAB® code from the different algorithms that have been employed in the calculation of the shear wave dispersion curve using Shear Wave Elastography data.

8.3 TWE characterization of the phantoms

The phantoms were tested when they reached the laboratory temperature (22 $\pm$ 1 °C) and a scale was employed to quantify the applied pressure during the measurement (see Figure 8.5). The pressure employed (100 $\pm$ 5 g) was chosen according to a previous experience using a normal testing procedure [60]. Each of the five bilayer phantoms was measured

in three different areas by an in-lab designed and prototyped probe capable of generating, receiving and analyzing torsional waves (see Chapter 6).

The propagated torsional wave is a burst composed of a 1-cycle sinusoid of frequency 1000 Hz with 10x averaging to increase the strength of the signal relative to noise. For each gelatine phantom, five measurements were performed at three different points, with the objective of reconstructing the viscoelastic parameters with mean and standard deviation. The torsional sensor receives a signal in terms of voltage that is representative of the interaction with the different layers of the phantom.

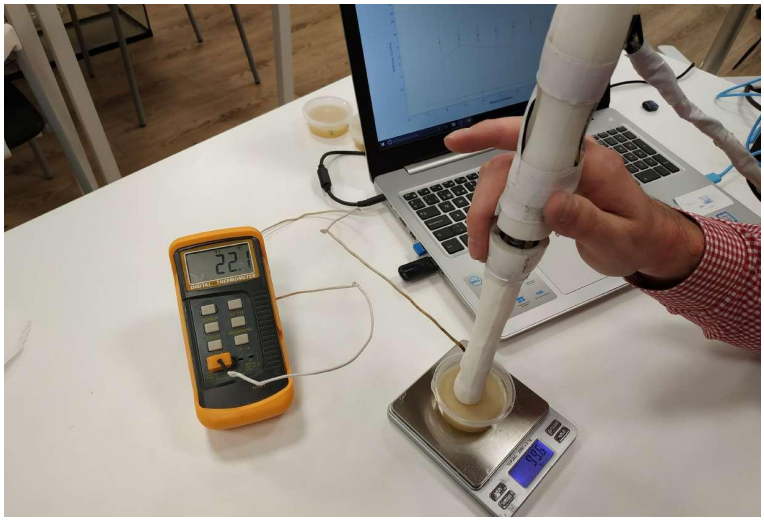

Figure 8.5: Picture of the experimental setup of TWE measurements. The phantoms were positioned on a balance to control the pressure applied.

8.4 Kelvin-Voigt 2D FDTD propagation model

With the aim of inferring the viscoelastic properties of the phantoms using the PIP (explained in detail in section 8.6), a 2D FDTD method has been proposed in order to simulate the torsional wave propagation through the tissue-mimicking phantoms. The FDTD formulation was developed in cylindrical coordinates since torsional waves propagate axisymmetrically from the center of the probe [60]. As discussed above, with the objective of simulating the nature of the cervical tissue, two layers have been taken into account in the numerical simulations (see Figure 8.6).

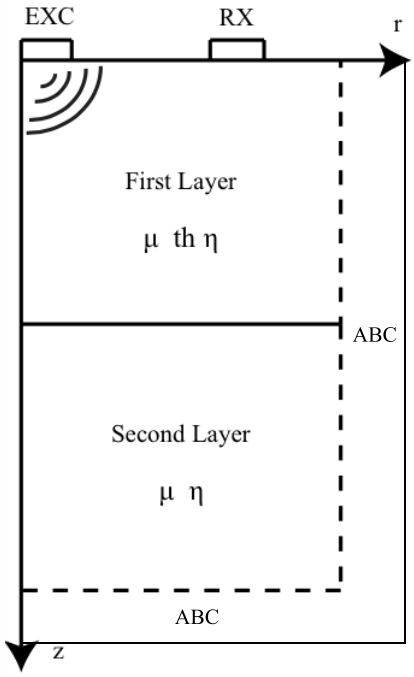

Figure 8.6: Two-dimensional scheme considering axial symmetry, phantom layers and absorbing boundary conditions.

One of the most used viscoelastic constitutive laws for modeling shear wave propagation in tissue is the KV model. Following the conclusions obtained by [60], the KV model is the one that best simulates the behavior of cervical tissue under the propagation of torsional waves.

The equations that govern the torsional wave propagation through the phantom for the KV model have been deduced taking into account the equations of motion, the kinematic relation, and the constitutive equations [272] (Appendix D):

$$\begin{cases} \rho \dot{v}_\theta = \dfrac{\partial \sigma_{r\theta}}{\partial r} + \dfrac{2}{r}\sigma_{r\theta} + \dfrac{\partial \sigma_{\theta z}}{\partial z} \\ \dot{\sigma}_{r\theta} = \mu \left[\dfrac{\partial v_\theta}{\partial r} - \dfrac{v_\theta}{r} \right] + \eta \left[\dfrac{\partial \dot{v}_\theta}{\partial_r} - \dfrac{\dot{v}_\theta}{r} \right] \\ \dot{\sigma}_{\theta z} = \mu \dfrac{\partial v_\theta}{\partial z} + \eta \dfrac{\partial \dot{v}_\theta}{\partial z} \end{cases} \tag{8.4}$$

where ρ denotes the phantom density, μ and η (KV parameters) the shear elasticity and viscosity respectively, r, θ and z the cylindrical components, v the particle velocity and σ the stress tensor.

The system of equations was simplified by neglecting all the normal components and solely leaving the deviatoric (torsional) components. According to the work carried out by Orescanin et al. [206], this simplification did not seem to affect the results due to the low level of normal pressure generated by the emitter, in this case, the torsional probe.

The time-staggering approach used in this work consist of computing all stress, strain, and displacement at the same time interval, according to previous work carried out by Orescanin et al. [206]. Time and space were uniformly sampled, with $a = i\Delta r/2$ and $b = j\Delta z/2$ for integers a, b and space step of discretization Δr and Δz. Shear stiffness and viscosity have been introduced into the model by setting their values at the grid points of the discretized space domain. The selected values of the parameters used for the numerical FDTD simulations are summarized in Table 7.3.

The system of equations 8.4 was discretized according to Taylor series expansions [240], For derivatives with respect to one of the spatial variables (r or z), a first-order accurate centered scheme finite difference discretization has been employed (see Figure 7.2 and subsection 7.2.5).

The boundary conditions used in the 2D space were (Figure 8.7): at the surface of the tissue-mimicking phantom the excitation source, the absence of the shear stress on the surface air-phantom ($\sigma_{\theta z}(r, 0, t_n) = 0$), the absence of velocity ($v_\theta(r_{reception}, 0, t_n) = 0$) in the grid point on the reception place due to the pressure applied between the receiver of the probe and the gelatine phantom and finally, the Absorbing Boundary Conditions (ABC). The ABC consist in a set of absorbing elements whose attenuation factor is leaded by an exponential law. The attenuation law ensures the reduction of reflections, thus simulating an infinite boundary condition.

The dimensions of the emitter, receiver, emitter-receiver and receiver-ABC are shown in Figure 8.7.

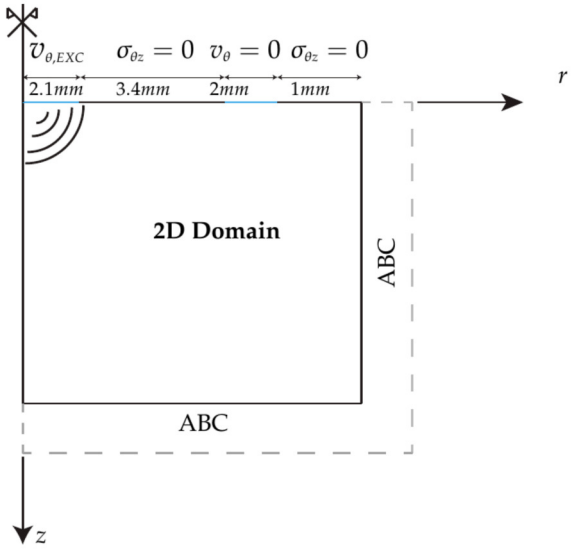

Figure 8.7: Spatial distribution of the boundary conditions of the model. 2D domain surrounded by absorbing boundary conditions, excitation, reception ($v_\theta = 0$) and free surface conditions. Dimensions of the emitter, receiver, emitter-receiver and receiver-ABC.

The average stress $\sigma_{\theta z}$ was obtained on the reception points. This received stress must be converted into voltage terms taking into account the layers of the receiver [60] in order

to compare it with the experimental signal received by the torsional sensor (in terms of voltage). Therefore, knowing the different layers of the receiver, PLA ring - piezoelectric element (NCE51), the voltage on the piezoelectric element is approximately the stress on the tissue by a correction factor α_c.

$$\frac{Voltage^{NCE51}}{\sigma_{\theta z}^{phantom}} = \alpha_c = T_{Phantom-PLA} \cdot T_{PLA-NCE51} \cdot \text{factor Stress-Voltage} \tag{8.5}$$

The transmission coefficient in terms of stresses between the phantom and PLA is calculated through the shear impedance of both media (see Table 8.5),

$$T_{Phantom-PLA} = \frac{2 \cdot Z_{PLA}}{Z_{Phantom} + Z_{PLA}} = 1.98 \tag{8.6}$$

where $Z = c_s \cdot \rho$ is the shear impedance, c_s the torsional wave speed and ρ the density of the medium.

The transmission coefficient in terms of stresses between the PLA and NCE51 and the factor stress-voltage are taken from literature [189].

$$T_{PLA-NCE51} = 0.78 \tag{8.7}$$

$$\text{factor Stress-Voltage} = 1.8275e-4 \tag{8.8}$$

Medium	$\rho(kg/m^3)$	$c_s(m/s)$	$Z(kg/(m^2s))$
Phantom	1000	2	2000
PLA	1180	200	236000

Table 8.5: Shear impedance for each medium [5].

8.5 Viscoelastic parameters reconstruction from SWE measurements

The KV viscoelastic parameters were acquired by fitting the dispersion shear wave speed curve obtained after analyzing Verasonics measurements (see section 8.2.2). The adjustment that was performed employs an inverse problem using a combination of genetic algorithms and quasi-Newton type optimization algorithms. The complex shear moduli for the KV model is,

$$G^{*KV}(\omega) = G^{'}(\omega) + iG^{''}(\omega) = \mu + i\omega\eta \tag{8.9}$$

where ω is the angular frequency. The relationship between the shear wave speed (c_s) and the complex shear modulus is well known to be [7],

$$c_s(\omega) = \sqrt{\frac{2(G'^2 + G''^2)}{\rho(G' + \sqrt{G'^2 + G''^2}}} \tag{8.10}$$

where ρ is de phantom density, in this work $\rho = 1000\, kg/m^3$.

This definition was employed to fit the experimental data.

8.6 Probabilistic inverse problem (PIP)

It is proposed a technique based on a PIP with logical inference framework to evaluate the most plausible parameters of the physical model for the particular case of characterizing a viscoelastic material [248] using a KV approach (more details about the PIP procedure can be found in Chapter 7). Then, the information-theoretic inverse problem framework is applied, describing the process of parametrization, the operation with discrete observation data of signals, and its extension to probabilistic parameter optimization.

The values of the search range of the parameters have been taken according to scientific evidence that are showed in [6, 7], and developed in the experimental setup under the consideration of a set of phantoms previously manufactured.

To derive the effectiveness of the PIP method, the following inverse problem is solved. The outcomes are the constitutive KV viscoelastic mechanical parameters of the phantoms evaluated.

The requested constitutive equation is defined as linear viscoelasticity that additively combines strains from consistency shear modulus of first and second layer, μ^E_{first} and μ^E_{second}, respectively, shear viscoelastic parameter η and thickness. The search range of these parameters are detailed in Table 8.6.

Kelvin-Voigt Model	
Parameter	**Search Range**
μ_{first}	0-20 kPa
μ_{second}	0-50 kPa
η	0-5 Pa · s
th	0-2000 μm

Table 8.6: The range of the parameters implemented for the FDTD model [6, 7].

Note that for each sample, the same percentage of oil has been used (main responsible of the shear viscosity), this is due to the results obtained in Chapter 12. This results in a reduction of the number of parameters that are reconstructed with the PIP, which produces a reduction in the computational cost.

To solve the PIP by assuming known or unknown viscoelastic constants, the linear viscoelastic model described previously is programmed using,

$$f = kf^0 \int_{\mathfrak{M}} f(\mathcal{M}) d\mathcal{M} = kI \tag{8.11}$$

where $\mathcal{M}$ are the model parameters, f^0 is a source from experimental observations of the system and the constant k [258]. The integral I,

$$I = \int_{\mathfrak{M}} e^{-J(\mathcal{M})} d\mathcal{M} \tag{8.12}$$

$$J = -\frac{1}{2} \int \sum_{i,j=1}^{N_i} \left(o_i(t,\mathcal{M}) - o_i^o(t)\right) \left(C_{ij}^o + C_{ij}^m\right)^{-1} \left(o_j(t,\mathcal{M}) - o_j^o(t)\right) dt \tag{8.13}$$

is approximated computationally by a standard Quasi-Monte Carlo sampling where J corresponds to a misfit function between synthetic signals from the KV model (o_i) and experimental signals (observations) (o_i^o), being C_{ij}^o and C_{ij}^m the covariance matrices that represent the error noise of the observations and model respectively, and $f(\mathcal{M})$ the classical probability density which approximates the integral of any integrand $f(x)$ that depends on the parameters x over a parameter subspace Ω using,

$$\int_{\Omega} f(x) = \frac{1}{N} \sum_{n=1}^{N} f(x_i) \tag{8.14}$$

where the integrand $f(x)$ is assessed at N random points $x_i \in \Omega$ called samples. The accurate of the algorithm is defined by the number of samples, they have been chosen as $N = 2^{14}$ points. This integral is uniquely calculated at the computation of the model.

9

Hyperelastic ex-vivo cervical tissue mechanical characterization

This chapter provides insight into a nonlinear *ex-vivo* characterization of human cervical tissue through a proposed hyperelastic model based on the Fourth Order Elastic Contants (FOEC) in the sense of Landau's theory.

Section 9.1 shows the theoretical relationship between stress and strain for the proposed hyperelastic model, Mooney-Rivlin and Odgen models. In Section 9.2, the obstetric characteristics of the population studied in this work are presented. Finally, the uniaxial tensile test procedure, the cervical hysterectomy preparation protocol and the cross-correlation algorithm for deformation monitoring are described in detail in Section 9.3.

9.1 Hyperelastic models

The equations of hyperelasticity for the models that will be presented in the following subsections have been carefully deduced in Section 5.2 of Chapter 5.

9.1.1 Proposed Fourth Order Elastic Constants nonlinear model

The derivation of Cauchy stress tensor for the nonlinear proposed model in the context of weakly nonlinear elasticity [211] yields the constitutive law defined in high order as follows,

$$\sigma_{11} = 2\mu a + (5\mu + A)a^2 + (7\mu + 3A + 4D)a^3 + \left(\frac{5}{2}\mu + 3A + 8D\right)a^4 + \frac{5}{2}(A + 4D)a^5 \quad (9.1)$$

In order to compare with the rest of the hyperelastic models, the aforementioned tensor is simplified (using two parameters, μ and A) as follows:

$$\sigma_{\text{Nonlinear}} = 2\mu a + (5\mu + A)a^2 \tag{9.2}$$

9.1.2 Mooney-Rivlin model

For the Mooney-Rivlin model, the Cauchy stress obtained employing 5.22 and using two parameters (c_1 and c_2) is,

$$\sigma_{\text{Mooney}} = 2\left(\lambda^2 - \frac{1}{\lambda}\right)\left(c_1 + c_2\frac{1}{\lambda}\right) \tag{9.3}$$

9.1.3 Odgen model

Using the equation 5.27, the Cauchy stress for the Odgen model is obtained as a function of two parameters (μ_r and α_r) as follows,

$$\sigma_{Odgen} = \mu_r\left(\lambda^{\alpha_r} - \lambda^{-\alpha_r/2}\right) \tag{9.4}$$

where μ_r (infinitesimal shear modulus) and α_r (stiffening parameter) are material constants.

The shear modulus μ in the Odgen model results from the expression,

$$\mu = \frac{\mu_r\alpha_r}{2} \tag{9.5}$$

9.2 Hysterectomy specimens

A total of 7 hysterectomy specimens from women with benign gynecological conditions were obtained from Health Campus Hospital in Granada. The study met the principles of the Declaration of Helsinki. Approvals of the Ethical Committee in Human Research of University of Granada and Ethical Commission and Health Research of Health Campus Hospital in Granada were achieved. All women enrolled in the evaluation provided agreement by signing a written consent and reading the information of the patient report.

Patient	Age	Hysterectomy indication
1	53	Vaginal prolapse
2	67	Subserous myoma
3	59	Vaginal prolapse
4	54	Cervical prolapse
5	50	Cervical prolapse
6	51	Cervical prolapse
7	71	Cervical prolapse

Table 9.1: Obstetric characteristics of the population in the study.

9.3 Mechanical tests

All the mechanical tests were performed using the tensile-compression press showed in Figure 9.2. The device was equipped with a 500 N force gauge (IMADA ZTA-500N) fixed to a platform that is operated by three motors with an accuracy of $0.3\mu m$. The tolerance of the force gauge is 0.1 N. The cervical tissue was fixed by two Acrylonitrile Butadiene Styrene (ABS) printed gripper jaws, one was attached to the press and another linked to a fixed support, that prevent the cervical tissue from undesired movement. According to the literature reviewed in soft tissue uniaxial tensile tests, the load step was 0.2 mm at a strain ramp rate used was $1\%/s$ [273]. A rule was used in the same plane in which the sample was contained for the calculation of deformations. Finally, a conventional camera (IPEVO Ziggi-HD High Definition USB CDVU-04IP model, 5 Mpix, 1280x720 resolution) was employed to acquire the image sequence at each loading step until the sample breakdown (Figure 9.3). The camera was synchronized with a MATLAB®programming environment (Release 2018b, MathWorks, Natick, United States) at the beginning of the experimental test. The code implemented in MATLAB®allowed to control each increment of load through an Arduino microcontroller, at the same time that recorded at a rate of 1 frame per load increment until the sample breakdown.

The sample preparation protocol is fundamental and consist of several steps:

1. All the seven cervical tissues were excised from the women and placed in phosphate buffered saline (PBS) to avoid loss of hydration after surgery. The samples were tested in the Ultrasonics Laboratory of the University of Granada. Two slices were cut manually from each cervical sample, one from the epithelial layer and another one from the connective layer. The epithelial layer was cut carefully to obtain a thickness between 0.5 and 1 mm. The connective layer was obtained below the epithelial layer. All the samples were cut with the same mold (see Figure 9.1) to maintain the same geometry, which is necessary to locate the most unfavorable section.
2. A random dot pattern was used in the cervix to improve deformation monitoring carried out by a cross correlation algorithm (PTVlab software), see Figure 9.4. For the speckle generation, acrylic black paint was used.
3. An optimal contrast obtained by a good illumination and an uniform background help the tracking algorithm.
4. It is worth underlining that the cervical tissue samples were kept continuously hydrated so as not to alter the mechanical properties during the experiment by spraying them with PBS.

The PTVlab is a free software that was developed by Dr Wernher Brevis (mainly developed the mathematical algorithms) and Antoine Patalano (adaptation of the graphical user interface (GUI) in MATLAB and the development of new functionalities) [274, 275]. The LSPTV method is employed by PTVlab and uses the binary correlation, the Gaussian mask and the dynamic threshold binarization techniques for the particle detection. A Gaussian

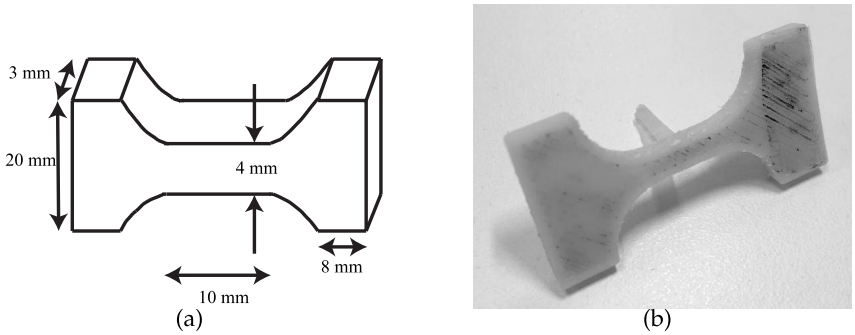

Figure 9.1: a) Mold printed with Acrylonitrile Butadiene Styrene (ABS) to maintain the geometry of the samples. b) Cervical tissue sample geometry.

mask with a correlation threshold 0.5 and a sigma of 3 px was used for the particle tracking. The PTV algorithm was cross-correlated by an interrogation area of 10 px, a minimum correlation of 0.6 px, and a similarity neighbor of 25%. The deformation was calculated in the most unfavorable area of the cervical tissue, which according to the printed mold corresponds to the central area.

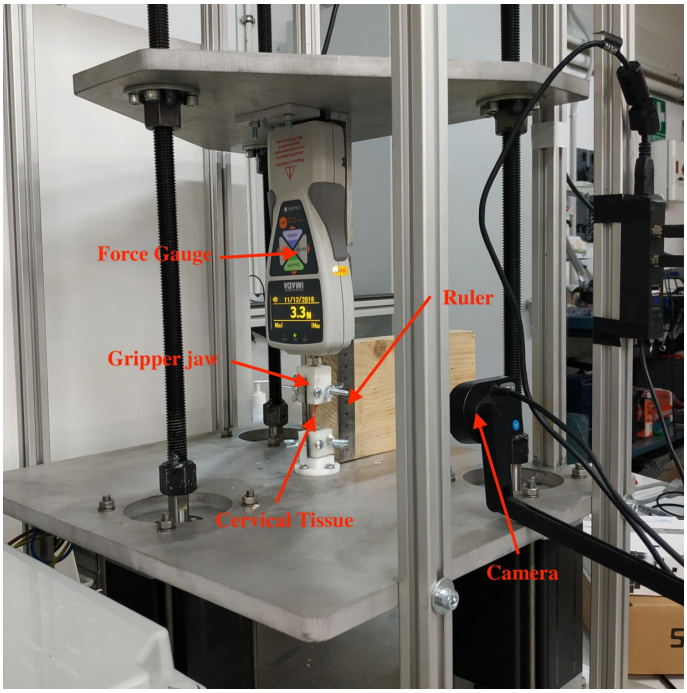

Figure 9.2: Experimental setup comprising a 500 N force gauge, gripper jaws for holding the sample attached and a conventional camera to register the loading process.

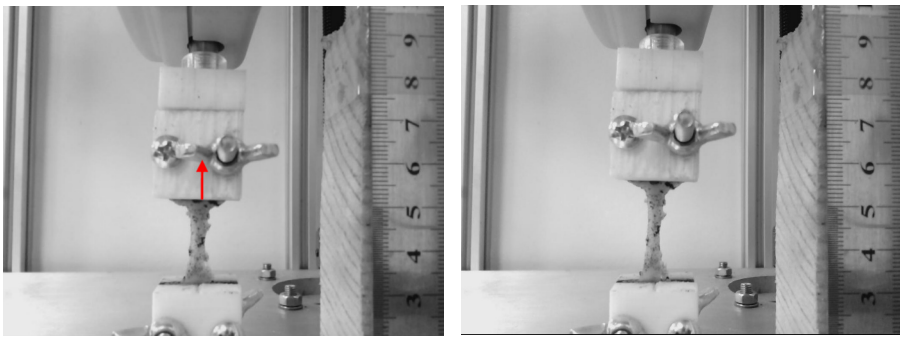

(a) Load=2.8 N (b) Load=10.7 N

(c) Load=0.3 N

Figure 9.3: Three different frames from a recording of an uniaxial tensile test in a cervical tissue sample. The tissue is stretched in the direction marked with red arrow.

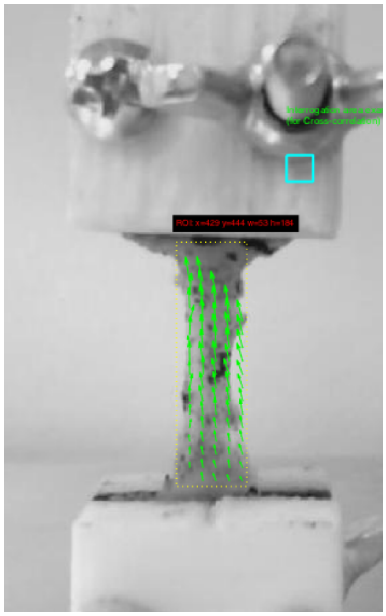

Figure 9.4: An illustrative example of cervical tissue attached to two gripper jaws that fix it during the uniaxial tensile test. A dashed yellow line was used to delimit the region of interest (ROI). The green arrows represent the displacements.

10

In vivo measurement of cervical elasticity on pregnant women by TWE: a preliminary study

This chapter describes the material and methods used in an *in-vivo* study in pregnant women [276]. The aim of this preliminary study was to evaluate the reliability and feasibility of TWE technique to provide consistent data on the changes of the cervical stiffness during pregnancy [1].

Section 10.1 exposes the design of the study and experimental protocol. In Section 10.2, it is shown the experimental setup, the post-processing procedure of the signals received and the safety considerations for the torsional wave sensor. Finally, Section 10.3 outlines the statistic analysis tools.

10.1 Design of the study

A cross-sectional study in healthy pregnant women was performed to assess stiffness modifications in cervix. The pre-pilot test study was carried out at San Cecilio University Hospital in Granada. The data were analyzed in the Ultrasonics Laboratory in the University of Granada. The study met the principles of the Declaration of Helsinki. Approvals of the Ethical Committee in Human Research of University of Granada and Ethical Commission and Health Research of San Cecilio University Hospital in Granada were achieved.

A total of 18 healthy women were recruited from their routine medical visits during pregnancy, and TWE technique explorations were performed in the Fetal Medicine Unit.

[1] Contribution: P. Massó, A. Callejas, J. Melchor, F. S. Molina and G. Rus. In-vivo measurement of cervical elasticity on pregnant women by torsional wave technique: a preliminary study. *Sensors*, 19(15), 2019.

The entire population of women in the study had pregnancies without any complication with a median of 26.4 (16wk-35wk+5d) gestation weeks, and there was no twin pregnancy. A statistical power analysis was designed to estimate the size of the population. A multivariate continuous regression with a power of 80%, and estimated significance in a two-tail distribution, and a recommended effect size ES=0.30, yielded a sample size of 17 subjects. Exclusion criteria were multiple pregnancies, previous cervical surgeries and patients with information relative to malignant changes in the cervical tissue. All women enrolled in the evaluation provided agreement by signing a written consent and reading the information of the patient report.

For the exploration with TWE technique, the participants empty their bladder before the exploration and then were placed in the dorsal lithotomy position. The intravaginal device was allocated in contact with the cervical internal OS (see Figure 10.1). The measurements of cervical length were obtained by a transvaginal sonography probe which was directed in the anterior fornix. A sagittal view was obtained. Three TWE technique and cervical length measurements per women were performed.

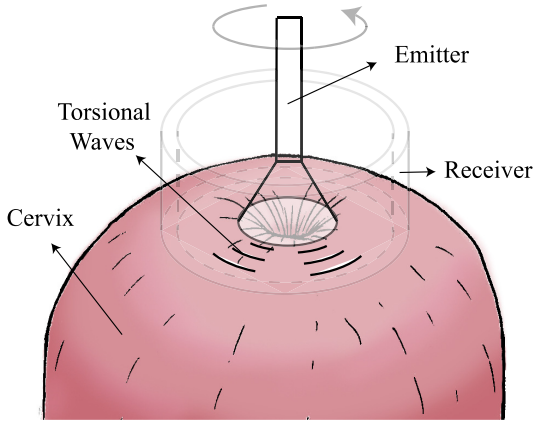

Figure 10.1: Schematic diagram for the exploration with TWE technique.

10.2 Torsional Wave elastography technique

Elastography quantification was achieved by the TWE probe [217], which generated waves under safe threshold of energies. The device consisted in three parts: a torsional wave sensor (probe), an electronic system for generating and receiving the signal, and an interface software (Figure 10.2).

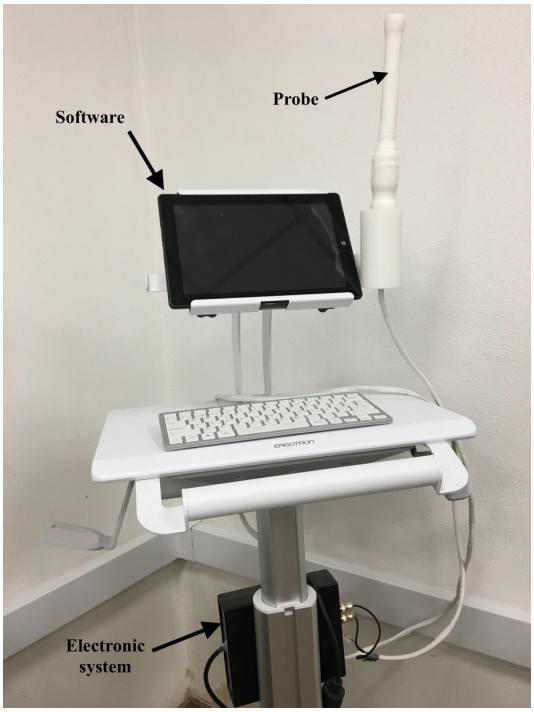

Figure 10.2: The prototyped TWE probe.

The probe was manufactured in 2017, and was composed of (1) an electromechanical actuator which deleted electronic cross-talk [60]; a receiver (2) based on two polylactic acid rings where the piezoelectric elements were fitted; a case (3) to contain the emitter and the receiver (more details can be found in Chapter 6). The shear modulus was obtained assuming an elastic and incompressible medium by the following equation,

$$\mu = \rho c_s^2 \tag{10.1}$$

where ρ is the density of the medium, and c_s is the torsional wave velocity, which is based on shear wave group velocity.

The excitation signal was a burst composed of a 1-cycle frequency f ranged from 0.5 to 1.5 kHz with $10\times$ averaging. The frequencies were chosen according to the results obtained in the work carried out by Callejas et al. [60].

An example of three different emitted and received signals is shown in Figure 10.3. The shear wave group velocity calculation algorithm was based on dividing the distance by the torsional wave time-of-flight. The signals were preprocessed by a low-pass filter close to the central frequency of the received signal. The time of flight was computed using three procedures, searching (1) the first time the signal raises 30% above the zero, (2) subtracting a quarter of the period (inverse of the received signal central frequency) to the first peak, (3) subtracting three quarters of the period (inverse of the received signal central frequency) to the second peak. All three methods provided similar estimates of the velocity, as shown in the results.

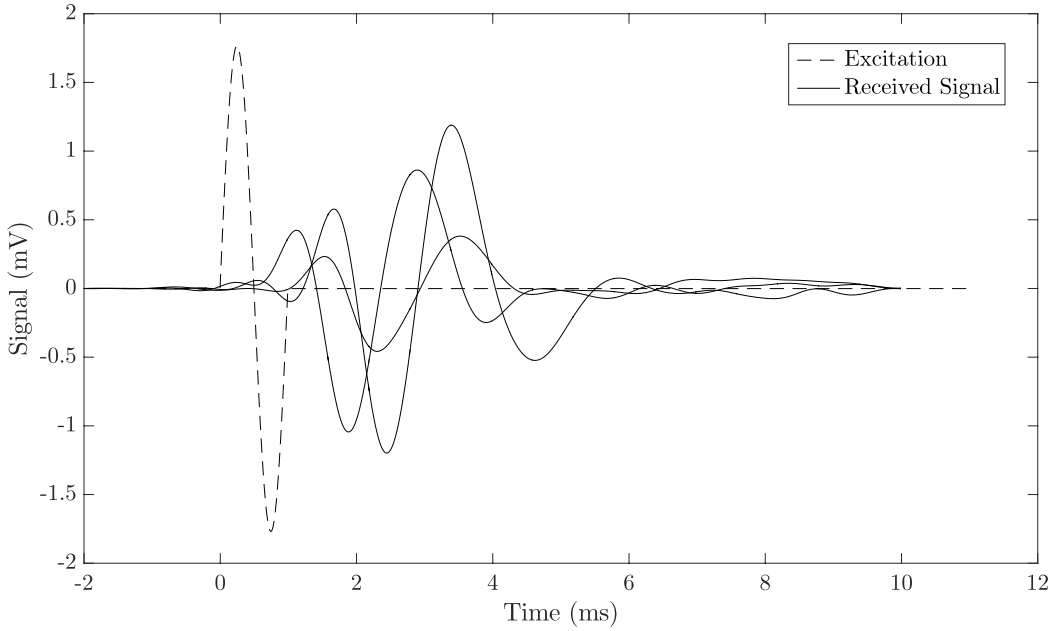

Figure 10.3: Example of three emitted and received 1 kHz signals.

10.2.1 Safety considerations

A new medical diagnostic equipment needs to follow the specifications described in the Food and Drug Administration (FDA) guidelines [277] for the application in clinical practice. It is necessary that the Torsional Wave technique be safe for humans. There are three parameters that should be evaluated according to the acoustic output in the use of Fetal Imaging & Other (FDA): the mechanical index ($MI < 1.9$), the spatial peak pulse average intensity ($ISPPA < 190\ W/cm^2$), and the spatial peak temporal average intensity ($ISPTA < 94\ mW/cm^2$). The calculation of these parameters was made as follows:

$$MI = PRP/\sqrt{F_c} \tag{10.2}$$

where PRP is the peak rarefactional pressure of the torsional wave in (MPa) and Fc is the center frequency (MHz).

$$ISPPA = P_0^2/(2 * \rho * c) \tag{10.3}$$

where P_0 is the maximal acoustic pressure generated by the electromechanical actuator, ρ is the density of the medium, and c is the sound speed in the medium.

$$ISPTA = ISPPA * \Delta t/1 \tag{10.4}$$

where Δt is the excitation pulse duration.

The three parameters were experimentally estimated. The excitation signal used was a low-frequency ultrasonic sine-burst at a central frequency of 1 kHz, consisting of 1 cycle

of 1 ms and 16 Vpp amplitude. This excitation signal was generated by a wave generator (Agilent 33220A, Santa Clara, CA, United States). The response signal was registered using a decibel sensor (YH-610 Environment Multimeter). The signal traveled through a water layer before arriving to the decibel sensor and different distances from 5 centimeters to 0 centimeters. To convert the pressure recorded by the decibel sensor into water acoustic pressure, the equation that relates the impedances of the two media (air-water) was used:

$$T = \frac{2 * Z_{air}}{Z_{air} + Z_{water}} \tag{10.5}$$

where T is the transmission coefficient, Z_{air} and Z_{water} are the acoustic impedance of the air and water respectively.

10.3 Statistic analysis

The evolution of cervical stiffness tissue during pregnancy was quantified. Normal distribution of the data was checked for each velocity calculation algorithm by the normal quantile-quantile plot (Q-Q plot) and the Shapiro-Wilk test. The mean values for each velocity calculation procedure were compared to the normal distribution of these values. The coefficient of determination (R^2) for linear regression analysis was calculated to provide the correlation between a) gestational age with cervical stiffness or velocity (c_s) using 0.5, 1 and 1.5 kHz torsional waves, for the three velocity calculation algorithms, b) gestational age and cervical length, and c) stiffness and cervical length. Data were analyzed using the MATLAB (Release 2014b Mathworks, Natick, United States). T-test was calculated to estimate p-values. A statistically significance for $p < 0.05$ was assumed.

Part III

RESULTS: EXPERIMENTAL CONTRIBUTIONS

11

Feasibility of a novel Torsional Wave Elastography technique

This chapter aims at testing the hypothesis on which the first objective of this thesis is based, i.e., evaluate the feasibility, sensitivity and capability of the torsional wave elastography technique for objectively quantify the viscoelastic properties of cervical tissue [1].

Section 11.1 shows a sensitivity analysis to evaluate the robustness of the proposed TWE technique. The variables object of the study were both, the applied pressure and the angle of incidence sensor-phantom. In Section 11.2, an *ex-vivo* cervical tissue characterization is presented. Four rheological models fitted the experimental data in order to analyze the dispersive behavior of the cervical tissue and a static independent testing method was employed. Finally, the results of the two contributions are discussed in Section 11.3.

11.1 Sensitivity analysis

Firstly, we explored the influence of the applied pressure in shear wave speed. Shear wave signals measured with TWE method at different applied pressures phantom-sensor and with the same frequency excitation (300 Hz) and gelatine concentration (10%) are shown in Figure 11.1.

[1] Contribution: A. Callejas, A. Gomez, J. Melchor, M. Riveiro, P. Massó, J. Torres, M. López-López and G. Rus. Performance study of a torsional wave sensor and cervical tissue characterization. *Sensors*, 17(9), 2017.

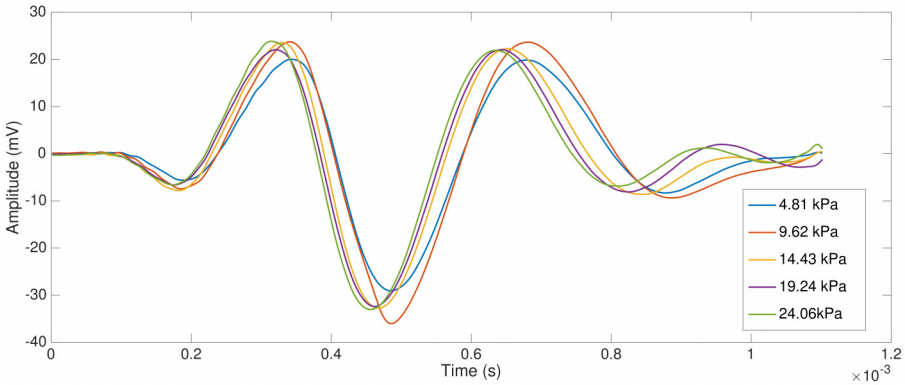

Figure 11.1: Shear wave signals at different phantom–sensors pressures (from 4.81 to 24.06 kPa), frequency: 300 Hz; gelatine concentration: 10%

The shear wave speeds calculated from measurements using the proposed time of flight method are shown in Figure 11.2. Box and whisker plots are represented for the designed phantoms at 8 and 10% gelatine concentration (three samples per concentration), 300 Hz frequency and for the five different pressures. It can be extracted from the plots that there is no correlation between the applied pressure and the shear wave speed.

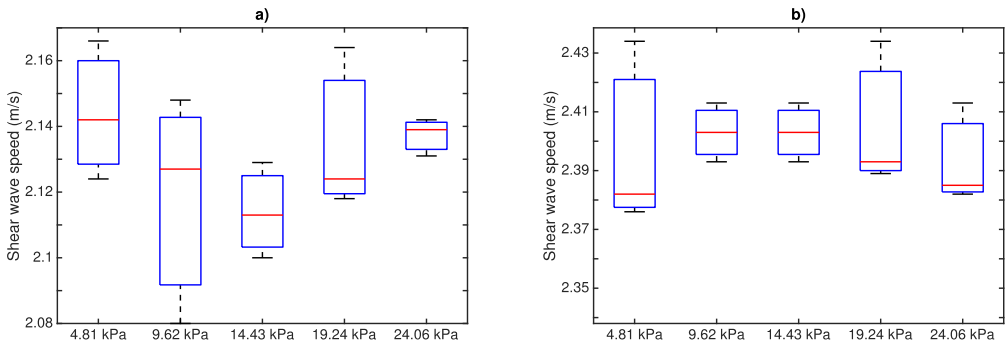

Figure 11.2: Box and whisker plots of shear wave speed measurements at different applied pressures phantom-sensor. Mean (lines within boxes), interquartile range (IQR, boxes) and extreme values (whiskers) are shown. (**a**) 8% gelatine; (**b**) 10% gelatine.

Secondly, to assess the other outcome of the sensor sensitivity study, two shear wave signals have been plotted at two different angles of incidence: 0 and 7.5° (see Figure 11.3).

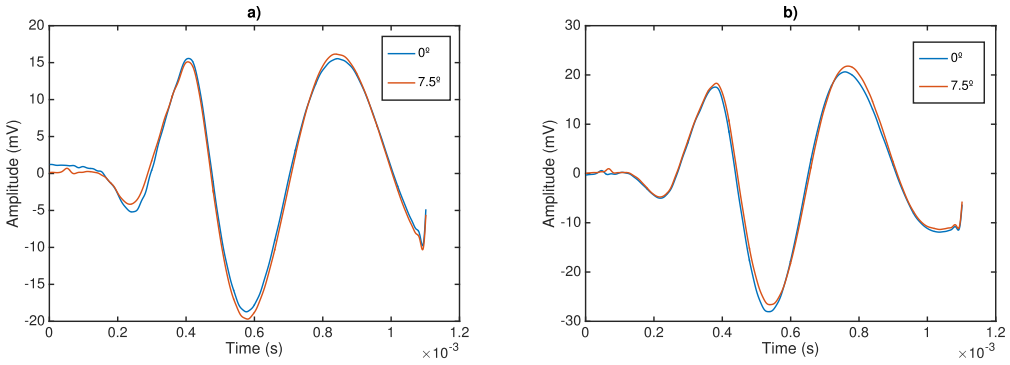

Figure 11.3: Measurement of shear wave speed at different angles of incidence sensor–phantom; frequency: 300 Hz. (**a**) 8% gelatine; (**b**) 10% gelatine.

Shear wave speed measurements are represented in Figure 11.4. Box and whisker plots are shown for the three designed phantoms at 8% and 10% gelatine concentration, 300 Hz frequency and for the two different angles of incidence. The same conclusion is extracted when varying the angle of incidence. No significant variations were obtained.

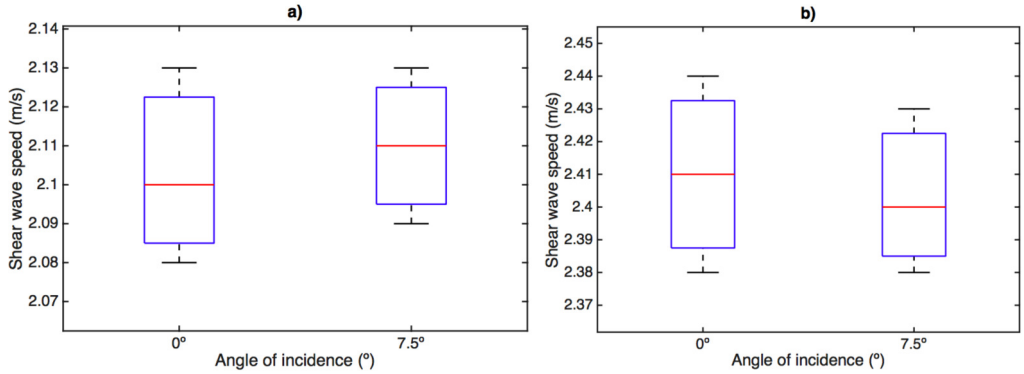

Figure 11.4: Box and whisker plots of shear wave speed measurements at different angles of incidence phantom–sensor. Mean (lines within boxes), interquartile range (IQR, boxes) and extreme values (whiskers) are shown; frequency: 300 Hz. (**a**) 8% gelatine; (**b**) 10% gelatine.

Figure 11.5 shows the real and imaginary part of the complex shear modulus measured in phantom 10% gelatine. Mean and standard deviation are represented for the three measurements performed. It is appreciated the viscoelastic behavior of the gelatine due to the values adopted by the loss modulus.

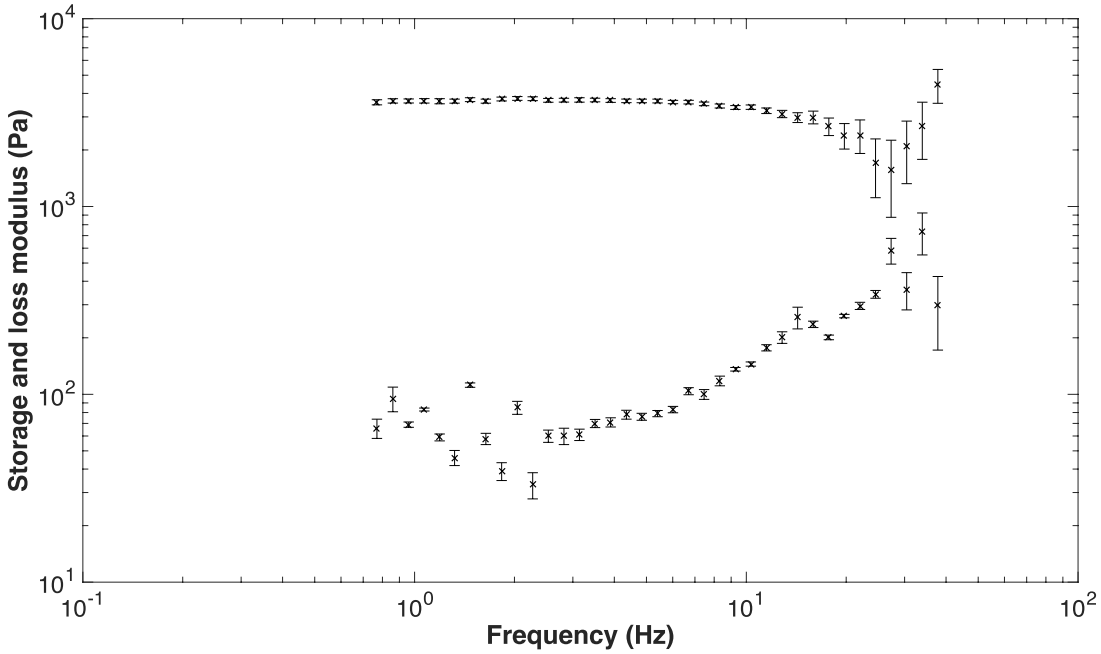

Figure 11.5: The storage and loss shear modulus measured by rheometry in phantom 10 % gelatine.

11.2 *Ex-vivo* cervical tissue characterization

The real and the imaginary part of the complex shear modulus measured in cervical tissue by rheometry are shown in Figure 11.6. The measurements were taken three times for each cervix to obtain the mean and the standard deviation.

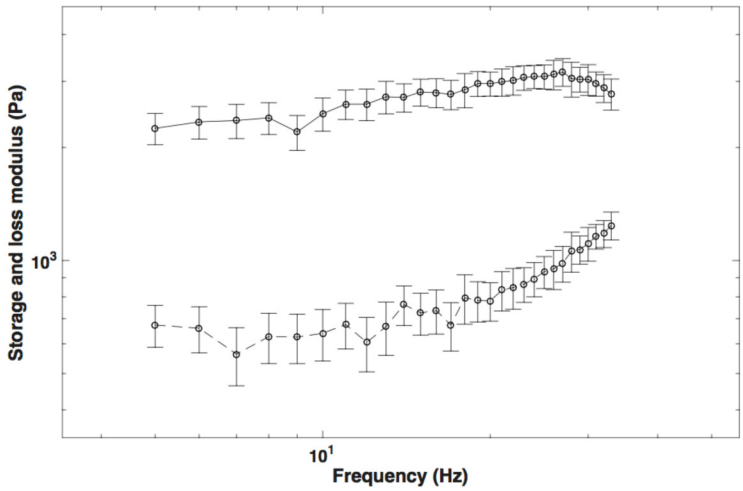

Figure 11.6: The storage and loss shear modulus measured by rheometry in cervical tissue.

Figure 11.7 shows the fitted curves using data from rheometry, elastography and both sources of data simultaneously, for each rheological model. Frequencies for rheometry measurements ranged from 4 to 30 Hz, while, for the elastography technique, there was a wider range from 300 to 1000 Hz.

Tables 11.1 and 11.2 show the viscoelastic parameters reconstructed using the data from rheometry, elastography and a combination of the two methods for Kelvin–Voigt and Kelvin–Voigt Fractional Derivative models. The high-frequency components of the dispersive curve play a much larger role than the low-frequency components. The curve shape or dispersive pattern is primarily determined by the high frequency components. KV and KVFD models matched satisfactorily all the data from the high to the low-frequency regime. The findings can also be confirmed by the results of Tables 11.1 and 11.2, showing that the elasticity and viscosity values obtained from the high-frequency TWE data were very similar those from the overall rheometry + TWE data, although they differ from those obtained from the low-frequency rheometry data.

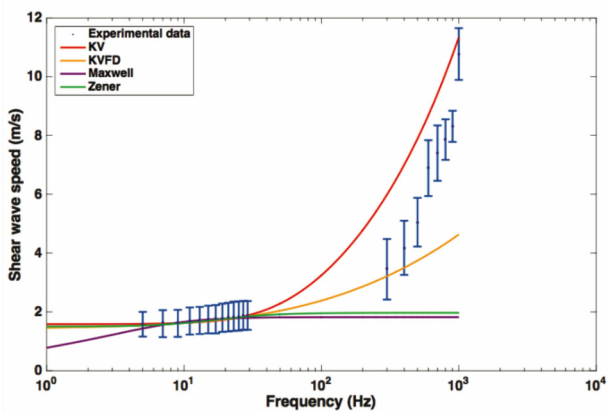

(a)

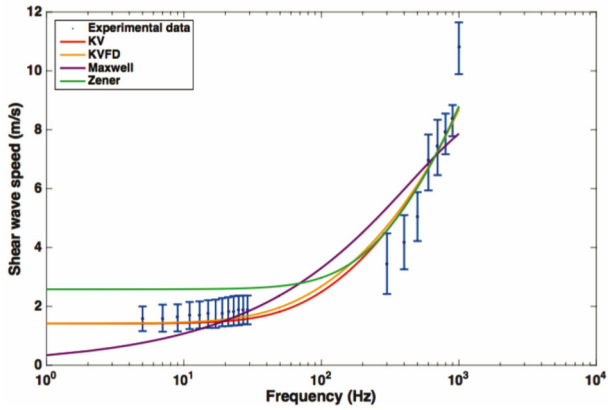

(b)

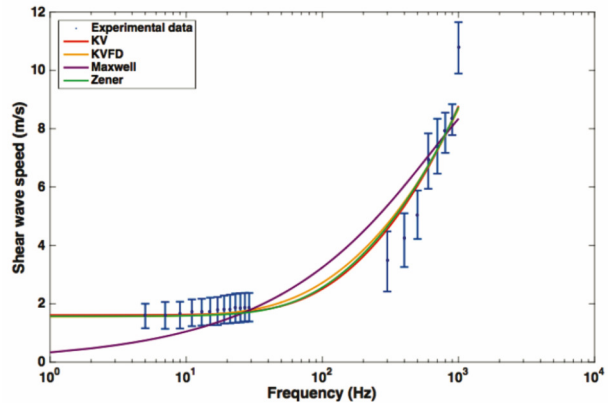

(c)

Figure 11.7: Fitted curves using data from rheometry, from elastography and using the combined data from the rheometry and elastography for each model. The circles are the mean values over the three cervix and the horizontal bars are the standard deviations. The curves for the Kelvin–Voigt (solid red line), Kelvin–Voigt Fractional Derivative (solid yellow line), Maxwell (solid purple line) and Zener model (solid green line) are shown. (**a**) data from rheometry; (**b**) data from elastography; (**c**) data from rheometry and elastography.

Cervix Number	Elasticity μ (kPa)			Viscosity η (Pa·s)		
	Rheometry	TWE	R + TWE	Rheometry	TWE	R + TWE
1	1.69	2.13	1.82	5.31	4.32	4.21
2	1.83	2.52	2.10	6.52	4.55	4.64
3	1.85	2.64	1.84	7.19	4.9	4.65
Mean	1.79	2.43	1.92	6.34	4.59	4.5
Standard Deviation	0.08	0.26	0.15	0.95	0.29	0.25

Table 11.1: Viscoelastic parameters using the data from rheometry, TWE, and a combination of the two methods for the Kelvin–Voigt model.

Cervix Number	Elasticity μ (kPa)			Viscosity η (Pa·s)			Fract. Deriv. Power α		
	Rheometry	TWE	R + TWE	Rheometry	TWE	R + TWE	Rheometry	TWE	R + TWE
1	1.10	2.13	2.07	12	4.02	4.54	0.42	0.98	0.99
2	0.80	1.93	2.22	31	4.21	4.73	0.13	0.99	0.96
3	0.86	2.12	1.74	26	4.46	4.65	0.20	0.94	0.99
Mean	0.92	2.06	2.01	23	4.23	4.64	0.25	0.97	0.98
Standard Deviation	0.15	0.11	0.24	9.84	0.22	0.09	0.15	0.02	0.01

Table 11.2: Viscoelastic parameters using the data from rheometry, TWE, and a combination of the two methods for the Kelvin–Voigt Fractional Derivative model.

11.3 Discussion

Characterization of the viscoelastic properties of soft tissues is a key step for the development in many medical applications based on elastography imaging. In the case of cervical tissue, a special interest lays on the study of the evolution of the viscoelastic properties during pregnancy, in addition to their correlation with the gestational age. Little data for the case of viscoelasticity of human cervical tissue can be found in the literature [278].

The increasing interest in elastography techniques for measuring viscoelastic parameters is demanding appropriate validation studies. Currently, the traditional standard for evaluating the viscoelastic properties of soft tissues is based on rheological methods. However, these techniques are limited to *in vitro* and *ex vivo* samples. In addition, whereas the trustful range of frequency in the rheological test is from the quasi-static regime to no more than 50 Hz, dynamic elastography techniques usually use a range from 100 Hz to 500 Hz. This discrepancy makes the comparison process a challenge. However, due to the lack of alternatives, the validation between both techniques has been accepted in previous studies [279, 280].

The presented TWE method is based on the transmission and detection of shear waves. Shear waves travel axisymmetrically from the center of the probe, where the mechanical actuator is placed, towards the outer side where the piezoceramic receivers are located. In this study, the TWE technique was proved capable of successful transmitting and receiving shear waves from 300 Hz to 1 kHz. This range of frequencies represents an obvious advantage when compared with commercial elastography devices [43], since a broader range

of frequencies provides more significant information about the viscoelastic behavior of the tissue, in particular for the viscous component, which is more sensitive to high frequencies [279].

Here, a study with respect of two variables involved during the testing procedure was presented: the normal pressure applied and the angle of incidence between the probe and the normal direction of the tissue surface. This simplified study may fall into a preliminary analysis of the intra-operator dependency of the method. The range of pressures (ranging from 4.81 kPa to 24.06 kPa) and angles (0° and 7°) were chosen in close relation with those experienced during a normal testing procedure. Gelatine phantoms with 8% and 10% concentration (w/w) were selected as an adequate representation of the viscoelastic behavior of soft tissues. As expected, higher concentration of gelatine produced higher shear wave speed due to higher stiffness. Variable levels of pressure produced a minimal variation in the shape of the collected signal, as can be seen in Figure 11.1. The standard deviation values of shear wave speed varied between 0.018 to 0.031 m/s, including all measurements for the range of frequencies studied (300–1000 Hz). The impact of this variation on the reconstructed values of shear wave speed was non-significant for all the frequencies. Therefore, no correlation between the level of pressure and shear wave speed was found in the small range of pressures analyzed. The same effects were observed when varying the angle of incidence. Figure 11.3 shows hardly noticeable variations in the measured signals. These observations were found consistent all over the different gelatine concentration phantoms tested, which seems to indicate that the TWE technique is, at least in gelatine-based phantoms, a robust and low user-dependent elastography method. However, as observed in the experiments, simple gelatine-based phantoms shows a low viscous behaviour, which is not proper of soft tissues. This low viscous behavior might be responsible for such stable results against the two variables of the user-dependency test. Different recipes for obtaining viscous elastography phantoms have been published, for instance by adding castor oil to the gelatine-based original recipe [281]. In further studies, elastography phantoms with higher viscosity will be tested. These analysis must be also extended to tissues exhibiting characteristics more similar to biological tissues, which may not be homogeneous [42] to define the validity limits of these studies and to develop clinical practice protocols to correct deviations when using the designed device.

After the positive outcomes of the sensitivity analysis, a series of experiments were performed on *ex vivo* human cervical tissue. The experiments aimed to combine information from rheometry and TWE providing two sources of data to find the most suitable rheological model to fit the cervical tissue behavior.

Figure 11.7 shows the dispersion curves of shear wave speed regarding the frequency. Since both rheometry and TWE techniques obtain shear wave speed values at different ranges of frequency, rheological models are required to combine the dispersive data. In this study, the classical models of Maxwell, Kelvin–Voigt, Zener and Kelvin–Voigt Fractional Derivative were employed to fit the dispersive data. As proposed by

Lin et al. [279], three types of fitted dispersion curves were obtained depending the data: (a) by using only the data from low-frequency regime generated by rheometry, (b) by using only the data from the high-frequency data provided by TWE, and (c) by fitting the data from both low and high-frequency ranges.

Whereas the fitted curves obtained by using the TWE data were overall in good agreement with the data from rheometry (Figure 11.7b), the curves using the rheometry data diverged from those using TWE (Figure 11.7a). Additionally, the dispersion curve after fitting the whole set of data, this is rheometry + TWE (Figure 11.7c), practically coincided with the curve generated by using only the TWE data. These findings agree with the observations by Lin et al. [279], and point out the relevancy of the viscous effects at higher frequencies. Furthermore, it uncovers the difficulty of characterizing the viscous effects of soft tissue by limiting the experiments to classical rheometry techniques.

When comparing the four rheological models, it can be observed that the Maxwell model showed difficulties to represent the dispersion of shear wave speed along the whole range of frequency. The Zener model adjusted the data successfully when considering both the rheometry and the TWE outcomes. However, when fitting only data from TWE, it showed some divergence at the low-frequency range.

On the other hand, Kelvin–Voigt and its fractional derivative version matched all the data satisfactorily from the high to the low-frequency regime. The fact that both models produced practically the same dispersive curve can be understood by observing Tables 11.1 and 11.2. The values obtained for the α parameters of the Kelvin–Voigt Fractional Derivative model were close to 1, which transforms the model directly into a classical Kelvin–Voigt. A two-parameter model as the Kelvin–Voigt usually will be preferred against a three-parameter model as the fractional version, due to practicality and faster computation. Further studies must be performed to analyze the consistency of all the findings above shown.

11.4 Conclusions

A TWE technique for characterizing the viscoelastic properties of soft tissue, and, in particular cervical tissue, is proposed. To our knowledge, this is the first report of dispersion in *ex-vivo* cervical tissue in women. The shear wave curve dispersions for cervical tissue produced by the TWE method were in good agreement with the data obtained from rheometry. However, these results from rheometry were not able to reproduce the viscous effect on the speed dispersion at high frequencies. Further studies must be carried out to analyze the consistency of these observations. The Kelvin–Voigt model and its fractional derivative version fit the cervix experimental data along the whole range of frequency successfully, and this is considering rheometry and TWE.

The results obtained in this study pave the way to carry out a cross sectional study, which aims the correlation between the gestational age and the viscoelastic properties of the cervix during pregnancy.

In Chapter 15, the results of the preliminary study are shown: ”In vivo measurement of cervical elasticity on pregnant women by Torsional Wave Elastography”. The study focused on assessing the feasibility of torsional wave elastography technique to quantify the changes in cervical stiffness during pregnancy, which were measured by shear stiffness modulus by calculating the time of flight of the received signal.

12

Viscoelastic model class selection for cervical tissue

In this chapter, we describe the results of a Probabilistic Inverse Procedure to rank the numerical model that best explain the viscoelasticity of cervical tissue from torsional wave propagation. To our knowledge, the results presented here constitute the first time the Kelvin-Voigt characterization was performed in *in-vivo* cervix. To this end, the numerical models have been implemented in finite differences. High-speed camera measurements were carried out to feed the numerical models. Slippery conditions between sensor-phantom, as well as the boundary conditions were studied after a video post-processing.

Section 12.1 presents the high-speed camera measurements carried out in order to study th slippery conditions between sensor-phantom and the boundary conditions of the numerical models. In Section 12.2, verification test for controlling numerical dispersion error in the three 2D FDTD viscoelastic models is shown. Section 12.3 exposes the model hypotheses ranking of the three viscoelastic models and the inferred Kelvin-Voigt parameters in cervical tissue. Finally, in Section 12.4 we discuss the ability of the proposed rheological model to reproduce the viscoelastic behavior of cervical tissue.

12.1 High-speed camera measurements

The high-speed camera tests were carried out to study the slippery conditions between sensor and phantom, as well as the boundary conditions of the numerical models after a video post-processing.

Different recordings were made with pressures between the sensor and the phantom ranged from 30 to 150 grams with the aim of selecting the pressure that does not generate

sliding conditions. One of the boundary conditions was the speed at grid points of the tissue that were in contact with the PLA receiver. Another boundary conditions of the numerical model was the excitation. In that vein, the reconstruction of the excitation of the electromechanical sensor was carried out by measuring the displacement of basalt microparticles embedded in the surface of the tissue-mimicking phantom. The implemented algorithm that was employed for this reconstruction is shown in Appendix A. The reconstructed signals for the two fabricated phantoms and for frequencies ranged from 300 to 1200 Hz are shown in Figures 12.1 and 12.2.

As an illustrative example, the results of the optical test using a high-speed camera for the reconstruction of the rotated angle in the propagation of the torsional wave through the surface of the phantom are presented in Figure 12.3. Both surfaces show the propagation of the torsional wave in the distance for the phantom with 10% gelatine and 5% oil. The amplitude of the signal decreased with distance, being zero in the sensor-phantom contact zone. It was also appreciated that the amplitude of the signal was lower for a higher frequency.

12.2 Convergence study of FDTD viscoelastic models

Verification tests for numerical dispersion error have been carried out in the three FDTD viscoelastic models. The number of elements considered per wavelength is a key factor for controlling numerical dispersion. Normal cervical tissue was adopted as the medium of propagation. No distinctions between layers have been made. The parameters used for the three viscoelastic models, according to previous works found in literature, are $\rho = 1000kg/m^3$, $\mu = 2kPa$, $\eta_{KV} = 1.5Pa \cdot s$ and $\eta_M = 15Pa \cdot s$ [7, 6]. The excitation signal used as a reference for the convergence study was 1000 Hz.

In order to analyze the numerical dispersion generated, the root mean square of the received signal for each spatial step size was compared with the root mean square of the received signal for a spatial step size small enough to avoid aliasing effects. The spatial step size in the axial direction Δz was set to be the same as that in the radial direction Δr. The range for these steps was from $0.5\mu m$ to $2000\mu m$. The time step size (Δt) was set as $1\mu s$ after an initial estimate using Equation 7.26 and taking into account the shear wave velocity found in the literature [60].

The calculated root-mean-square of signals for each viscoelastic model has been normalized by a simulated signal with time and spatial steps size ($\Delta t = 1\mu s, \Delta r = \Delta z = 0.5\mu m$) small enough to avoid numerical dispersion.

12.3 Ranking of model hypothesis

To answer the question of how much we can trust the assumed physics among a set of candidates, or which model complexity is best by assuming known or unknown physical constants, the model hypotheses ranking of the three hypothesis described in section 7.2 is computed using Equations 7.36 and 7.39. The hypothesis reliability are showed in % by rescaling the information density from Equation 7.37.

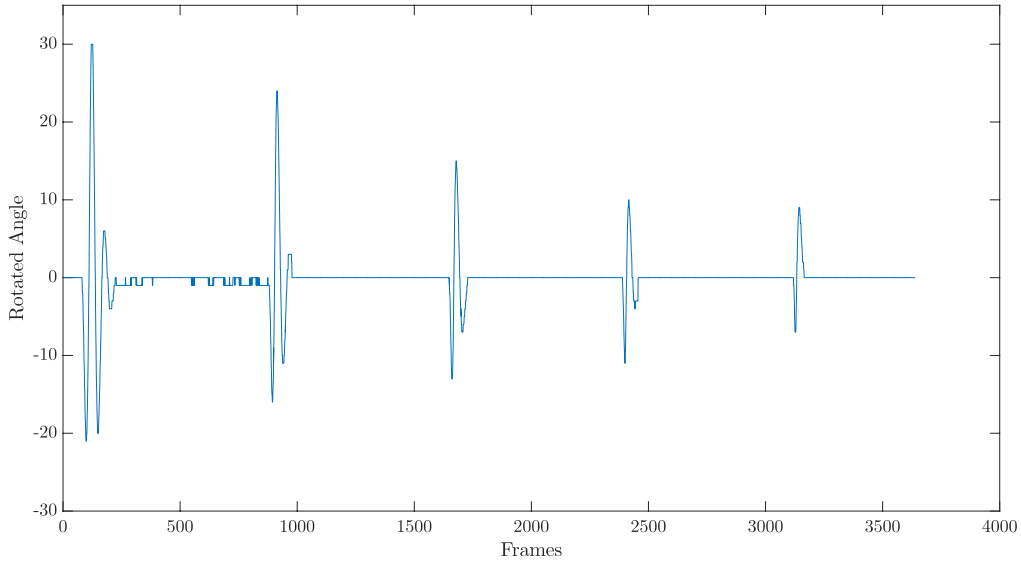

(a)

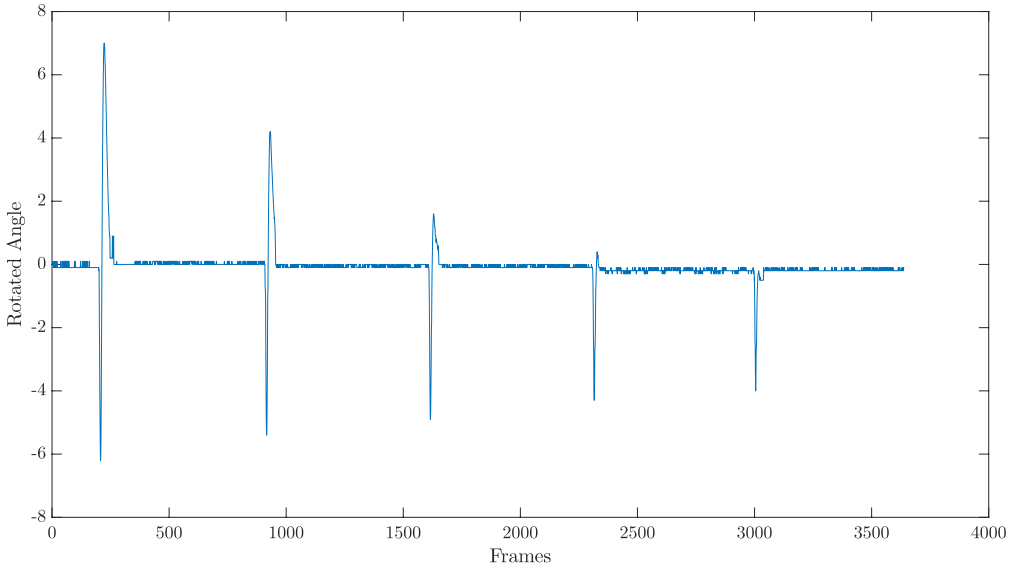

(b)

Figure 12.1: Results of the high-speed camera test for the reconstruction of the emitted signal by the emitter of the torsional wave sensor. Rotated angle by the emitter (sexageximal degrees) versus frames recorded by the high-speed camera. The time step between frames was 1×10^{-4} seconds. (**a**) Phantom 7.5 % gelatine and 5 % oil, frequencies 300-700 Hz (from left to right); (**b**) Phantom 7.5 % gelatine and 5 % oil, frequencies 800-1200 Hz (from left to right).

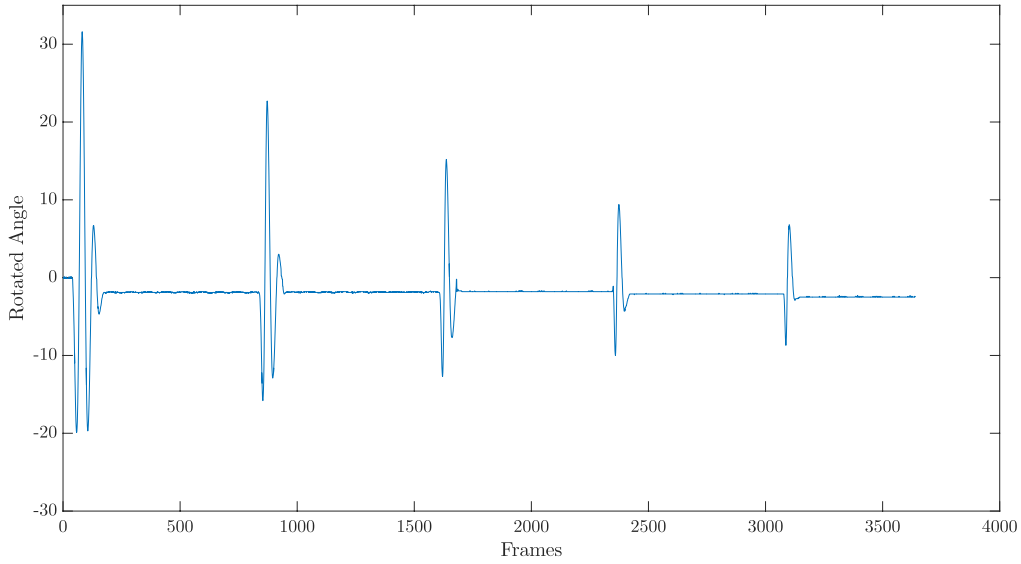

(a)

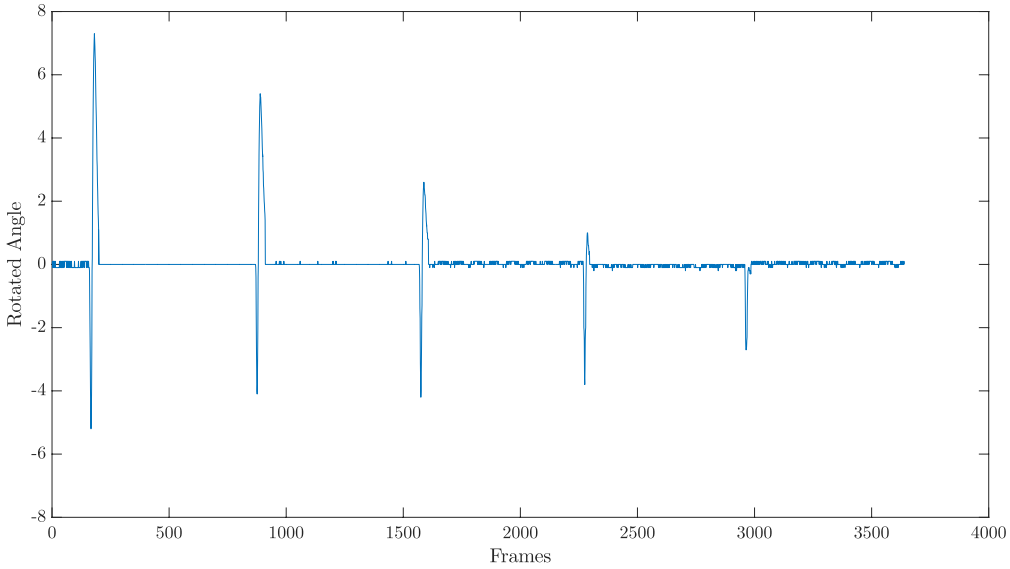

(b)

Figure 12.2: Results of the high-speed camera test for the reconstruction of the emitted signal by the emitter of the torsional wave sensor. Rotated angle by the emitter (sexageximal degrees) versus frames recorded by the high-speed camera. The time step between frames was 1×10^{-4} seconds. (**a**) Phantom 10 % gelatine and 5 % oil, frequencies 300-700 Hz (from left to right); (**b**) Phantom 10 % gelatine and 5 % oil, frequencies 800-1200 Hz (from left to right).

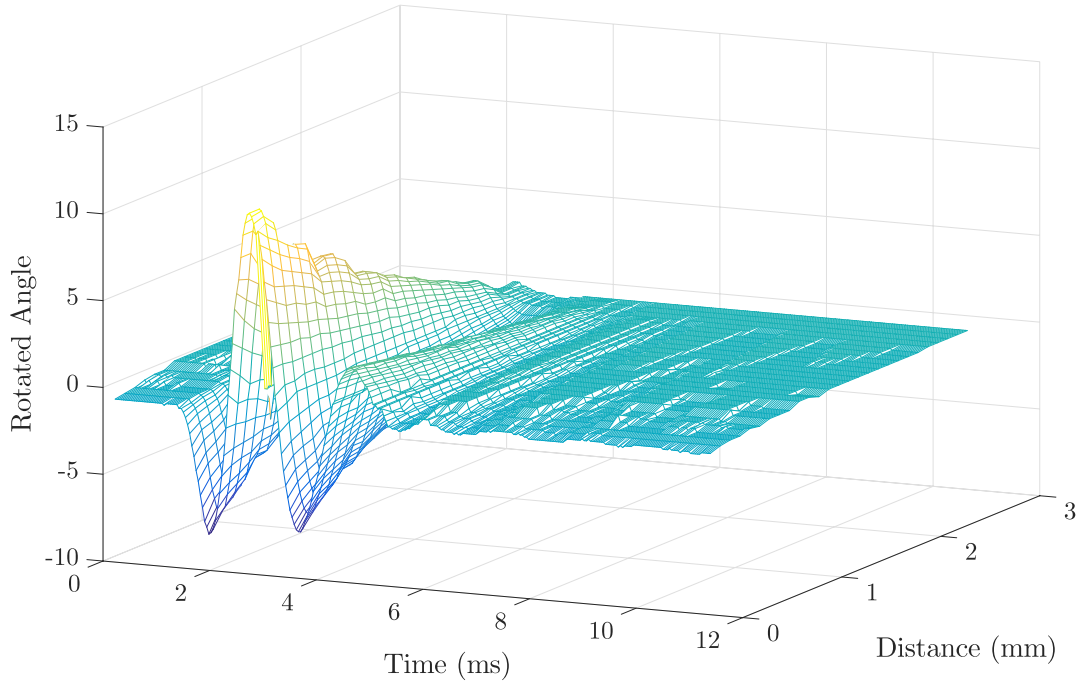

(a)

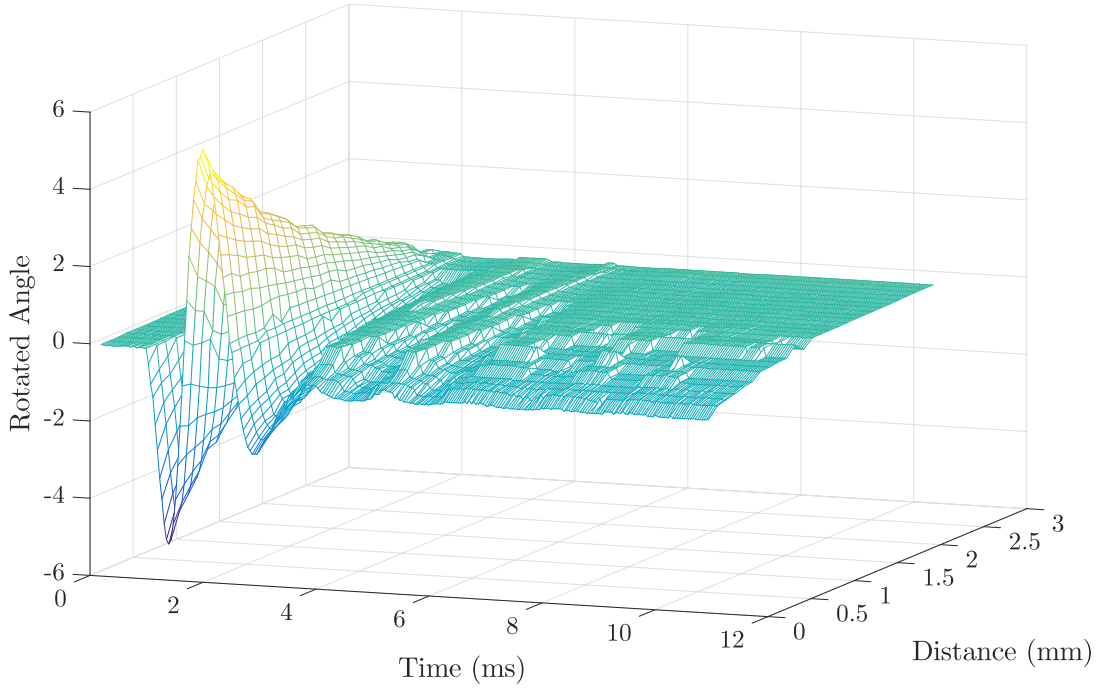

(b)

Figure 12.3: Results of the optical test using a high-speed camera for the reconstruction of the rotated angle in the propagation of the torsional wave through the surface of the phantom. The angle of rotation refers to the center of the disk emitter. Distance refers to radial distance whose origin is the end of the disk emitter. (**a**) Phantom 10 % gelatine, frequency 400 Hz; (**b**) Phantom 10 % gelatine, frequency 600 Hz.

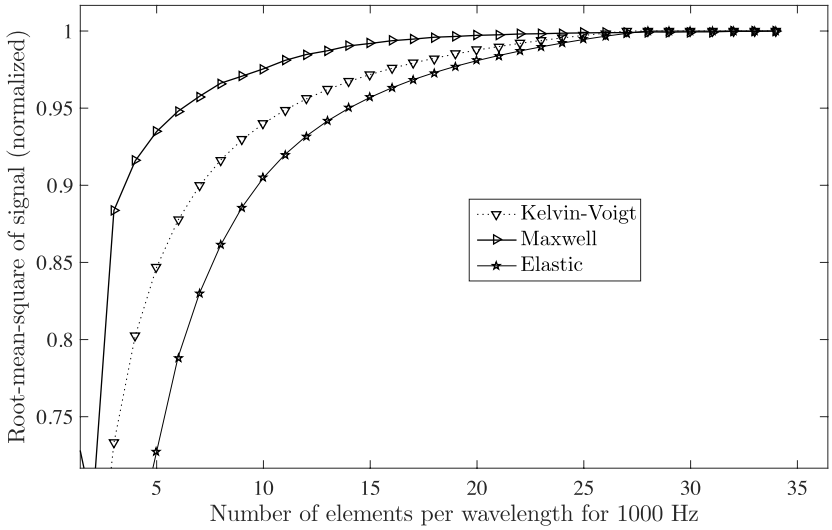

Figure 12.4: Numerical dispersion measured as a root-mean-square of signal (normalized) as a function of the number of elements per wavelength for a frequency of 1000 Hz. Marks represent the root-mean-squared (normalized) for each FDTD viscoelastic model.

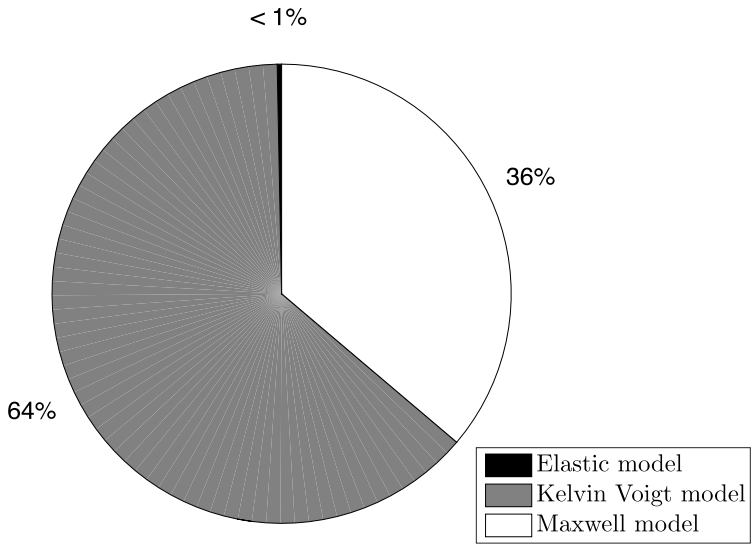

Figure 12.5: Ranking of viscoelastic models.

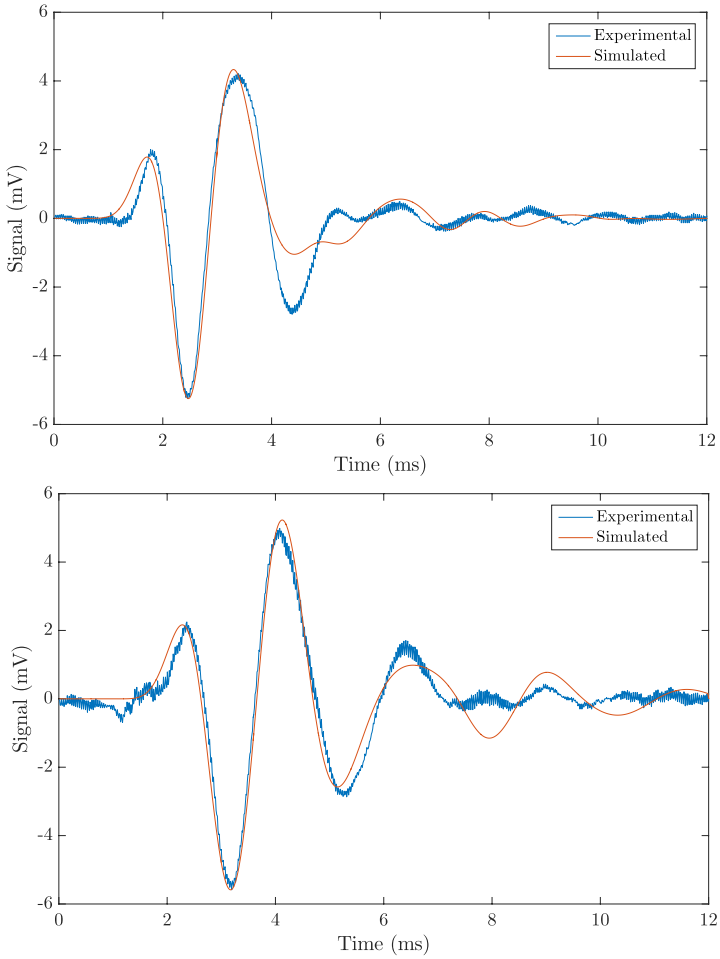

Figure 12.6: Examples of fitting of experimental and simulated observations: Kelvin-Voigt model, time domain.

In Figure 12.5, it is shown the ranking of viscoelastic models. As an example, the fitting of experimental and simulated observations using the most plausible Kelvin-Voigt model and the corresponding FDTD simulation are shown in Figure 12.6 and Figure 12.7.

12.3.1 Marginal plausibility

In order to answer the question of how we can know about the values of the viscoelastic parameters $\mathcal{M} = \{\mu^{KV}_{epithelial}, \eta^{KV}_{epithelial}, \mu^{KV}_{connective}, \eta^{KV}_{connective}, th^{KV}_{epithelial}\}$, under the most plausible model (Kelvin-Voigt model), the marginal probability density can be computed using the equations 7.38 and 7.39. The results are shown in Figure 12.8. Considering the intrinsic noise of experimental measurement, the five parameters are successfully estimated (squares with error bars on each plot of Figure 12.8), as well as their reliability.

12.3.2 Plausibility maps

To answer the question of how coupled the unknown Kelvin-Voigt model parameters $\mathcal{M} = \{\mu^{KV}_{epithelial}, \eta^{KV}_{epithelial}, \mu^{KV}_{connective}, \eta^{KV}_{connective}, th^{KV}_{epithelial}\}$ are, taking into account the number of variables inferred, it would be require 5-dimensional plot. For a better visual-

ization of the dependence between the parameters, we slice it in two 2D contour plots. On each plausibility map, the model parameters are evaluated by moving two and fixing the remaining parameters as the most plausible values. Figure 12.9 shows the contour plots, where the optimal parameters are marked with a plus sign and the most plausible values are: $\mu^{KV}_{epithelial} = 1.9 \pm 0.84\ kPa, \eta^{KV}_{epithelial} = 0.42 \pm 0.21\ Pa \cdot s, \mu^{KV}_{connective} = 7.9 \pm 3.41\ kPa, \eta^{KV}_{connective} = 0.49 \pm 0.24\ Pa \cdot s, th^{KV}_{epithelial} = 0.51 \pm 0.15\ mm.$

12.4 Discussion

This study is aimed at understanding the torsional wave-tissue interactions, which may determine the optimal rheological model, and the boundary conditions of the numerical models implemented, to finally characterize the viscoelasticity of cervix.

High-speed camera test were carried out to study the slippery conditions between sensor and phantom, as well as the boundary conditions of the numerical models after a video post-processing. The pressures between sensor and phantom ranged from 30 to 150 grams. It was observed that for pressures greater than 60 grams, there was no slippage. A pressure between the sensor and the phantom of 100 grams was chosen, enough to ensure no slippage and so that the compression did not affect the mechanical properties of the phantom. One of the boundary conditions was the speed at grid points of the tissue that were in contact with the PLA receiver. The speed at those points was zero due to the pressure exerted by the torsional wave sensor on the phantom. Another boundary conditions of the numerical model was the excitation. The reconstruction of excitation of the electromechanical sensor was carried out by measuring the displacement of basalt microparticles embedded in the surface of the tissue-mimicking phantom. In Appendix A, it is shown the implemented algorithm employed for the reconstruction of these displacements. According to previous results (Chapter 11), the range of frequencies used was from 300 to 1200 Hz. It was observed how the amplitude of the rotated angle was independent of the stiffness of the phantom. However, the signal amplitude decreased as the excitation frequency increased due to the performance of the electromechanical actuator. A cut-off-frequency of 1000 Hz was selected to infer mechanical properties at a lower scale, also taking into account the attenuation in wave propagation.

Verification tests for numerical dispersion error is a key to avoid instabilities. These tests were preformed in the three FDTD viscoelastic models. For that purpose, the number of elements considered is essential for controlling numerical dispersion. The parameters employed in these simulations consider normal cervical tissue as a medium of propagation. No distinctions between layers have been considered. Besides, the excitation frequency used as a reference for the convergence study was 1000 Hz. In order to analyze the numerical dispersion generated, the root mean square of the received signal for each spatial step size was compared with the root mean square of the received signal for a spatial step size small enough to avoid aliasing effects. Taking into account the frequency spectrum of the received signal (Figure 12.10) and the dispersion effects in the torsional wave propagation due to the

viscoelastic nature of the model employed, the number of spatial intervals per wavelength has to be enough to avoid aliasing effect. To this end, 28 elements per wavelength (excitation frequency 1000 Hz) have been employed, see Figure 12.4.

A Probabilistic Inverse Problem (PIP) was employed for ranking the most plausible model by comparing the *in-vivo* measurements in cervical tissues obtained from the TWE technique with the synthetic signals from the 2D Finite Difference Time Domain (FDTD) wave propagation models (elastic, Kelvin-Voigt and Maxwell models). The results of the ranking of model hypothesis show how the most plausible viscoelastic model is Kelvin-Voigt model, Figure 12.5, involving epithelium shear modulus, epithelium viscosity, epithelium thickness, connective layer shear modulus and connective layer viscosity. It is closely followed by the Maxwell model, whereas the elastic model does not provide relevant information for all proposed signals. The main reason why the elastic model is the least plausible is the number of parameters employed, three parameters versus five of the other two models. According to the evidence found in literature, it is not yet clear which rheological model best describes the response of cervical tissue. Peralta et at. [234] concluded that the Maxwell model is the rheological law that best describes the cervical tissue behavior. By contrast, the study carried out in samples from hysterectomies by Callejas et al. [60], agree with the results found in this work, yielding that the model that best describes the response of the cervical tissue is the Kelvin-Voigt model.

In order to answer the question of how we can know about the values of the KV viscoelastic parameters, the marginal probability density was calculated (Figure 12.8). Considering the intrinsic noise of experimental measurement, the five parameters are successfully estimated (squares with error bars), as well as their reliability. The shape of the distribution function shows discontinuities due to a larger number of reconstructed parameters (5 parameters) versus the number of iterations performed. Despite this, the computational cost of the probabilistic inverse problem was approximately ten days.

In order to analyze the coupling between the reconstructed parameters, 2D contour plots were generated, in which the model parameters were evaluated by moving two and fixing the remaining parameters as the most plausible values. The mean values with standard deviations, that represent the 18 measurements of pregnant women, are: $\mu^{KV}_{epithelial} = 1.9 \pm 0.84\ kPa, \eta^{KV}_{epithelial} = 0.42 \pm 0.21\ Pa \cdot s, \mu^{KV}_{connective} = 7.9 \pm 3.41\ kPa, \eta^{KV}_{connective} = 0.49 \pm 0.24\ Pa \cdot s, th^{KV}_{epithelial} = 0.51 \pm 0.15\ mm$. It can be appreciate the difference in stiffness of the epithelial layer with respect to the connective layer. The result makes sense since the stiffness of the cervical tissue is governed mainly by collagen fibers, the main constituents of the connective layer [49, 50]. The dramatic changes during cervical maturation in collagen fibers of connective tissue is compatible with the high standard deviation of the shear stiffness found, $3.41\ kPa$. It should be taken into account that the results are representative of a set of data of pregnant women with different gestational ages. In contrast, according to the literature, the content of collagen fibers in epithelial tissue is less than 1% [110]. This may be the reason why the standard deviation of the shear stiffness of epithelial

layer is low, 0.84 kPa. To our knowledge, there are no references in the literature about the stiffness of the epithelial layer. Notwithstanding, the inferred values of the stiffness of the connective layer are within the ranges found in literature [198, 33]. It is worth pointing out the viscosity of the epithelial and connective layers. They present similar values in terms of mean and standard deviation, a result that could lead to the reduction of a parameter in the numerical model. The viscous parameters of cervical tissue have scarcely been studied so far in medical diagnosis [51, 52], but the few references present in the literature, none in test in pregnant women *in-vivo*, suggest that viscoelastic properties are particularly sensitive to the gestation process [53, 54, 55, 56, 57, 58]. Finally, the reconstructed value of the epithelial thickness is 0.51 ± 0.15 mm. One of the few studies about the epithelial tissue morphology in pregnant women, carried out by Danforth [112], showed a thickness of the squamous epithelium around $0.45 - 0.5$ mm, while the thickness of the squamocolumnar junction was $0.35 - 0.5$ mm. Therefore, the range of epithelial thickness was in good agreement with the values found in the work mentioned above.

12.5 Conclusions

In this work, the characterization of the viscoelastic parameters in the epithelial and connective layer from torsional waves was studied. A probabilistic inverse problem to obtain the viscoelastic properties of cervical tissue has been employed by comparing the experimental signals in cervical tissue using the Torsional Wave Elastography technique and the synthetic signals from three finite difference time domain numerical models (Elastic, Kelvin-Voigt and Maxwell models). Moreover, it has been concluded that the best rheological model to describe the nature of cervical tissue is Kelvin-Voigt's law. Finally, the Kelvin-Voigt viscoelastic parameters in cervical tissue were inferred and compared with those found in the literature. Future works, motivated by the need for obstetricians to evaluate the viscoelastic mechanical parameter changes during pregnancy, should consider a wider group of pregnant women.

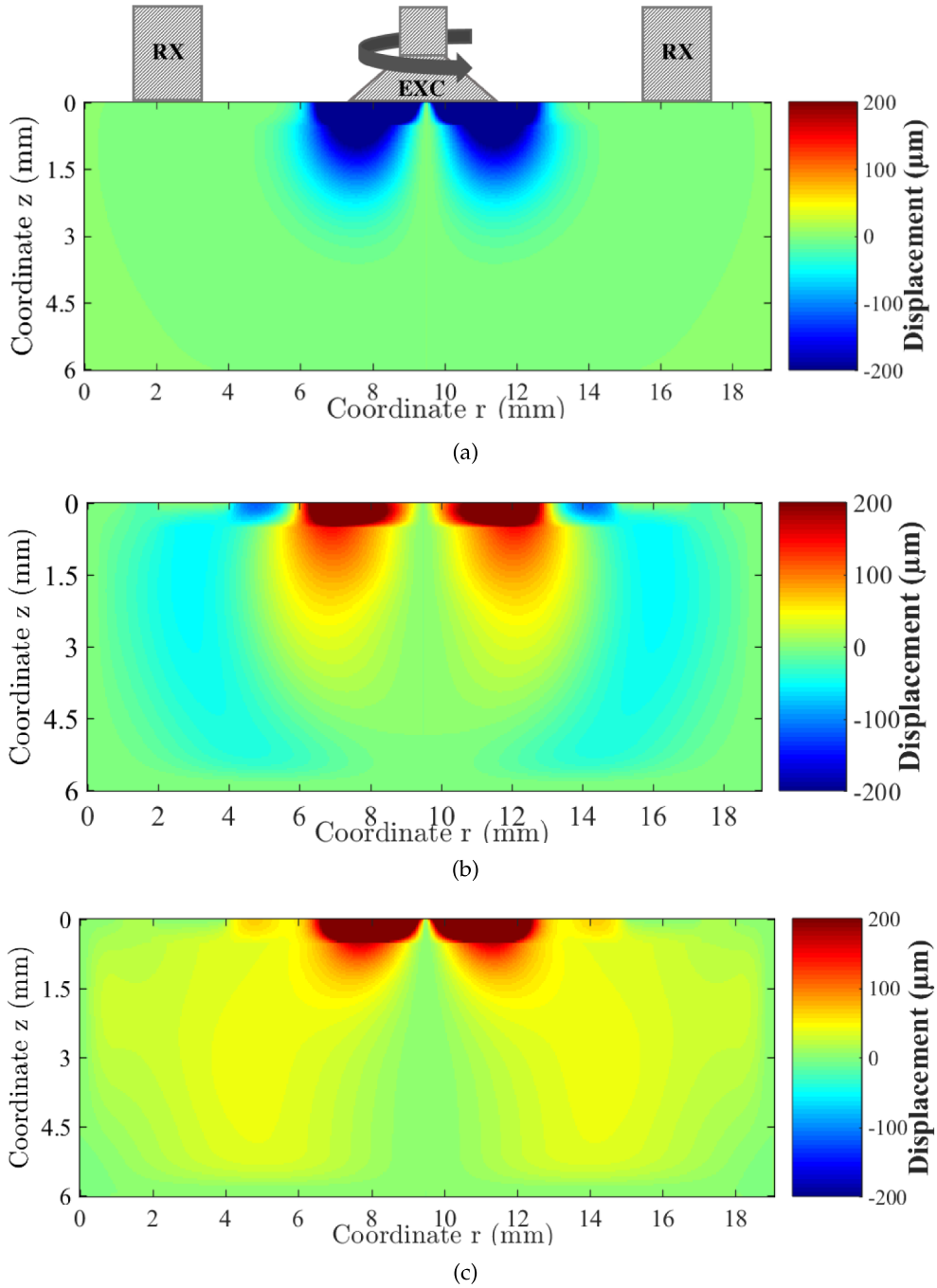

Figure 12.7: 2D FDTD model simulations for different time steps using the Kelvin-Voigt model and the most plausible KV parameters computed. (**a**) 0.9 milliseconds; (**b**) 1.9 milliseconds; (**c**) 3 milliseconds.

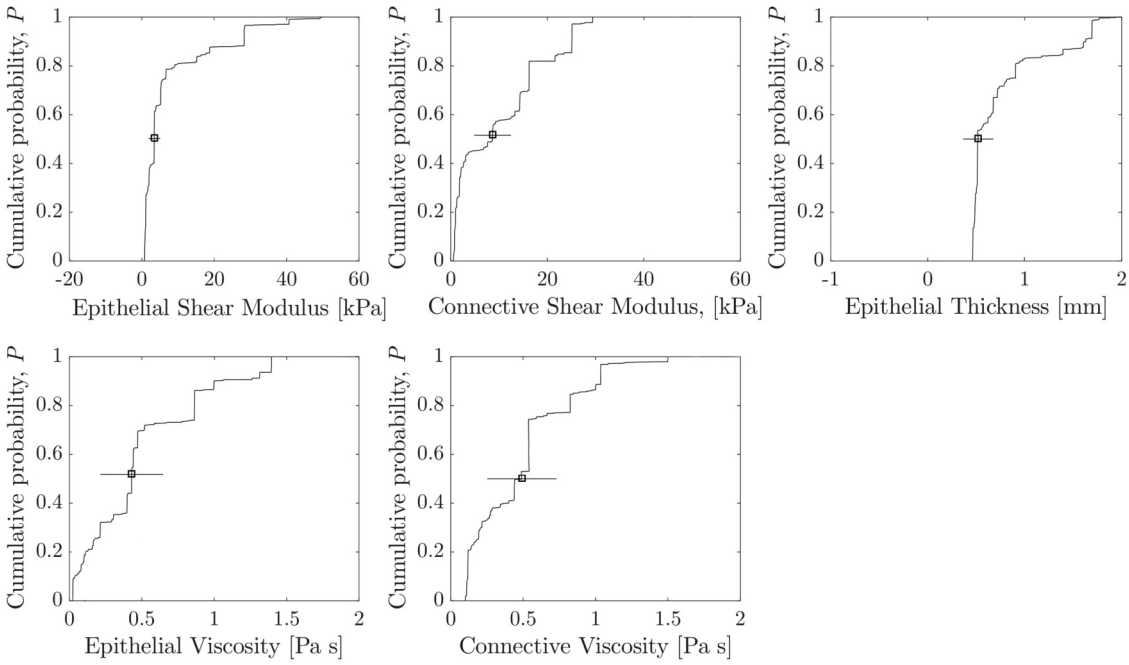

Figure 12.8: Marginal plausibility maps of model parameters using the Kelvin-Voigt model. The expected values ($p = 50\%$) are marked, as well as their standard deviation bars.

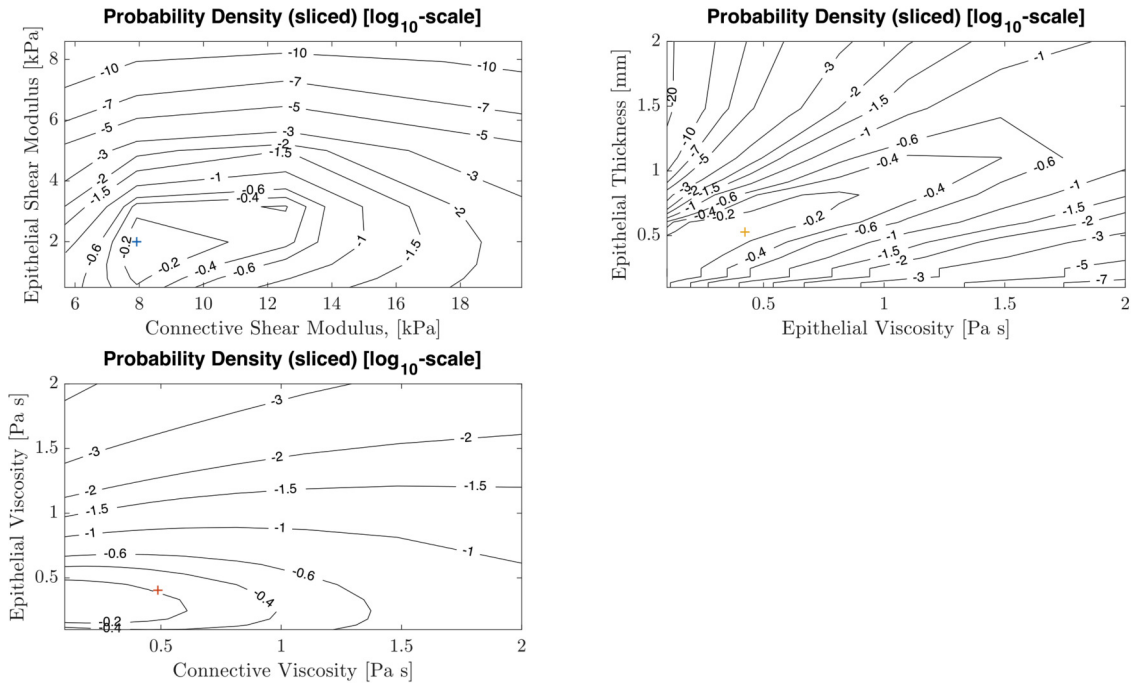

Figure 12.9: Plausibility maps of Kelvin-Voigt parameters. Epithelium shear modulus versus connective shear modulus (**top left**). Epithelium thickness versus epithelium viscosity (**top right**). Epithelium viscosity versus connective viscosity (**down left**). The crosses represent the optimal parameters.

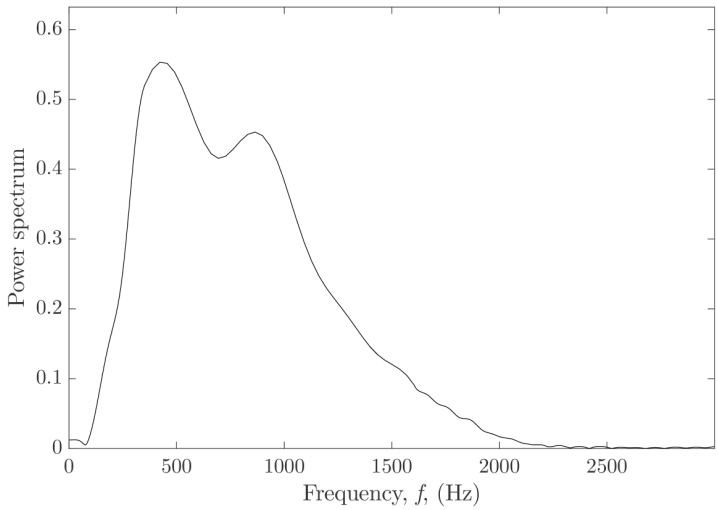

Figure 12.10: A discrete Fourier analysis of the received signal for a 1000 Hz excitation signal.

13

Validation of the KV reconstruction parameters method in cervical tissue-mimicking phantoms

This chapter aims at testing the validation of a new method to reconstruct Kelvin-Voigt viscoelastic parameters of cervical tissue-mimicking phantoms by Torsional Wave Elastography technique [1].

Section 13.1 outlines the results of the reconstruction of KV parameters from SWE measurements. In Section 13.2, the procedure to infer the KV parameters from TWE through a PIP procedure is shown. Section 13.3 presents the comparison between the results obtained with TWE and SWE by a Student's T-test and a Pearson's correlation study. Finally, we discuss the feasibility of the new method for the reconstruction of the KV viscoelastic parameters in Section 13.4.

13.1 KV parameters reconstruction from SWE measurements

An illustrative example showing a sequence of shear wave displacement images generated by ARFI for 15% gelatine and 10% oil batch is shown in Figure 13.1.

Experimental particle displacement versus time profiles at the focal depth resulting from the ARFI excitation for 15% gelatine and 10% oil batch is observed in Figure 13.2. Each displacement trace indicates a lateral position starting from zero to 24 lateral positions.

Shear wave speeds (dots), obtained after analyzing the data of Verasonics (see Section 8.2.2), as a function of frequency are depicted in Figure 13.3. The range of frequencies for

[1] Contribution: A. Callejas, A. Gomez, I. H. Faris, J. Melchor and G. Rus. Kelvin-Voigt parameters reconstruction of cervical tissue-mimicking phantoms using torsional wave elastography. *Sensors*, 19(15), 2019.

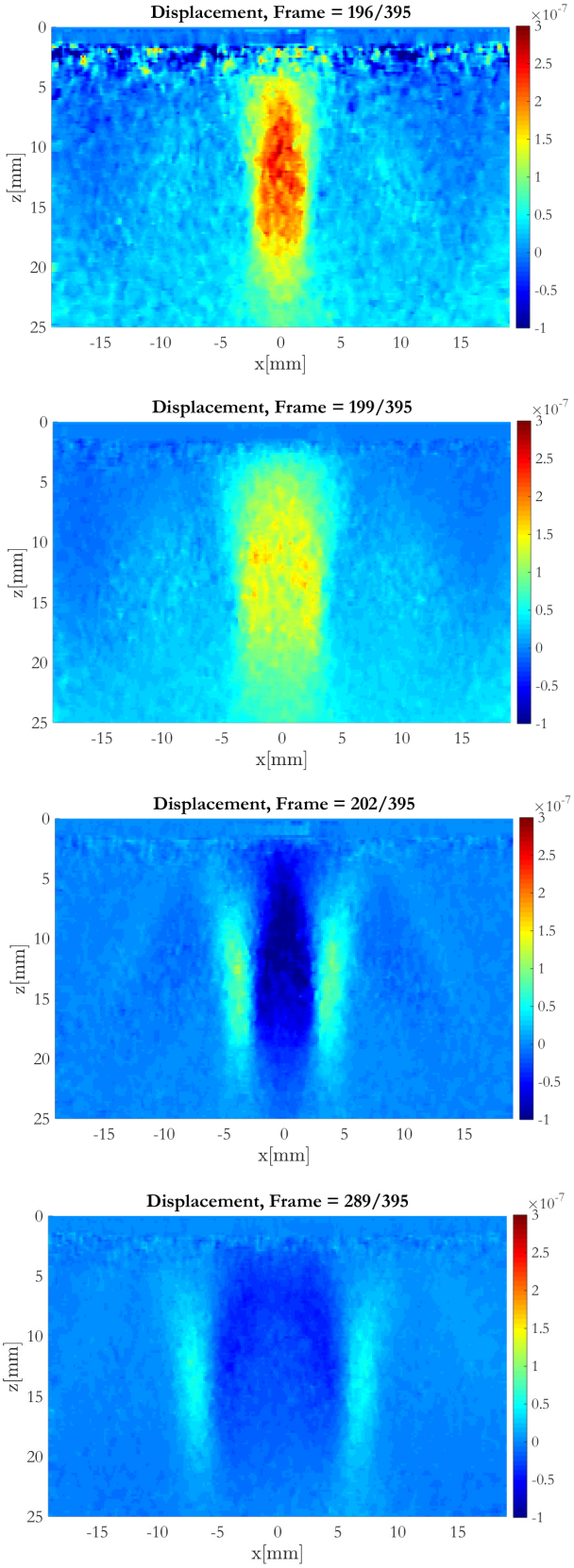

Figure 13.1: Sequence of displacement map (displacements are in meters) for the batch 15% gelatine 10% oil due to ARFI excitation. The box represents the ROI chosen.

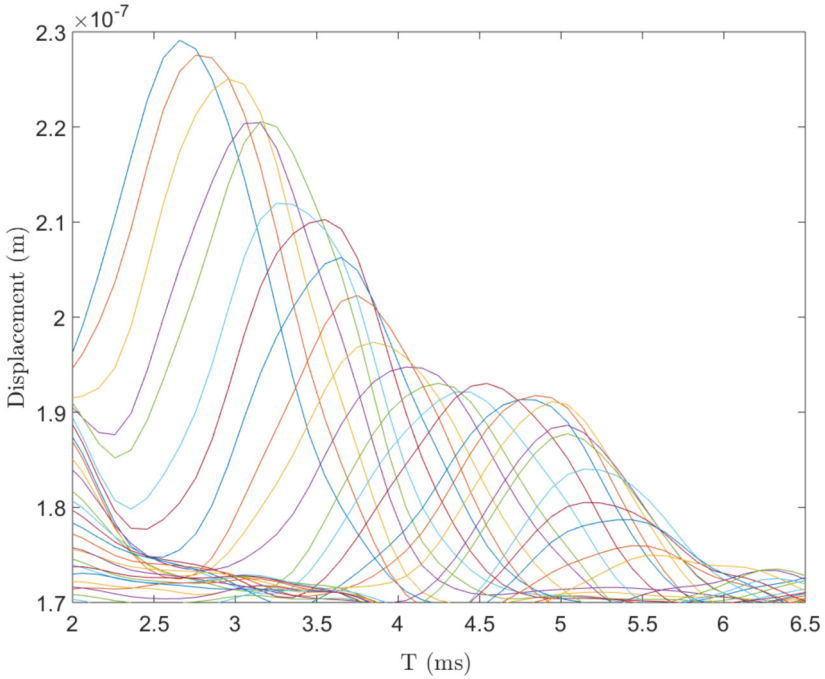

Figure 13.2: Experimental particle displacement (in meters) versus time (in milliseconds) profiles at the focal depth resulting from the ARFI excitation for 15% gelatine and 10% oil batch. Each displacement trace indicates a lateral position starting from zero to 24 lateral positions.

each of the plots was selected according to the distribution of power into frequency components composing the shear wave signals (see Figure 13.4). The solid black lines are the optimal fits from the KV model for each single-layer phantom and the dashed lines are 95% confidence intervals. The KV parameters for each fitted curve are shown in Table 13.2. Mean and standard deviation values were estimated from three independent measurements with the SWE technique.

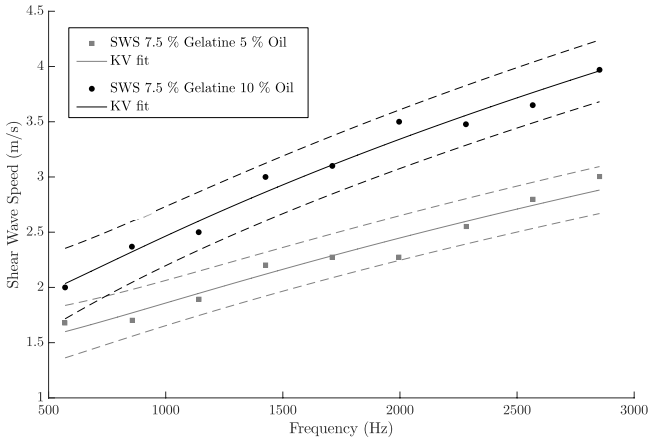

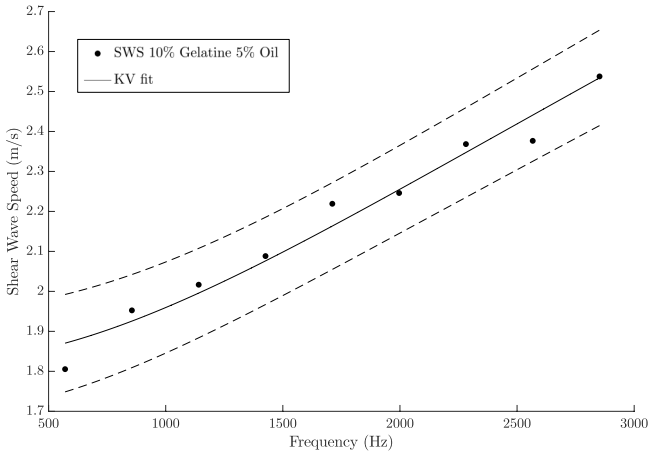

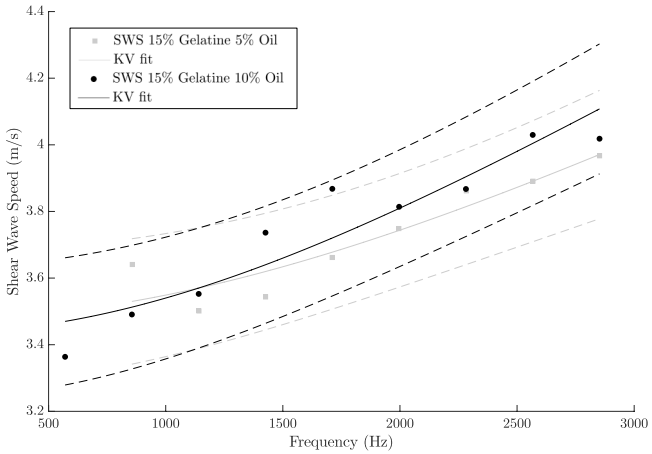

Figure 13.3: Dispersion curve for each batch of gelatine (shear wave speed data points acquired from Verasonics). The curves for Kelvin-Voigt model (solid black lines) and 95% confidence intervals (dashed lines) are shown.

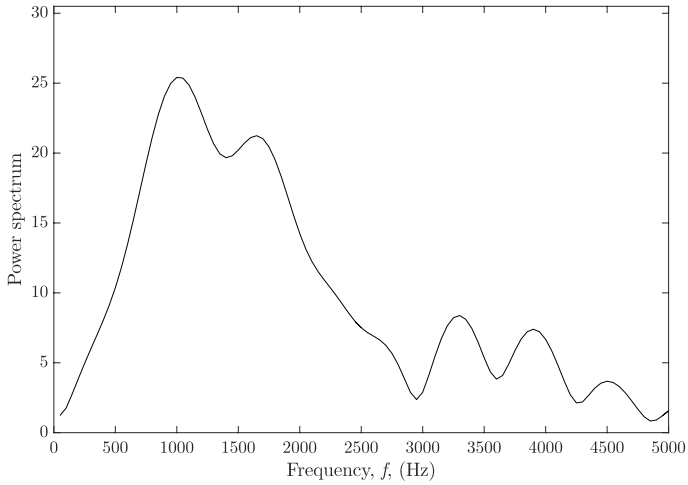

Figure 13.4: Power spectrum of the shear wave tracked for 7.5% Gelatine and 10% oil batch (data acquired from Verasonics).

13.2 KV parameters reconstruction from TWE measurements

After performing the probabilistic inverse problem that mainly consists of comparing the experimental signals (acquired from TWE measurements) with those obtained from the FDTD KV model (section 8.4), the inferred parameters are presented in Table 13.1. Shear elasticity, shear viscosity and the thickness of the first layer were reconstructed after solving the PIP. Mean and standard deviations values were calculated from the three independent measurements made in each specimen. Examples of the fit of experimental and simulated signals for phantoms 1 and 5 are shown in Figure 13.5.

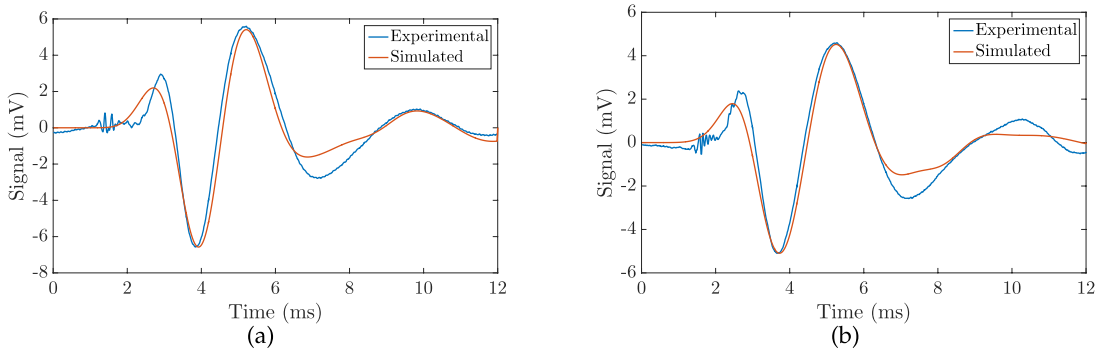

Figure 13.5: Examples of the fit of the experimental and simulated signals: Kelvin-Voigt model, time domain. a) Phantom 1; b) Phantom 5.

Phantoms	Layer	$\mu(kPa)$	$\eta(Pa \cdot s)$	Th (mm)
1	First layer	1.14 ± 0.15	0.20 ± 0.03	1.00 ± 0.12
	Second layer	6.31 ± 0.62		-
2	First layer	1.43 ± 0.17	0.22 ± 0.02	0.79 ± 0.11
	Second layer	6.02 ± 0.55		-
3	First layer	0.72 ± 0.045	0.19 ± 0.05	1.15 ± 0.38
	Second layer	2.12 ± 0.52		-
4	First layer	1.17 ± 0.10	0.30 ± 0.04	0.87 ± 0.19
	Second layer	6.52 ± 0.54		-
5	First layer	0.91 ± 0.16	0.20 ± 0.04	0.56 ± 0.23
	Second layer	6.79 ± 0.57		-

Table 13.1: Kelvin Voigt parameters reconstruction from TWE. Data from the first and second layer is shown (shear elasticity and shear viscosity), including the thickness of the first layer for each of the five phantoms.

13.3 Validation of the Kelvin-Voigt parameters reconstruction method

The following table (Table 13.2) summarizes the values obtained with TWE and SWE for each batch of gelatine. The mean and standard deviation of the shear elasticity and shear viscosity are shown.

	TWE		**SWE**	
	$\mu \pm std$ (kPa)	$\eta \pm std$ (Pa · s)	$\mu \pm std$ (kPa)	$\eta \pm std$ (Pa · s)
7.5% Gelatine 5% Oi	0.923 ± 0.11	0.196 ± 0.04	0.993 ± 0.31	0.224 ± 0.02
7.5% Gelatine 10% Oil	1.17 ± 0.10	0.30 ± 0.04	1.494 ± 0.42	0.420 ± 0.08
10% Gelatine 5% Oil	1.77 ± 0.34	0.20 ± 0.03	1.673 ± 0.23	0.150 ± 0.03
15% Gelatine 5% Oil	6.37 ± 0.58	0.21 ± 0.03	6.111 ± 0.30	0.269 ± 0.04
15% Gelatine 10% Oil	6.52 ± 0.54	0.30 ± 0.04	6.249 ± 0.41	0.369 ± 0.05

Table 13.2: Kelvin Voigt parameters from TWE versus Verasonics for each batch of gelatine.

In order to study the degree of agreement between the reconstructed KV viscoelastic parameters with TWE and SWE, a Student's T-test and a Pearson's correlation study were carried out. Overall, the T-test yielded values higher than 0.05, which indicates that the sets of values reconstructed by both techniques are not significantly different (see Table 13.3). The Pearson's correlation studied showed a high degree of agreement between the shear stiffness values obtained from both techniques (see Figure 13.6), with a Pearson value of $r = 0.9942$. In the case of the shear viscosity, the degree of agreement was lower (see Figure 13.7), with a Pearson value of $r = 0.8913$.

	p-value	
Batch	μ	η
7.5% Gelatine 5% Oil	0.365	0.1640
7.5% Gelatine 10% Oil	0.134	0.041*
10% Gelatine 5% Oil	0.262	0.0551
15% Gelatine 5% Oil	0.274	0.0553
15% Gelatine 10% Oil	0.263	0.067

Table 13.3: Shear elasticity and shear viscosity measurements comparison between TWE and SWE for each batch of gelatine. P-value obtained from the Student's T-test was the metric used for this comparison. (* $p - value < 0.05$).

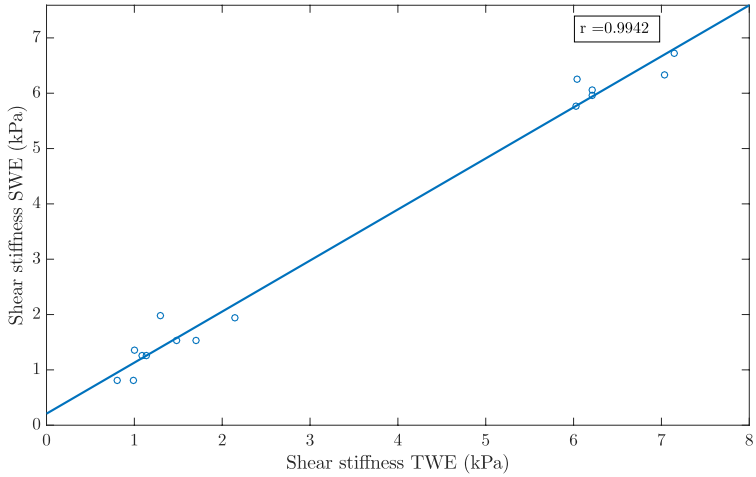

Figure 13.6: Pearson's correlation between shear stiffness measured with TWE and shear stiffness obtained with SWE. Pearson correlation coefficient $r = 0.9942$.

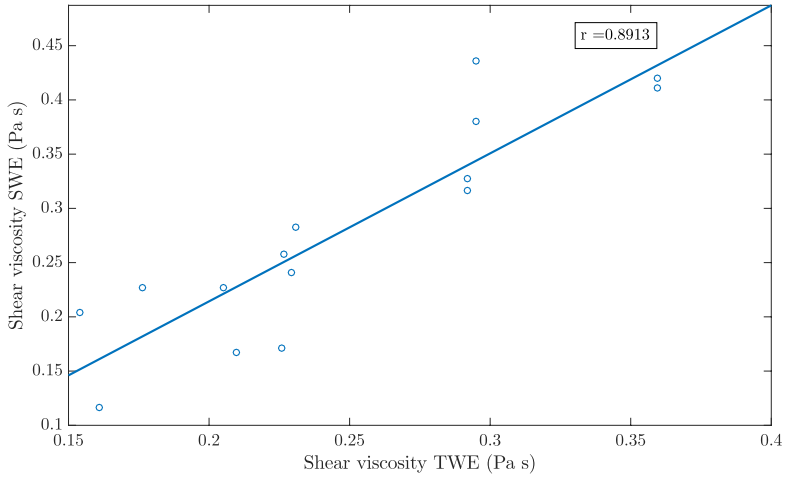

Figure 13.7: Pearson's correlation between shear viscosity measured with TWE and shear viscosity obtained with SWE. Pearson correlation coefficient $r = 0.8913$.

Figures 13.8 and 13.9 show the mean and standard values of shear elasticity and shear viscosity respectively for each batch of gelatine and elastography technique.

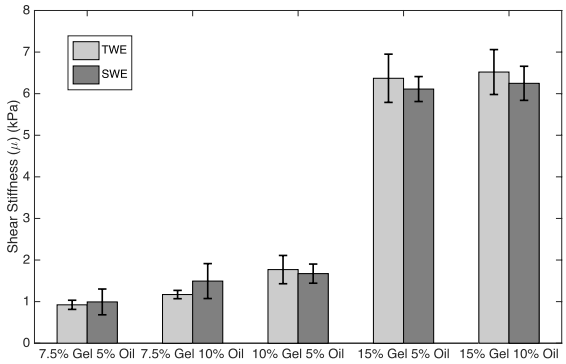

Figure 13.8: Mean and standard deviations of the shear elasticity for each batch of gelatine. Light gray bars represent TWE measurements whilst those in dark gray show SWE measurements.

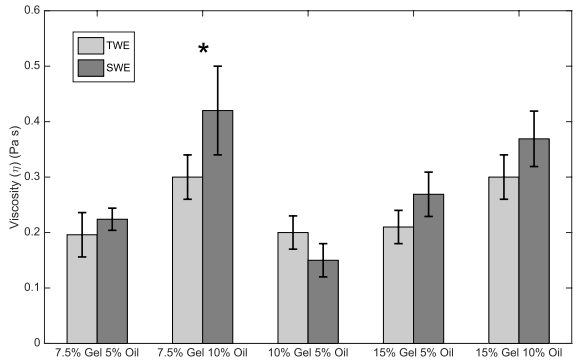

Figure 13.9: Mean and standard deviations of the shear viscosity for each batch of gelatine. Light gray bars represent TWE measurements whilst those in dark gray are SWE measurements (* $p - value < 0.05$).

13.4 Discussion

The main purpose of this study is to propose and experimentally validate the results of a new method for the reconstruction of the viscoelastic parameters of cervical tissue-mimicking phantoms by the TWE technique. The TWE technique, developed by our group, aims to locally measure the mechanical parameters of the cervix, so they can be correlated with the different stages of the cervix maturing during pregnancy [60]. The previously developed reconstruction approach used is based on a TOF procedure. This approach does not take into account the fact that the waves detected on the cervix surface are altered by the mechanical response of both the epithelial and connective tissue layers of the cervix. In fact, the provided reconstructed parameter is the apparent shear wave speed measured at the surface of the cervix, which is linked to the combined mechanical response of the two tissue layers in an unknown manner. The presented reconstruction approach is based on a PIP procedure, which uses a forward model of the propagation of torsional waves in a bilayer axisymmetric cervix-like medium (see Figure 8.6), numerically solved by a self-developed FDTD algorithm. This way to solve the inverse problem provides the thickness of the epithelial layer, thus reconstructing separately the shear elastic modulus and the shear viscosity of each cervical layer. Furthermore, the probabilistic framework has been employed rather than the deterministic one to solve the limitations of noise in the measurements performed, heterogeneity in the properties of the sample, and even the fact that the model used to simulate its behavior is an approximation of reality.

The mechanical behavior of the cervix is viscoelastic, as most of the soft biological tissue. A viscoelastic KV constitutive law was implemented into the wave propagation model, as the KV model was found to be the simplest model in terms of a number of parameters that provides the best approximation to the mechanical behavior of *ex vivo* cervical tissue in our previous characterization study [60].

Five *ad hoc* oil-in-gelatine phantoms were fabricated to test the new reconstruction technique. The phantoms were composed of two layers to resemble the epithelial and connective

cervical structure, labeled as first and second layers, respectively (see Figure 8.2). Different proportion of gelatine and oil were used for fabricating each layer and each phantom, so that different viscoelastic parameters where achieved (see Table 8.2).

The resulting viscoelastic parameters of each layer, i.e., the shear elastic modulus and the shear viscosity, fell within the range of values observed in the literature. In this study, the range obtained for the shear elasticity reconstructed parameter for the second layer (connective layer) is within the range of values estimated by Carlson et al. [44] (4.45-12.67 kPa). As far as shear viscosity in the same layer is concerned, the range obtained in this study is also in good agreement with the value found in the work performed by Peralta et al. [234] (0.26 Pa $\cdot$ s). To our knowledge, there are no references regarding shear elasticity and shear viscosity in the epithelial layer.

Two thickness values for the first layer were selected, 0.5 and 1 mm, which is in concordance with the values observed in the study performed by Patton et al. [6]. The thickness of the second layer was kept at 15 mm, shorter than the values found for the connective tissue layer in the literature, and sufficiently large to fully attenuate reflections from the bottom side of the phantom. Reconstructed values using the TWE technique in conjunction with the PIP approach are shown in Table 13.1. It can be claimed, without not much mistake, that the thickness of each phantom was satisfactorily reconstructed. Inferred thickness values were very close to the expected ones, keeping the error of reconstruction below 21%, and the standard deviation between 0.11 and 0.38 mm.

Characterization of the different oil-in-gelatine batches was needed in order to analyze the quality of the reconstruction of the viscoelastic parameters. This characterization was carried out by a well-established technique, such SWE, in this case, performed by a Verasonics system. Homogeneous phantoms were fabricated from the same oil-in-gelatine batches used before for producing the cervix-like phantoms. The propagation of the shear waves generated by the ARF yielded a shear wave dispersion speed curve for a broad range of frequency, with maximum energy between 500 and 3000 Hz (see Figure 13.4). This range of frequency was in agreement with the experimental SWE study in *ex vivo* porcine cornea [282]. As concluded by the authors, tissue targets with direct contact, such as the case of the *ex vivo* porcine cornea study, allow a higher range of frequency when using SWE ARF-based applications, compared to deep organs, such as breast, liver or prostate [282]. Oil-in-gelatine mixtures with the lower proportion of gelatine, 7.5%, and the higher proportion of oil, 10%, showed higher dispersion, i.e. steeper shear wave speed curves. Moreover, the 95% confidence intervals in this curve were also wider compared with the rest of the curves, around ± 0.45 m/s against ± 0.2 m/s averaged for the rest of the curves. On the contrary, mixtures with the higher proportion of gelatine, 15%, and the lower proportion of oil, 5%, showed less dispersion with a flatter variation of values in the shear wave curves. The value of the viscoelastic parameters of the different oil-in-gelatine mixtures was extracted by fitting the theoretical expression of the shear wave speed according to the KV model (a combination of Equations 8.2 and 8.9) to the values obtained in the SWE tests (see Table 13.2). A direct

comparison between the values obtained by both the TWE and the SWE techniques is also shown in Table 13.2.

The reconstruction of the viscoelastic parameters by using the TWE technique with the new proposed inversion method was validated against the SWE technique by using two approaches, a Student's T-test and a Pearson's correlation study. T-test results were shown in Table 13.3, in terms of the p-value for the shear elasticity and the shear viscosity from each oil-in-gelatine batch. Most of the p-values obtained were above 0.05, which can be considered to represent a not significant difference between the parameters reconstructed by the two techniques. Only the shear viscosity for the batch containing 7.5% of gelatine and 10% oil showed a lower p-value of 0.042. Nevertheless, the reconstruction of this parameter by the SWE also showed the higher range of variability, i.e. the higher standard deviation. The explanation for this low p-value can be associated to both the high dispersion effect of this oil-in-gelatine batch and the higher variability in the SWE measurements. Further tests should be carried out in high dispersive oil-in-gelatine phantoms in order to clarify the origin of the low correlation value.

Results from the Pearson's correlation study were shown in Figures 13.6 and 13.7, for the reconstruction of the shear stiffness and the shear viscosity parameters, respectively. As can be observed in the Figures 13.6 and 13.7, the correlation between results from both techniques, the TWE and the SWE were high, specially for the shear stiffness, which yielded a Pearson's correlation coefficient $r = 0.9942$. The Pearson's correlation coefficient for the shear viscosity was lower, with $r = 0.8913$. This may be due to the larger effect that shear elastic modulus has on the torsional wave received compared to that produced by the shear viscosity. Furthermore, the reconstructions were more similar, for both the shear elasticity and shear viscosity when excluding the most dispersive batch (that made of 7.5% gelatine and 10% oil).

In general, by the obtained results from the T-test and the Pearson's correlation study, it can be concluded that the viscoelastic parameters reconstructed by the TWE technique in conjunction with the new inversion approach are similar to those provided by the SWE technique. Therefore, it can be concluded that this new inversion method is validated for its use in the TWE technique. In order to study the performance of the new inversion method in a scenario closer to the final medical application, future work must be carried out on experimental studies using *ex vivo* cervical tissue samples.

13.5 Conclusions

In this work, the results of a new method based on a Probabilistic Inverse Problem (PIP) for the reconstruction of the viscoelastic parameters of cervical tissue-mimicking phantoms by the TWE technique were presented and experimentally validated. Five *ad-hoc* oil-in-gelatine phantoms were fabricated with different gelatine batches, simulating the anatomy of the cervical tissue composed mainly by the epithelial and connective layer, to test the new reconstruction technique. On the one hand, a probabilistic approach was employed

that reconstruct the KV viscoelastic parameters by comparing the results obtained from TWE technique with the synthetic signals from the FDTD KV model. On the other hand, the characterization for each batch of gelatines was performed by SWE measurements. The validation of the method was carried out by comparing the KV parameters reconstructed from the PIP with those inferred from the shear wave speed curve obtained with SWE measurements. Finally, the degree of agreement between both techniques was tested using a Student's T-test and a Pearson's correlation study. As a conclusion, it can be confirmed that the viscoelastic parameters reconstructed by the TWE technique in conjunction with the PIP approach were in good agreement with those obtained by SWE technique. Future research lines must be carried out on experimental studies using *ex vivo* cervical tissue samples in order to test the performance of the new method.

14

Hyperelastic ex-vivo cervical tissue mechanical characterization

This chapter presents the results of the comparison between a proposed nonlinear model and the two most contrasted models in the literature, Mooney-Rivlin and Odgen models. To achieve this goal, the experimental data of an uniaxial tensile test in *ex-vivo* cervical tissue samples were fitted with the aforementioned hyperelastic models. The final aim of this chapter is to validate the previous reconstructed mechanical properties of epithelial and connective layer of cervical tissue by PIP procedure (Chapter 12).

Section 14.1 shows the results of the fits of the experimental data with the three hyperelastic models. In Section 14.2, the validation of the previous inferred mechanical properties in epithelial and connective layers is presented. Finally, in Section 14.3, the main findings of this study are discussed.

14.1 Comparison between hyperelastic models

The experimental data of the uniaxial tensile tests for each of the cervical tissue samples are represented as stress-strain curves (Figure 14.1). In these curves it can be appreciated the three zones that are explained in Figure 14.3: nonlinear, quasi-linear and rupture. The results of the fits of the experimental data with the three hyperelastic models are shown in Tables 14.1, 14.2 and 14.3. These fitted curves were performed with MATLAB ® (Release 2018b, MathWorks, Natick, United States) Curve Fitting Toolbox. The metric used to see the goodness of fit was the R^2 coefficient, defined as the ratio of the sum of squares of the regression (SSR) and the total sum of squares (SST).

$$R^2 = \frac{SSR}{SST} \tag{14.1}$$

An illustrative example of the comparison of the hyperelastic theoretical models with the experimental results obtained from connective layer of Cervix 2 is showed in Figure 14.2.

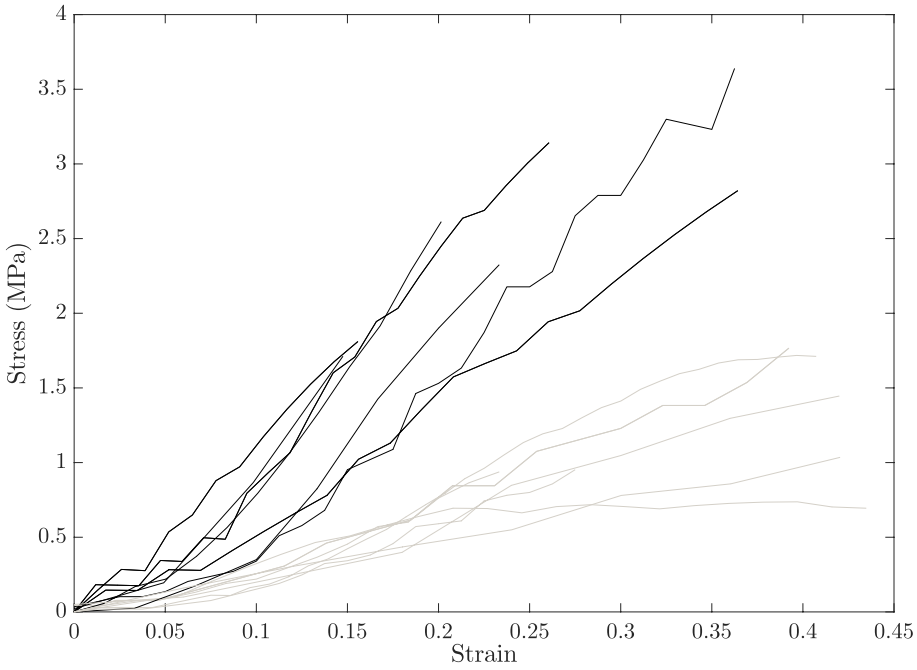

Figure 14.1: Experimental stress-strain relationship for cervical samples tested under uniaxial tensile test. Solid black and gray lines represent the connective and epithelial layer respectively.

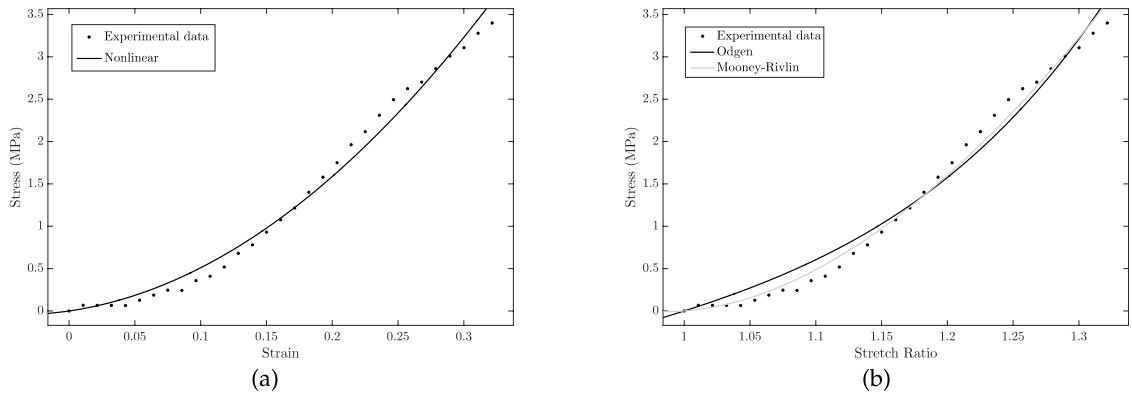

Figure 14.2: Comparison of the hyperelastic theoretical models with the experimental results obtained from the connective layer of Cervix 2. (**a**) The proposed nonlinear Fourth Order Elastic Constant (FOEC) nonlinear model; (**b**) Mooney-Rivlin and Odgen models.

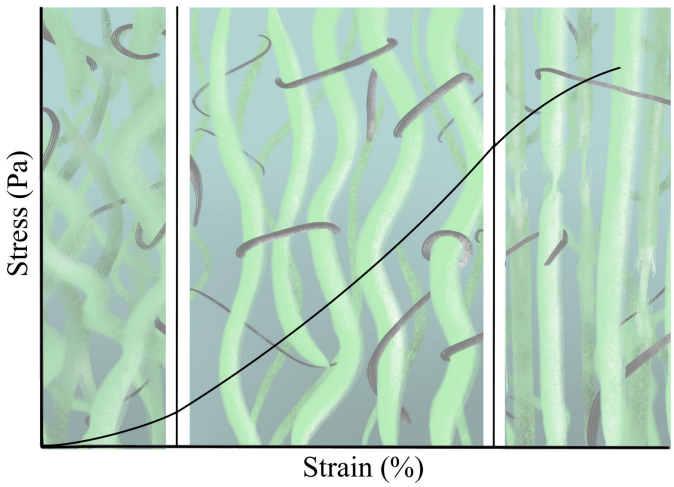

Figure 14.3: Representation of stress-strain behavior of soft tissues. The curve is divided into three zones: nonlinear, quasi-linear and rupture. The state of elastin (black color) and collagen (green color) is represented at the bottom of each zone.

	Nonlinear Model					
	Epithelial Layer			**Connective Layer**		
Cervix	μ	A	R^2	μ	A	R^2
1	1.13	22.6	0.989	3.58	3.49	0.987
2	1.22	-6.08	0.995	4.72	-7.63	0.994
3	1.35	-3.06	0.986	2.64	-5.92	0.993
4	1.57	28.3	0.994	3.30	27.6	0.997
5	1.35	-2.35	0.990	3.51	73.6	0.995
6	1.13	2.32	0.976	3.49	70.1	0.988
7	1.27	30.72	0.990	3.96	25.7	0.986

Table 14.1: Results of the fits of experimental data with the proposed nonlinear model. Shear modulus μ and TOEC A in MPa.

	Odgen Model					
	Epithelial Layer			**Connective Layer**		
Cervix	μ_r	α_r	R^2	μ_r	α_r	R^2
1	0.41	7.94	0.979	0.941	6.01	0.984
2	1.01	1.62	0.995	1.16	5.63	0.994
3	0.42	4.54	0.985	0.97	4.13	0.992
4	0.35	9.94	0.992	0.85	11.1	0.991
5	0.47	4.31	0.988	0.82	10.25	0.989
6	0.39	5.27	0.977	0.57	11.54	0.974
7	0.40	9.05	0.982	1.29	6.40	0.979

Table 14.2: Results of the fits of the experimental data with the Odgen model. The infinitesimal shear modulus μ_r in MPa

	Mooney-Rivlin Model					
	Epithelial Layer			Connective Layer		
Cervix	c_1	c_2	R^2	c_1	c_2	R^2
1	6.93	-6.73	0.991	5.87	-4.77	0.988
2	0.33	-0.08	0.995	4.7	-3.15	0.994
3	1.22	-0.78	0.986	2.51	-1.68	0.994
4	8.25	-7.84	0.994	59.9	-59.3	0.997
5	1.47	-1.05	0.990	20.56	-19.67	0.996
6	2.35	-2.06	0.976	15.7	-15.9	0.990
7	8.69	-8.44	0.992	12.1	-11.1	0.988

Table 14.3: Results of the fits of the experimental data with the Mooney-Rivlin model.

14.2 Shear modulus estimation

The shear modulus can be obtained directly by means of the μ parameter of the FOEC proposed model, through the slope of the stress-strain curve in the linear region or also trough a combination of the two parameters of the Odgen model, the infinitesimal shear modulus μ_r and the stiffening parameter α_r (see Equation 9.5). Table 14.4 shows the values of the shear modulus for each hyperelastic model and for each sample. The mean and standard deviations values of the Young's modulus obtained from the slope of the stress-strain curve for the epithelial and connective layer are presented in the bar graph of Figure 14.4.

	Shear Modulus					
	Epithelial Layer			Connective Layer		
Cervix	**Nonlinear**	**Odgen**	**Curve**	**Nonlinear**	**Odgen**	**Curve**
1	1.13	1.65	0.82	3.58	2.83	4.17
2	1.22	0.82	0.69	4.72	3.28	3.78
3	1.35	0.95	1.43	2.64	2.01	3.62
4	1.57	1.77	1.82	3.30	4.71	3.26
5	1.35	1.02	0.44	3.51	4.22	5.25
6	1.13	1.03	0.90	3.49	3.30	4.42
7	1.27	1.84	1.08	3.96	4.15	3.17
Mean $\pm$ Std	1.29 ± 0.15	1.30 ± 0.43	1.02 ± 0.46	3.60 ± 0.63	3.50 ± 0.92	3.95 ± 0.72

Table 14.4: Shear modulus estimation for the proposed nonlinear model, Odgen model and the slope of the linear region of the stress-strain curve. Mean and standard deviation of the values for the seven samples are presented in MPa.

In order to study the degree of agreement between the obtained shear modulus with the nonlinear model, Odgen model and the slope of the curve stress-strain for each cervical layer, a Student's T-test was used (see Table 14.5).

	Epithelial Layer			Connective Layer		
	Nonlinear	**Odgen**	**Curve**	**Nonlinear**	**Odgen**	**Curve**
Nonlinear	-	0.477	0.08	-	0.408	0.176
Odgen	0.477	-	0.131	0.408	-	0.164
Curve	0.08	0.131	-	0.176	0.164	-

Table 14.5: Comparison of shear modulus extracted from the proposed nonlinear model, Odgen model and the slope of the stress-strain curve for each cervical layer. P-value obtained from the Student's T-test was the metric used for this comparison.

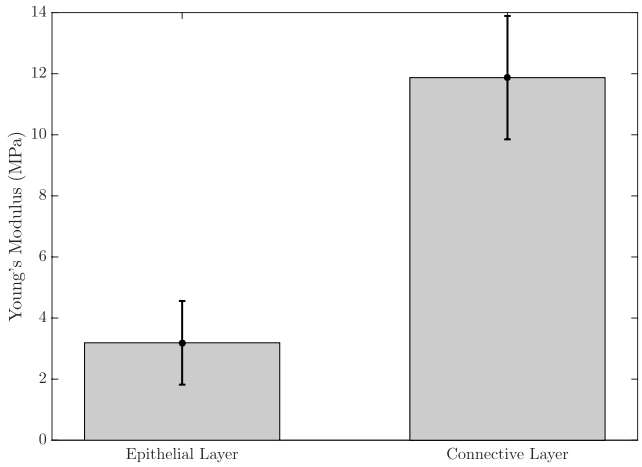

Figure 14.4: Comparison between Young's modulus of epithelial and connective layer. The results are presented as mean $\pm$ standard deviation.

14.3 Discussion

According to the evidences found in literature, Myers et al. [93] investigated the nonlinear time-dependent stress response of cervical samples from different human hysterectomy specimens. Results showed the nonlinear response of cervical stroma, which was dependent on obstetric history. However, to our knowledge, there is no study in the literature that has investigated nonlinear parameters in cervical tissue.

This work aims at representing a first step toward a nonlinear characterization of human cervical tissue. The nonlinear elastic properties of *ex-vivo* cervical tissue have been obtained for the first time by uniaxial tensile tests.

There is a challenge among researchers for employing a strain energy density which can represent the nonlinear behavior of soft tissues and have the least number of parameters to be as simple as possible mathematically. The simplicity of the proposed model in conjunction with a good correlation with the experimental data can be presented as an accurate and simple model in computational solid mechanics field.

The first contribution of this study is to propose a new hyperelastic model (nonlinear model) based on the Fourth Order Elastic Constants in the sense of Landau's theory [283]

and compare the obtained results with the most used hyperelastic models in the literature, Mooney-Rivlin and Odgen models [213, 215].

As a second contribution, a validation of the previous reconstructed mechanical properties of epithelial and connective cervical tissue by PIP procedure (Chapter 12) is presented. The TWE technique proposed in this dissertation aims to locally measure the mechanical parameters of the cervix that can be correlated with the different stages of the cervix maturing during pregnancy [60]. Bilayer viscoelastic models for the reconstruction of these properties are based on the propagation of torsional waves along the tissue, numerically solved by a self-developed FDTD algorithm (Chapter 7). These waves interact not only with the superficial layer, the epithelial layer, but also with the deeper layers, i.e., connective layer. Therefore, a validation of the mechanical parameters reconstructed in both layers is necessary through uniaxial tensile tests of *ex-vivo* samples from hysterectomies of healthy women.

The mechanical behavior of the cervix is nonlinear, as most of the soft biological tissues. The nonlinear parameters of the FOEC proposed model were obtained through a fit of the experimental data measured in the uniaxial tensile tests with the theoretical law that governs the hyperelastic model. The same procedure was carried out in order to get the nonlinear parameters from the two most employed hyperelastic models to characterize soft biological tissue in the literature, Mooney-Rivlin and Odgen models. In order to compare the three models, the R^2 coefficient was obtained to analyze the goodness of each of the fits performed. The resulting R^2 coefficient calculated show that the models analyzed adjusted the experimental data successfully. Specifically, the proposed FOEC model is appropriate to model cervical tissue in tension for the strain ramp rate considered, $1\%/s$ [273].

The proposed FOEC hyperelastic model, Equation 9.1, presents three parameters, the shear modulus μ, the third order elastic constant A and the fourth order elastic constant D. In this study, the proposed theoretical stress-strain relationship has been simplified with the aim of comparing with the two-term Mooney-Rivlin and Odgen models. The two parameters that have adjusted the experimental data were the shear modulus μ and the third order elastic constant A. Analyzing the results of the shear modulus, there was no significant variation in both, the epithelial $1.29 \pm 0.15 MPa$ and the connective layer $3.60 \pm 0.63 MPa$ for each of the hysterectomy samples, see Table 14.4. The values of the shear stiffness are highly dependent of the strain ramp rate used, the larger strain rate, the larger shear modulus [284, 285]. The obtained values for cervical tissue agree with those found in literature [1, 93]. However, regarding the nonlinear parameter A, large variation was observed, varying the parameter from positive to negative values (see Table 14.1). It is worth pointing out that, to our knowledge, this is the first work that studies the nonlinear parameters of the FOEC hyperelastic model in cervical tissue. The variability found in the third elastic constant parameter A could be associated with the heterogeneity of the tissue [201].

The shear modulus is one of the most used parameters in the characterization of soft biological tissues by various techniques. This value can be extracted directly by means of

the μ parameter of the FOEC proposed model, through the slope of the stress-strain curve in the linear region or also through a combination of the two parameters of the Odgen model, the infinitesimal shear modulus μ_r and the stiffening parameter α_r. The values of the shear modulus for each reconstruction technique and for each sample are shown in Table 14.4. The parameters that govern the Mooney-Rivlin model have no physical sense and, therefore, it can not be extracted the shear modulus from them. The results of the shear modulus for each reconstruction technique and for each cervical layer were compared by using a Student's T-test. T-test results are shown in Table 14.5, in terms of p-values. All of these values were above 0.05, which can be considered to represent a not significant difference between the shear modulus obtained by the three models in the epithelial and connective layers. The shear modulus was dependent on anatomical location of the cervical tissue as shown in Table 14.4. Variations of the same order of magnitude were obtained after the reconstruction of the shear modulus with numerical models through a PIP procedure (see Figure 12.8).

In general, by the obtained results, it can be concluded that the three hyperelastic models analyzed adjusted the experimental data successfully. Specifically, the proposed FOEC model was appropriate to model cervical tissue in tension for the strain ramp rate considered. In addition, the calculated shear modulus depended on the anatomical location of the cervical tissue.

14.4 Conclusions

In this work, as a first contribution, we proposed a new hyperelastic model (nonlinear model) based on the Fourth Order Elastic Constants (FOEC) in the sense of Landau's theory to reconstruct the nonlinear parameters in cervical tissue by fitting the experimental data with this model. The results obtained were later compared with the most used hyperelastic models in the literature, Mooney-Rivlin and Odgen models. The three models fitted the experimental data successfully and, in particular, the proposed FOEC model was appropriate to model cervical tissue in tension for the strain ramp rate considered. As a second contribution, a validation of the previous reconstructed mechanical properties of epithelial and connective layers by PIP procedure (Chapter 12) was performed. The conclusion is that shear modulus was dependent on anatomical location of the cervical tissue. Variations of the same order of magnitude were obtained after the reconstruction of the cited shear modulus with the PIP procedure.

15

In vivo measurement of cervical elasticity on pregnant women by TWE: a preliminary study

This chapter presents the results of a preliminary study to assess the feasibility and reliability of TWE technique to provide consistent data on the changes of the cervical stiffness during pregnancy [1].

Section 15.1 shows the results obtained to evaluate the three security parameters of TWE technique according to the Food and Drug Administration guidelines. In Section 15.2, the characteristics of the population in the study are outlined. The results of the statistical analysis are presented in Section 15.3. Finally, the feasibility of using TWE technique to assess cervical maturation is discussed in Section 15.4.

15.1 Safety considerations

The experimental results obtained to evaluate the three security parameters according to the Food and Drug Administration guidelines were as follows.

The maximum pressure registered after converting the pressure recorded by the decibel sensor into water acoustic pressure was $3.99 * 10^{-5}$ MPa.

The maximal acoustic pressure and the peak rarefactional pressure of the torsional wave in water was $P_0 = 3.99 * 10^{-4}$ bars. The three previous parameters were obtained with the cited experimental conditions:

[1] Contribution: P. Massó, A. Callejas, J. Melchor, F. S. Molina and G. Rus. In-vivo measurement of cervical elasticity on pregnant women by torsional wave technique: a preliminary study. *Sensors*, 19(15), 2019.

$$MI = 0.0013 < 1.9 \tag{15.1}$$

$$ISPPA = P_0^2/(2 * \rho * c) = 5.3\ W/cm^2 < 190\ W/cm^2 \tag{15.2}$$

considering the density of the medium $\rho = 1000 kg/m^3$, and the sound speed in the medium $1500 m/s$.

$$ISPTA = ISPPA * \Delta t/1 = 5.3\ mW/cm^2 < 94\ mW/cm^2 \tag{15.3}$$

15.2 Characteristics of the population in the study

The obstetric characteristics of the population in the study are shown in Table 15.1.

Characteristics	**Value**
Total population (N)	18
Gestational age at test (weeks)	26.4 (16w - 35w+5d)
Nulliparous (N)	2 (11 %)
Cervical length (mm)	33 (10 - 49)

Table 15.1: Features of the population in the study.

15.3 Statistical results

A total of three measurements of TWE stiffness and cervical length per subject were determined from all women. A normal distribution for the three velocity calculation procedures was found through Q-Q test (Figure 15.1) and Shapiro Wilk test. Boxplots of these data observed in each patient were calculated and a linear regression was fitted with 80% confidence intervals (see Figure 15.2). In this work, the three frequencies were used to study the effect of attenuation on the cervical tissue. The selected frequency configuration was 1 kHz, which was the optimal measure to yield the highest amplitude signals, the best shear wave speed reconstructions and a significant correlation with gestational age. In some measurements, frequencies equal to or higher than 1.5 kHz, yielded amplitudes of signal similar to the amplitude of noise probably due to attenuation, and consequently anomalous values of the cervical stiffness were obtained. In contrast, the noise masked the amplitude of the signal in some data with frequencies of 0.5 kHz and below. All missing data were due to signal noise.

A stronger association between gestational age and cervical stiffness was found ($R^2 = 0.370$, $p = 0.0074$, Figure 15.2) compared to gestational age and cervical length correlation ($R^2 = 0.025$, $p = 0.6043$, Figure 15.5). The decrease of the stiffness is computed from the data in Figure 15.2 using Equation 10.1. The error bars are estimated from the three velocity estimation algorithms described in the methods. The three overlapping regressions

(continuous and dashed lines in Figures 15.2, 15.3 and 15.4) correspond to each velocity estimation algorithms.

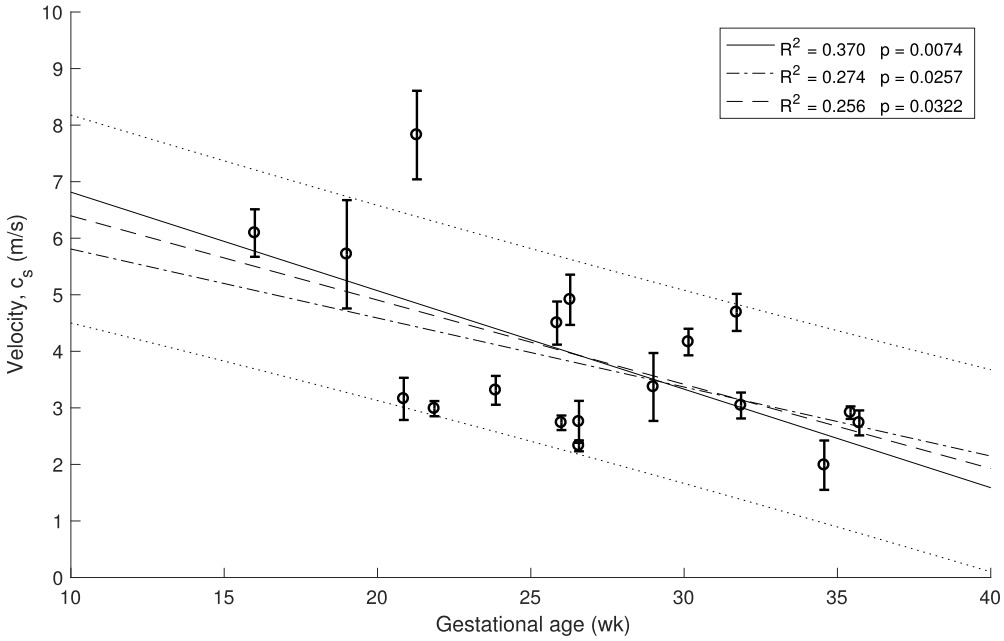

Figure 15.2: Relationship between cervical stiffness assessed by shear wave speed using 1 kHz waves and gestational age at time of examination.

Similar correlations are shown in Figures 15.3 and 15.4 for 1.5 kHz and 0.5 kHz respectively, where some of the measurements were rejected due to noise in the signal.

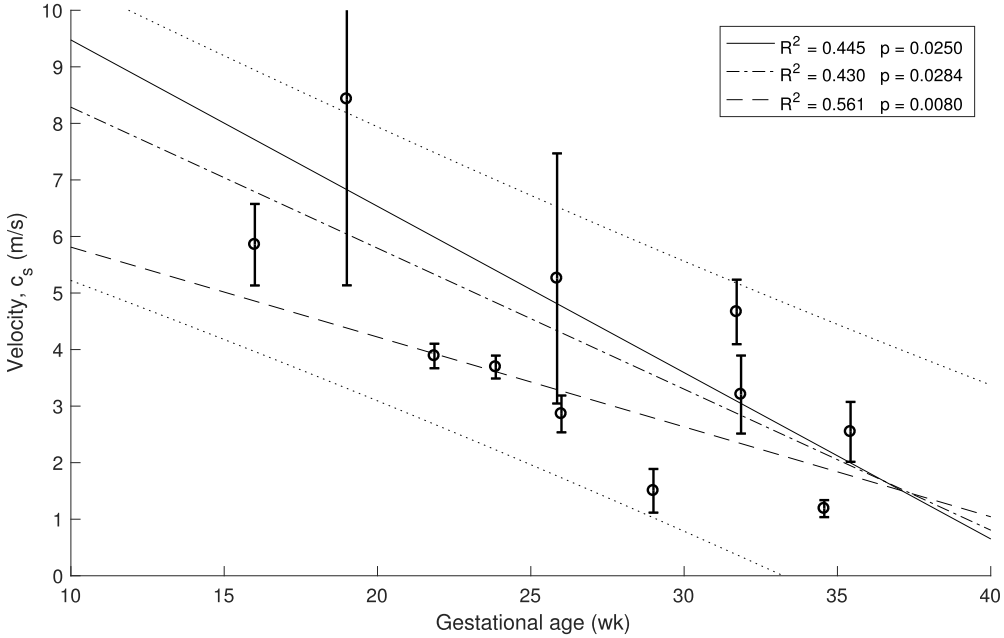

Figure 15.3: Relationship between cervical stiffness assessed by shear wave speed using 1.5 kHz waves and gestational age at time of examination.

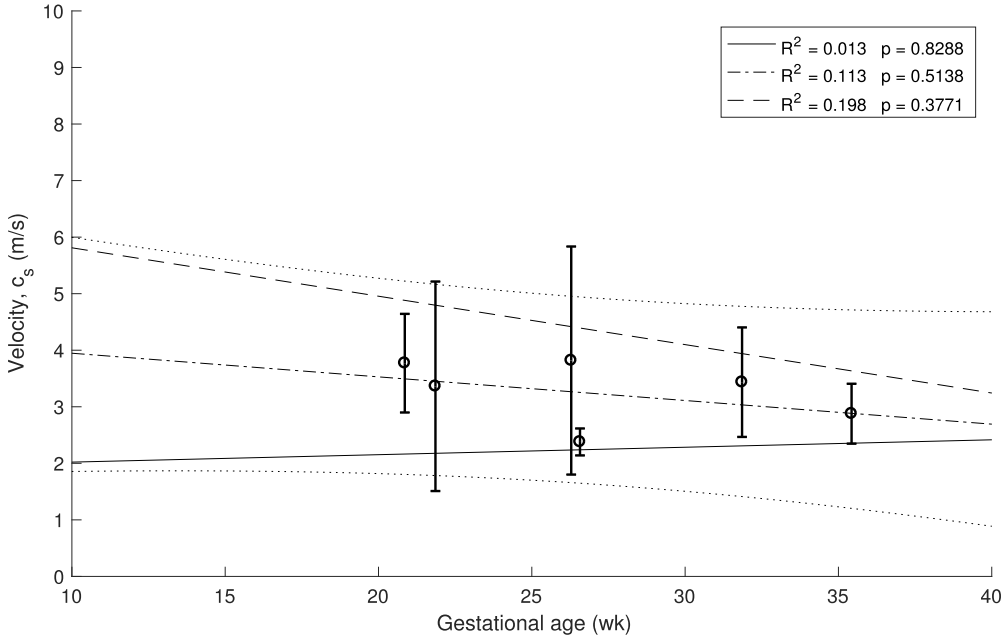

Figure 15.4: Relationship between cervical stiffness assessed by shear wave speed using 0.5 kHz waves and gestational age at time of examination.

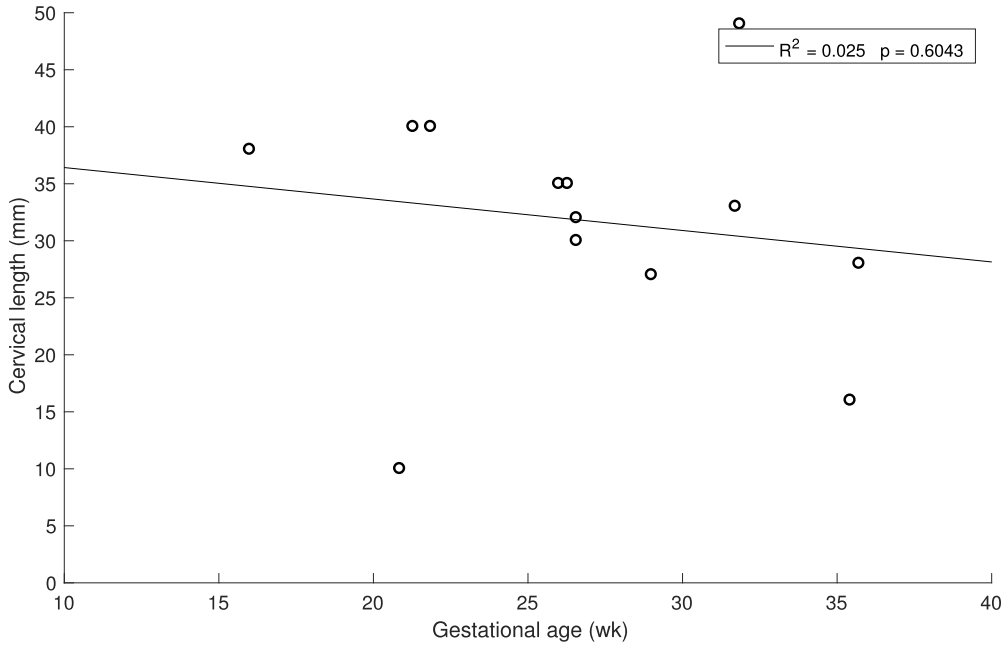

Figure 15.5: Relationship between cervical length and gestational age at time of examination.

No high associations ($R^2 < 0.5$ for all cases) and no significant correlation ($p > 0.05$) were obtained between stiffness and cervical length (Figure 15.6).

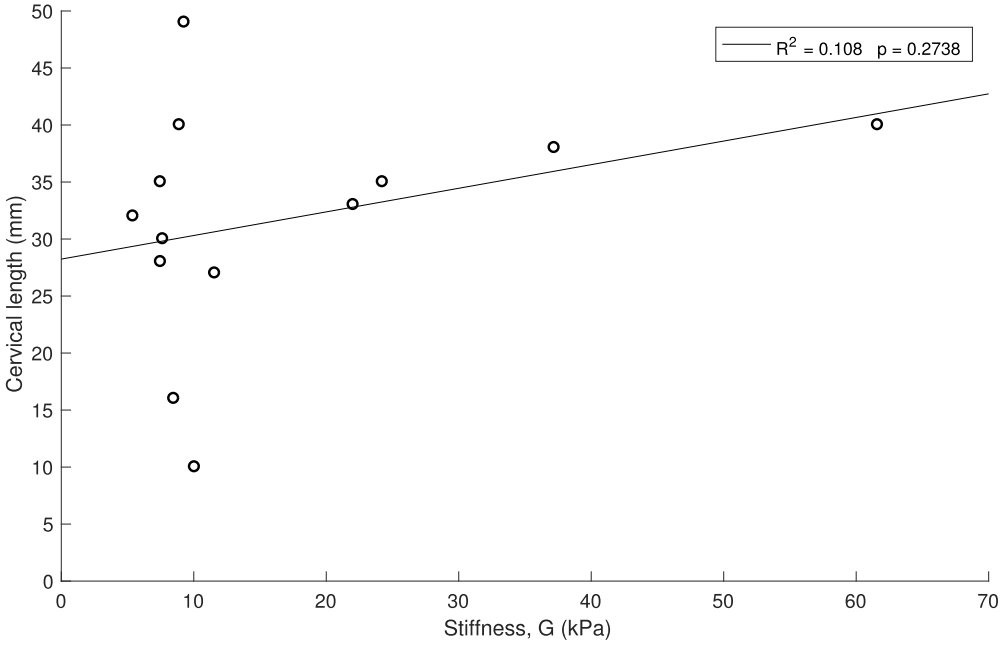

Figure 15.6: Relationship between cervical stiffness and cervical length.

15.4 Discussion

This work was focused on assessing the feasibility of torsional wave technique to quantify the changes in cervical stiffness during pregnancy, which were measured by shear stiffness modulus. The presented results showed, for the first time *in vivo*, the viability of torsional waves to objectively measure cervical elasticity in pregnant women. The observed data therefore support the hypothesis 1 that torsional wave technique has the capacity to quantify cervical stiffness defined by its elastic modulus.

The presented observations also support hypothesis 2, that the shear stiffness decreases during pregnancy. Cervical stiffness was shown to significantly decrease with gestational age, which is compatible with observations by former researchers that assessed cervical ripening by different techniques [34, 142, 286, 144]. A gradual reduction from about 40 kPa at the beginning of pregnancy to close to zero at delivery was obtained in the study carried out by Peralta et al. [34]. A correction due to the difference of range of shear wave frequencies of ARFI was considered, about an order of magnitude higher, which affect the apparent stiffness given the viscoelastic behaviour of cervical tissue. Thus, cervical ripening is directly related to the time to delivery. Correlation between cervical stiffness and gestational age assessed by TWE technique showed a higher correlation to gestational aged compared to quantification through shear wave speed (SSI) ($R^2 = 0.37$ vs $R^2 = 0.29$) [33].

A weaker correlation was found between cervical stiffness and cervical length than with gestational age, which is compatible with previous studies [34, 145], using dynamic and quasi-static elastography respectively, but contrary to observations by Hernandez-Andrade et al. [69], who found that associations between cervical tissue strain and cervical length was higher than with gestational age. This inconsistency feeds a debate, which could be at least

partially explained by the inherent limitations of the commercially available quasi-static elastography technologies [38, 39, 42, 69], as this technique provides a qualitative estimation of the cervical stiffness through an indirect measurement.

The experiment results support that TWE technique is safe to be used in pregnant women. All the values obtained were far below the thresholds according to the Food and Drug Administration (FDA) guidelines reference parameters in Fetal Imaging & Other. The mechanical index (MI) was 0.0013 (< 1.9), the spatial peak pulse average intensity ($ISPPA$) was $5.3 W/cm^2$ ($< 190 W/cm^2$), and the spatial peak temporal average intensity ($ISPTA$) was $5.3 mW/cm^2$ ($< 94 mW/cm^2$).

The limitations of this research are linked to the nature of propagation of torsional wave in cervical tissue, but also to its complex microarchitecture. Some mechanical hypothesis have been raised in the literature about the hystologic features of the cervix to estimate the shear stiffness elasticity, assuming homogeneous, non viscous, isotropic and semi-infinite medium [44, 165, 234, 287, 288]. The equation employed in this work to estimate the cervix stiffness is only based on shear wave group velocity. However, the behavior of cervical tissue is dispersive, that is, the higher shear wave frequencies, the higher shear waves speeds and therefore, phase-velocity-based techniques would lead to a direct calculation of shear modulus. The time of flight technique measured the shear wave group velocity, which is dependent on the envelope of the propagating elastic wave.

Finally, due to the exploratory nature of this study about the feasibility of torsional wave technique to assess cervical maturation, a small population of patients was recruited. To extend the validity and reliability of the proposed technology, larger complementary studies are needed. The protocol of measurements by TWE technique will be enhanced by applying the optimal contact conditions between the probe and the cervix [289]. We are positive that torsional waves are a tool with potential to objectively diagnose early cervical ripening disorders and preterm birth.

15.5 Conclusions

The presented experimental observations prove that firstly, cervical stiffness was a valuable predictor variable of gestational age at the moment of evaluation. Secondly, TWE technique is a tool that allows to quantify cervical shear stiffness during pregnancy. Finally this technique is safe to be used in pregnant women.

TWE technique might provide clinically relevant data on the cervical ripening in addition to that obtained from digital exploration and standard sonography. Further researches are required to assess the TWE technique feasibility in obstetric evaluations, such as probabilistic inverse problems based on viscoelastic models for the prediction of preterm delivery and labour induction failure.

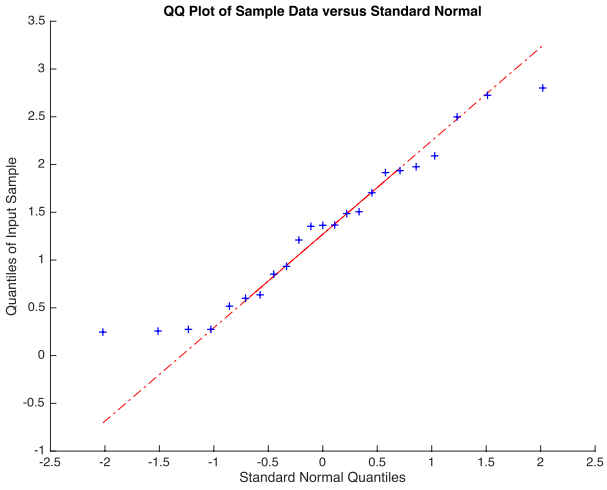

a) The first velocity calculation procedure

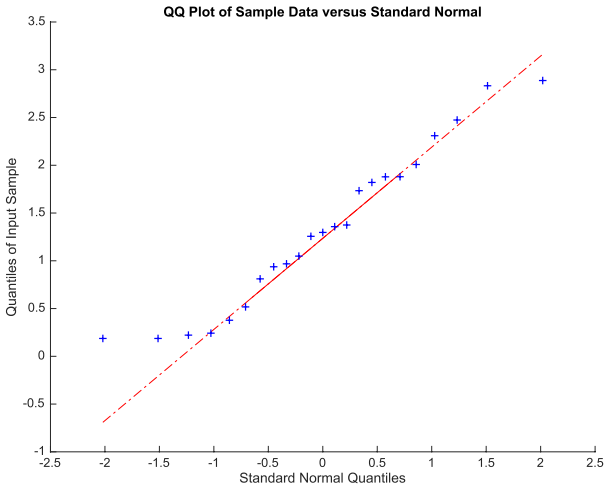

b) The second velocity calculation procedure

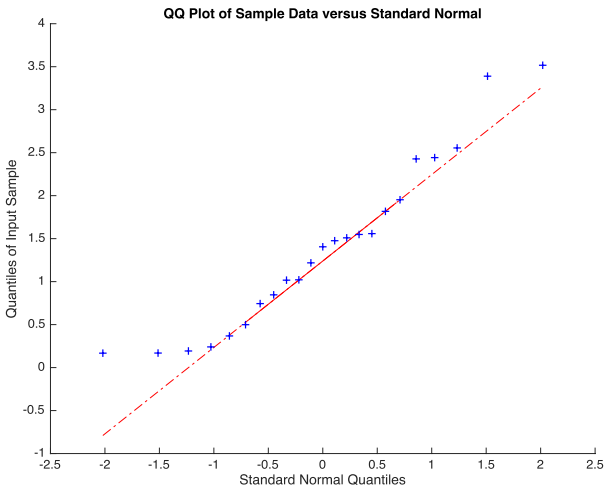

c) The third velocity calculation procedure

Figure 15.1: Normal quantile-quantile plots for the three velocity calculation procedures.

Part IV

CONCLUSIONS AND FUTURE WORKS

16
Conclusions and future works

This chapter presents the most relevant conclusions of the obtained results, along with a discussion regarding the exposed contributions. In addition, some future works currently under development are commented.

In addition, the following relevant conclusions are extracted from each of research hypothesis proposed in Chapter 2. Their limitations and future works are also described.

Viscoelastic assessment with TWE technique

Research objective 1: Propose and evaluate the feasibility of a novel Torsional Wave Elastography technique to objectively quantify the viscoelastic properties of soft tissues, and specifically the cervical tissue.

In this dissertation, the TWE technique was proved capable to successful transmitting and receiving shear waves from 300 Hz to 1 kHz (**Chapter 11**). This range of frequencies represents an obvious advantage when compared with commercial elastography devices, since a broader range of frequencies provides more significant information about the viscoelastic behavior of the tissue, in particular for the viscous component, which is more sensitive to high frequencies. In **Chapter 6** we have proposed a study for a preliminary analysis of the intra-operator dependency. The variables were the normal pressure applied and the angle of incidence between the probe and the normal direction of the tissue surface. Gelatine phantoms with 8% and 10% concentration (w/w) were selected as an adequate representation of the viscoelastic behavior of soft tissues to test the robustness of TWE technique. Variable levels of pressure produced a minimal variation in the shape of the collected signal and, therefore, the impact of this variation on the reconstructed values of shear wave speed was non-significant for all the frequencies. As a consequence, no correlation between the level of

pressure and shear wave speed was found in the small range of pressures analyzed. Higher pressures could produce variations in the shear wave speed and, therefore, the nonlinear characterization of the tissue. The same effects were observed when varying the angle of incidence sensor-phantom. These observations were found consistent all over the different gelatine concentration phantom tested, which seem to indicate that the TWE technique is, at least in gelatine-based phantoms, a robust and low user-dependent elastography method. However, as observed in the experiments, simple gelatine-based phantoms shows a low viscous behavior, which is not proper of soft tissues. This low viscous behavior might be responsible for such stable results against the two variables of the user-dependency test. Future research in that vein were conducted, especially with phantoms with higher viscosity to define the validity limits of these studies and to develop clinical practice protocols to correct deviations when using the designed device.

A series of experiments were performed on *ex-vivo* human cervical tissue with the aim of combining information from rheometry (low frequencies) and TWE (high frequencies), providing two sources of data to find the most suitable rheological model to fit the cervical tissue behavior. Whereas the fitted curves obtained by using TWE data were overall in good agreement with the data from rheometry, the curves using the rheometry data diverged from those using TWE. Additionally, the dispersion curve after fitting the whole set of data, this is rheometry + TWE, practically coincided with the curve generated by using only the TWE data. These findings point out the relevancy of the viscous effects at higher frequencies. Furthermore, it uncovers the difficulty of characterizing the viscous effects of soft tissue by limiting the experiments to classical rheometry techniques.

On the one hand, when comparing the four rheological models, it can be observed that the Maxwell model showed difficulties to represent the dispersion of shear wave speed along the whole range of frequency. The Zener model adjusted the data successfully when considering both the rheometry and the TWE outcomes. However, when fitting only data from TWE, it showed some divergence at the low-frequency range. On the other hand, Kelvin-Voigt and its fractional derivative version matched all the data satisfactorily from the high to the low-frequency regime. The values obtained for the α parameters of the Kelvin-Voigt Fractional Derivative model were close to 1, which transforms the model directly into a classical Kelvin-Voigt. A two-parameter model as the Kelvin-Voigt usually will be preferred against a three-parameter model as the fractional version, due to practicality and faster computation. Further studies are presented in **Chapters 7** and **12** to analyze the consistency of all the findings shown.

Model hypothesis ranking

Research objective 2: Rank the most plausible rheological model to infer the viscoelastic behavior of cervical tissue in different layers using a probabilistic inverse procedure and explore the possibility of quantifying both elasticity and viscosity from the selected model.

Chapters 7 and **12** are aimed at understanding the torsional wave-tissue interactions, which may determine the optimal rheological model, to finally characterize the viscoelasticity of cervical tissue. A Probabilistic Inverse Problem (PIP) was described for ranking the most plausible model by comparing the *in-vivo* measurements in cervical tissues obtained from the TWE technique with the synthetic signals from the 2D Finite Difference Time Domain (FDTD) wave propagation models (elastic, Kelvin-Voigt and Maxwell models).

High-speed camera test were carried out to study the slippery conditions between sensor and tissue-mimicking phantoms, as well as the boundary conditions of the numerical models after a video post-processing. On one hand, a pressure between the sensor and the phantom of 100 grams was chosen, enough to ensure no slippage and so that the compression did not affect the mechanical properties of the phantom. On the other hand, the speed at grid points of the tissue was zero due to the pressure exerted by the torsional wave sensor on the phantom. Finally, the reconstruction of excitation of the electromechanical actuator was carried out by measuring the displacement of basalt microparticles embedded in the surface of the tissue-mimicking phantom. The amplitude of the rotated angle was independent of the stiffness of the phantom, however, the signal amplitude decreased as the excitation frequency increased due to the performance of the electromechanical actuator. A cut-off-frequency of 1000 Hz was selected to infer mechanical properties at a lower scale, also taking into account the attenuation in wave propagation.

After a verification of numerical dispersion to avoid instabilities in the three FDTD viscoelastic models, the results of the ranking of model hypothesis show how the most plausible viscoelastic model, that best simulates the cervical tissue behavior, is the Kelvin-Voigt model. The results are in good agreement with those obtained in **Chapters 6** and **11**. The model parameters are epithelium shear modulus, epithelium viscosity, epithelium thickness, connective layer shear modulus and connective layer viscosity.

Once the viscoelastic model was selected, the parameters related to the model were reconstructed from 18 experimental measurements in pregnant women. Results show a notable difference in stiffness of the epithelial layer with respect to the connective layer. The result makes sense since the stiffness of the cervical tissue is governed mainly by collagen fibers, main constituents of the connective layer. The dramatic changes during cervical maturation in collagen fibers of connective tissue is compatible with the high standard deviation of the shear stiffness. It should be taken into account that the results obtained are representative of a set of data of pregnant women with different gestational ages. In contrast, the content of collagen fibers in the epithelial layer is practically negligible. This may be the reason why standard deviation of the shear stiffness of epithelial layer is low. It is worth pointing out the viscosity of the epithelial and connective layers. They present similar values in term of mean and standard deviation, result that was taken into account for the validation of the method of reconstruction of KV parameters (**Chapter 13**), reducing the number of parameters when considering both viscosities the same. The viscous parameters of cervical tissue have scarcely been studied so far in medical diagnosis, but the few references present

in the literature, none in test in pregnant women *in-vivo*, suggest that viscoelastic properties are particularly sensitive to the gestation process. Finally, the range reconstructed for the epithelial thickness was in good agreement with the values found in the literature.

Although in this study the anatomy of the cervical tissue and viscoelasticity has been considered, one of its limitations lies in considering isotropy. It is well known that cervical tissue, like most tissues, is anisotropic and, therefore, considering that there are variations in mechanical parameters in different directions is essential. The measurements made in this study have been carried out by centering the sensor on the cervical canal and considering the hypothesis that radially the tissue does not change its mechanical properties. Therefore, future research works should consider anisotropy by sectorizing the ring receiver.

Mechanical reconstruction from TWE

Research objective 3: Propose and experimentally validate a method based on PIP approach to infer the KV viscoelastic properties in cervical tissue from TWE technique.

Chapter 8 was devoted to presenting and validating a reconstruction approach based on a probabilistic inverse problem procedure, which uses a Kelvin-Voigt forward model of the propagation of torsional waves in a bilayer axisymmetric cervix-like medium, numerically solved by a self-developed FDTD algorithm. Five *ad-hoc* oil-in-gelatine phantoms were fabricated with different gelatine batches, simulating the anatomy of the cervical tissue composed mainly by the epithelial and connective layer, to test the new reconstruction technique. On the one hand, a probabilistic approach was employed that reconstruct the KV viscoelastic parameters by comparing the results obtained from TWE technique with the synthetic signals from the FDTD KV model. On the other hand, the characterization for each batch of gelatines was performed by SWE measurements in order to analyze the quality of the reconstruction of the viscoelastic parameters. The validation of the method was carried out by comparing the KV parameters reconstructed from the PIP with those inferred from the shear wave speed curve obtained with SWE measurements. Kelvin-Voigt constitutive law was implemented into the wave propagation model, since the KV model was found to be the simplest model in terms of a number of parameters that provides the best approximation to the mechanical behavior of *ex vivo* cervical tissue in our previous characterization study **Chapter 11**.

The resulting viscoelastic parameters showed in **Chapter 13** fell within the range of values observed in the literature. The shear elasticity and shear viscosity reconstructed for the second layer (connective layer) are in good agreement with the values found in the literature. To our knowledge, there are no references regarding shear elasticity and viscosity in the epithelial layer. Regarding the thickness of each phantom, it can be claimed, without not much mistake, that was satisfactorily reconstructed. The reconstruction of the viscoelastic parameters by using the TWE technique with the new proposed inversion method was validated against the SWE technique by using two approaches, a Student's T-test and a Pearson's correlation study. T-test results were in terms of the p-values for the shear elasticity

and the shear viscosity from each oil-in-gelatine batch. Most os the p-values obtained were above 0.05, which can be considered to represent a not significant difference between the parameters reconstructed by the two techniques. Only shear viscosity for the batch containing 7.5% of gelatine and 10% oil showed a lower p-value of 0.042. Nevertheless, the reconstruction of this parameter by the SWE also showed the higher range of variability, i.e. the higher standard deviation. The explanation for this low p-value can be associated to both the high dispersion effect of this oil-in-gelatine batch and the higher variability in the SWE measurements. Further tests should be carried out in high dispersive oil-in-gelatine phantoms in order to clarify the origin of the low correlation value. The correlation between results from both techniques, TWE and SWE were high, specially for the shear stiffness, which yielded a Pearson's correlation coefficient $r = 0.9942$. The Pearson's correlation coefficient for the shear viscosity was lower, with $r = 0.8913$. This may be due to the larger effect that shear elastic modulus has on the torsional wave received compared to that produced by the shear viscosity. Furthermore, the reconstructions were more similar for both the shear elasticity and shear viscosity when excluding the most dispersive batch.

In general, by the obtained results from the T-test and the Pearson's correlation study, it can be concluded that the viscoelastic parameters reconstructed by the TWE technique in conjunction with the new inversion approach were similar to those provided by the SWE technique. Therefore, it can be concluded that this new inversion method was validated for its use in the TWE technique. In order to study the performance of the new inversion method in a scenario closer to the final medical application, future work should be carried out on *ex vivo* cervical tissue samples.

The main limitation of this approach was related to the computational cost in numerical simulations. The purpose of this method is to use it in clinical practice and obtain results of cervix mechanical parameters in real time. According to the methodology proposed in this thesis, this approach required several days of calculation to solve the inverse problem and to infer these parameters with acceptable accuracy. Therefore, future research in that vein should be conducted, especially on the use of neural networks, a new method based on artificial intelligence, that would provide information in clinical practice about the mechanical parameters of the cervical tissue in real time.

Nonlinearity assessment

Research objective 4: Propose a hyperelastic model based on Fourth Order Elastic Constants (FOEC) in the sense of Landau's theory to characterize the nonlinearity of cervical tissue and validate the mechanical parameters inferred in *Research objective 2*.

The work presented in **Chapters 9** and **14** aims at representing a first step toward a nonlinear characterization of human cervical tissue. The nonlinear elastic properties of *ex vivo* cervical tissue were obtained for the first time by uniaxial tensile tests. The first contribution of this study is to propose a new hyperelastic model (nonlinear model) based on the Fourth Order Elastic Constants in the sense of Landau and compare the obtained results with the

most used hyperelastic models in the literature, Mooney-Rivlin and Odgen models. As a second contribution, a validation of the previous reconstructed mechanical properties of epithelial and connective cervical tissue by PIP (**Chapter 12**) is presented.

The nonlinear paremeters of the FOEC proposed model, as well as with Mooney-Rivlin and Odgen models were obtained through a fit of the experimental data measured in the uniaxial tensile test (see procedure in **Chapter 9** and results in **Chapter 14**). In order to compare the three models, the R^2 coefficient was obtained to analyze the goodness of each of the fits performed. The resulting R^2 coefficient calculated show that the models analyzed adjusted the experimental data successfully. Specially, the proposed FOEC model is appropriate to model cervical tissue in tension for the strain ramp rate considered, 1%/s. The FOEC model presents three parameters, the shear modulus μ, the third order elastic constant A, and the fourth order elastic constant D. In this study, the theoretical stress-strain relationship was simplified with the aim of comparing with the two-term Mooney-Rivlin and Odgen models. The two parameters that have adjusted the experimental data were the shear modulus and the third order elastic constant. Analyzing the results of the shear modulus, there was no significant variation in both, the epithelial and the connective layer for each of the hysterectomy samples. The values of the shear stiffness were highly dependent of the strain ramp rate used, the larger strain rate, the larger shear modulus. The obtained values for cervical tissue agree with those found in literature. However, regarding the nonlinear parameter A, large variation was observed, varying the parameter from positive to negative values. The variability found in the third elastic constant parameter A could be associated with the heterogeneity of the tissue. It is worth pointing out that, to our knowledge, this is the first work that studies the nonlinear parameters of the FOEC hyperelastic model in cervical tissue.

The values of the shear modulus were extracted directly by means of the μ parameter of the FOEC proposed model, through the slope of the stress-strain curve in the linear region or also through a combination of the two parameters of the Odgen model, the infinitesimal shear modulus μ_r and the stiffening parameter α_r. The parameters that govern the Mooney-Rivlin model have no physical sense and, therefore, it can not be extracted the shear modulus from them. The results of the shear modulus of each cervical layer were compared by using a Student's T-test. T-test results are expressed in terms of p-values. All of these values were above 0.05, which can be considered to represent a not significant difference between the shear modulus obtained by the three models in the epithelial and connective layers. The shear modulus was dependent on anatomical location of the cervical tissue. Variations of the same order of magnitude were obtained after the reconstruction of the shear modulus with numerical models through a PIP procedure (**Chapter 12**).

One of the limitations of this study is related to the press used for uniaxial tensile tests. The tolerance of the force gauge is 0.1 N, which does not allow obtaining the necessary experimental data in small deformations, in which tolerances around two orders of magnitude lower are necessary. In this dissertation, the propagation of torsional waves was carried out

considering small deformations, and, therefore, future tests in which the force gauge has a greater tolerance are necessary to be able to validate the mechanical parameters of cervical tissue reconstructed by means of PIP approach.

Gestational assessment

Research objective 5: Evaluate the feasibility and reliability of Torsional Wave Elastography technique to provide consistent data on the changes of the cervical tissue stiffness during pregnancy.

The results presented in **Chapter 15** showed, for the first time *in-vivo*, the viability of torsional waves to objectively measure cervical elasticity in pregnant women. We showed that it is possible to objectively quantify cervical stiffness during pregnancy using torsional wave elastography. Besides, the experimental results support that TWE technique is safe to be used in pregnant women. All the values obtained were far below the thresholds according to the Food and Drug Administration guidelines reference parameters in Fetal Imaging and Other.

A preliminary study was designed in **Chapter 10** with the aim of providing *in-vivo* information about cervical elasticity throughout normal pregnancy. A total of 18 healthy women were recruited from their routine medical visits during pregnancy, and TWE explorations were performed. The entire population of women in the study had pregnancies without any complication with a median of 26.4 (16wk-35wk+5d) gestation weeks. Exclusion criteria were multiple pregnancies, previous cervical surgeries and patients with information relative to malignant changes in the cervical tissue.

The observed data support, firstly the hypothesis that torsional wave technique has the capacity to quantify cervical stiffness defined by its elastic modulus, and secondly, that shear stiffness decreases during pregnancy. In this work, three frequencies were used to study the effect of attenuation on the cervical tissue. The selected frequency configuration was 1 kHz, which was the optimal measure to yield the highest amplitude signals, the best shear wave speed reconstructions and a significant correlation with gestational age. In some measurement, frequencies $\geq$ 1.5 kHz, yielded amplitudes of signal similar to the amplitude of noise probably due to attenuation, and consequently anomalous values of the cervical stiffness were obtained. In contrast, the noise masked the amplitude of the signal in some data with frequencies $\leq$ 0.5 kHz. For the selected frequency, a stronger association between gestational age and cervical stiffness was found, compared to gestational age and cervical length correlation. Additionally, no high associations and no significant correlation were obtained between stiffness and cervical length.

The limitations of this research are linked to the nature of propagation of torsional wave in cervical tissue as well as its complex microarchitecture. Some mechanical hypotheses have been raised in the literature about the hystologic features of the cervix to estimate the shear stiffness elasticity, assuming homogeneous, non viscous, isotropic and semi-infinite medium. The equation employed in this study to estimate the cervix stiffness is only based

on shear wave group velocity. However, the behavior of cervical tissue is dispersive, that is, the higher are the shear wave frequencies, the higher are the shear waves speeds and, therefore, phase-velocity-based techniques would lead to a direct calculation of shear modulus. The time-of-flight technique measured the shear wave group velocity, which is dependent on the envelope of the propagating elastic wave.

Finally, due to the exploratory nature of this study about the feasibility of torsional wave technique to assess cervical maturation, a small population of patients was recruited. To extend the validity and reliability of the proposed technology, larger complementary studies are needed in which the proposed method in this thesis (**Chapter 8**), based on PIP approach to infer the KV viscoelastic properties in cervical tissue from TWE technique, is employed. We are positive that torsional waves are a tool with potential to objectively diagnose early cervical ripening disorders and preterm birth.

17

Conclusiones y trabajos futuros

Este capítulo presenta las conclusiones más relevantes, provenientes de los resultados obtenidos, junto con una discusión de las contribuciones expuestas y limitaciones. También, se comentan algunos trabajos futuros actualmente en desarrollo.

Evaluación viscoelástica con la técnica TWE

Objetivo 1: Proponer y evaluar la viabilidad de una nueva técnica de elastografía de ondas de torsión para cuantificar objetivamente las propiedades viscoelásticas de tejidos blandos, y específicamente el tejido cervical.

En esta tesis doctoral, la técnica TWE demostró la capacidad de transmitir y recibir con éxito ondas de cizalla de 300 Hz a 1 kHz (**Capítulo 11**). Este rango de frecuencias representa una ventaja obvia en comparación con los dispositivos comerciales de elastografía, ya que un mayor rango de frecuencias proporciona información más significativa sobre el comportamiento viscoelástico del tejido, en particular para la componente viscosa, que es más sensible a las frecuencias altas. En el **Capítulo 6** se ha propuesto un análisis preliminar de la dependencia intraoperadora. Las variables objeto de estudio fueron la presión normal aplicada y el ángulo de incidencia entre la sonda y la dirección normal de la superficie del tejido. Las muestras con una concentración de gelatina del 8% y 10% (p/p) se seleccionaron para evaluar la robustez de la técnica propuesta. Los niveles variables de presión aplicada produjeron una variación mínima en la forma de la señal registrada y, por lo tanto, el resultado de esta variación en los valores reconstruidos de la velocidad de onda de cizalla no fue significativo para las frecuencias estudiadas. Como consecuencia, no se encontró correlación entre el nivel de presión y la velocidad de onda de cizalla para el pequeño rango

de presiones analizado. Un mayor rango de presiones estudiado podría producir variaciones en la velocidad de cizalla y, por consiguiente, la caracterización no lineal del tejido. Los mismos resultados se observaron al variar el ángulo de incidencia entre el sensor y la muestra de gelatina. Estas observaciones fueron similares en todas las muestras de gelatina estudiadas, lo que parece indicar que la técnica TWE es, al menos en muestras de gelatina, un método robusto y poco dependiente del usuario. Sin embargo, las muestras de gelatina estudiadas muestran un comportamiento poco viscoso, que no es apropiado para tejidos blandos. Este comportamiento podría ser responsable de resultados tan estables respecto a las dos variables estudiadas en el test de dependencia del usuario. Se realizarán investigaciones futuras en esa línea, especialmente con muestras de gelatina de mayor viscosidad para definir los límites de validez de estos estudios y desarrollar protocolos en la práctica clínica que corrijan las desviaciones ocasionadas por el uso del dispositivo diseñado.

Se realizaron una serie de experimentos en tejido cervical humano *ex-vivo* con el objetivo de combinar información de reometría (bajas frecuencias) y TWE (altas frecuencias), proporcionando dos fuentes de datos para encontrar el modelo reológico más adecuado que simule el comportamiento del tejido cervical. Mientras que las curvas de los modelos ajustados a los datos experimentales obtenidos con TWE se ajustaban bien a los datos obtenidos con reometría, las curvas ajustadas a los datos de reometría divergen de los datos obtenidos con TWE. Además, la curva de dispersión después de ajustar todo el conjunto de datos, es decir reometría + TWE, prácticamente coincidió con la curva ajustada al usar solo los datos de la técnica TWE. Estos resultados destacan la relevancia de los efectos viscosos a frecuencias más altas. Además se muestra la dificultad de caracterizar los efectos viscosos de los tejidos blandos usando las técnicas clásicas de reometría.

Por un lado, al comparar los cuatro modelos reológicos, se puede observar que el modelo Maxwell mostró dificultades para representar la dispersión de la velocidad de onda de cizalla a lo largo de todo el rango de frecuencias estudiado. El modelo Zener ajustó los datos con éxito al considerar tanto los datos de reometría como los obtenidos con TWE. Sin embargo, al ajustar solo los datos de TWE, el modelo mostró cierta divergencia en el rango de baja frecuencia. Por otro lado, el modelo Kelvin-Voigt y su versión de derivada fraccional ajustaron los datos satisfactoriamente desde el régimen de baja frecuencia hasta el régimen de alta frecuencia. Los valores obtenidos para el parámetro α fueron cercanos a 1, lo que transforma el modelo directamente en el modelo Kelvin-Voigt clásico. Un modelo de dos parámetros, como el Kelvin-Voigt, generalmente se prefiere frente a un modelo de tres parámetros como la versión fraccional, debido a la rapidez en el cálculo y la practicidad. Estudios adicionales se presentan en los **Capítulos 7** and **12** para analizar la consistencia de todos los resultados mostrados.

Clasificación de modelos reológicos

Objetivo 2: Clasificar el modelo reológico más plausible para inferir el comportamiento viscoelástico del tejido cervical en diferentes capas utilizando un problema inverso prob-

abilista y explorar la posibilidad de cuantificar tanto la elasticidad como la viscosidad del tejido cervical usando el modelo seleccionado.

Los **Capítulos 7** y **12** tienen como objetivo comprender las interacciones de la onda de torsión con el tejido, lo que puede determinar el modelo reológico óptimo, para finalmente caracterizar la viscoelasticidad del cervix. Un problema inverso probabilista (PIP) se presenta para seleccionar el modelo reológico más plausible, comparando las medidas *in-vivo* en tejido cervical obtenidas mediante la técnica TWE con las señales sintéticas de los modelos de propagación 2D (modelo elástico, Kelvin-Voigt y Maxwell) implementados en diferencias finitas.

Se llevaron a cabo ensayos con cámara de alta velocidad para estudiar las condiciones de deslizamiento entre el sensor y las muestras de gelatina que imitan el comportamiento de tejidos, así como las condiciones de contorno de los modelos numéricos después de un postprocesado de las grabaciones realizadas. Por un lado, se seleccionó una presión entre el sensor y la muestra de 100 gramos, suficiente para asegurar el no deslizamiento y para que la compresión no afectase las propiedades mecánicas de la muestra. Por otro lado, se tomó la velocidad en los puntos del mallado como nula debido a la presión ejercida por el sensor sobre la muestra. Finalmente, se llevó a cabo la reconstrucción de la excitación del actuador electromecánico midiendo los desplazamientos de micropartículas de basalto embebidas en la superficie de la muestra de gelatina. La amplitud del ángulo rotado por el excitador era independiente de la rigidez de la muestra, sin embargo, la amplitud de la señal disminuía a medida que la frecuencia de excitación aumentaba debido al rendimiento del actuador electromecánico. Se seleccionó una frecuencia de corte de 1000 Hz para inferir las propiedades mecánicas a pequeña escala, también teniendo en cuenta los efectos de atenuación en la propagación de la onda.

Después de la verificación de la dispersión numérica para evitar inestabilidades en los modelos de diferencias finitas, los resultados de la clasificación de dichos modelos muestran como el modelo viscoelástico más plausible, que mejor simula el comportamiento del tejido cervical, es el modelo Kelvin-Voigt. Los resultados coinciden con los obtenidos en los **Capítulos 6** y **11**. Los parámetros del modelo seleccionado son la viscosidad y el módulo de cizalla tanto de la capa epitelial como de la conectiva, así como el espesor de la capa epitelial.

Una vez seleccionado el modelo viscoelástico, se reconstruyeron los parámetros del mismo de las medidas en 18 mujeres embarazadas. Los resultados muestran una notable diferencia en la rigidez de la capa epitelial respecto a la capa conectiva. Dichos resultados tienen sentido ya que la rigidez del tejido cervical está gobernada principalmente por las fibras de colágeno, principales constituyentes de la capa conectiva. Los cambios radicales durante la maduración cervical en las fibras de colágeno del tejido conectivo son compatibles con la alta variación estándar obtenida en la medida del parámetro de rigidez de cizalla. Se debería tener en cuenta que los resultados obtenidos son representativos de un conjunto de datos de mujeres embarazadas con diferentes edades gestacionales. Por el contrario, el contenido de fibras de colágeno en la capa epitelial es prácticamente despreciable. Esta podría

ser la razón por la que la desviación estándar del módulo de cizalla de la capa epitelial es bajo. Merece la pena destacar la viscosidad en la capa epitelial y conectiva. Los resultados presentan valores similares en términos de media y desviación estándar, resultados que se tuvieron en cuenta para la validación del método de reconstrucción de los parámetros KV (**Capítulo 13**), reduciendo el número de parámetros al considerar la misma viscosidad en ambas capas. Los parámetros viscosos del tejido cervical han sido poco estudiados hasta la fecha en el diagnóstico médico, pero las pocas referencias presentes en la literatura, ninguna en ensayos en mujeres embarazadas *in-vivo*, sugieren que las propiedades viscoelásticas son particularmente sensibles al proceso gestacional. Finalmente, el valor del espesor epitelial reconstruido era muy similar a los valores encontrados en la literatura.

Aunque en este estudio se ha considerado la anatomía del tejido cervical y su viscoelasticidad, una de sus limitaciones consiste en considerar isotropía. Es bien conocido que el cervix, como la mayoría de los tejidos, es anisotrópico y, por lo tanto, es esencial considerar que existen variaciones en los parámetros mecánicos en diferentes direcciones. Las medidas realizadas en este estudio se han llevado a cabo centrando el sensor en el canal cervical y considerando la hipótesis de que radialmente el tejido no cambia sus propiedades mecánicas. Por lo tanto, futuros trabajos de investigación deberían considerar anisotropía, sectorizando el anillo receptor del sensor de ondas de torsión.

Reconstrucción mecánica con la técnica TWE

Objetivo 3: Proponer y experimentalmente validar un método basado en el PIP para inferir las propiedades viscoelásticas KV en tejido cervical usando la técnica TWE.

El **Capítulo 8** se dedicó a presentar y validar un procedimiento de reconstrucción basado en un problema inverso probabilista, que usa un modelo directo de propagación de ondas de torsión Kelvin-Voigt en un medio axilsimétrico bicapa, numéricamente solucionado por un algoritmo de diferencias finitas en el dominio del tiempo de desarrollo propio. Cinco muestras se fabricaron con diferentes lotes de gelatina, simulando la anatomía del tejido cervical compuesto principalmente por una capa epitelial y una capa conectiva, para testear la nueva técnica de reconstrucción. Por un lado, un enfoque probabilístico que reconstruye los parámetros viscoelásticos KV comparando los resultados obtenidos mediante la técnica TWE con las señales sintéticas provenientes del modelo de diferencias finitas KV fue empleado. Por otro lado, se llevó a cabo la caracterización de cada lote de gelatinas a través de medidas con elastografía de ondas de cizalla (SWE) para analizar la calidad de la reconstrucción de los parámetros viscoelásticos. La validación del método se llevó a cabo comparando los parámetros reconstruidos con el PIP con los inferidos de la curva de dispersión obtenida con la técnica SWE. La ley constitutiva Kelvin-Voigt se implementó en el modelo de propagación de ondas, debido a la conclusión obtenida de que dicho modelo era el modelo más simple en términos de número de parámetros que proporciona la mejor aproximación del comportamiento mecánico *ex-vivo* del tejido cervical, según el estudio previo presentado en el **Capítulo 11**.

Los parámetros viscoelásticos resultantes mostrados en el **Capítulo 13** estaban dentro de los rangos de los valores presentes en la literatura. La elasticidad y la viscosidad de cizalla reconstruídas para la segunda capa (simulando la capa conectiva) eran similares a las evidencias encontradas en la literatura. Según nuestro conocimiento, no hay referencias relativas a la elasticidad y la viscosidad de cizalla de la capa epitelial. Respecto al espesor inferido de cada muestra, se puede afirmar, sin mucho error, que fue reconstruido satisfactoriamente. La reconstrucción de los parámetros viscoelásticos usando la técnica TWE con el nuevo método de inversión propuesto se validó contra la técnica SWE usando dos enfoques, el test de Student y el coeficiente de correlación de Pearson. Los resultados del test de Student se expresaron en términos de p-valor para la elasticidad y viscosidad de cizalla de cada lote de gelatina. Los valores de la mayoría de los p-valores obtenidos eran superiores a 0.05, por lo que se puede deducir que no hay una diferencia significativa entre los parámetros reconstruidos por las dos técnicas. Únicamente la viscosidad de cizalla para el lote que contiene 7.5% de gelatina y 10% de aceite tenía asociado un p-valor de 0.042. Sin embargo, la reconstrucción de este parámetro mediante SWE también mostraba el mayor rango de variabilidad, representado por la desviación estándar. La explicación para este bajo p-valor puede estar asociada a la alta dispersión de este lote de gelatina y a la alta variabilidad en las medidas con SWE. Un mayor número de ensayos se debería llevar a cabo en muestras de gelatina con alta dispersión para clarificar el origen de este bajo valor de correlación. La correlación entre los resultados obtenidos con TWE y SWE eran altos, especialmente para la rigidez de cizalla, con un valor del coeficiente de correlación de Pearson de $r = 0.9942$. El valor de dicho coeficiente para la viscosidad de cizalla era más bajo, $r = 0.8913$. Esto podía ser debido al mayor efecto que tiene el módulo elástico en la onda de torsión recibida comparado con el que produce la viscosidad de cizalla. Además, las reconstrucciones fueron muy similares para la elasticidad y viscosidad de cizalla cuando no se tiene en cuenta el lote más dispersivo.

En general, teniendo en cuenta los resultados obtenidos con el test de Student y con el estudio de correlación de Pearson, se puede concluir que los parámetros viscoelásticos reconstruidos usando la técnica TWE en conjunción con el nuevo enfoque de inversión eran similares a los obtenidos con la técnica SWE. Por lo tanto, se puede concluir que este nuevo método de inversión fue validado para su uso con la técnica TWE. Con el objetivo de estudiar el comportamiento de dicho método en un escenario parecido al de la aplicación médica final, futuros trabajos de investigación deberían llevarse a cabo usando muestras de tejido cervical *ex-vivo*.

La principal limitación de este estudio se asocia con el coste computacional de las simulaciones numéricas. El propósito de este método es usarlo en la práctica clínica, obteniendo resultados de los parámetros mecánicos del cervix en tiempo real. Según la metodología propuesta en esta tesis, este enfoque requiere varios días de cálculo para resolver el problema inverso e inferir los parámetros con una precisión aceptable. Por lo tanto, futuros trabajos en esta línea deberían llevarse a cabo, especialmente usando redes neuronales, un

nuevo método basado en inteligencia artificial que proporcionaría información acerca de parámetros reconstruidos en tejido cervical en tiempo real.

Evaluación de la no linealidad

Objetivo 4: Proponer un modelo hiperelástico basado en las constantes de cuarto orden (FOEC) en el sentido de la teoría de Landau para caracterizar la no linealidad del tejido cervical y validar los parámetros mecánicos inferidos en el **Objetivo 2**.

El trabajo presentado en los **Capítulos 9** and **14** muestra el primer paso hacia la caracterización no lineal del tejido cervical humano. Las propiedades elásticas no lineales del cervix *ex-vivo* se obtuvieron por primera vez en ensayos de tracción uniaxiales. La primera contribución de este estudio consiste en proponer un nuevo modelo hiperelástico (modelo no lineal) basado en las constantes de cuarto orden en el sentido de la teoría de Landau y comparar los resultados obtenidos con los resultados de los modelos hiperelásticos más empleados en la literatura, el modelo Mooney-Rivlin y Odgen. Como segunda contribución, una validación de los previos parámetros reconstruidos en el tejido cervical mediante PIP (**Capítulo 12**) es presentada. Los parámetros no lineales del modelo FOEC propuesto, así como los de los modelos Mooney-Rivlin y Odgen se obtuvieron a través de un ajuste de los datos experimentales obtenidos en los ensayos de tracción (ver procedimiento en **Capítulo 9** y resultados en **Capítulo 14**). Con el objetivo de comparar los tres modelos, el coeficiente R^2 se obtuvo para analizar la bondad de cada uno de los ajustes realizados. El valor resultante de R^2 muestra que los modelos analizados ajustaron los datos experimentales satisfactoriamente. Especialmente, el modelo FOEC propuesto es apropiado para modelar el tejido cervical bajo carga de tracción para la tasa de deformación considerada, 1%/s. El modelo propuesto presenta tres parámetros, el módulo de corte μ, la constante de tercer orden A, y la constante de cuarto orden D. En este estudio, la relación teórica tensión-deformación fue simplificada con el objetivo de comparar los resultados con los modelos de dos parámetros Mooney-Rivlin y Odgen. Los dos parámetros que ajustaron los datos experimentales fueron el módulo de cizalla y la constante de tercer orden. Analizando los resultados del módulo de cizalla, no se encontró variación tanto en la capa epitelial como en la conectiva para cada muestra de histerectomía. Los valores de rigidez de cizalla eran altamente dependientes del ratio de deformación usado, aumentando el valor del módulo al aumentar el ratio de deformación. Dichos valores obtenidos para el tejido cervical coincidían con los encontrados en la literatura. Sin embargo, con respecto al parámetro no lineal A, una gran variación se encontró, variando el parámetro de valores positivos a negativos. La variabilidad encontrada en la constante de tercer orden A podría estar asociada a la heterogeneidad del tejido. Merece la pena destacar, según nuestro conocimiento, que este es el primer trabajo que estudia los parámetros no lineales de cuarto orden en el sentido de Landau en tejido cervical.

Los valores del módulo de cizalla se obtuvieron directamente mediante el parámetro μ del modelo FOEC, a través de la pendiente de la curva tensión-deformación en el tramo

lineal, y a través de una combinación de los dos parámetros del modelo Odgen, el módulo de cizalla infinitesimal μ_r y el parámetro de rigidez α_r. Los parámetros que gobiernan el modelo Mooney-Rivlin no tienen sentido físico y, por lo tanto, no se puede extraer el módulo de cizalla de ellos. Los valores del módulo de cizalla para cada capa cervical se compararon usando el test de Student, expresando los resultados mediante p-valores. Todos esos p-valores estaban por encima de 0.05, lo que significa que no existía una diferencia significativa entre el módulo de cizalla obtenido mediante los tres modelos para las capas epitelial y conectiva. Dicho módulo era dependiente de la localización anatómica en el tejido cervical. Se obtuvieron variaciones del mismo orden de magnitud en el parámetro reconstruido con el modelo numérico KV (**Capítulo 12**). Una de las limitaciones de este estudio está relacionada con la prensa usada para los ensayos uniaxiales de tracción. La tolerancia de la célula de carga es 0.1 N, lo que no permite obtener los datos experimentales considerando pequeñas deformaciones, en las que se necesitan tolerancias alrededor de dos órdenes de magnitud inferiores. En esta tesis doctoral, la propagación de las ondas de torsión se llevó a cabo considerando pequeñas deformaciones y, por lo tanto, futuros trabajos son necesarios en los que la célula de carga tenga una mayor tolerancia para validar los parámetros mecánicos reconstruidos en tejido cervical mediante el enfoque de PIP.

Evaluación de la gestación

Objetivo 5: Evaluar la viabilidad y fiabilidad de la técnica elastográfica de ondas de torsión para proporcionar datos consistentes acerca de los cambios en la rigidez del tejido cervical durante el embarazo.

Los resultados presentados en el **Capítulo 15** mostraron, por primera vez *in-vivo*, la viabilidad de las ondas de torsión para para medir objetivamente la elasticidad cervical en mujeres embarazadas. Se demostró que es posible cuantificar objetivamente la rigidez cervical durante el embarazo usando elastografía de ondas de torsión. Además los resultados experimentales muestran la seguridad de la técnica para ser usada en mujeres embarazadas. Todos lo valores obtenidos estaban lejos de los límites establecidos por la Administración de Alimentos y Medicamentos.

Se diseñó un estudio preliminar (**Capítulo 10**) con el propósito de proveer información *in-vivo* sobre la elasticidad cervical durante un embarazo normal. Un total de 18 mujeres sanas fueron reclutadas de sus visitas médicas rutinarias durante en el embarazo, y exploraciones con la técnica TWE se llevaron a cabo. Todas las mujeres que participaron en el estudio eran mujeres con embarazos sin ninguna complicación, con una media de 26.4 (16 semanas-35 semanas + 5 días) semanas de gestación. Los criterios de exclusión fueron múltiples embarazos, cirugías cervicales anteriores y pacientes con información relativa a cambios malignos en el cervix.

Los datos observados confirman, primero la hipótesis de que la técnica TWE tiene la capacidad de cuantificar la rigidez cervical definida por su módulo elástico y, en segundo

lugar, que la rigidez cervical decrece durante el embarazo. En este trabajo se usaron tres frecuencias para estudiar los efectos de atenuación en el tejido. La configuración de frecuencia seleccionada fue de 1 kHz, frecuencia que era la óptima para obtener la máxima amplitud de las señales, las mejores reconstrucciones de velocidad de onda de cizalla y una correlación significativa frente a la edad gestacional. En algunas medidas, frecuencias mayores o iguales a 1.5 kHz generaban amplitudes de señal similares a la amplitud del sonido, probablemente debido a la atenuación y, consecuentemente, se obtuvieron valores anómalos de la rigidez cervical. Por otro lado, el ruido enmascaraba la amplitud de la señal en algunas medidas con frecuencias inferiores o iguales a 0.5 kHz. Para la frecuencia seleccionada, se encontró una mayor asociación entre la edad gestacional y la rigidez cervical, comparada con la correlación entre la longitud cervical y la edad gestacional. Adicionalmente, no se encontraron correlaciones significativas entre la rigidez y la longitud cervical.

Las limitaciones de esta investigación están relacionadas con la naturaleza de la propagación de las ondas de torsión en tejido cervical, así como su compleja microarquitectura. En la literatura se han asumido algunas hipótesis mecánicas acerca de las características histológicas del cervix para estimar la rigidez de cizalla, asumiendo un medio homogéneo, no viscoso, isótropo y semi-infinito. La ecuación empleada en este estudio para estimar la rigidez cervical está basada en la velocidad de grupo de las ondas de cizalla. Sin embargo, el comportamiento del tejido es dispersivo, a mayor frecuencia mayor velocidad de onda y, por lo tanto, las técnicas basadas en la velocidad de fase proporcionarían un cálculo directo del módulo de cizalla. La técnica basada en el tiempo de vuelo mide la velocidad de grupo de la onda, la cual es dependiente de la envolvente de la onda elástica propagada.

Finalmente, debido a la naturaleza exploratoria de este estudio sobre la viabilidad de la técnica de ondas de torsión propuesta para evaluar la maduración cervical, se reclutó una pequeño grupo de pacientes. Para extender la validez y fiabilidad de la tecnología propuesta, se necesitan estudios complementarios más completos en los que se emplee el método propuesto en esta tesis (**Capítulo 8**), basado en el enfoque PIP para inferir las propiedades viscoelásticas del modelo KV en el tejido cervical a partir de la técnica TWE. Se cree que las ondas de torsión son una herramienta con potencial para diagnosticar objetivamente los trastornos provocados por una maduración cervical temprana y el parto prematuro.

Part V

APPENDICES

A

Matlab codes

This appendix contains the MATLAB® code from the different algorithms that have been employed in the reconstruction of the emitted signal that was used as boundary condition in the numerical models implemented in this thesis (Chapters 7 and 8).

```matlab
%%%%%%%%%%%%%%%%%%%%%%%%%%%%%%%%%%%%%%%%%%%%%%%%%%%%%%%%%%%%%%%%%%%%%%%%%%%%%
% Cross-correlation algorithm to reconstruct the emitted signal used in the three numerical models - Elastic, Kelvin-Voigt and Maxwell models
% Antonio Callejas 2017-05-08
%%%%%%%%%%%%%%%%%%%%%%%%%%%%%%%%%%%%%%%%%%%%%%%%%%%%%%%%%%%%%%%%%%%%%%%%%%%%%

addpath([pwd '/Videos Jaen 24 mayo']);

clear all; clc; close all;

% Read video frames
v = VideoReader('Peso_100_Per_10_A_50_00.avi'); % Load the movie
frames=read(v); % Read frame by frame

% Declaring variables
oversampling=1;
numFrames=v.NumberOfFrames; % Store frames in a matrix

```

```
% Declaring the reference frame
video = frames(:,:,1);

centers(1)=300; % x coordinate of the center
centers(2)=438; % y coordinate of the center
radii=145;      % radio of the circumference

% Creation of the circular mask
[rr, cc] = meshgrid(1:768,1:768);
C = sqrt((rr-centers(1)).^2+(cc-centers(2)).^2)<=radii; % circular
    mask
C=imresize(double(C),oversampling,'bicubic'); % oversampling of the
     mask
video=im2double(video).*C;

% Crop the frame with the circular mask
I1 = imcrop(video,[round(centers(1))-round(radii) round(centers(2))
    -round(radii) 2*round(radii) 2*round(radii)]);

% Add elements in x coordinate in case the disk emitter is cut in
    the video
if size(I1,1)<2*radii
tam1=size(I1,1);
recorrido=2*radii-tam1;
for count=1:recorrido
I1(count+tam1,1:2*radii)=0;
end
end

% Add elements in y coordinate in case the disk emitter is cut in
    the video
if size(I1,2)<2*radii
tam2=size(I1,2);
recorrido2=2*radii-tam2;
for count=1:recorrido2
I1(count+tam2,1:2*radii)=0;
end
end

%  Loop to sweep all frames
```

```
53 vectorMaxAngulos=[];
54 for iii=1:numFrames
55
56 iii   % Display on the screen the progress of the calculation
57
58 % Declaring the frame i
59 video2 = im2double(frames(:,:,iii));
60
61 % Creation of the circular mask
62 [rr, cc] = meshgrid(1:768,1:768);
63 C = sqrt((rr-centers(1)).^2+(cc-centers(2)).^2)<=radii;
64
65 % Oversampling of the mask
66 C=imresize(double(C),oversampling,'bicubic');
67
68 video2=video2.*C;
69
70 % Crop the frame with the circular mask
71 I2 = imcrop(video2,[round(centers(1))-round(radii) round(centers(2)
    )-round(radii) 2*round(radii) 2*round(radii)]);
72
73 % Add elements in x coordinate in case the disk emitter is cut in
    the video
74 if size(I2,1)<2*radii
75 tam3=size(I2,1);
76 recorrido3=2*radii-tam3;
77 for count=1:recorrido3
78 I2(count+tam3,1:2*radii)=0;
79 end
80 end
81
82 % Add elements in y coordinate in case the disk emitter is cut in
    the video
83 if size(I2,2)<2*radii
84 tam4=size(I2,2);
85 recorrido4=2*radii-tam4;
86 for count=1:recorrido4
87 I2(count+tam4,1:2*radii)=0;
88 end
89 end
```

```
90
91 % Definition of the angle swept by the loop
92 vectorangulos=[-45:0.1:45];i=1;
93
94 % Loop to calculate the rotated angle in each frame
95 for angle=vectorangulos
96 disp(angle);
97 I11=imrotate(I1,angle,'bicubic','crop'); % Rotation of the
       reference frame
98 rrr(i)=corr2(I11,I2); % Cross_correlation between frames
99 i=i+1;
100 end
101 angulo=vectorangulos(find(rrr==max(rrr))); % Search for the highest
       cross-correlation
102
103 vectorMaxAngulos=[vectorMaxAngulos angulo]; % Storage of the angle
       with maximum cross-correlation
104
105 plot(vectorMaxAngulos) % Plotting the reconstructed signal in terms
       of rotated angle
106 end
107
108 % Save the rotated angle for each frame
109 save('result/Peso_100_Per_10_A_50_00.mat','vectorMaxAngulos');
```

B

Matlab codes

This appendix contains the MATLAB® code from the different algorithms that have been employed in the calculation of the shear wave dispersion curve using Shear Wave Elastography data. The inverse problem algorithm was used in Chapters 8 and 13.

```
%%%%%%%%%%%%%%%%%%%%%%%%%%%%%%%%%%%%%%%%%%%%%%%%%%%%%%%%%%%%%%%%%%%%
% Inverse problem algorithm to obtain shear wave dispersion curve from Shear Wave Elastography data
% Antonio Callejas, Guillermo Rus 2018-05-15
%%%%%%%%%%%%%%%%%%%%%%%%%%%%%%%%%%%%%%%%%%%%%%%%%%%%%%%%%%%%%%%%%%%%

% Clear variables
clear all
clc

% Load the file
load('19_03_2019_gelatine_7_5gel_10oil.mat')

% Declaring variables
window=1:100; % Average values in the Y dimension of the speed field
l2x=0.197; % Constant to convert the wavelength (Verasonics output variable) to meters
```

```
16 xs=SWIaxisChannel*12x*1e-3; % Assignment of variable X data (
       propagation distance) and change to international system units
17 time_mov=(1:(na-1))*100*1e-6; % Assignment of variable data T (
       elapsed time) and change to international system units
18
19 xinicio=60; % Start x value to filter data
20 xfin=110; % Final x value to filter data
21 tinicio=10; % Start time value to filter data
22 tfin=30; % End time value to filter data
23 uxt=squeeze(mean(SWIgrusMovies(window,xinicio:xfin,tinicio:tfin)
       ,1))/SWIgrusAveraging; % Displacement field used after
       filtering data
24 xs=xs(xinicio:xfin); time_mov=time_mov(tinicio:tfin); % Variable X
        and T after filtering
25
26 figure(1)
27 surf(uxt) % Plot the displacement field in 3D
28
29 X=interpn(uxt,4,'spline'); % Interpolation to increase the
       resolution in the displacement field data
30 X=diff(X); % Obtaining speeds from displacements
31
32 xs1=linspace(xs(1),xs(end),size(X,1)); % Interpolation in x axis
33 time=linspace(time_mov(1),time_mov(end),size(X,2)); %
       Interpolation in time
34
35 % Obtaining the phase of the wave for each frequency
36 [pf,fr,Y]=poanf((X(200:300,:))',time(:)',[0 5000],[]); % Function
       to obtain the Fast Fourier Transform
37
38 phase1(200:300,:)=unwrap(angle(Y)); % Function to obtain the phase
        for each of the frequencies
39
40 % Plot the speed field
41 figure
42 plot(time(:)',X(200:300,:)')
43
44 % Plot the Fast Fourier Transform
45 figure
46 plot(fr,pf)
```

```
47
48
49  % Filter to remove steps in the phase of the wave
50  for zzzz=1:size(phase1,2)
51  for iiii=1:size(phase1,1)-1
52  if abs(phase1(iiii,zzzz)-phase1(iiii+1,zzzz))>pi/20
53  phase1(iiii+1:end,zzzz)=phase1(iiii+1:end,zzzz)-abs(phase1(iiii,
        zzzz)-phase1(iiii+1,zzzz));
54  end
55  end
56  end
57
58  % Loop for calculating the shear wave speed
59  for z=2:length(fr)/2-1;
60  pte=polyfit(transpose(xs1(aa:bb)),phase1(aa:bb,z),1); %
        Calculation of wave phase slopes for each frequency
61  css(z)=fr(z)*2*pi/(-pte(1)); % Shear wave speed for each frequency
62  end
63
64  % Calculation of the wave speed regression line for the
        frequencies
65  freqinicial=1;
66  freqfinal=size(fr,2)/2-1;
67  p = polyfit(fr(freqinicial:freqfinal),css(freqinicial:freqfinal)
        ,1);
68  f = polyval(p,fr(freqinicial:freqfinal));
69
70  % Plot shear wave speed versus frequency and linear regression
71  plot(fr(freqinicial:freqfinal),css(freqinicial:freqfinal),fr(
        freqinicial:freqfinal),f)
72  title('Shear Wave Velocity')
73  xlabel('f (Hz)')
74  ylabel('Cs (m/s)')
```

C

Matlab codes

This appendix contains the MATLAB® codes from the different algorithms that have been used for the Kelvin-Voigt torsional wave propagation model described in Chapters 7, 12, and Appendix D.

C.1 Main code

```
%%%%%%%%%%%%%%%%%%%%%%%%%%%%%%%%%%%%%%%%%%%%%%%%%%%%%%%%%%%%%%%%%%
% BILAYER KELVIN-VOIGT model
% Iterative process for FDTD 2D simulation in the plane R-Z
% Antonio Callejas, Guillermo Rus, Antonio Gomez  2017-06-05
%%%%%%%%%%%%%%%%%%%%%%%%%%%%%%%%%%%%%%%%%%%%%%%%%%%%%%%%%%%%%%%%%%

% Load data
name1 = 'dat/setup_viscoelastic_bilayer'; run(name1); % Grid data
name2 = 'dat/healthy_cervical_tissue_viscoelastic_bilayer'; run(
    name2); % Media data
load('eps/Peso_100_Por_20_00.mat')

% Time parameters
dt = (1e-6);
tD = ceil(tt/dt); % Number of time steps

% Declaring components of equations (1==r, 2==theta, 3==z)
```

```
17 u2 = 0.*o; v2 = u2; v2_old = u2; % angular displacement and speeds
18 v2_1 = u2; v2_2 = u2; v2_3 = u2; % speeds, and splitted components
19 s12 = u2; s12_1 = u2; s12_2 = u2; % stresses, and splitted
       components
20 s23 = u2; s23_3 = u2;
21
22 % Declaring array to attenuate signals (Absorbing Boundary
       Conditions - ABC)
23 ab=ab_r2;
24 as = [exp(-10.^-(.8:2.2/(ab-2):3)) 1]; ag=o*as(end); % absorber
25
26 for j=0:ab-2
27 ag(round(j+thickness/dz+1),1:round(rS/dr)+1+j) = as(end-j);
28 end
29
30 for k=0:ab-2
31 ag((1):round((thickness/dz)+k),round(rS/dr)+1+k) = as(end-k);
32 end
33
34 % Excitation signal in displacements
35 ft=zeros(tD,1);
36 ft(1:62,1)=vectorMaxAngulos(4:65).*(2*pi*2.1e-3)/360;
37 ft=smooth(ft);
38
39 % Excitation signal in speeds
40 dt1=1e-4; % time steps of recordings with high speed camera
41 dft1 = 1/dt1*diff([2*ft(1)-ft(2); ft]);
42
43 % Time vector
44 time1=(0:1e-4:(length(dft1)*1e-4)-1e-4);
45 time=(0:dt:tt);
46 dft1=interp1(time1,dft1,time);
47 dft1=smooth(dft1);
48
49 %% Iterative process, discrete equations
50
51 % Video setup
52 plotfreq = 20; % time step to catch each frame
53 fi = figure; % creating the figure
```

```
writerObj = VideoWriter('eps/elastic_2D_FDTD_cervix'); % defining
    the video object
open(writerObj); % opening the edition

% Setting the graphs
set(fi,'MenuBar','none','Color',[0.6 0.6 0.6],'NumberTitle','off','
    units','pixels');
colormap jet; iptsetpref('ImshowBorder','tight');
set(gca,'position',[0 0 1 1],'units','normalized');
tic; clear('signal','mov');

% Loop
for n = 1:tD-1;
if ~mod(n,plotfreq),fprintf('Time step %d / %d    remaining: %dmin\
    n',n,tD,round((tD-n)/n*toc/60)); end; % time integration

% Velocity components at n+1
v2_1 = ag.*v2_1+ag.*(dt./(rho.*dr)).*diff([zeros(zD,1) s12]')';
v2_2 = ag.*v2_2+ag.*(2*dt./(rho.*dist_r)).*((s12+[zeros(zD,1) s12
    (:,1:end-1)])/2);
v2_3 = ag.*v2_3+ag.*(dt./(rho.*dz)).*diff([s23 ; zeros(1,rD)]);

v2_old = v2;
v2 = v2_1+v2_2+v2_3;

% Boundary condition in speeds
v2(1,round(((thick_r_emitter+thick_r_tissue)/dr+1)):round(((
    thick_r_emitter+thick_r_tissue+thick_r_PLA)/dr)))=0;

% Boundary condition, linear excitation
for i=1:round(emitter_ra/dz+1)
v2(thick_PLA/dz+1,i)=1/(round(emitter_ra/dz+1))*i*dft1(n);
end

% Stress components at n+1
s12_1 = ag.*s12_1+ag.*(dt*mo./dr).*diff([v2 zeros(zD,1)]')'...
+ag.*(dt*shv./(dr*dt)).*diff([v2 zeros(zD,1)]')'...
-ag.*(dt*shv./(dr*dt)).*diff([v2_old zeros(zD,1)]')';
s12_2 = ag.*s12_2-ag.*(dt*mo./(dist_r)).*(v2+[v2(:,2:end) zeros(zD
    ,1)]/2)...
```

```
88 -ag.*(dt*shv./(dt*dist_r)).*(v2+[v2(:,2:end) zeros(zD,1)]/2)...
89 +ag.*(dt*shv./(dt*dist_r)).*(v2_old+[v2_old(:,2:end) zeros(zD,1)
       ]/2);
90 s23_3 = ag.*s23_3+ag.*(dt*mo./dz).*diff([zeros(1,rD); v2])...
91 +ag.*(dt*shv./(dz*dt)).*diff([zeros(1,rD); v2])...
92 -ag.*(dt*shv./(dz*dt)).*diff([zeros(1,rD); v2_old]);
93 s12 = s12_1+s12_2;
94 s23 = s23_3;
95
96 % Boundary conditions
97 s23(1,round(((thick_r_emitter)/dr+1)):round(((thick_r_emitter+
       thick_r_tissue)/dr)))=0;
98 s23(1,round(((thick_r_emitter+thick_r_tissue+thick_r_PLA)/dr+1)):
       round(((rS)/dr)))=0;
99
100 % Showing the pictures
101 if ~mod(n,plotfreq), %% plot every plotfreq steps
102 imagesc((ab_r1+1:rD-ab_r2-1)*dr,(ab_z1+1:zD-ab_z2)*dz,u2(ab_z1+1:zD
       -ab_z2,ab_r1+1:rD-ab_r2),[-20e-5 20e-5]); axis off; axis equal;
       set(gcf, 'Name', sprintf('t=%.3f us FDTD',n*dt*1e6)); colormap(
       hot); drawnow;
103 frame=getframe; writeVideo(writerObj,frame); %recording the movie
104 end;
105
106 % Saving the stress and speed signals measured at the PLA's
       location
107 v22(:,n)=v2(2,round((thick_r_emitter+thick_r_tissue)/dr):round((
       thick_r_emitter+thick_r_tissue+thick_r_PLA)/dr));
108 s23_record(:,n)=s23(2,round((thick_r_emitter+thick_r_tissue)/dr):
       round((thick_r_emitter+thick_r_tissue+thick_r_PLA)/dr));
109
110 end;
111
112 toc, close(writerObj);
113
114 siz=size(s23_record);
115 senial=zeros(siz(2),1);
116 senial=senial';
117
118 % Saving the stress signals
```

```
for iiii=1:round(thick_r_PLA/dr)
senial=senial+squeeze(s23_record(iiii,1:round(tt/dt)));
end
senial=senial/(thick_r_PLA/dr)*1.98*0.78*1.8275e-4; % signal multiplied by a correction factor

% Saving output variables
save('eps/kelvin_voigt_bilayer.mat','v22','senial','time','s23_record','dft1');
```

C.2 Code for setting the 2D geometry and probe configuration

```
%%%%%%%%%%%%%%%%%%%%%%%%%%%%%%%%%%%%%%%%%%%%%%%%%%%%%%%%%%%%%%%%%%%%%%%%%%%
% GEOMETRY AND DEVICE CONFIGURATION, 2D DOMAIN R-Z FDTD MODEL
% Antonio Callejas   2017-06-05
%%%%%%%%%%%%%%%%%%%%%%%%%%%%%%%%%%%%%%%%%%%%%%%%%%%%%%%%%%%%%%%%%%%%%%%%%%%

% Layer thickness in Z direction
thick_PLA = 0e-3; % PLA thickness (receiver)
%thick_1 = 1e-3; % inferred value with PIP
thick_2 = 6e-3-thick_1; % thickness of the second layer
thickness = 6e-3;

% Layer thickness in R direction
thick_r_emitter = 2.1e-3; % emitter
thick_r_tissue = 3.4e-3; % tissue
thick_r_PLA = 2e-3; % PLA

% 2D domain and total time
rS = 8.5e-3; % real radius of domain [m]
zS = thickness; % real size of domain at Z direction [m]
tt = 12.0e-3; % total time [s]
dr = 75e-6; % spacing r [m]
dz = dr; % spacing z [m]
ab_r1 = 0; % number of elements in the absorber layers radial inside
ab_r2 = 100; % number of elements in the absorber layers radial outside
ab_z1 = 0; % number of elements in the absorber layers top surface
ab_z2 = 100; % number of elements in the absorber layers botton surface
```

```

% Configuration of emitters and receivers:
emitter_ra = 2.1e-3; % emitter radius [m]

% Grid
rD = round((rS/dr+ab_r1+ab_r2)/2)*2; % number of elements in R direction
zD = round((zS/dz+ab_z1+ab_z2)/2)*2; % number of elements in Z direction
o = ones(zD,rD); % empty grid
```

C.3 Code for setting the properties of the medium

```
%%%%%%%%%%%%%%%%%%%%%%%%%%%%%%%%%%%%%%%%%%%%%%%%%%%%%%%%%%%%%%%%%%%%%%%%%%%%%%%%
% CERVICAL TISSUE MECHANICAL PROPERTIES, 2D FDTD MODEL
% Antonio Callejas, Guillermo Rus    2017-06-05
%%%%%%%%%%%%%%%%%%%%%%%%%%%%%%%%%%%%%%%%%%%%%%%%%%%%%%%%%%%%%%%%%%%%%%%%%%%%%%%%

% Mechanical parameters:
mo=o; % shear stiffness [Pa]
mo(:,:)=mo_2; % defined by PIP

rho=o; % density [kg/m^3]
rho(:,:)=1000;

shv=o; % viscosity [Pa*s] (shear viscosity)
shv(:,:)=shv_2; % defined by PIP

% Matrix of distances
rs=8.5e-3; % real radius of domain [m]
for di=1:rD
dist_r(1:zD,di+1)=dr*di;
end
dist_r = dist_r(:,2:end); % matrix of distances

% Cervical tissue - First layer
%mo_1    = 4610; % defined by PIP
rho_1   = 1000;    rho_2   = 1000;
%shv_1   = 1; % defined by PIP

```

```
28 mo (round(thick_PLA/dz+1):round((thick_PLA+thick_1)/dz+1),1:round(
       rs/dr+1)) = mo_1; % shear stiffness [Pa]
29 rho(round(thick_PLA/dz+1):round((thick_PLA+thick_1)/dz+1),1:round(
       rs/dr+1)) = rho_1; % density [kg/m^3]
30 shv(round(thick_PLA/dz+1):round((thick_PLA+thick_1)/dz+1),1:round(
       rs/dr+1)) = shv_1; % viscosity [Pa*s] (shear viscosity)
```

D

Viscoelastic models equations

This appendix describes the equations for the elastic, Kelvin-Voigt and Maxwell models employed in Chapters 7 and 12. The equations are simplified according to the axial symmetry hypothesis and that in the propagation of the torsional waves along the tissue only shear waves are considered, removing the compressional waves.

D.1 Elastic model

It is well known that the equations that govern the propagation of the mechanical waves are expressed in terms of partial differential equations, being the displacement field unknown.

The dynamic equilibrium equation independent of the coordinate system is as follows:

$$\nabla\sigma + F = \rho\ddot{u} \tag{D.1}$$

where ρ denotes the tissue density, σ the stress tensor, u particle displacement and F is the volume force density.

The dynamic equilibrium equation is as split in the equations below [239]:

$$\begin{aligned}
r \Rightarrow \rho\ddot{u}_r &= \frac{\partial\sigma_{rr}}{\partial r} + \frac{1}{r}\frac{\partial\sigma_{r\theta}}{\partial\theta} + \frac{\partial\sigma_{rz}}{\partial z} + \frac{1}{r}(\sigma_{rr} - \sigma_{\theta\theta}) + F_r \\
\theta \Rightarrow \rho\ddot{u}_\theta &= \frac{\partial\sigma_{r\theta}}{\partial r} + \frac{1}{r}\frac{\partial\sigma_{\theta\theta}}{\partial\theta} + \frac{2}{r}\sigma_{r\theta} + \frac{\partial\sigma_{\theta z}}{\partial z} + F_\theta \\
z \Rightarrow \rho\ddot{u}_z &= \frac{\partial\sigma_{rz}}{\partial z} + \frac{1}{r}\frac{\partial\sigma_{\theta z}}{\partial\theta} + \frac{1}{r}\sigma_{rz} + \frac{\partial\sigma_{zz}}{\partial z} + F_z
\end{aligned} \tag{D.2}$$

The relationship between the stress and the strain tensors for an elastic medium is established with the following constitutive equation:

$$\sigma_{ij} = \lambda \epsilon_{kk} \delta_{ij} + 2\mu \epsilon_{ij} \tag{D.3}$$

where λ and μ are the Lamé constants, ϵ is the strain tensor and δ is the Kronecker delta.

Finally, the displacement field u is related to the strain tensor ϵ according to the kinematic relation as follows:

$$\epsilon = \frac{1}{2}\left[\nabla u + (\nabla u)^T\right] \tag{D.4}$$

The components of the gradient of a displacement field in cylindrical coordinates are:

$$\nabla u = \begin{bmatrix} \dfrac{\partial u_r}{\partial r} & \dfrac{1}{r}\dfrac{\partial u_r}{\partial \theta} - \dfrac{u_\theta}{r} & \dfrac{\partial u_r}{\partial z} \\ \dfrac{\partial u_\theta}{\partial r} & \dfrac{1}{r}\dfrac{\partial u_\theta}{\partial \theta} + \dfrac{u_r}{r} & \dfrac{\partial u_\theta}{\partial z} \\ \dfrac{\partial u_z}{\partial r} & \dfrac{1}{r}\dfrac{\partial u_z}{\partial \theta} & \dfrac{\partial u_z}{\partial z} \end{bmatrix} \tag{D.5}$$

The components of the strain tensor are:

$$\varepsilon_{rr} = \frac{\partial u_r}{\partial r} \tag{D.6}$$

$$\varepsilon_{r\theta} = \frac{1}{2}\left[\frac{1}{r}\frac{\partial u_r}{\partial \theta} + \frac{\partial u_\theta}{\partial r} - \frac{u_\theta}{r}\right] \tag{D.7}$$

$$\varepsilon_{rz} = \frac{1}{2}\left[\frac{\partial u_r}{\partial z} + \frac{\partial u_z}{\partial r}\right] \tag{D.8}$$

$$\varepsilon_{\theta z} = \frac{1}{2}\left[\frac{\partial u_\theta}{\partial z} + \frac{1}{r}\frac{\partial u_z}{\partial \theta}\right] \tag{D.9}$$

$$\varepsilon_{\theta\theta} = \frac{1}{r}\left[\frac{\partial u_\theta}{\partial \theta} + u_r\right] \tag{D.10}$$

$$\varepsilon_{zz} = \frac{\partial u_z}{\partial z} \tag{D.11}$$

Let us denote $\psi = \epsilon_{rr} + \epsilon_{\theta\theta} + \epsilon_{zz}$. The components of the constitutive equation are:

$$\sigma_{rr} = \lambda\psi + 2\mu\frac{\partial u_r}{\partial r} \tag{D.12}$$

$$\sigma_{\theta\theta} = \lambda\psi + \frac{2\mu}{r}\left[\frac{\partial u_\theta}{\partial \theta} + u_r\right] \tag{D.13}$$

$$\sigma_{zz} = \lambda\psi + 2\mu\frac{\partial u_z}{\partial z} \tag{D.14}$$

$$\sigma_{r\theta} = \mu\left[\frac{1}{r}\frac{\partial u_r}{\partial \theta} + \frac{\partial u_\theta}{\partial r} - \frac{u_\theta}{r}\right] \tag{D.15}$$

$$\sigma_{rz} = \mu\left[\frac{\partial u_z}{\partial_z} + \frac{\partial u_z}{r}\right] \tag{D.16}$$

$$\sigma_{\theta z} = \mu\left[\frac{\partial u_\theta}{\partial z} + \frac{1}{r}\frac{\partial u_z}{\partial \theta}\right] \tag{D.17}$$

Taking into account the nature of torsional waves propagation, displacements in r and z directions are zero ($u_r = 0, u_z = 0$), the strain equations are simplified as follows:

$$\epsilon_{rr} = 0 \tag{D.18}$$

$$\varepsilon_{r\theta} = \frac{1}{2}\left[\frac{\partial u_\theta}{\partial r} - \frac{u_\theta}{r}\right] \tag{D.19}$$

$$\varepsilon_{rz} = 0 \tag{D.20}$$

$$\varepsilon_{\theta\theta} = \frac{1}{r}\frac{\partial u_\theta}{\partial \theta} \tag{D.21}$$

$$\varepsilon_{\theta z} = \frac{1}{2}\frac{\partial u_\theta}{\partial z} \tag{D.22}$$

$$\varepsilon_{zz} = 0 \tag{D.23}$$

Therefore, after applying the previous simplifications, $\psi = \frac{1}{r}\frac{\partial u_\theta}{\partial \theta}$

$$\sigma_{rr} = \lambda\frac{1}{r}\frac{\partial u_\theta}{\partial \theta} \tag{D.24}$$

$$\sigma_{r\theta} = \mu\left[\frac{\partial u_\theta}{\partial r} - \frac{u_\theta}{r}\right] \tag{D.25}$$

$$\sigma_{rz} = 0 \tag{D.26}$$

$$\sigma_{\theta\theta} = \lambda\frac{1}{r}\frac{\partial u_\theta}{\partial \theta} + \frac{2\mu}{r}\frac{\partial u_\theta}{\partial \theta} \tag{D.27}$$

$$\sigma_{\theta z} = \mu\frac{\partial u_\theta}{\partial z} \tag{D.28}$$

$$\sigma_{zz} = \lambda \frac{1}{r} \frac{\partial u_\theta}{\partial \theta} \tag{D.29}$$

The hypothesis of axial symmetry is $\frac{\partial}{\partial \theta} = 0$.

$$\sigma_{rr} = 0 \tag{D.30}$$

$$\sigma_{r\theta} = \mu \left[\frac{\partial u_\theta}{\partial r} - \frac{u_\theta}{r} \right] \tag{D.31}$$

$$\sigma_{rz} = 0 \tag{D.32}$$

$$\sigma_{\theta\theta} = 0 \tag{D.33}$$

$$\sigma_{\theta z} = \mu \frac{\partial u_\theta}{\partial z} \tag{D.34}$$

$$\sigma_{zz} = 0 \tag{D.35}$$

The simplified dynamic equilibrium equation is defined as:

$$r \Rightarrow \quad 0 = 0 \tag{D.36}$$

$$\theta \Rightarrow \mu \frac{\partial^2 u_\theta}{\partial r^2} - \frac{\mu}{r} \frac{\partial u_\theta}{\partial r} + \mu \frac{u_\theta}{r^2} + \frac{2\mu}{r} \frac{\partial u_\theta}{\partial r} - \frac{2\mu u_\theta}{r^2} + \mu \frac{\partial^2 u_\theta}{\partial z^2} = \rho \ddot{u_\theta} \tag{D.37}$$

$$z \Rightarrow \quad 0 = 0 \tag{D.38}$$

The following equations are obtained by combining three different types of equations: dynamic equilibrium equation, the constitutive equation for an elastic medium and the linear kinematic equation:

$$\begin{cases} \rho \ddot{u_\theta} = \dfrac{\partial \sigma_{r\theta}}{\partial r} + \dfrac{2}{r} \sigma_{r\theta} + \dfrac{\partial \sigma_{\theta z}}{\partial z} \\ \sigma_{r\theta} = \mu \left[\dfrac{\partial u_\theta}{\partial r} - \dfrac{u_\theta}{r} \right] \\ \sigma_{\theta z} = \mu \dfrac{\partial u_\theta}{\partial z} \end{cases} \tag{D.39}$$

We can write the equations in terms of velocities to remove one-time derivative ($\ddot{u_\theta} = \dot{v_\theta}$, $\dot{u_\theta} = v_\theta$),

$$\begin{cases} \rho\dot{v}_\theta = \dfrac{\partial\sigma_{r\theta}}{\partial r} + \dfrac{2}{r}\sigma_{r\theta} + \dfrac{\partial\sigma_{\theta z}}{\partial z} \\ \dot{\sigma}_{r\theta} = \mu\left[\dfrac{\partial v_\theta}{\partial r} - \dfrac{v_\theta}{r}\right] \\ \dot{\sigma}_{\theta z} = \mu\dfrac{\partial v_\theta}{\partial z} \end{cases} \tag{D.40}$$

D.2 Kelvin-Voigt model

With the aim of implementing the Kelvin-Voigt model in finite differences, stress and strain tensors are split into volumetric and deviatoric parts with the objective of simplifying the equations [205],

$$\sigma_{ij} = \underbrace{-p\delta_{ij}}_{\text{volumetric}} + \underbrace{\tau_{ij}}_{\text{deviatoric}}, p = -\frac{1}{3}\sigma_{kk} \tag{D.41}$$

$$\epsilon_{ij} = \underbrace{-v\delta_{ij}}_{\text{volumetric}} + \underbrace{d_{ij}}_{\text{deviatoric}}, v = -\frac{1}{3}\epsilon_{kk} \tag{D.42}$$

where p is the hydrostatic pressure, v the volumetric strain, τ_{ij} the deviatoric stress tensor and d_{ij} the deviatoric strain tensor.

The equations presented above are based on the assumption that the medium is isotropic elastic, notwithstanding, soft tissues are viscoelastic media, therefore, a different law is required. Following the references found in the literature [65, 205, 206, 207], the linear and viscous terms are adopted for the 3D Kelvin-Voigt model,

$$\begin{aligned} p &= \underbrace{3Kv}_{\text{linear elastic}} + \underbrace{3\eta^v\dot{v}}_{viscous} \\ \tau_{ij} &= \underbrace{2\mu d_{ij}}_{\text{linear elastic}} + \underbrace{2\eta\dot{d}_{ij}}_{\text{viscous}} \end{aligned} \tag{D.43}$$

where K is the compressional modulus and η and η^v are the shear and volumetric viscosity respectively.

Taking into account that the propagation of torsional waves produces shear stresses, only deviatoric components (τ_{ij}) are considered ($p = v = 0$). According to the schematic representation of the Kelvin-Voigt model, the total stress is the sum of the elastic and viscous terms.

$$\sigma_{ij} = \tau_{ij} = 2\mu d_{ij} + 2\eta\dot{d}_{ij} = 2\mu\epsilon_{ij} + 2\eta\dot{\epsilon}_{ij} \tag{D.44}$$

Considering the dynamic equilibrium equation (Equation D.2), the kinematic relation (Equation D.4) and the constitutive equation (Equation D.44), the remaining equations for

the Kelvin-Voigt model after simplifying the problem, as well as transformations to remove one time derivative ($\ddot{u}_\theta = \dot{v}_\theta$) are:

$$\begin{cases} \rho\dot{v}_\theta = \dfrac{\partial\sigma_{r\theta}}{\partial r} + \dfrac{2}{r}\sigma_{r\theta} + \dfrac{\partial\sigma_{\theta z}}{\partial z} \\ \dot{\sigma}_{r\theta} = \mu\left[\dfrac{\partial v_\theta}{\partial r} - \dfrac{v_\theta}{r}\right] + \eta\left[\dfrac{\partial\dot{v}_\theta}{\partial r} - \dfrac{\dot{v}_\theta}{r}\right] \\ \dot{\sigma}_{\theta z} = \mu\dfrac{\partial v_\theta}{\partial z} + \eta\dfrac{\partial\dot{v}_\theta}{\partial z} \end{cases} \tag{D.45}$$

D.3 Maxwell model

Following the same steps as in the KV model, to implement the Maxwell model in finite differences, strain tensor is split into volumetric and deviatoric parts with the aim of simplifying equations (see Equation D.42) [205].

Considering Equation D.44 and for the same reasons as in KV model, only elastic and viscous components of the deviatoric term of the strain tensor are adopted ($v = 0$),

$$d_{ij} = \underbrace{\frac{\tau_{ij}}{2\mu}}_{\text{elastic}}, \dot{d}_{ij} = \underbrace{\frac{\tau_{ij}}{2\eta}}_{\text{viscous}} \tag{D.46}$$

The constitutive equation for the 3D Maxwell model is obtained by adding the elastic and viscous terms presented in Equation D.46,

$$\dot{d}_{ij} = \frac{\dot{\tau}_{ij}}{2\mu} + \frac{\tau_{ij}}{2\eta} \tag{D.47}$$

$$\tau_{ij} = 2\eta\dot{d}_{ij} - \frac{\eta}{\mu}\dot{\tau}_{ij} \tag{D.48}$$

Combining equations D.41 and D.47, it results,

$$\sigma_{ij} = -p\delta_{ij} + 2\eta\dot{\varepsilon}_{ij} - \frac{\eta}{\mu}\dot{\tau}_{ij} \tag{D.49}$$

The constitutive equation after considering $p = 0$, $\dot{\varepsilon} = \dot{d}_{ij}$ and $\dot{\sigma}_{ij} = \dot{\tau}_{ij}$ is as follows,

$$\sigma_{ij} + \frac{\eta}{\mu}\dot{\sigma}_{ij} = 2\eta\dot{\varepsilon}_{ij} \tag{D.50}$$

Taking into account the dynamic equilibrium equation (Equation D.2), the kinematic relation (Equation D.4) and the constitutive equation (Equation D.50), the remaining equations for the Maxwell model after simplifying the problem, as well as transformations to remove one time derivative ($\ddot{u}_\theta = \dot{v}_\theta$) are:

$$\begin{cases} \rho\dot{v}_\theta = \dfrac{\partial\sigma_{r\theta}}{\partial r} + \dfrac{2}{r}\sigma_{r\theta} + \dfrac{\partial\sigma_{\theta z}}{\partial z} \\ \sigma_{r\theta} + \dfrac{\eta}{\mu}\dot{\sigma}_{r\theta} = \eta\left[\dfrac{\partial v_\theta}{\partial r} - \dfrac{v_\theta}{r}\right] \\ \sigma_{\theta z} + \dfrac{\eta}{\mu}\dot{\sigma}_{\theta z} = \eta\dfrac{\partial v_\theta}{\partial z} \end{cases} \tag{D.51}$$

E

Piezoelectricity

In this appendix the physical foundations of piezoelectricity are described. In the numerical models implemented in this thesis (Chapter 7), the propagation of torsional waves is simulated in terms of velocities and stresses. However, the signal received by the torsional wave sensor, composed of four piezoelectric elements, has voltage units. A conversion factor obtained through the constituent piezoelectric equation is necessary.

Piezoelectricity is the ability of certain materials to develop an electrical charge proportional to a mechanical stress (direct effect) or to deform in the presence of an electric field (inverse effect).

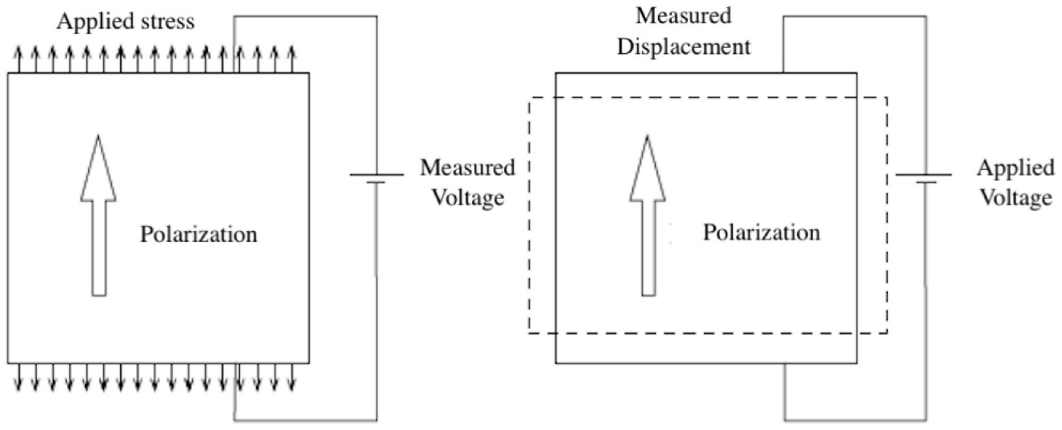

Figure E.1: Left: direct effect on piezoelectric materials. Right: inverse effect

Piezoelectric ceramics are formed by an aggregate of ferroelectric microcrystals, each of which have the same probability of being spatially oriented. Thus, on average, there will be a random arrangement and the net polarization (sum of the dipole moments of each crystal) will be zero. Therefore, it is necessary to subject the ceramic to a polarization process. Polarization process is called to the previous treatment that is made to the ceramic until it reaches the piezoelectric property. From a technical point of view, this process consists of aligning the electric dipoles in such a way that a permanent macroscopic dipole moment appears, preventing it from returning to the initial random situation. For this, a high electric field, polarization field is applied, keeping the temperature slightly below the Curie temperature of the material.

Although equilibrium and compatibility equations, both elastic and electric, remain in the piezoelectric problem, the constitutive relationships change because new coupling properties known as piezoelectric properties appear. The objective is to couple the elastic and electric fields.

Let us introduce the constitutive equations. The constitutive laws are in Stress-Charge form:

$$\mathbf{T} = \mathbf{C}_E \cdot \mathbf{S} + \mathbf{e}^T \cdot \mathbf{E} \tag{E.1}$$

$$\mathbf{D} = \mathbf{e} \cdot \mathbf{S} - \varepsilon_{\mathbf{S}} \cdot \mathbf{E} \tag{E.2}$$

where $\mathbf{C_E}$ is the piezoelectric stiffness matrix, $\mathbf{e}$ is the piezoelectric coupling coefficient matrix, $\mathbf{e}^T$ is its transposed and $\varepsilon_{\mathbf{S}}$ is permitivity coefficient matrix.

For the particular case of cylindrical coordinates, the Stress-Charge matrix is given by

$$\begin{bmatrix} T_{rr} \\ T_{\theta\theta} \\ T_{zz} \\ T_{\theta z} \\ D_z \\ D_\theta \end{bmatrix} = \begin{bmatrix} C_{E11} & C_{E12} & C_{E13} & 0 & 0 & -e_{31} \\ C_{E12} & C_{E11} & C_{E13} & 0 & 0 & -e_{31} \\ C_{E13} & C_{E13} & C_{E33} & 0 & 0 & -e_{33} \\ 0 & 0 & 0 & C_{E44} & -e_{15} & 0 \\ 0 & 0 & 0 & e_{15} & \varepsilon_{11}^S & 0 \\ e_{31} & e_{31} & e_{33} & 0 & 0 & \varepsilon_{33}^S \end{bmatrix} \begin{bmatrix} S_{rr} \\ S_{\theta\theta} \\ S_{zz} \\ 2S_{\theta z} \\ E_z \\ E_\theta \end{bmatrix} \tag{E.3}$$

The strain-charge to stress-charge transformation equations are as follows,

$$\mathbf{C_E} = \mathbf{S_E}^{-1} \tag{E.4}$$

$$\mathbf{e} = \mathbf{d} \cdot \mathbf{S_E}^{-1} \tag{E.5}$$

$$\varepsilon_S = \varepsilon_T - \mathbf{d} \cdot \mathbf{S_E}^{-1} \cdot \mathbf{d^T} \tag{E.6}$$

Figure E.2 shows the polarization of the piezoelectric elements used in the torsional sensor (θ direction), the direction of the electric field (z direction), the piezoelectric dimensions and the deformation of it.

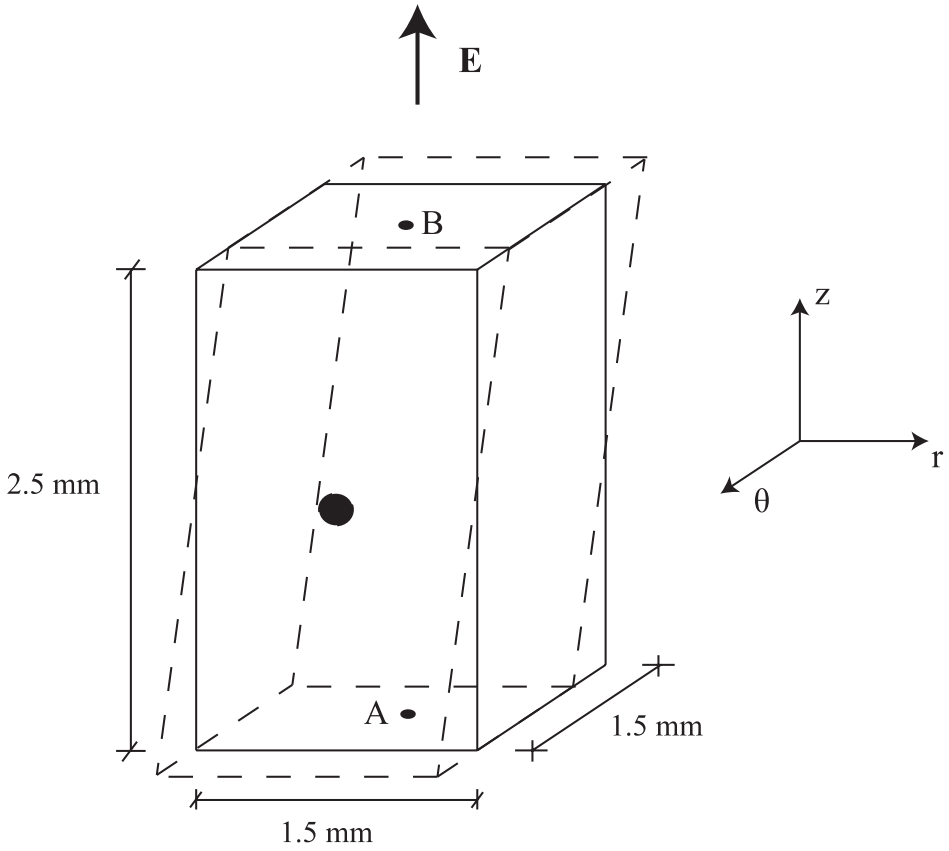

Figure E.2: Schematic view of the piezoelectric element used in the torsional sensor.

The electric field can be obtained as the gradient of a scalar potential: the electric potential,

$$\mathbf{E} = -\nabla \cdot \phi \tag{E.7}$$

$$\mathbf{E}(z) = \frac{\partial \phi(z)}{\partial z} \tag{E.8}$$

$$\phi(z) = \int_A^B \mathbf{E}_z dz \tag{E.9}$$

$$\phi(B) - \phi(A) = \bar{\mathbf{E}}_z L_{AB} \tag{E.10}$$

where L_{AB} is the length of the piezoelectric element in z direction and $\bar{\mathbf{E}}_3$ the average value of the electric field between A and B.

The piezoelectric material used in the torsional sensor is NCE51 which is a standard soft material, particularly suitable for actuators and low power non-resonant applications.

The elastic compliance matrix is,

$$\mathbf{S_E} = \begin{bmatrix} 17 & -5.36 & -8.69 & 0 & 0 & 0 \\ -5.36 & 17 & -8.69 & 0 & 0 & 0 \\ -8.69 & -8.69 & 21.3 & 0 & 0 & 0 \\ 0 & 0 & 0 & 48.9 & 0 & 0 \\ 0 & 0 & 0 & 0 & 48.9 & 0 \\ 0 & 0 & 0 & 0 & 0 & 44.6 \end{bmatrix} * 10^{-12} \ [\mathrm{m}^2/\mathrm{N}] \tag{E.11}$$

The charge constant matrix is,

$$\mathbf{d} = \begin{bmatrix} 0 & 0 & 0 & 0 & 669 & 0 \\ 0 & 0 & 0 & 669 & 0 & 0 \\ -208 & -208 & 443 & 0 & 0 & 0 \end{bmatrix} * 10^{-12} \ [\mathrm{C}/\mathrm{N}] \tag{E.12}$$

For a high-impedance receiver, the equation that relates the stress with the electric field is [290],

$$\mathbf{T}_{\theta z} \simeq e_{15}^{t} \mathbf{E}_3 \tag{E.13}$$

The piezoelectric coupling coefficient matrix is obtained using the equation E.5,

$$\mathbf{e} \quad = \quad \mathbf{d} \cdot \mathbf{S_E}^{-1} = \begin{bmatrix} 0 & 0 & 0 & 0 & 13.68 & 0 \\ 0 & 0 & 0 & 13.68 & 0 & 0 \\ -5.99 & -5.99 & 15.9 & 0 & 0 & 0 \end{bmatrix} * [\mathrm{C}/\mathrm{m}^2] \tag{E.14}$$

and its transpose,

$$\mathbf{e}^t \quad = \quad \begin{bmatrix} 0 & 0 & -5.99 \\ 0 & 0 & -5.99 \\ 0 & 0 & 15.90 \\ 0 & 13.68 & 0 \\ 13.68 & 0 & 0 \\ 0 & 0 & 0 \end{bmatrix} * [\mathrm{C}/\mathrm{m}^2] \tag{E.15}$$

Combining the equations E.16 and E.13, the relationship between the measured signal (in volts) and the stress received by the piezoelectric element ($\sigma_{\theta z}$ - see Figure E.3) is,

$$Signal(Volts) = \bar{\mathbf{E}}_z L_{AB} = \frac{L_{AB}}{e_{15}^t} \mathbf{T}_{\theta z} \tag{E.16}$$

The multiplication factor that is used in the numerical model is $1.8275e-4 \ \ m^3/C$.

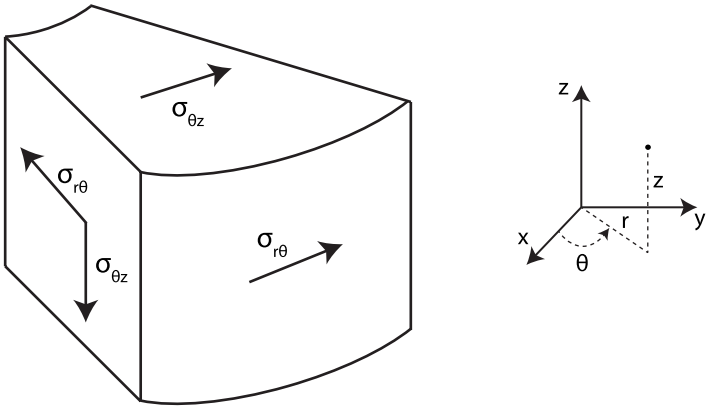

Figure E.3: Infinitesimal element according to a cyclindrical coordinate system. Representation of stresses σ after axial symmetric simplifications.

F

Contributions

The outcomes, transversal applications and contributions from this thesis, are reflected in the refereed journal publications, national and international conferences, and books enumerated below.

- Refereed journal publications:
  - ▷ A. Callejas, A. Gomez, I. H. Faris, J. Melchor and G. Rus. "Kelvin-Voigt parameters reconstruction of cervical tissue-mimicking phantoms using torsional wave elastography," *Sensors (Basel)*, 25; 19(15), 2019.
  - ▷ P. Massó, A. Callejas, J. Melchor, F. S. Molina and G. Rus. "In vivo measurement of cervical elasticity on pregnant women by torsional wave technique: a preliminary study," *Sensors (Basel)*, 24; 19(15), 2019.
  - ▷ J. Naranjo, M. Riveiro, A. Callejas, G. Rus and J. Melchor. "Nonlinear torsional wave propagation in cylindrical coordinates to assess biomechanical parameters," *Journal of Sound and Vibration*, 445, p. 103-116, 2019.
  - ▷ A. Callejas and G. Rus. "Experimental configuration to determine the nonlinear parameter β in PMMA and CFRP with the Finite Amplitude Method," *Sensors (Basel)*, 19(5): 1156, 2019.
  - ▷ J. Torres, I. H. Faris and A. Callejas. "Histobiomechanical remodeling of the cervix during pregnancy: proposed framework," *Mathematical Problems in Engineering*, 5957432, 2019.
  - ▷ R. Palma and A. Callejas. "Extended poroelasticity: an analytical solution and its application to p-wave propagation in cervical tissues," *Mathematical Problems in Engineering*, 5280141, 2019.

- ▷ G.Rus, J. Melchor, I. H. Faris, A. Callejas, M. Riveiro, F. S. Molina and J. Torres. "Mechanical biomarkers by torsional shear ultrasound for medical diagnosis," *The Journal of the Acoustical Society of America*, 144, 1747, 2018.
- ▷ A. Callejas, A. Gomez, J. Melchor, M. Riveiro, P. Massó, J. Torres, M. López and G. Rus. "Performance study of a torsional wave sensor and cervical tissue characterization," *Sensors (Basel)*, 11; 17(9), 2017.

- National and international conferences:
  - ▷ A. Callejas, J. Melchor, I. H. Faris, J. Torres and G. Rus. "Assessing viscoelasticity of torsional wave propagation in cervical tissue," *International Congress on Ultrasonics*, 2019.
  - ▷ I. H. Faris, A. Callejas, J. Torres, S. Contreras, J. Melchor and G. Rus. "Ex-vivo human cervix acoustical shear ultrasonic properties," *International Congress on Ultrasonics*, 2019.
  - ▷ J. Melchor, G. Rus, M. Hurtado, E. López, J. Soto, G. Jiménez, A. Callejas et al. "Role of ultrasonic bioreactors in soft tissue mechanics," *International Congress on Ultrasonics*, 2019.
  - ▷ B. Blanco, A. Gomez, I. H. Faris, J. Torres, A. Callejas et al. "Validation of the transurethral shear wave elastography probe in prostate-like gelatine phantoms," *International Congress on Ultrasonics*, 2019.
  - ▷ J. Torres, A. Callejas, I. H. Faris, J. Melchor and G. Rus. "Impact of different contact conditions on the human cervix using a torsional elastographic probe," *International Congress on Ultrasonics*, 2019.
  - ▷ G. Rus, J. Torres, R. Muñoz, J. Melchor, R. Molina, A. Callejas et al. "Mechanical biomarkers by torsional wave elastography for gestational diagnosis," *International Congress on Ultrasonics*, 2019.
  - ▷ G. Rus, A. Callejas et al. "Gestational disorders diagnosis via torsional wave elastography," *27 International Conference on Composites Nano/Engineering*, 2019.
  - ▷ J. Melchor, A. Callejas et al. "Real time mechanical characterization of soft tissue in an ultrasonic bioreactor system," *27 International Conference on Composites Nano/Engineering*, 2019.
  - ▷ Inas H. Faris, A. Callejas et al. "Assessment of mechanical biomarkers of ex-vivo liver samples," *27 International Conference on Composites Nano/Engineering*, 2019.
  - ▷ J. Torres, J. Melchor, A. Callejas et al. "Measuring different performance hypothesis of a torsional wave probe on voluntary women," *27 International Conference on Composites Nano/Engineering*, 2019.
  - ▷ B. Blanco, A. Gómez, J. Torres, Inas H. Faris, A. Callejas et al. "Performance study of a transurethral shear wave probe in prostate phantoms," *27 International Conference on Composites Nano/Engineering*, 2019.
  - ▷ R. Marqués, J. Melchor, I. Sánchez, P. Hernández, O. Roda, M. Alaminos, B. Blanco, Inas H. Faris, J. Torres, A. Callejas et al. "Biomechanical finite element

method model of the proximal carpal row and experimental characterization of the interosseous scapholunate ligament," *27 International Conference on Composites Nano/Engineering*, 2019.

- ▷ A. Callejas, J. Melchor, Inas H. Faris and G. Rus. "Probabilistic inverse problem to characterize cervical tissue mechanical properties," *Euroson*, 2019.
- ▷ Inas H. Faris, A. Callejas, J. Torres, S. Contreras, J. Melchor and G. Rus. "Acoustical biomechanical properties of ex-vivo human cervix," *Euroson*, 2019.
- ▷ J. Melchor, G. Rus, M. Hurtado, E. López, J. Soto, G. Jiménez, A. Callejas et al. "Emerging techniques of ultrasonic bioreactors for soft tissue characterization," *Euroson*, 2019.
- ▷ A. Callejas, J. Melchor, Inas H. Faris and G. Rus. "Selección del modelo viscoelástico de ondas de torsión más plausible para tejido cervical," *VIII Reunión del Capítulo Español de la Sociedad Europea de Biomecánica (ESB)*, 2018.
- ▷ Inas H. Faris, A. Callejas, Juan Melchor and Guillermo Rus. "Propiedades ultrasónicas de cizallamiento acústico de muestras ex-vivo en hígado animal," *VIII Reunión del Capítulo Español de la Sociedad Europea de Biomecánica (ESB)*, 2018.
- ▷ Inas H. Faris, J. Melchor, G. Rus, A. Callejas et al. "In-bioreactor ultrasonic monitoring of 3D culture human engineered cartilage," *World Congress of Biomechanics*, 2018.
- ▷ Inas H. Faris, J. Melchor, G.Rus and A. Callejas. "Experimental analysis and validation of cervical tissue biomechanical properties using SWE," *World Congress of Biomechanics*, 2018.
- ▷ M. Riveiro, J. Naranjo, A. Callejas, Inas H. Faris, R. Muñoz, J. Melchor and G. Rus. "Nonlinear torsional wave propagation in general coordinates to model biomechanical parameters in soft tissue," *World Congress of Biomechanics*, 2018.
- ▷ A. Callejas, M. Riveiro, J. Melchor, J. Torres, Inas H. Faris and G. Rus. "Cervical viscoelastic shear wave propagation model class selection," *World Congress of Biomechanics*, 2018.
- ▷ A. Callejas, J. Melchor, Inas H. Faris and G. Rus. "Tissue ultrasound mechanics and bioreactors," *1st Conference on Structural Dynamics*, 2018.
- ▷ A. Callejas, J. Melchor, M. Riveiro, R. Molina, P. Massó and G. Rus. "Performance study of a torsional ultrasonic transducer for elastography," *23 Congress of the European Society of Biomechanics*, 2017.
- ▷ G. Rus, R. Muñoz, J. Melchor, R. Molina, A. Callejas, M. Riveiro and P. Massó. "Medical diagnosis based on mechanical biomarkers," *23 Congress of the European Society of Biomechanics*, 2017.
- ▷ G. Rus, R. Muñoz, R. Molina, A. Callejas, M. Riveiro, P. Massó and J. Melchor. "A prognostic framework for evolutive biomechanical properties," *23 Congress of the European Society of Biomechanics*, 2017.

- ▷ J. Melchor, G. Rus, R. Muñoz, A. Callejas, P. Massó, R. Molina and M. Riveiro. "Nonlinear shear torsion ultrasound for soft tissue characterization," *23 Congress of the European Society of Biomechanics*, 2017.
- ▷ J. Melchor, A. Callejas et al. "Mechanics of nonlinear ultrasound in soft tissue," *VI Reunión del Capítulo Nacional Español de la Sociedad Europea de Biomecánica*, 2016.
- ▷ J. Melchor, G. Rus, A. Callejas, M. Riveiro. "Nonlinear mixing: evaluation of nonlinear ultrasonic parameter," *EuroRegio*, 2016.
- ▷ G. Rus, J. Melchor, A. Callejas, G. Jiménez, C. Antich, E. López and J. Marchal. "Ultrasonic monitoring of chondrocyte proliferation in a bioreactor," *EuroRegio*, 2016.
- ▷ J. Melchor, G. Rus and A. Callejas. "De la Ingeniería a la Medicina". Noche europea de los investigadores, 2015.
- ▷ G. Rus, J. Melchor and A. Callejas. "Nonlinear ultrasonics for early damage assessment," *Workshop on Acoustic Emission and other NDT Methods*, 2014.

- Books chapters:
  - ▷ R. Muñoz, G. Rus, N. Bochud, D. Barnard, J. Melchor, J. Chiachío, M. Chiachío, S. Cantero, A. Callejas, L. Peralta. *Nonlinear ultrasonics as an early damage signature*, Emerging Design Solutions in Structural Health Monitoring Systems, Advances in Civil and Industrial Engineering Series, *Ed. IGI Global.*

References

[1] Adwoa Baah-Dwomoh, Jeffrey McGuire, Ting Tan, and Raffaella De Vita. Mechanical properties of female reproductive organs and supporting connective tissues: a review of the current state of knowledge. *Applied Mechanics Reviews*, 68(6):060801, 2016, American Society of Mechanical Engineers (ASME).

[2] The University of Utah. Web path - the internet pathology laboratory for medical education, 2019.

[3] K N Singh and P Badkur. *Colposcopic appearance of normal cervix*. Spinger, 2017.

[4] Philip E Castle. Beyond human papillomavirus: the cervix, exogenous secondary factors, and the development of cervical precancer and cancer. *Journal of lower genital tract disease*, 8(3):224–230, 2004.

[5] Jeremy Bercoff, Mickaex0308l Tanter, and M K Fink. Supersonic shear imaging: a new technique for soft tissue elasticity mapping. *IEEE Transactions on Ultrasonics, Ferroelectrics and Frequency Control*, 51:396–409, 2004.

[6] Dorothy L Patton, Soe Soe Thwin, Amalia Meier, Thomas M Hooton, Ann E Stapleton, and David A Eschenbach. Epithelial cell layer thickness and immune cell populations in the normal human vagina at different stages of the menstrual cycle. *American journal of obstetrics and gynecology*, 183(4):967–973, 2000.

[7] S Catheline, J-L Gennisson, G Delon, M Fink, R Sinkus, S Abouelkaram, and J Culioli. Measurement of viscoelastic properties of homogeneous soft solid using transient elastography: An inverse problem approach. *The Journal of the Acoustical Society of America*, 116(6):3734–3741, 2004.

[8] Li Liu, Shefali Oza, Daniel Hogan, Jamie Perin, Igor Rudan, Joy E Lawn, Simon Cousens, Colin Mathers, and Robert E Black. Global, regional, and national causes of child mortality in 2000–13, with projections to inform post-2015 priorities: an updated systematic analysis. *The Lancet*, 385(9966):430–440, 2015.

[9] Jennifer Bryce, Robert E Black, and Cesar G Victora. Millennium development goals 4 and 5: progress and challenges. *BMC medicine*, 11(1):225, 2013.

[10] Jeffrey D Sachs. From millennium development goals to sustainable development goals. *The Lancet*, 379(9832):2206–2211, 2012.

[11] Derek Osborn, Amy Cutter, and Farooq Ullah. Universal sustainable development goals. *Understanding the Transformational Challenge for Developed Countries*, 2015.

[12] Fernando Althabe. *Born too soon: the global action report on preterm birth*. World Health Organization, 2012.

[13] WHO. Fact sheet - preterm birth. *Magnetic Resonance in Medicine*, 2016.

[14] World Health Organization et al. Born too soon: the global action report on preterm birth. 2012.

[15] Vincenzo Berghella. Post-term pregnancy. *Obstetric Evidence Based Guidelines*, page 183, 2007.

[16] Andrea K Sue-A-Quan, Mary E Hannah, Marsha M Cohen, Gary A Foster, and Robert M Liston. Effect of labour induction on rates of stillbirth and cesarean section in post-term pregnancies. *Cmaj*, 160(8):1145–1149, 1999.

[17] Luis Sanchez-Ramos, Felicia Olivier, Isaac Delke, and Andrew M Kaunitz. Labor induction versus expectant management for postterm pregnancies: a systematic review with meta-analysis. *Obstetrics & Gynecology*, 101(6):1312–1318, 2003.

[18] World Health Organization et al. *WHO recommendations for induction of labour*. World Health Organization, 2011.

[19] Joyce A Martin, Brady E Hamilton, Michelle JK Osterman, Anne K Driscoll, and TJ Mathews. Births: final data for 2015. 2017.

[20] Anneke Kwee, Michiel L Bots, Gerard HA Visser, and Hein W Bruinse. Obstetric management and outcome of pregnancy in women with a history of caesarean section in the netherlands. *European Journal of Obstetrics & Gynecology and Reproductive Biology*, 132(2):171–176, 2007.

[21] Helen Feltovich. Labour and delivery: a clinician's perspective on a biomechanics problem. *Interface Focus*, 9(5):20190032, 2019.

[22] Edward H Bishop. Pelvic scoring for elective induction. *Obstetrics & Gynecology*, 24(2):266–268, 1964.

[23] RB Newman, RL Goldenberg, JD Iams, PJ Meis, BM Mercer, AH Moawad, E Thom, M Miodovnik, SN Caritis, M Dombrowski, et al. Preterm prediction study: comparison of the cervical score and bishop score for prediction of spontaneous preterm delivery. *Obstetrics and gynecology*, 112(3):508, 2008.

[24] Jay D Iams, Robert L Goldenberg, Paul J Meis, Brian M Mercer, Atef Moawad, Anita Das, Elizabeth Thom, Donald McNellis, Rachel L Copper, Francee Johnson, et al. The length of the cervix and the risk of spontaneous premature delivery. *New England Journal of Medicine*, 334(9):567–573, 1996.

[25] E Celik, M To, K Gajewska, GCS Smith, and KH Nicolaides. Cervical length and obstetric history predict spontaneous preterm birth: development and validation of a model to provide individualized risk assessment. *Ultrasound in Obstetrics and Gynecology: The Official Journal of the International Society of Ultrasound in Obstetrics and Gynecology*, 31(5):549–554, 2008.

[26] P Rozenberg, S Chevret, and Y Ville. Comparison of pre-induction ultrasonographic cervical length and bishop score in predicting risk of cesarean section after labor induction with prostaglandins. *Gynecologie, obstetrique & fertilite*, 33(1-2):17–22, 2005.

[27] N Sananes, B Langer, A Gaudineau, R Kutnahorsky, G Aissi, G Fritz, E Boudier, B Viville, I Nisand, and R Favre. Prediction of spontaneous preterm delivery in singleton pregnancies: where are we and where are we going? a review of literature. *Journal of Obstetrics and Gynaecology*, 34(6):457–461, 2014.

[28] Michael G Ross and Marie H Beall. Prediction of preterm birth: nonsonographic cervical methods. In *Seminars in perinatology*, volume 33, pages 312–316. Elsevier, 2009.

[29] Helen Feltovich, Timothy J Hall, and Vincenzo Berghella. Beyond cervical length: emerging technologies for assessing the pregnant cervix. *American journal of obstetrics and gynecology*, 207(5):345–354, 2012.

[30] Mohammed R Khalil, Poul Thorsen, and Niels Uldbjerg. Cervical ultrasound elastography may hold potential to predict risk of preterm birth. *Dan Med J*, 60(1):A4570, 2013.

[31] M Swiatkowska-Freund and K Preis. Elastography of the uterine cervix: implications for success of induction of labor. *Ultrasound in Obstetrics & Gynecology*, 38(1):52–56, 2011.

[32] Susana Pereira, Alexander P Frick, Leona C Poon, Akaterina Zamprakou, and Kypros H Nicolaides. Successful induction of labor: prediction by preinduction cervical length, angle of progression and cervical elastography. *Ultrasound in Obstetrics & Gynecology*, 44(4):468–475, 2014.

[33] Marie Muller, Dora Aït-Belkacem, Mahdieh Hessabi, Jean-Luc Gennisson, Gilles Grangé, Francois Goffinet, Edouard Lecarpentier, Dominique Cabrol, Mickaël Tanter, and Vassilis Tsatsaris. Assessment of the cervix in pregnant women using shear wave elastography: a feasibility study. *Ultrasound in medicine & biology*, 41(11):2789–2797, 2015.

[34] Laura Peralta, Francisca Sonia Molina, Juan Melchor, Luisa Fernanda Gómez, Paloma Massó, Jesús Florido, and Guillermo Rus. Transient elastography to assess the cervical ripening during pregnancy: A preliminary study. *Ultraschall in der Medizin-European Journal of Ultrasound*, 38(04):395–402, 2017.

[35] Arrigo Fruscalzo, Ambrogio P Londero, and Ralf Schmitz. Quantitative cervical elastography during pregnancy: influence of setting features on strain calculation. *Journal of Medical Ultrasonics*, 42(3):387–394, 2015.

[36] GR Sutherland, MJ Stewart, KWE Groundstroem, CM Moran, A Fleming, FJ Guell-Peris, RA Riemersma, LN Fenn, KAA Fox, and WN McDicken. Color doppler myocardial imaging: a new technique for the assessment of myocardial function. *Journal of the American Society of Echocardiography*, 7(5):441–458, 1994.

[37] Anke Thomas, Sherko Kümmel, Ole Gemeinhardt, and Thomas Fischer. Real-time sonoelastography of the cervix: tissue elasticity of the normal and abnormal cervix. *Academic radiology*, 14(2):193–200, 2007.

[38] FS Molina, LF Gomez, J Florido, MC Padilla, and KH Nicolaides. Quantification of cervical elastography: a reproducibility study. *Ultrasound in Obstetrics & Gynecology*, 39(6):685–689, 2012.

[39] Arrigo Fruscalzo, R Schmitz, W Klockenbusch, and J Steinhard. Reliability of cervix elastography in the late first and second trimester of pregnancy. *Ultraschall in der Medizin-European Journal of Ultrasound*, 33(07):E101–E107, 2012.

[40] Arun Thitaikumar and Jonathan Ophir. Effect of lesion boundary conditions on axial strain elastograms: a parametric study. *Ultrasound in medicine & biology*, 33(9):1463–1467, 2007.

[41] Edgar Hernandez-Andrade, Roberto Romero, Steven J Korzeniewski, Hyunyoung Ahn, Alma Aurioles-Garibay, Maynor Garcia, Alyse G Schwartz, Lami Yeo, Tinnakorn Chaiworapongsa, and Sonia S Hassan. Cervical strain determined by ultrasound elastography and its association with spontaneous preterm delivery. *Journal of perinatal medicine*, 42(2):159–169, 2014.

[42] H Feltovich and TJ Hall. Quantitative imaging of the cervix: setting the bar. *Ultrasound in Obstetrics & Gynecology*, 41(2):121–128, 2013.

[43] Jeffrey Bamber, D Cosgrove, CF Dietrich, J Fromageau, J Bojunga, F Calliada, V Cantisani, J-M Correas, M Donofrio, EE Drakonaki, et al. Efsumb guidelines and recommendations on the clinical use of ultrasound elastography. part 1: Basic principles and technology. *Ultraschall in der Medizin-European Journal of Ultrasound*, 34(02):169–184, 2013.

[44] Lindsey C Carlson, Helen Feltovich, Mark L Palmeri, Jeremy J Dahl, A Munoz del Rio, and Timothy J Hall. Estimation of shear wave speed in the human uterine cervix. *Ultrasound in Obstetrics & Gynecology*, 43(4):452–458, 2014.

[45] Rebecca C Booi, Paul L Carson, Matthew O¡¯Donnell, Marilyn A Roubidoux, Anne L Hall, and Jonathan M Rubin. Characterization of cysts using differential correlation coefficient values from two dimensional breast elastography: preliminary study. *Ultrasound in medicine & biology*, 34(1):12–21, 2008.

[46] Marie Muller, Jean-Luc Gennisson, Thomas Deffieux, Mickaël Tanter, and Mathias Fink. Quantitative viscoelasticity mapping of human liver using supersonic shear imaging: preliminary in vivo feasability study. *Ultrasound in medicine & biology*, 35(2):219–229, 2009.

[47] Joy Y Vink, Sisi Qin, Clifton O Brock, Noelia M Zork, Helen M Feltovich, Xiaowei Chen, Paul Urie, Kristin M Myers, Timothy J Hall, Ronald Wapner, et al. A new paradigm for the role of smooth muscle cells in the human cervix. *American journal of obstetrics and gynecology*, 215(4):478–e1, 2016.

[48] M Fernandez, M House, S Jambawalikar, N Zork, J Vink, R Wapner, and K Myers. Investigating the mechanical function of the cervix during pregnancy using finite element models derived from high-resolution 3d mri. *Computer methods in biomechanics and biomedical engineering*, 19(4):404–417, 2016.

[49] Michael House, David L Kaplan, and Simona Socrate. Relationships between mechanical properties and extracellular matrix constituents of the cervical stroma during pregnancy. In *Seminars in perinatology*, volume 33, pages 300–307. Elsevier, 2009.

[50] Phyllis C Leppert. Anatomy and physiology of cervical ripening. *Clinical obstetrics and gynecology*, 38(2):267–279, 1995.

[51] Miklos Z Kiss, Maritza A Hobson, Tomy Varghese, Josephine Harter, Mark A Kliewer, Ellen M Hartenbach, and James A Zagzebski. Frequency-dependent complex modulus of the uterus: preliminary results. *Physics in Medicine & Biology*, 51(15):3683, 2006.

[52] Xuyuan Jiang, Patrick Asbach, Kaspar-Josche Streitberger, Anke Thomas, Bernd Hamm, Jürgen Braun, Ingolf Sack, and Jing Guo. In vivo high-resolution magnetic resonance elastography of the uterine corpus and cervix. *European radiology*, 24(12):3025–3033, 2014.

[53] Ivan M Rosado-Mendez, Mark L Palmeri, Lindsey C Drehfal, Quinton W Guerrero, Heather Simmons, Helen Feltovich, and Timothy J Hall. Assessment of structural heterogeneity and viscosity in the cervix using shear wave elasticity imaging: initial results from a rhesus macaque model. *Ultrasound in medicine & biology*, 43(4):790–803, 2017.

[54] Brenda Timmons, Meredith Akins, and Mala Mahendroo. Cervical remodeling during pregnancy and parturition. *Trends in Endocrinology & Metabolism*, 21(6):353–361, 2010.

[55] Edgar Hernandez-Andrade, Eli Maymon, Suchaya Luewan, Gaurav Bhatti, Mohammad Mehrmohammadi, Offer Erez, Percy Pacora, Bogdan Done, Sonia S Hassan, and Roberto Romero. A soft cervix, categorized by shear-wave elastography, in women with short or with normal cervical length at 18–24 weeks is associated with a higher prevalence of spontaneous preterm delivery. *Journal of perinatal medicine*, 46(5):489–501, 2018.

[56] Ivan M Rosado-Mendez, Lindsey C Carlson, Kaitlin M Woo, Andrew P Santoso, Quinton W Guerrero, Mark L Palmeri, Helen Feltovich, and Timothy J Hall. Quantitative assessment of cervical softening during pregnancy in the rhesus macaque with shear wave elasticity imaging. *Physics in Medicine & Biology*, 63(8):085016, 2018.

[57] Barbara L McFarlin, Viksit Kumar, Timothy A Bigelow, Douglas G Simpson, Rosemary C White-Traut, Jacques S Abramowicz, and William D O'Brien Jr. Beyond cervical length: A pilot study of ultrasonic attenuation for early detection of preterm birth risk. *Ultrasound in medicine & biology*, 41(11):3023–3029, 2015.

[58] Wang Yao, Kyoko Yoshida, Michael Fernandez, Joy Vink, Ronald J Wapner, Cande V Ananth, Michelle L Oyen, and Kristin M Myers. Measuring the compressive viscoelastic mechanical properties of human cervical tissue using indentation. *Journal of the mechanical behavior of biomedical materials*, 34:18–26, 2014.

[59] Juan Melchor and Guillermo Rus. Torsional ultrasonic transducer computational design optimization. *Ultrasonics*, (54):1950–1962, 2014.

[60] Antonio Callejas, Antonio Gomez, Juan Melchor, Miguel Riveiro, Paloma Massó, Jorge Torres, Modesto López-López, and Guillermo Rus. Performance study of a torsional wave sensor and cervical tissue characterization. *Sensors*, 17(9):2078, 2017.

[61] Eric Reissner and HF Sagoci. Forced torsional oscillations of an elastic half-space. i. *Journal of Applied Physics*, 15(9):652–654, 1944.

[62] Helen Feltovich, Timothy J. Hall, and Vincenzo Berghella. Beyond cervical length: emerging technologies for assessing the pregnant cervix. *American Journal of Obstetrics & Gynecology*, 207(5):345–354, 2012.

[63] Alan K Walden and Thomas R Howarth. Torsional shear wave transducer, June 14 1994. US Patent 5,321,333.

[64] Hannah Blencowe, Simon Cousens, Doris Chou, Mikkel Oestergaard, Lale Say, Ann-Beth Moller, Mary Kinney, Joy Lawn, and Born Too Soon Preterm Birth Action Group. Born too soon: the global epidemiology of 15 million preterm births. *Reproductive health*, 10(Suppl 1):S2–S2, 2013.

[65] Antonio Gomez. *Transurethral Shear Wave Elastography for prostate cancer*. PhD thesis, University College London, 2018.

[66] Stephane Cotin Herve Delingette Na. Efficient linear elastic models of soft tissues for real-time surgery simulation. Technical report, Tech. rep., Institut National de Recherche en Informoatique et en Automatique, 1998.

[67] Chenxi Zhang, Manning Wang, and Zhijian Song. A brain-deformation framework based on a linear elastic model and evaluation using clinical data. *IEEE Transactions on Biomedical Engineering*, 58(1):191–199, 2010.

[68] Cora Wex, Susann Arndt, Anke Stoll, Christiane Bruns, and Yuliya Kupriyanova. Isotropic incompressible hyperelastic models for modelling the mechanical behaviour of biological tissues: a review. *Biomedical Engineering/Biomedizinische Technik*, 60(6):577–592, 2015.

[69] Edgar Hernandez-Andrade, Sonia S Hassan, Hyunyoung Ahn, Steven J Korzeniewski, Lami Yeo, Tinnakorn Chaiworapongsa, and Roberto Romero. Evaluation of cervical stiffness during pregnancy using semiquantitative ultrasound elastography. *Ultrasound in Obstetrics & Gynecology*, 41(2):152–161, 2013.

[70] D Cosgrove, F Piscaglia, J Bamber, J Bojunga, J-M Correas, OH Gilja, AS Klauser, I Sporea, F Calliada, V Cantisani, et al. Efsumb guidelines and recommendations on the clinical use of ultrasound elastography. part 2: Clinical applications. *Ultraschall in der Medizin-European Journal of Ultrasound*, 34(03):238–253, 2013.

[71] David N Danforth. The morphology of the human cervix. *Clinical obstetrics and gynecology*, 26(1):7–13, 1983.

[72] ST Blackburn and DL Loper. Parturition and uterine physiology. *Maternal, Fetal, and Neonatal Physiology. A Clinical Perspective*, 1992.

[73] John OL DeLancey. Anatomie aspects of vaginal eversion after hysterectomy. *American journal of obstetrics and gynecology*, 166(6):1717–1728, 1992.

[74] Kristin M Myers, Helen Feltovich, Edoardo Mazza, Joy Vink, Michael Bajka, Ronald J Wapner, Timothy J Hall, and Michael House. The mechanical role of the cervix in pregnancy. *Journal of biomechanics*, 48(9):1511–1523, 2015.

[75] R Ann Word, Xiang-Hong Li, Michael Hnat, and Kelley Carrick. Dynamics of cervical remodeling during pregnancy and parturition: mechanisms and current concepts. In *Seminars in reproductive medicine*, volume 25, pages 069–079. Copyright© 2007 by Thieme Publishers, Inc., 333 Seventh Avenue, New York, 2007.

[76] Charles P Read, R Ann Word, Monika A Ruscheinsky, Brenda C Timmons, and Mala S Mahendroo. Cervical remodeling during pregnancy and parturition: molecular characterization of the softening phase in mice. *Reproduction*, 134(2):327–340, 2007.

[77] Jorge Torres, Inas Faris, and Antonio Callejas. Histobiomechanical remodeling of the cervix during pregnancy: Proposed framework. *Mathematical Problems in Engineering*, 2019, 2019.

[78] Joseph Jordan, Albert Singer, Howard Jones, and Mahmood Shafi. *The cervix*. John Wiley & Sons, 2009.

[79] Meredith L Akins, Katherine Luby-Phelps, Ruud A Bank, and Mala Mahendroo. Cervical softening during pregnancy: regulated changes in collagen cross-linking and composition of matricellular proteins in the mouse. *Biology of reproduction*, 84(5):1053–1062, 2011.

[80] Akira Ito, Kenji Kitamura, Yo Mori, and Shun Hirakawa. The change in solubility of type i collagen in human uterine cervix in pregnancy at term. *Biochemical medicine*, 21(3):262–270, 1979.

[81] Noelia M Zork, Kristin M Myers, Kyoko Yoshida, Serge Cremers, Hongfeng Jiang, Cande V Ananth, Ronald J Wapner, Jan Kitajewski, and Joy Vink. A systematic evaluation of collagen cross-links in the human cervix. *American journal of obstetrics and gynecology*, 212(3):321–e1, 2015.

[82] Peter Fratzl. Collagen: structure and mechanics, an introduction. In *Collagen*, pages 1–13. Springer, 2008.

[83] Markus J Buehler. Nanomechanics of collagen fibrils under varying cross-link densities: atomistic and continuum studies. *Journal of the mechanical behavior of biomedical materials*, 1(1):59–67, 2008.

[84] Elizabeth G Canty and Karl E Kadler. Procollagen trafficking, processing and fibrillogenesis. *Journal of cell science*, 118(7):1341–1353, 2005.

[85] Ellen AG Chernoff and Donald A Chernoff. Atomic force microscope images of collagen fibers. *Journal of Vacuum Science & Technology A: Vacuum, Surfaces, and Films*, 10(4):596–599, 1992.

[86] T Ushiki. Collagen fibers, reticular fibers and elastic fibers. *A comprehensive*.

[87] Y Lanir. A structural theory for the homogeneous biaxial stress-strain relationships in flat collagenous tissues. *Journal of biomechanics*, 12(6):423–436, 1979.

[88] Kristin Myers, Simona Socrate, Dimitrios Tzeranis, and Michael House. Changes in the biochemical constituents and morphologic appearance of the human cervical stroma during pregnancy. *European Journal of Obstetrics & Gynecology and Reproductive Biology*, 144:S82–S89, 2009.

[89] Meredith L Akins, Katherine Luby-Phelps, and Mala Mahendroo. Second harmonic generation imaging as a potential tool for staging pregnancy and predicting preterm birth. *Journal of biomedical optics*, 15(2):026020, 2010.

[90] WC Dale and Eric Baer. Fibre-buckling in composite systems: a model for the ultrastructure of uncalcified collagen tissues. *Journal of Materials Science*, 9(3):369–382, 1974.

[91] SP Magnusson, K Qvortrup, Jytte Overgaard Larsen, S Rosager, P Hanson, P Aagaard, M Krogsgaard, and M Kjaer. Collagen fibril size and crimp morphology in ruptured and intact achilles tendons. *Matrix biology*, 21(4):369–377, 2002.

[92] Carrie E Barnum, Jennifer L Fey, Stephanie N Weiss, Guillermo Barila, Amy G Brown, Brianne K Connizzo, Snehal S Shetye, Michal A Elovitz, and Louis J Soslowsky. Tensile mechanical properties and dynamic collagen fiber re-alignment of the murine cervix are dramatically altered throughout pregnancy. *Journal of biomechanical engineering*, 139(6):061008, 2017.

[93] Kristin M Myers, Simona Socrate, Anastassia Paskaleva, and Michael House. A study of the anisotropy and tension/compression behavior of human cervical tissue. *Journal of biomechanical engineering*, 132(2):021003, 2010.

[94] Richard M Aspden. Collagen organisation in the cervix and its relation to mechanical function. *Collagen and related research*, 8(2):103–112, 1988.

[95] Stephan Weiss, Thomas Jaermann, Peter Schmid, Philipp Staempfli, Peter Boesiger, Peter Niederer, Rosmarie Caduff, and Michael Bajka. Three-dimensional fiber architecture of the nonpregnant human uterus determined ex vivo using magnetic resonance diffusion tensor imaging. *The Anatomical Record Part A: Discoveries in Molecular, Cellular, and Evolutionary Biology: An Official Publication of the American Association of Anatomists*, 288(1):84–90, 2006.

[96] Lisa M Reusch, Helen Feltovich, Lindsey C Carlson, Gunnsteinn Hall, Paul J Campagnola, Kevin W Eliceiri, and Timothy J Hall. Nonlinear optical microscopy and ultrasound imaging of human cervical structure. *Journal of biomedical optics*, 18(3):031110, 2013.

[97] Phyllis C Leppert, Stephen Keller, Joseph Cerreta, Yvonne Hosannah, and Ines Mandl. The content of elastin in the uterine cervix. *Archives of biochemistry and biophysics*, 222(1):53–58, 1983.

[98] JF Woessner and Phyllis Carolyn Leppert. *The Extracellular matrix of the uterus, cervix, and fetal membranes: synthesis, degradation, and hormonal regulation*. Perinatology Press, 1991.

[99] Martin Guthold, Wenhua Liu, EA Sparks, LM Jawerth, L Peng, Michael Falvo, Richard Superfine, Roy R Hantgan, and Susan T Lord. A comparison of the mechanical and structural properties of fibrin fibers with other protein fibers. *Cell biochemistry and biophysics*, 49(3):165–181, 2007.

[100] Mieke MJF Koenders, Lanti Yang, Ronnie G Wismans, Kees O van der Werf, Dieter P Reinhardt, Willeke Daamen, Martin L Bennink, Pieter J Dijkstra, Toin H van Kuppevelt, and Jan Feijen. Microscale mechanical properties of single elastic fibers: the role of fibrillin–microfibrils. *Biomaterials*, 30(13):2425–2432, 2009.

[101] Pavel Dutov, Olga Antipova, Sameer Varma, Joseph PRO Orgel, and Jay D Schieber. Measurement of elastic modulus of collagen type i single fiber. *PloS one*, 11(1):e0145711, 2016.

[102] Zhilei Liu Shen, Mohammad Reza Dodge, Harold Kahn, Roberto Ballarini, and Steven J Eppell. In vitro fracture testing of submicron diameter collagen fibril specimens. *Biophysical journal*, 99(6):1986–1995, 2010.

[103] Marco PE Wenger, Laurent Bozec, Michael A Horton, and Patrick Mesquida. Mechanical properties of collagen fibrils. *Biophysical journal*, 93(4):1255–1263, 2007.

[104] Heath B Henninger, William R Valdez, Sara A Scott, and Jeffrey A Weiss. Elastin governs the mechanical response of medial collateral ligament under shear and transverse tensile loading. *Acta biomaterialia*, 25:304–312, 2015.

[105] Andreas J Schriefl, Thomas Schmidt, Daniel Balzani, Gerhard Sommer, and Gerhard A Holzapfel. Selective enzymatic removal of elastin and collagen from human abdominal aortas: Uniaxial mechanical response and constitutive modeling. *Acta biomaterialia*, 17:125–136, 2015.

[106] John E Scott. Proteoglycan-fibrillar collagen interactions. *Biochemical Journal*, 252(2):313, 1988.

[107] Lars Cöster. Structure and properties of dermatan sulphate proteoglycans, 1991.

[108] Yucel Akgul, Roxane Holt, Mark Mummert, Ann Word, and Mala Mahendroo. Dynamic changes in cervical glycosaminoglycan composition during normal pregnancy and preterm birth. *Endocrinology*, 153(7):3493–3503, 2012.

[109] EMAD El Maradny, N Kanayama, H Kobayashi, B Hossain, S Khatun, S Liping, T Kobayashi, and T Terao. The role of hyaluronic acid as a mediator and regulator of cervical ripening. *Human Reproduction (Oxford, England)*, 12(5):1080–1088, 1997.

[110] K v Maillot and BK Zimmermann. The solubility of collagen of the uterine cervix during pregnancy and labour. *Archives of Gynecology and Obstetrics*, 220(4):275–280, 1976.

[111] Ikuo Konishi, Shingo Fujii, Hirofumi Nonogaki, Yoshihiko Nanbu, Toshiko Iwai, and Takahide Mori. Immunohistochemical analysis of estrogen receptors, progesterone receptors, ki-67 antigen, and human papillomavirus dna in normal and neoplastic epithelium of the uterine cervix. *Cancer*, 68(6):1340–1350, 1991.

[112] DN Danforth. The squamous epithelium and squamocolumnar junction of the cervix during pregnancy. *American Journal of Obstetrics & Gynecology*, 60(5):985–999, 1950.

[113] Donald R Ostergard. The effect of pregnancy on the cervical squamocolumnar junction in patients with abnormal cervical cytology. *American journal of obstetrics and gynecology*, 134(7):759–760, 1979.

[114] Lorie M Harper, Aaron B Caughey, Anthony O Odibo, Kimberly A Roehl, Qiuhong Zhao, and Alison G Cahill. Normal progress of induced labor. *Obstetrics & Gynecology*, 119(6):1113–1118, 2012.

[115] Nicole S Carlson, Teri L Hernandez, and K Joseph Hurt. Parturition dysfunction in obesity: time to target the pathobiology. *Reproductive Biology and Endocrinology*, 13(1):135, 2015.

[116] Brian S Garra, E Ignacio Cespedes, Jonathan Ophir, Stephen R Spratt, Rebecca A Zuurbier, Colette M Magnant, and Marie F Pennanen. Elastography of breast lesions: initial clinical results. *Radiology*, 202(1):79–86, 1997.

[117] Shiu Yeh Yu, Carol A Tozzi, Joanne Babiarz, and Phyllis C Leppert. Collagen changes in rat cervix in pregnancy, polarized light microscopic and electron microscopic studies. *Proceedings of the Society for Experimental Biology and Medicine*, 209(4):360–368, 1995.

[118] Mikitaka Obara, Hideto Hirano, Masaki Ogawa, Hiromitsu Tsubaki, Naoko Hosoya, Yuko Yoshida, Satoshi Miyauchi, and Toshinobu Tanaka. Changes in molecular weight of hyaluronan and hyaluronidase activity in uterine cervical mucus in cervical ripening. *Acta obstetricia et gynecologica Scandinavica*, 80(6):492–496, 2001.

[119] SM Yellon, AM Mackler, and MA Kirby. The role of leukocyte traffic and activation in parturition. *Journal of the Society for Gynecologic Investigation*, 10(6):323–338, 2003.

[120] Benjamin D Byers, Egle Bytautiene, Maged M Costantine, Catalin S Buhimschi, Irina Buhimschi, George R Saade, and Nima Goharkhay. Hyaluronidase modifies the biomechanical properties of the rat cervix and shortens the duration of labor independent of myometrial contractility. *American journal of obstetrics and gynecology*, 203(6):596–e1, 2010.

[121] Ulla B Knudsen, Niels Uldbjerg, Tomasz Rechberger, and Kjeld Fredens. Eosinophils in human cervical ripening. *European Journal of Obstetrics & Gynecology and Reproductive Biology*, 72(2):165–168, 1997.

[122] N Uldbjerg, G Ekman, A Malmström, B Sporrong, U Ulmsten, and L Wingerup. Biochemical and morphological changes of human cervix after local application of prostaglandin e, in pregnancy. *The Lancet*, 317(8214):267–268, 1981.

[123] Niels Uldbjerg, Gunvor Ekman, Anders Malmström, Kjell Olsson, and Ulf Ulmsten. Ripening of the human uterine cervix related to changes in collagen, glycosaminoglycans, and collagenolytic activity. *American journal of obstetrics and gynecology*, 147(6):662–666, 1983.

[124] Kristin M Myers, AP Paskaleva, Michael House, and Simona Socrate. Mechanical and biochemical properties of human cervical tissue. *Acta biomaterialia*, 4(1):104–116, 2008.

[125] Mala Mahendroo. Cervical remodeling in term and preterm birth: insights from an animal model. *Reproduction*, 143(4):429–438, 2012.

[126] RE Garfield, George Saade, C Buhimschi, I Buhimschi, L Shi, SQ Shi, and K Chwalisz. Control and assessment of the uterus and cervix during pregnancy and labour. *Human Reproduction Update*, 4(5):673–695, 1998.

[127] R Osmers, W Rath, BC Adelmann-Grill, C Fittkow, M Kuloczik, M Szeverenyi, Harald Tschesche, and W Kuhn. Origin of cervical collagenase during parturition. *American Journal of Obstetrics and Gynecology*, 166(5):1455–1460, 1992.

[128] Yucel Akgul and Mala Mahendroo. Assessment of changes in the peripartum cervix. In *The Guide to Investigation of Mouse Pregnancy*, pages 723–731. Elsevier, 2014.

[129] Edoardo Mazza, Alessandro Nava, Margit Bauer, Raimund Winter, Michael Bajka, and Gerhard A Holzapfel. Mechanical properties of the human uterine cervix: an in vivo study. *Medical image analysis*, 10(2):125–136, 2006.

[130] Sabrina Badir, Michael Bajka, and Edoardo Mazza. A novel procedure for the mechanical characterization of the uterine cervix during pregnancy. *Journal of the mechanical behavior of biomedical materials*, 27:143–153, 2013.

[131] Charles Albert Elsberg. *Dr. Edwin Smith Surgical Papyrus and the Diagnosis and Treatment of Injuries to the Skull and Spine 5000 Years Ago*. 1931.

[132] Kevin J Parker, Marvin M Doyley, and Deborah J Rubens. Imaging the elastic properties of tissue: the 20 year perspective. *Physics in medicine & biology*, 56(1):R1, 2010.

[133] Peter R Hoskins, Kevin Martin, and Abigail Thrush. *Diagnostic ultrasound: physics and equipment*. Cambridge University Press, 2010.

[134] Christopher Rowland Hill, Jeff C Bamber, and Gail R ter Haar. Physical principles of medical ultrasonics, 2004.

[135] Thomas L Szabo. *Diagnostic ultrasound imaging: inside out*. Academic Press, 2004.

[136] K Kirk Shung. *Diagnostic ultrasound: Imaging and blood flow measurements*. CRC press, 2005.

[137] Jonathan Ophir, Ignacio Cespedes, Hm Ponnekanti, Youseph Yazdi, and Xin Li. Elastography: a quantitative method for imaging the elasticity of biological tissues. *Ultrasonic imaging*, 13(2):111–134, 1991.

[138] MM Maurer, S Badir, M Pensalfini, M Bajka, P Abitabile, R Zimmermann, and Edoardo Mazza. Challenging the in-vivo assessment of biomechanical properties of the uterine cervix: A critical analysis of ultrasound based quasi-static procedures. *Journal of biomechanics*, 48(9):1541–1548, 2015.

[139] A Fruscalzo and R Schmitz. Quantitative cervical elastography in pregnancy. *Ultrasound in Obstetrics & Gynecology*, 40(5):612–612, 2012.

[140] Aabir Chakraborty, Jeffrey C Bamber, and Neil L Dorward. Slip elastography: a novel method for visualising and characterizing adherence between two surfaces in contact. *Ultrasonics*, 52(3):364–376, 2012.

[141] Christopher Uff, Leo Garcia, Jeremie Fromageau, Aabir Chakraborty, Neil Dorward, and Jeffrey Bamber. Further characterization of changes in axial strain elastograms due to the presence of slippery tumor boundaries. *Journal of Medical Imaging*, 5(2):021211, 2018.

[142] Katja Köbbing, A Fruscalzo, K Hammer, M Möllers, M Falkenberg, R Kwiecien, W Klockenbusch, and R Schmitz. Quantitative elastography of the uterine cervix as a predictor of preterm delivery. *Journal of Perinatology*, 34(10):774, 2014.

[143] Fatma Doğa Öcal, Yasemin Cekmez, Emre Erdoğdu, Murad Gezer, İnci Fanuscu, Handan Özkan, Osman Fadil Kara, and Tuncay Kücüközkan. The utility of cervical elastosonography in prediction of cervical insufficiency: cervical elastosonography and cervical insufficiency. *The Journal of Maternal-Fetal & Neonatal Medicine*, 28(7):812–818, 2015.

[144] M Parra-Saavedra, L Gomez, A Barrero, G Parra, F Vergara, and E Navarro. Prediction of preterm birth using the cervical consistency index. *Ultrasound in Obstetrics & Gynecology*, 38(1):44–51, 2011.

[145] Slawomir Wozniak, Piotr Czuczwar, Piotr Szkodziak, Pawel Milart, Ewa Wozniakowska, and Tomasz Paszkowski. Elastography in predicting preterm delivery in asymptomatic, low-risk women: a prospective observational study. *BMC pregnancy and childbirth*, 14(1):238, 2014.

[146] LS Wilson, DE Robinson, and MJ Dadd. Elastography-the movement begins. *Physics in Medicine & Biology*, 45(6):1409, 2000.

[147] Hiroyasu Morikawa, Katsuhiko Fukuda, Sawako Kobayashi, Hideki Fujii, Shuji Iwai, Masaru Enomoto, Akihiro Tamori, Hiroki Sakaguchi, and Norifumi Kawada. Real-time tissue elastography as a tool for the noninvasive assessment of liver stiffness in patients with chronic hepatitis c. *Journal of gastroenterology*, 46(3):350–358, 2011.

[148] Paola Taroni, Daniela Comelli, Antonio Pifferi, Alessandro Torricelli, and Rinaldo Cubeddu. Absorption of collagen: effects on the estimate of breast composition and related diagnostic implications. *Journal of Biomedical Optics*, 12(1):014021, 2007.

[149] Raghu Ambekar, Tung-Yuen Lau, Michael Walsh, Rohit Bhargava, and Kimani C Toussaint. Quantifying collagen structure in breast biopsies using second-harmonic generation imaging. *Biomedical optics express*, 3(9):2021–2035, 2012.

[150] Robert M Lerner, Kevin J Parker, Jarle Holen, Raymond Gramiak, and Robert C Waag. Sono-elasticity: Medical elasticity images derived from ultrasound signals in mechanically vibrated targets. In *Acoustical imaging*, pages 317–327. Springer, 1988.

[151] Mostafa Fatemi and James F Greenleaf. Ultrasound-stimulated vibro-acoustic spectrography. *Science*, 280(5360):82–85, 1998.

[152] Laurent Sandrin, Mickaël Tanter, J-L Gennisson, Stefan Catheline, and Mathias Fink. Shear elasticity probe for soft tissues with 1-d transient elastography. *IEEE transactions on ultrasonics, ferroelectrics, and frequency control*, 49(4):436–446, 2002.

[153] Jérémy Bercoff, Mickael Tanter, and Mathias Fink. Supersonic shear imaging: a new technique for soft tissue elasticity mapping. *IEEE transactions on ultrasonics, ferroelectrics, and frequency control*, 51(4):396–409, 2004.

[154] Kathryn Nightingale, Mary Scott Soo, Roger Nightingale, and Gregg Trahey. Acoustic radiation force impulse imaging: in vivo demonstration of clinical feasibility. *Ultrasound in medicine & biology*, 28(2):227–235, 2002.

[155] Stefan Catheline, J-L Thomas, Francois Wu, and Mathias A Fink. Diffraction field of a low frequency vibrator in soft tissues using transient elastography. *IEEE transactions on ultrasonics, ferroelectrics, and frequency control*, 46(4):1013–1019, 1999.

[156] Stefan Catheline, Francois Wu, and Mathias Fink. A solution to diffraction biases in sonoelasticity: The acoustic impulse technique. *The Journal of the Acoustical Society of America*, 105(5):2941–2950, 1999.

[157] Laurent Sandrin, Stefan Catheline, Mickaël Tanter, Xavier Hennequin, and Mathias Fink. Time-resolved pulsed elastography with ultrafast ultrasonic imaging. *Ultrasonic imaging*, 21(4):259–272, 1999.

[158] TA Krouskop, DR Dougherty, FS Vinson, et al. A pulsed doppler ultrasonic system for making noninvasive measurements of the mechanical properties of soft tissue. *J Rehabil Res Dev*, 24(2):1–8, 1987.

[159] KJ Parker, SR Huang, RA Musulin, and RM Lerner. Tissue response to mechanical vibrations for sonoelasticity imaging. *Ultrasound in medicine & biology*, 16(3):241–246, 1990.

[160] R Muthupillai, DJ Lomas, PJ Rossman, James F Greenleaf, Armando Manduca, and Richard Lorne Ehman. Magnetic resonance elastography by direct visualization of propagating acoustic strain waves. *science*, 269(5232):1854–1857, 1995.

[161] Laurent Castéra, Julien Vergniol, Juliette Foucher, Brigitte Le Bail, Elise Chanteloup, Maud Haaser, Monique Darriet, Patrice Couzigou, and Victor de Lédinghen. Prospective comparison of transient elastography, fibrotest, apri, and liver biopsy for the assessment of fibrosis in chronic hepatitis c. *Gastroenterology*, 128(2):343–350, 2005.

[162] Laurent Sandrin, Bertrand Fourquet, Jean-Michel Hasquenoph, Sylvain Yon, Céline Fournier, Frédéric Mal, Christos Christidis, Marianne Ziol, Bruno Poulet, Farad Kazemi, et al. Transient elastography: a new noninvasive method for assessment of hepatic fibrosis. *Ultrasound in medicine & biology*, 29(12):1705–1713, 2003.

[163] Mathias Fink. Time reversal of ultrasonic fields. i. basic principles. *IEEE transactions on ultrasonics, ferroelectrics, and frequency control*, 39(5):555–566, 1992.

[164] J Bercoff, S Chaffai, M Tanter, L Sandrin, S Catheline, M Fink, JL Gennisson, and M Meunier. In vivo breast tumor detection using transient elastography. *Ultrasound in medicine & biology*, 29(10):1387–1396, 2003.

[165] J-L Gennisson, Thomas Deffieux, Mathias Fink, and Michaël Tanter. Ultrasound elastography: principles and techniques. *Diagnostic and interventional imaging*, 94(5):487–495, 2013.

[166] Kathryn R Nightingale, Mark L Palmeri, Roger W Nightingale, and Gregg E Trahey. On the feasibility of remote palpation using acoustic radiation force. *The Journal of the Acoustical Society of America*, 110(1):625–634, 2001.

[167] Wesley L Nyborg. Acoustic streaming near a boundary. *The Journal of the Acoustical Society of America*, 30(4):329–339, 1958.

[168] Armen P Sarvazyan, Oleg V Rudenko, and Wesley L Nyborg. Biomedical applications of radiation force of ultrasound: historical roots and physical basis. *Ultrasound in medicine & biology*, 36(9):1379–1394, 2010.

[169] Douglas Christensen. *Ultrasonic bioinstrumentation*. wiley, 1988.

[170] Gianmarco F Pinton, Jeremy J Dahl, and Gregg E Trahey. Rapid tracking of small displacements with ultrasound. *IEEE transactions on ultrasonics, ferroelectrics, and frequency control*, 53(6):1103–1117, 2006.

[171] Tsuyoshi Shiina, Kathryn R Nightingale, Mark L Palmeri, Timothy J Hall, Jeffrey C Bamber, Richard G Barr, Laurent Castera, Byung Ihn Choi, Yi-Hong Chou, David Cosgrove, et al. Wfumb guidelines and recommendations for clinical use of ultrasound elastography: Part 1: basic principles and terminology. *Ultrasound in medicine & biology*, 41(5):1126–1147, 2015.

[172] Mark L Palmeri and Kathryn R Nightingale. Acoustic radiation force-based elasticity imaging methods. *Interface focus*, 1(4):553–564, 2011.

[173] Kathryn Nightingale, Stephen McAleavey, and Gregg Trahey. Shear-wave generation using acoustic radiation force: in vivo and ex vivo results. *Ultrasound in medicine & biology*, 29(12):1715–1723, 2003.

[174] Armen P Sarvazyan, Oleg V Rudenko, Scott D Swanson, J Brian Fowlkes, and Stanislav Y Emelianov. Shear wave elasticity imaging: a new ultrasonic technology of medical diagnostics. *Ultrasound in medicine & biology*, 24(9):1419–1435, 1998.

[175] Wei Meng, Guangchen Zhang, Changjun Wu, Guozhu Wu, Yan Song, and Zhaoling Lu. Preliminary results of acoustic radiation force impulse (arfi) ultrasound imaging of breast lesions. *Ultrasound in medicine & biology*, 37(9):1436–1443, 2011.

[176] Liang Zhai, John Madden, Wen-Chi Foo, Mark L Palmeri, Vladimir Mouraviev, Thomas J Polascik, and Kathryn R Nightingale. Acoustic radiation force impulse imaging of human prostates ex vivo. *Ultrasound in medicine & biology*, 36(4):576–588, 2010.

[177] Kathryn Nightingale, Mark Palmeri, and Gregg Trahey. Analysis of contrast in images generated with transient acoustic radiation force. *Ultrasound in medicine & biology*, 32(1):61–72, 2006.

[178] Mark L Palmeri, Michael H Wang, Ned C Rouze, Manal F Abdelmalek, Cynthia D Guy, Barry Moser, Anna Mae Diehl, and Kathryn R Nightingale. Noninvasive evaluation of hepatic fibrosis using acoustic radiation force-based shear stiffness in patients with nonalcoholic fatty liver disease. *Journal of hepatology*, 55(3):666–672, 2011.

[179] J Bercoff, M Pernot, M Tanter, and M Fink. Monitoring thermally-induced lesions with supersonic shear imaging. *Ultrasonic imaging*, 26(2):71–84, 2004.

[180] Ivan Z Nenadic, Matthew W Urban, James F Greenleaf, Jean-Luc Gennisson, Miguel Bernal, and Mickael Tanter. *Ultrasound Elastography for Biomedical Applications and Medicine*. John Wiley & Sons, 2019.

[181] Jeremy Bercoff, Mickael Tanter, Sana Chaffai, and Mathias Fink. Ultrafast imaging of beamformed shear waves induced by the acoustic radiation force. application to transient elastography. In *Proceedings of the 2002 IEEE Ultrasonics Symposium*, volume 2, pages 1899–1902, 2002.

[182] Jeremy Bercoff, Mickaël Tanter, and Mathias Fink. Sonic boom in soft materials: The elastic cerenkov effect. *Applied Physics Letters*, 84(12):2202–2204, 2004.

[183] Thomas Deffieux, Jean-Luc Gennisson, Benoit Larrat, Mathias Fink, and Mickael Tanter. The variance of quantitative estimates in shear wave imaging: theory and experiments. *IEEE transactions on ultrasonics, ferroelectrics, and frequency control*, 59(11):2390–2410, 2012.

[184] Mel E Stratmeyer and Frederic L Lizzi. Special issue on the biological effects of ultrasound. *IEEE transactions on ultrasonics, ferroelectrics, and frequency control*, 33(2):137–138, 1986.

[185] Stanley B Barnett and George Kossoff. *Safety of diagnostic ultrasound*. London, Parthenon, 1998.

[186] Abderrahmane Ouared, Emmanuel Montagnon, and Guy Cloutier. Generation of remote adaptive torsional shear waves with an octagonal phased array to enhance displacements and reduce variability of shear wave speeds: Comparison with quasi-plane shear wavefronts. *Physics in Medicine & Biology*, 60(20):8161, 2015.

[187] Davide Valtorta and Edoardo Mazza. Dynamic measurement of soft tissue viscoelastic properties with a torsional resonator device. *Medical Image Analysis*, 9(5):481–490, 2005.

[188] A Gomez, G Rus, and N Saffari. Use of shear waves for diagnosis and ablation monitoring of prostate cancer: a feasibility study. In *Journal of Physics: Conference Series*, volume 684, page 012006. IOP Publishing, 2016.

[189] Juan Manuel Melchor Rodríguez. *Mechanics of nonlinear ultrasound in tissue*. PhD thesis, Universidad de Granada, 2016.

[190] A Thomas. Imaging of the cervix using sonoelastography. *Ultrasound in Obstetrics and Gynecology: The Official Journal of the International Society of Ultrasound in Obstetrics and Gynecology*, 28(3):356–357, 2006.

[191] Joyce A Martin, Brady E Hamilton, Stephanie J Ventura, Michelle JK Osterman, and TJ Mathews. Births: final data for 2011. 2013.

[192] A Fruscalzo, AP Londero, C Fröhlich, U Möllmann, and R Schmitz. Quantitative elastography for cervical stiffness assessment during pregnancy. *BioMed research international*, 2014, 2014.

[193] Edoardo Mazza, Miguel Parra-Saavedra, Michael Bajka, Eduard Gratacos, Kypros Nicolaides, and Jan Deprest. In vivo assessment of the biomechanical properties of the uterine cervix in pregnancy. *Prenatal diagnosis*, 34(1):33–41, 2014.

[194] Arrigo Fruscalzo, Edoardo Mazza, Helen Feltovich, and Ralf Schmitz. Cervical elastography during pregnancy: a critical review of current approaches with a focus on controversies and limitations. *Journal of Medical Ultrasonics*, 43(4):493–504, 2016.

[195] Han Sung Hwang, In Sook Sohn, and Han Sung Kwon. Imaging analysis of cervical elastography for prediction of successful induction of labor at term. *Journal of Ultrasound in Medicine*, 32(6):937–946, 2013.

[196] Lene Hee, Christina K Rasmussen, Jacob M Schlütter, Puk Sandager, and Niels Uldbjerg. Quantitative sonoelastography of the uterine cervix prior to induction of labor as a predictor of cervical dilation time. *Acta obstetricia et gynecologica Scandinavica*, 93(7):684–690, 2014.

[197] Lindsey C Carlson, Helen Feltovich, Mark L Palmeri, Alejandro Munoz del Rio, and Timothy J Hall. Statistical analysis of shear wave speed in the uterine cervix. *IEEE transactions on ultrasonics, ferroelectrics, and frequency control*, 61(10):1651–1660, 2014.

[198] Lindsey C Carlson, Stephanie T Romero, Mark L Palmeri, A Muñoz del Rio, Sean M Esplin, Veronica M Rotemberg, Timothy J Hall, and Helen Feltovich. Changes in shear wave speed pre-and post-induction of labor: a feasibility study. *Ultrasound in Obstetrics & Gynecology*, 46(1):93–98, 2015.

[199] Edgar Hernandez-Andrade, Alma Aurioles-Garibay, Maynor Garcia, Steven J Korzeniewski, Alyse G Schwartz, Hyunyoung Ahn, Alicia Martinez-Varea, Lami Yeo, Tinnakorn Chaiworapongsa, Sonia S Hassan, et al. Effect of depth on shear-wave elastography estimated in the internal and external cervical os during pregnancy. *Journal of perinatal medicine*, 42(5):549–557, 2014.

[200] Lindsey C Carlson, Timothy J Hall, Ivan M Rosado-Mendez, Mark L Palmeri, and Helen Feltovich. Detection of changes in cervical softness using shear wave speed in early versus late pregnancy: An in vivo cross-sectional study. *Ultrasound in medicine & biology*, 44(3):515–521, 2018.

[201] Lei Shi, Wang Yao, Yu Gan, Lily Zhao, William Eugene McKee, Joy Vink, Ronanld Wapner, Christine Hendon, and Kristin Myers. Anisotropic material characterization of human cervix tissue based on indentation. *Journal of biomechanical engineering*, 2019.

[202] Sasiwan Suthasmalee and Sakita Moungmaithong. Cervical shear wave elastography as a predictor of preterm delivery during 18–24 weeks of pregnancy. *Journal of Obstetrics and Gynaecology Research*, 2019.

[203] Lindsey C Carlson, Timothy J Hall, Ivan M Rosado-Mendez, Lu Mao, and Helen Feltovich. Quantitative assessment of cervical softening during pregnancy with shear wave elasticity imaging: an in vivo longitudinal study. *Interface Focus*, 9(5):20190030, 2019.

[204] Karl F Graff. *Wave motion in elastic solids*. Courier Corporation, 2012.

[205] Guillermo Rus. Nature of acoustic nonlinear radiation stress. *Applied Physics Letters*, 105(12):121904, 2014.

[206] Marko Orescanin, Yue Wang, and Michael F Insana. 3-d fdtd simulation of shear waves for evaluation of complex modulus imaging. *IEEE transactions on ultrasonics, ferroelectrics, and frequency control*, 58(2):389–398, 2011.

[207] Jérémy Bercoff, Mickaël Tanter, Marie Muller, and Mathias Fink. The role of viscosity in the impulse diffraction field of elastic waves induced by the acoustic radiation force. *IEEE transactions on ultrasonics, ferroelectrics, and frequency control*, 51(11):1523–1536, 2004.

[208] LD Landau and EM Lifshitz. Elasticity theory. 1975.

[209] Mark F Hamilton, Yurii A Ilinskii, and Evgenia A Zabolotskaya. Separation of compressibility and shear deformation in the elastic energy density (l). *The Journal of the Acoustical Society of America*, 116(1):41–44, 2004.

[210] A Cemal Eringen and ES Suhubi. Nonlinear theory of simple micro-elastic solids. *International Journal of Engineering Science*, 2(2):189–203, 1964.

[211] Rafael Muñoz and Juan Melchor. Nonlinear classical elasticity model for materials with fluid and matrix phases. *Mathematical Problems in Engineering*, 2018, 2018.

[212] Melvin Mooney. A theory of large elastic deformation. *Journal of applied physics*, 11(9):582–592, 1940.

[213] RS Rivlin. Large elastic deformations of isotropic materials iv. further developments of the general theory. *Philosophical Transactions of the Royal Society of London. Series A, Mathematical and Physical Sciences*, 241(835):379–397, 1948.

[214] PALS Martins, RM Natal Jorge, and AJM Ferreira. A comparative study of several material models for prediction of hyperelastic properties: Application to silicone-rubber and soft tissues. *Strain*, 42(3):135–147, 2006.

[215] Raymond William Ogden. Large deformation isotropic elasticity–on the correlation of theory and experiment for incompressible rubberlike solids. *Proceedings of the Royal Society of London. A. Mathematical and Physical Sciences*, 326(1567):565–584, 1972.

[216] Guillermo Rus, Rafael Muñoz, Juan Melchor, Ruben Molina, Antonio Callejas, Miguel Riveiro, Paloma Massó, Jorge Torres, Gerardo Moreu, Francisca Molina, et al. Torsion ultrasonic sensor for tissue mechanical characterization. In *2016 IEEE International Ultrasonics Symposium (IUS)*, pages 1–4. IEEE, 2016.

[217] J Melchor and G Rus. Torsional ultrasonic transducer computational design optimization. *Ultrasonics*, 54(7):1950–1962, 2014.

[218] Juan Melchor, Rafael Muñoz, and Guillermo Rus. Torsional ultrasound sensor optimization for soft tissue characterization. *Sensors*, 17(6):1402, 2017.

[219] Robert L Taylor. *FEAP-ein finite element analysis programm*. Ing.-Gemeinschaft Klee & Wrigges, 1987.

[220] Jin O Kim and Oh Soo Kwon. Vibration characteristics of piezoelectric torsional transducers. *Journal of sound and vibration*, 264(2):453–473, 2003.

[221] Dieter Klatt, Uwe Hamhaber, Patrick Asbach, Jürgen Braun, and Ingolf Sack. Noninvasive assessment of the rheological behavior of human organs using multifrequency mr elastography: a study of brain and liver viscoelasticity. *Physics in Medicine & Biology*, 52(24):7281, 2007.

[222] Shigao Chen, Mostafa Fatemi, and James F Greenleaf. Quantifying elasticity and viscosity from measurement of shear wave speed dispersion. *The Journal of the Acoustical Society of America*, 115(6):2781–2785, 2004.

[223] Christopher W Macosko and Ronald G Larson. Rheology: principles, measurements, and applications. 1994.

[224] Lloyd B Eldred, William P Baker, and Anthony N Palazotto. Kelvin-voigt versus fractional derivative model as constitutive relations for viscoelastic materials. *AIAA journal*, 33(3):547–550, 1995.

[225] Matthew W Urban, Ivan Z Nenadic, Scott A Mitchell, Shigao Chen, and James F Greenleaf. Generalized response of a sphere embedded in a viscoelastic medium excited by an ultrasonic radiation force. *The Journal of the Acoustical Society of America*, 130(3):1133–1141, 2011.

[226] Carolina Amador, Randall R Kinnick, Matthew W Urban, Mostafa Fatemi, and James F Greenleaf. Viscoelastic tissue mimicking phantom validation study with shear wave elasticity imaging and viscoelastic spectroscopy. In *2015 IEEE International Ultrasonics Symposium (IUS)*, pages 1–4. IEEE, 2015.

[227] José M Carcione. *Wave fields in real media: Wave propagation in anisotropic, anelastic, porous and electromagnetic media*, volume 38. Elsevier, 2007.

[228] Marko Orescanin and Michael F Insana. Shear modulus estimation with vibrating needle stimulation. *IEEE transactions on ultrasonics, ferroelectrics, and frequency control*, 57(6):1358–1367, 2010.

[229] Alexander Ya Malkin and Avraam I Isayev. *Rheology: concepts, methods, and applications*. Elsevier, 2017.

[230] Roger W Chan and Ingo R Titze. Viscoelastic shear properties of human vocal fold mucosa: Measurement methodology and empirical results. *The Journal of the Acoustical Society of America*, 106(4):2008–2021, 1999.

[231] Fernando Campos, Ana B Bonhome-Espinosa, Laura García-Martínez, Juan DG Durán, Modesto T López-López, Miguel Alaminos, María Carmen Sánchez-Quevedo,

and Víctor Carriel. Ex vivo characterization of a novel tissue-like cross-linked fibrin-agarose hydrogel for tissue engineering applications. *Biomedical Materials*, 11(5):055004, 2016.

[232] IA Rodriguez, MT López-López, ACX Oliveira, MC Sánchez-Quevedo, A Campos, M Alaminos, and JDG Durán. Rheological characterization of human fibrin and fibrin–agarose oral mucosa substitutes generated by tissue engineering. *Journal of tissue engineering and regenerative medicine*, 6(8):636–644, 2012.

[233] YC Fung. Biomechanical aspects of growth and tissue engineering. In *Biomechanics*, pages 499–546. Springer, 1990.

[234] L Peralta, G Rus, N Bochud, and FS Molina. Assessing viscoelasticity of shear wave propagation in cervical tissue by multiscale computational simulation. *Journal of biomechanics*, 48(9):1549–1556, 2015.

[235] Luciano Alonson Renteria and Juan M Perez Oria. A modified finite differences method for analysis of ultrasonic propagation in nonhomogeneous media. *Journal of Computational Acoustics*, 18(01):31–45, 2010.

[236] Kane Yee. Numerical solution of initial boundary value problems involving maxwell's equations in isotropic media. *IEEE Transactions on antennas and propagation*, 14(3):302–307, 1966.

[237] Raul Madariaga. Dynamics of an expanding circular fault. *Bulletin of the Seismological Society of America*, 66(3):639–666, 1976.

[238] Jean Virieux. P-sv wave propagation in heterogeneous media: Velocity-stress finite-difference method. *Geophysics*, 51(4):889–901, 1986.

[239] Jidong Zhao and Dorival Pedroso. Strain gradient theory in orthogonal curvilinear coordinates. *International Journal of Solids and Structures*, 45(11-12):3507–3520, 2008.

[240] Peter J Olver. *Introduction to partial differential equations*. Springer, 2014.

[241] Thomas G Moore, Jeffery G Blaschak, Allen Taflove, and Gregory A Kriegsmann. Theory and application of radiation boundary operators. *IEEE Transactions on Antennas and Propagation*, 36(12):1797–1812, 1988.

[242] Barbrina Dunmire, John C Kucewicz, Stuart B Mitchell, Lawrence A Crum, and K Michael Sekins. Characterizing an agar/gelatin phantom for image guided dosing and feedback control of high-intensity focused ultrasound. *Ultrasound in medicine & biology*, 39(2):300–311, 2013.

[243] Tobias Leutenegger and Jürg Dual. Non-destructive testing of tubes using a time reverse numerical simulation (trns) method. *Ultrasonics*, 41(10):811–822, 2004.

[244] Daniel Gsell, Tobias Leutenegger, and Jürg Dual. Modeling three-dimensional elastic wave propagation in circular cylindrical structures using a finite-difference approach. *The Journal of the Acoustical Society of America*, 116(6):3284–3293, 2004.

[245] P Fellinger, R Marklein, KJ Langenberg, and S Klaholz. Numerical modeling of elastic wave propagation and scattering with efit, elastodynamic finite integration technique. *Wave motion*, 21(1):47–66, 1995.

[246] Allen Taflove and Susan C Hagness. *Computational electrodynamics: the finite-difference time-domain method*. Artech house, 2005.

[247] INNITIUS Patent. Dispositivo emisor de ondas ultrasónicas de torsión y transductor que lo comprende. *Extensiones Internacionales, PCT/ES2016/070540*, 2015.

[248] Guillermo Rus and Juan Melchor. Logical inference framework for experimental design of mechanical characterization procedures. *Sensors*, 18(9):2984, 2018.

[249] Richard T Cox. Probability, frequency and reasonable expectation. *American journal of physics*, 14(1):1–13, 1946.

[250] John Maynard Keynes. *A treatise on probability*. Courier Corporation, 2013.

[251] Rudolf Carnap. Philosophy and logical syntax, kegan paul, trench, trubner & co. *Ltd., London*, 1935.

[252] Guillermo Rus, Juan Chiachío, and Manuel Chiachío. Logical inference for inverse problems. *Inverse Problems in Science and Engineering*, 24(3):448–464, 2016.

[253] Andrei N Kolmogorov. Three approaches to the quantitative definition ofinformation'. *Problems of information transmission*, 1(1):1–7, 1965.

[254] Albert Tarantola. *Inverse problem theory and methods for model parameter estimation*, volume 89. siam, 2005.

[255] Philip R Bevington, D Keith Robinson, J Morris Blair, A John Mallinckrodt, and Susan McKay. Data reduction and error analysis for the physical sciences. *Computers in Physics*, 7(4):415–416, 1993.

[256] Stuart L Meyer. Data analysis for scientists and engineers. 1975.

[257] Frederick James. *Statistical methods in experimental physics*. World Scientific Publishing Company, 2006.

[258] Richard T Cox. The algebra of probable inference. *American Journal of Physics*, 31(1):66–67, 1963.

[259] Antonio Callejas, Antonio Gomez, Inas H Faris, Juan Melchor, and Guillermo Rus. Kelvin–voigt parameters reconstruction of cervical tissue-mimicking phantoms using torsional wave elastography. *Sensors*, 19(15):3281, 2019.

[260] Rosa M.S. Sigrist, Joy Liau, Ahmed El Kaffas, Maria Cristina Chammas, and Juergen K. Willmann. Ultrasound elastography: Review of techniques and clinical applications. In *Theranostics*, 2017.

[261] Jonathan Ophir, I Céspedes, Hari Ponnekanti, Youseph Yazdi, and Xingzhong Li. Elastography: a quantitative method for imaging the elasticity of biological tissues. *Ultrasonic imaging*, 13 2:111–34, 1991.

[262] Jean luc Gennisson, Thomas Deffieux, Mathias Fink, and Mickaël Tanter. Ultrasound elastography: principles and techniques. *Diagnostic and interventional imaging*, 94 5:487–95, 2013.

[263] Yufeng Deng, Ned C. Rouze, Mark L. Palmeri, and Kathryn Nightingale. Ultrasonic shear wave elasticity imaging (swei) sequencing and data processing using a verasonics research scanner. In *IEEE Transactions on Ultrasonics, Ferroelectrics, and Frequency Control*, 2016.

[264] Mark L. Palmeri, Stephen A. McAleavey, Gregg E. Trahey, and Kathryn Nightingale. Ultrasonic tracking of acoustic radiation force-induced displacements in homogeneous media. *IEEE Transactions on Ultrasonics, Ferroelectrics and Frequency Control*, 53:1300–1313, 2006.

[265] Thomas Deffieux, Jean luc Gennisson, Benoît Larrat, Maximilian Fink, and Mickaël Tanter. The variance of quantitative estimates in shear wave imaging: Theory and experiments. *IEEE Transactions on Ultrasonics, Ferroelectrics and Frequency Control*, 59, 2012.

[266] Thanasis Loupas, J. Powers, and R. W. Gill. An axial velocity estimator for ultrasound blood flow imaging, based on a full evaluation of the doppler equation by means of a two-dimensional autocorrelation approach. *IEEE Transactions on Ultrasonics, Ferroelectrics and Frequency Control*, 42:672–688, 1995.

[267] Alfonso Rodriguez-Molares, Ole Marius Hoel Rindal, Olivier Bernard, Hervé Liebgott, Andreas Austeng, and Lasse Lovstakken. The ultrasound toolbox. *2017 IEEE International Ultrasonics Symposium (IUS)*, pages 1–1, 2017.

[268] Hans L Oestreicher. Field and impedance of an oscillating sphere in a viscoelastic medium with an application to biophysics. *The Journal of the Acoustical Society of America*, 23(6):707–714, 1951.

[269] Yoshiki Yamakoshi, Junichi Sato, and Takuso Sato. Ultrasonic imaging of internal vibration of soft tissue under forced vibration. *IEEE transactions on ultrasonics, ferroelectrics, and frequency control*, 37(2):45–53, 1990.

[270] Shigao Chen, Matthew W Urban, Cristina Pislaru, Randall Kinnick, Yi Zheng, Aiping Yao, and James F Greenleaf. Shearwave dispersion ultrasound vibrometry (sduv) for measuring tissue elasticity and viscosity. *IEEE transactions on ultrasonics, ferroelectrics, and frequency control*, 56(1):55–62, 2009.

[271] Farid G Mitri, Matthew W Urban, Mostafa Fatemi, and James F Greenleaf. Shear wave dispersion ultrasonic vibrometry for measuring prostate shear stiffness and viscosity: an in vitro pilot study. *IEEE transactions on biomedical engineering*, 58(2):235–242, 2011.

[272] Antonio Jesús Gómez Fernández. *Transurethral shear wave elastography for prostate cancer*. PhD thesis, UCL (University College London), 2018.

[273] MR Mansouri and H Darijani. Constitutive modeling of isotropic hyperelastic materials in an exponential framework using a self-contained approach. *International Journal of Solids and Structures*, 51(25-26):4316–4326, 2014.

[274] Antoine Patalano, Carlos Marcelo García, and Andrés Rodríguez. Rectification of image velocity results (river): a simple and user-friendly toolbox for large scale water

surface particle image velocimetry (piv) and particle tracking velocimetry (ptv). *Computers & Geosciences*, 109:323–330, 2017.

[275] A Patalano, CM Garcia, W Brevis, T Bleninger, N Guillen, L Moreno, and A Rodriguez. Recent advances in eulerian and lagragian large-scale particle image velocimetry. In *E-proceedings of the 36th IAHR World Congress, The Hauge, Netherlands*, 2015.

[276] Paloma Massó, Antonio Callejas, Juan Melchor, Francisca S Molina, and Guillermo Rus. In vivo measurement of cervical elasticity on pregnant women by torsional wave technique: A preliminary study. *Sensors*, 19(15):3249, 2019.

[277] Food and Drug Administration, "Information for Manufacturers Seeking Marketing Clearance of Diagnostic Ultrasound Systems and Transducer". *U. S. Dept. Health and Human Services, Food and Drug Administration, Center for Devices and Radiological Health*, 1997.

[278] Laura Peralta, Eve Mourier, Christophe Richard, Gilles Charpigny, Thibaut Larcher, Dora Aït-Belkacem, Naveen K Balla, Sophie Brasselet, Mickael Tanter, Marie Muller, et al. In vivo evaluation of cervical stiffness evolution during induced ripening using shear wave elastography, histology and 2 photon excitation microscopy: insight from an animal model. *PloS one*, 10(8):e0133377, 2015.

[279] Haoming Lin, Yuanyuan Shen, Xin Chen, Ying Zhu, Yi Zheng, Xinyu Zhang, Yanrong Guo, Tianfu Wang, and Siping Chen. Viscoelastic properties of normal rat liver measured by ultrasound elastography: Comparison with oscillatory rheometry. *Biorheology*, 53(5-6):193–207, 2016.

[280] Miguel Bernal, Jean-Luc Gennisson, Patrice Flaud, and Mickael Tanter. Correlation between classical rheometry and supersonic shear wave imaging in blood clots. *Ultrasound in medicine & biology*, 39(11):2123–2136, 2013.

[281] Man M Nguyen, Shiwei Zhou, Jean-luc Robert, Vijay Shamdasani, and Hua Xie. Development of oil-in-gelatin phantoms for viscoelasticity measurement in ultrasound shear wave elastography. *Ultrasound in medicine & biology*, 40(1):168–176, 2014.

[282] M Tanter, D Touboul, J L Gennisson, J Bercoff, and M Fink. High-resolution quantitative imaging of cornea elasticity using supersonic shear imaging. *IEE Transactions on medical imaging*, 28(12):1881–1893, 2009.

[283] LD Landau. Lifshitz (1970) theory of elasticity.

[284] Badar Rashid, Michel Destrade, and Michael D Gilchrist. Mechanical characterization of brain tissue in tension at dynamic strain rates. *Journal of the mechanical behavior of biomedical materials*, 33:43–54, 2014.

[285] Miroslav Zemánek, Jiří Burša, and Michal Děták. Biaxial tension tests with soft tissues of arterial wall. *Engineering Mechanics*, 16(1):3–11, 2009.

[286] Sabrina Badir, Edoardo Mazza, Roland Zimmermann, and Michael Bajka. Cervical softening occurs early in pregnancy: characterization of cervical stiffness in 100 healthy women using the aspiration technique. *Prenatal diagnosis*, 33(8):737–741, 2013.

[287] L Peralta, G Rus, N Bochud, and FS Molina. Mechanical assessment of cervical remodelling in pregnancy: insight from a synthetic model. *Journal of biomechanics*, 48(9):1557–1565, 2015.

[288] Temel K Yasar, Thomas J Royston, and Richard L Magin. Wideband mr elastography for viscoelasticity model identification. *Magnetic resonance in medicine*, 70(2):479–489, 2013.

[289] G Rus, M Riveiro, and FS Molina. Effect of contact conditions of torsional wave elastographic probe on human cervix. *Mathematical Problems in Engineering*, 2018, 2018.

[290] J David N Cheeke. *Fundamentals and applications of ultrasonic waves*. CRC press, 2016.